Nonlinear Optical Phenomena in Hybrid TeO_2-Si_3N_4 Waveguides

NONLINEAR OPTICAL PHENOMENA IN HYBRID TeO_2-Si_3N_4 WAVEGUIDES

By Hamidu M. Mbonde,

A thesis submitted to the School of Graduate Studies in partial fulfillment of the requirements for the Degree Ph.D.

McMaster University

Ph.D. (2022)

Hamilton, Ontario (Department of Engineering Physics)

TITLE: Nonlinear Optical Phenomena in Hybrid TeO_2-Si_3N_4 Waveguides

AUTHOR: Hamidu M. Mbonde (McMaster University)

SUPERVISOR: Dr. Jonathan D. B. Bradley

NUMBER OF PAGES: xxiii, 194

Abstract

Over the last few decades nonlinear integrated optical devices have emerged as an enabling technology for a number of important applications in communications, computing, sensing, medical, and defense and security systems. It all has been possible through the advancement of micro and nano-fabrication techniques and the development of nonlinear optical materials that can leverage the mature complementary metal-oxide semiconductor (CMOS) infrastructure. Among the materials explored for integrated nonlinear photonics silicon nitride (Si_3N_4) is one of the most suitable and widely used. Despite its maturity and prominence, there are a few challenges that persist. One of them is the difficulty in the fabrication of thick low-loss Si_3N_4 waveguides suitable for nonlinear applications using conventional wafer-scale methods. In particular, a waveguide thickness of at least 700 nm is needed to attain anomalous dispersion which is critical for efficient nonlinear processes. However, fabricating such waveguides through the preferred method of low-pressure chemical vapor deposition is challenging due to cracks developing during deposition caused by the differences in tensile stress between the Si_3N_4 layer and substrate. Tellurium oxide (TeO_2) is among the oxide glasses with the most attractive optical properties. TeO_2 has a relatively large linear refractive index, wide transparency, high nonlinearity, high Raman gain, high acousto-optic figure of merit, negligible nonlinear losses, and high rare earth dopants solubility making it a good candidate for linear, nonlinear, and active optical devices. This work presents a study of nonlinear optical phenomena in a hybrid TeO_2-coated Si_3N_4 platform. The platform is based on a thin commercial foundry Si_3N_4 which avoids the need for customized fabrication processes and highly nonlinear TeO_2 that is deposited at a low temperature by reactive radio frequency magnetron sputtering which is compatible with back-end-of the line CMOS processing. Importantly, the required anomalous dispersion is attained by adding the TeO_2 coating which also helps to enhance waveguide nonlinearity owing to its higher nonlinearity than Si_3N_4. In addition, the TeO_2

can host rare-earth dopants for waveguide amplifiers and lasers, offering the potential for monolithic linear, nonlinear, and active functionalities in the same platform. Chapter 1 presents an overall discussion on material platforms that have been studied for integrated nonlinear photonics in comparison to Si_3N_4 and TeO_2. Chapter 2 covers the theoretical background of nonlinear optics, discusses the main nonlinear processes, nonlinear integrated devices under study, and their applications, and introduces the hybrid TeO_2-Si_3N_4 platform. Chapter 3 presents an analytical and numerical study on waveguide nonlinearity enhancement and dispersion engineering. The results presented show enhancement of the nonlinear parameter for TeO_2-Si_3N_4 waveguides of up to three times that of stoichiometric Si_3N_4 and calculated anomalous dispersion at near-infrared wavelengths for 400-nm Si_3N_4 coated with varying TeO_2 thicknesses. Chapter 4 provides an experimental proof-of-concept for the hybrid TeO_2 on a 400-nm-thick Si_3N_4 platform as a candidate for monolithic linear, nonlinear and active photonic circuits. Dispersion measurements results are presented showing anomalous dispersion for a 400 nm thick, 1.6 μm wide Si_3N_4 strip waveguide coated with a 424 nm TeO_2 film, with values of ~25 and ~78 ps/nm·km at 1552 nm for the fundamental transverse electric and transverse magnetic modes, respectively. Microring resonator frequency combs with up to 8 comb lines covering a 1000-nm wavelength span for a pump power of 251 mW coupled into the bus waveguide are presented. Multimode lasing and a net gain of 2.8 dB in an Er-doped TeO_2-coated Si_3N_4 microdisk resonator and a 6.7 cm long paperclip waveguide, respectively, are also reported. Chapter 5 presents experimental results on supercontinuum generation where an octave-spanning supercontinuum covering wavelengths from 940 to 1930 nm is demonstrated at a low peak pump power of just 258 W for 100 fs pulses centered at 1565 nm. Chapter 6 covers a comprehensive analytical and numerical study of Raman amplification in the hybrid platform. The results are promising and show high potential for on-chip Raman amplification at reasonable powers, device footprint, and lower losses that can be reached by improving fabrication methods and waveguide designs. For example, for

a projected loss of 0.01 dB/cm which is lower than our current figure but higher than the state-of-the-art Si_3N_4 loss a net gain of up to 10 dB is shown for 1 W pump power in a 1.3 m long TeO_2-coated Si_3N_4 spiral waveguide. Chapter 7 summarizes and discusses the results presented and provides propositions for future work.

Acknowledgments

First and foremost, I would like to thank my academic supervisor Dr. Jonathan Bradley for allowing me to join the Nanophotonic Materials and Devices group. His support and mentorship have been critical towards the completion of my doctorate and without him none of what is to follow would have been possible. Also, special thanks to my committee members Dr. Qiying Fang, Dr. Harold Haugen, and Dr. Chang Qing Xu for providing critique, comments, and much-needed guidance to my research progress.

To my colleagues in Bradley's research group, particularly Henry Frankis, Dawson Bonneville, Khadije Kiani, and Bruno L.S Frare for being supportive team members and friends. Also, thanks to Dr. Andy Knights for his support and counseling, and his group members for always being great collaborators and neighbors.

To my colleagues at DESY in Hamburg, particularly Dr. Franz X. Kärtner for accepting me as a guest researcher in his team, and special thanks to his team members Dr. Neetesh Singh and Dr. Milan Sinobad. Likewise, thanks to Dr. Tobias Herr and his team for collaborating and helping throughout my time at DESY.

To my friends, the "the boys" at 160 Bowman particularly Dr. Steve Cygu and Mark Kamukama for being great housemates and proving immense support, especially during a difficult time in the early days of the Covid19 pandemic. Special thanks to my friends and brothers Hemed Kaporo and Jamal Juma for always being there to offer support and good advice. Also, to Arthur Méndez-Rosales for hosting me during the writing of this thesis and providing the endless supply of the best coffee anyone could wish for.

To my wife, my mother, and all members of Mbonde's family for being patient and supportive of my passionate quest for knowledge.

Table of Contents

List of Figures

List of Tables

Acronyms

BEOL	Back end of the line
BS	Beam splitter
CEO	Carrier envelope offset
CFEL	Center for free-electron laser science
CMOS	Complementary metal-oxide-semiconductor
CMP	Chemical-mechanical polishing
CW	Continuous wave
DESY	Deutsches elektronen-synchrotron
DW	Dispersive wave
FEM	Finite element method
FEOL	Front end of a line
FSR	Free spectra range
FWHM	Full width half maximum
FWM	Four-wave mixing
GNLSE	Generalized nonlinear Schrödinger equation
GVD	Group velocity dispersion
HWP	Half wave plate
KCG	Kerr comb generation
LIDAR	Light detection and ranging
LN	Lithium niobate
LNOI	Lithium niobate-on-insulator
LPCVD	Low pressure chemical vapor deposition
MIR	Mid infrared
MLL	Mode locked laser

NIR	Near infrared
NLSE	Nonlinear Schrödinger equation
OCT	Optical coherent tomography
OFC	Optical frequency comb
OPO	Optical parametric oscillator
OSA	Optical spectrum analyzer
PC	Polarization controller
PD	Photo detector
PECVD	Plasma enhanced chemical vapor deposition
PIC	Photonic integrated circuit
PIC	Photonic integrated circuits
QWP	Quarter wave plate
RF	Radio frequency
RIE	Reactive ion etch
SBS	Stimulated Brillouin scattering
SCG	Supercontinuum generation
SEM	Scanning electron microscope
SHG	Second harmonic generation
SOI	Silicon-on-insulator
SPM	Self-phase-modulation
SRN	Silicon-rich-nitride
SRS	Stimulated Raman scattering
SSFM	Split-step Fourier method
TE	Transverse electric
TEC	Thermo-electric cooler
TM	Transverse magnetic

TPA	Two-photon absorption
WDM	Wavelength division multiplexing
WGM	Whispering gallery mode
XPM	Cross-phase modulation

Declaration of Authorship

I, Hamidu M. Mbonde, declare that this thesis, "Nonlinear optical phenomena in hybrid TeO_2-Si_3N_4 waveguides" was written by and presents research work lead by myself.

Contributions made by others to this work are as listed:

Chapter 3

- Dr. Henry Frankis helped by measuring and fitting data for the TeO_2 material dispersion

Chapter 4

- Silicon-nitride photonic chips were fabricated at the LioniX International foundry
- Dr. Henry Frankis helped by developing a setup for active devices characterization
- Bruno L. S. Frare helped by depositing the TeO_2 films
- Pooya Torab Ahmadi and Batoul Hashemi helped by doing the ellipsometry and prism coupling measurements in the TeO_2 film characterization
- Thibault Wildi helped with microring resonators dispersion measurements, which were carried out in Dr. Tobias Herr's lab at CFEL-DESY and the University of Hamburg.

Chapter 5

- Silicon-nitride photonic chips were fabricated at the LioniX International foundry
- Bruno L. S. Frare helped by depositing the TeO_2 film
- Dr. Neetesh Singh and Dr. Milan Sinobad helped in conducting the supercontinuum generation experiments, which were carried out in Dr. Franz Kärtner's lab at CFEL-DESY and the University of Hamburg.

Chapter 1

Introduction

1.1 Silicon Photonics Overview

The tremendous increase in internet traffic in recent years has overwhelmed the current electronic-based interconnects and telecommunication infrastructure calling for new innovative technologies to complement it[1,2]. There has been an exponential increase in data traffic driven by the ever-increasing consumer demand for media streaming, social media content, and other cloud services. This has created major challenges in both short and long-haul communications systems. The first concern is the amount of power consumed by the traditional metal interconnects for short-haul communication in data centers. It is estimated that power consumption in data centers in terms of percentage share of global electricity consumption will increase from 1.15% to 2.06% between 2016 to 2030 given that all currently known growth factors remain the same [3,4]. Another problem is the constantly increasing bandwidth requirement that will eventually not be met by the current infrastructure, including the performance of electronic systems which are nearing their theoretical limits.

In recent years, silicon photonics has emerged and grown to become a leading candidate technology capable of being directly integrated with electronic circuits and systems to address the challenges of today and future communication technology. The term silicon photonics in this context refers to the technology to fabricate photonic integrated circuits

(PICs) with silicon as a base material using the same mature fabrication processes developed in the microelectronics industry, i.e. complementary metal-oxide semiconductor (CMOS) process technology [5]. The main motivation is to leverage the existing multimillion-dollar infrastructure of a well-developed microelectronics industry to make mass manufacture of photonic circuits possible. Also, to enable direct incorporation of photonic devices into electronic circuits. Integrating PICs with existing electronic systems not only reduce power consumption but also increase bandwidth that is readily accessible in photonics through the wavelength division multiplexing (WDM).

The increased interest in silicon photonics has also been heavily motivated by other application areas besides telecommunication and computing. These areas include applications in biomedical sensing and diagnostic technologies such as the optical coherent tomography (OCT). Also, there are applications for environmental sensing ad monitoring as well as the emerging Lidar technology. Lidar is particular of significant interest as the enabling technology for the futuristic autonomous vehicles [6]. Furthermore, silicon photonic has span and will continue to play an important role in areas of optical metrology, defense and security.

To date, silicon photonics has reached the maturity stage where a significant number of devices have been experimentally demonstrated and optimized from components and circuits to the system level and are penetrating the commercial market. At a component level, there are compact low-loss waveguides for guiding and routing light and critical circuit building blocks such as modulators, filters, photodetectors, and waveguide amplifiers [1,7]. At the circuit and systems levels there are the so-called photonics integrated circuits where monolithic and hybrid integration of multiple building blocks for multiple functionalities and a higher-level performance have been demonstrated [8−10].

1.2 Integrated Nonlinear Photonics

Most of the well-developed traditional photonic devices are based on linear optical phenomena which follow the linear response of a medium to an incoming light wave characterized by linear electromagnetic polarization. On the other hand, the advancement of microfabrication processes aided by the large core-cladding index contrast of silicon-based photonic materials has allowed the fabrication of optical waveguides with a very small cross-section and device footprint. Such small areas have allowed for high power density to be attained leading to the onset of nonlinear optical phenomena. Nonlinear photonics results from the nonlinear response of a medium to an intense input light beam. Such behavior is characterized in part by the so-called nonlinear refractive index (n_2), an intensity-dependent term added to the regular refractive index of a medium. The study of nonlinear phenomena in silicon photonics has led to the discovery of different devices that have become essential in a number of applications areas beyond traditionally heavily studied areas such as telecom and computing. These areas include but are not limited to medical sensing [11], Lidar [12], spectroscopy [13], metrology, and quantum information processing [14].

Research in integrated nonlinear photonics typically involves three parts which are material studies, waveguide design and optimization, and development of specific nonlinear devices. Material studies in this context constitute the search for the right nonlinear medium, studying and measuring its basic linear and nonlinear properties and developing optimal fabrication methods. Properties of interest in a potential material platform include its transparency, nonlinearity, dispersion, and physical and thermal properties. The material side of nonlinear photonic research is addressed in the next section and in further detail in Chapter 2. The second aspect is waveguide design and optimization which aims at developing an optimal waveguide structure to get the best of the material's linear and nonlinear optical properties. Such properties include propagation loss, refractive index

contrast, nonlinear, and dispersion parameters. While low loss, wide transparency, and high refractive index contrast are generally desired properties in integrated photonics, nonlinearity and dispersion are of particular interest in nonlinear integrated photonics. It is desirable to optimize waveguide nonlinearity which helps in lowering the threshold power needed for the onset of various nonlinear optical phenomena. On the other hand, despite being a linear optical property, dispersion plays a key role in many nonlinear photonic processes. In waveguides, dispersion is represented by the group velocity dispersion (GVD) parameter, which can take a negative or a positive sign, referred to as normal and anomalous dispersion, respectively. The waveguide nonlinear and dispersion parameters are defined in Chapter 2 and their optimization study is presented in Chapter 3. The last aspect of integrated nonlinear photonic research involves the design of devices tailored for specific applications. In particular, this include the engineering of waveguides into a structure that enhances one/combination of specific nonlinear phenomena that lead to desired useful outcomes. For, example a waveguide can be looped back to itself to form a ring resonator that trap light and enhance its intensity leading to manifestation of certain nonlinear processes. Different optical phenomena arising from the intensity-dependent refractive index with their subsequent applications are be introduced in Chapter 2 of this thesis. The phenomena of interests which include the formation of optical frequency combs (OFCs), supercontinuum generation (SCG), and Raman amplification are addressed in Chapters 4, 5 and 6 respectively.

1.3 Materials for Integrated Nonlinear Photonics

In silicon photonics, the primary material of interest is silicon through the silicon-on-insulator (SOI) platform. The high index contrast between the silicon core and SiO_2 cladding in SOI allows for tight confinement of light which increases the extent of nonlinear interactions in waveguides through enhanced light intensity. However, the

prevalent nonlinear losses around telecommunication wavelengths (1.3 and 1.5 μm) due to multiphoton absorption and free carrier generation render it a highly inefficient nonlinear medium [15,16]. Several approaches have been attempted to overcome this problem such as removing the generated free carriers using pin junctions and/or operating with pump wavelengths just above the multiphoton absorption edge [17]. While the former is highly inefficient due to the amount of voltage needed to achieve any significant performance, the latter is of less interest for conventional application wavelengths within the telecommunication band. The most feasible alternative that has been largely pursued by the photonics research community is to use other CMOS compatible materials that can be fabricated directly on silicon in the foundry process or with a back end of a line process. Such materials include doped silica, silicon nitride, silicon-rich nitrides (SRN), silicon-germanium (SiGe), and tantalum pentoxide (Ta_2O_5). Table 1.1 presents a quantitative summary of parameters for the most prominent CMOS-compatible nonlinear platforms, followed by a brief discussion about each material in the next paragraphs. The parameters in the table are the linear refractive index (n), the nonlinear refractive index (n_2), the nonlinear parameter (γ) that describes the strength of n_2 with respect to the propagating light frequency and waveguide effective area, the two photon absorption coefficient (β_{TPA}) describing the extent of nonlinear losses in terms of two-photon absorption, and the propagation loss (α). The parameters n_2, γ, and β_{TPA} are defined and discussed in further detail in Chapter 2.

Table 1.1. Nonlinear parameters of various silicon photonics platforms (all wavelength–dependent parameters are reported values at 1550 nm)

Platform	**Transparency (μm)**	***n***	**$\times n_2$ of silica**	**γ W^{-1}/m**	**β_{TPA} $cmGW^{-1}$**	**α dB/cm**	**Reference(s)**
Silica	0.18 – 3.5	1.44	1	nil	nil	<0.01	[18]
a-Si	1.1 – 8	3.4 – 3.7	1730	1200	0.25	4.5	[19,20]
c-Si	1.1 – 8	3.48	807	300	0.45	1	[19,20]]
Si_3N_4	0.25 – 4	2.0	10	0.65	nil	0.0008	[21]
Hydex	0.18 – 3.5	1.5 – 1.9	5	0.25	nil	0.06	[22]
SRN	Varies[a]	2.2 – 3.1	54 – 1077[1]	6.1 – 550[a]	nil	1 – 4.5	[20]
SiGe	1.8 – 14	Varies[b]	430[2]	25	3.3	1.4	[23,24]
Chalcogenide*	>20	2 – 3	>1000	high	6.2	~ 0.1	[25,26]
Ta_2O_5	0.32 – 8	> 2	30	-	nil	0.03	[27,28]
TeO_2	0.4 – 5	2.08	50	1 – 2.5	nil	0.2	[29,30]

Silica: Silica glass has the lowest nonlinearity among silicon photonics materials listed in Table 1.1. However, building on its mature fabrication methods and widespread application in optical fibers, its ultra-low losses allow for the fabrication of very long waveguides [31] and high Q micro-resonators [32] providing enough length and optical field intensity for efficient nonlinear processes at low pump powers [33]. In addition, taking advantage of its transparency within telecommunication bands different nonlinear devices have been demonstrated [34−36]. A relatively large footprint imposed by the large bend radius requirement of such a low index waveguide material is one of the major limitations of integrating silica devices into photonic circuits.

[1] SNR - Silicon rich nitride whose values vary depending on the composition, see ref [20]
[2] SiGe - Silicon germanium whose values vary depending on the composition, see ref [23]
*Only representative parameters are included but there is significant variation in these parameters depending on composition

Silicon: Through the SOI platform, silicon photonic devices can be directly fabricated in a CMOS foundry and offer superior mode confinement by the higher index contrast between the Si core and the SiO_2 cladding. Silicon has the highest nonlinear refractive index among CMOS photonic materials listed in Table 1.1. Tight mode confinement allows for very small footprint devices and ultra-high intensity leading to various nonlinear processes in waveguides. However, for pump wavelengths below ~2 μm, it is quite difficult to achieve an efficient nonlinear process due to the narrow bandgap of silicon which results in higher nonlinear losses. The losses mainly arise from multiphoton absorption and free carrier generation. Nevertheless, by shortening the free carrier lifetime through pin junctions or operating at a wavelength above 2 μm, various nonlinear processes can efficiently be achieved. The former has attracted interest for applications within telecommunication wavelengths (1.3 to 1.7 μm) and numerous nonlinear devices have been demonstrated such as on-chip Raman amplifiers/lasers [37] and frequency combs [38]. The latter is for application beyond telecom wavelengths in the mid-infrared region where SOI devices have performed quite well in the absence of nonlinear losses [39,40]. Also, recently there has been a rise of low-loss multi-mode silicon waveguide approaches where free carrier density is highly minimized by the large mode volume reducing nonlinear losses [41]. This could ultimately lower threshold power to below the limit of nonlinear absorption at telecom wavelengths.

Silicon nitride: Over the last two decades, stoichiometric Si_3N_4 has been well established to be the favorable platform for development of various on-chip nonlinear devices from the visible to mid-infrared (MIR) wavelength region. The Si_3N_4 platform offers the advantage of full compatibility with CMOS processing through which highly compact and low loss waveguides can be fabricated. In addition, Si_3N_4 has a reasonably high bandgap, thus is free from multi-photon absorption and free carrier generation allowing highly efficient nonlinear processes within telecom wavelengths window. Different nonlinear devices have

been demonstrated on an integrated Si_3N_4 platform mainly for supercontinuum generation and ultra-broadband frequency comb generation [7,42]. As an ideal nonlinear medium, Si_3N_4 has only minor shortcomings among other CMOS materials. Relatively weak nonlinearity is one of the issues. It has been readily addressed by significantly reducing waveguide propagation losses to the ultra-low loss regime [43,44], where threshold powers for nonlinear processes are significantly reduced counterbalancing it's weaker nonlinearity. Another issue arises from the difficulties of fabricating thick low-loss waveguides needed for nonlinear processes from conventional CMOS procedures. This is due to cracks caused by stress in the film introduced during low-pressure chemical vapor deposition (LPCVD). This issue has been widely studied and addressed by using alternate deposition techniques such as the damascene reflow process [45] or applying stress release patterns technique [46]. Although these processes have proven to be effective in meeting the end goal, they nonetheless introduce undesired complexities into the fabrication process. Furthermore, the resulting Si_3N_4 waveguides have large core cross-sections, thus are highly multi-mode, which may be detrimental for implementing various linear or active optical functionalities on the same platform. Nevertheless, highly optimized fabrication process leading to ultra-low loss waveguides and recently demonstration of integrated linear and nonlinear functionalities on one chip [47] cement Si_3N_4's position as currently the most suitable platform for nonlinear silicon photonics.

Silicon-rich nitride: While the SOI platform suffers from higher nonlinear losses, Si_3N_4 suffers from lower nonlinearity, and to take advantages of both platforms by complementing each other's strengths came SRN. The so-called silicon-rich nitride, can be tailored to have widely varying optical properties. Different varieties of the SRN have band gaps which are engineered to values high enough to inhibit multiphoton absorption while retaining the strong nonlinearity of silicon. A significant number of nonlinear devices have been demonstrated in this platform with a detailed review of its progress given in [20,48].

Despite showing promising performances, the platform has not yet taken full advantage of the ultra-low loss feature of Si_3N_4 as expected and hence higher waveguide propagation loss remains as a major challenge for the platform.

Hydex: Hydex is a doped-silica glass platform first introduced in 2003 [49], with a composition aimed at exploiting the low loss property of silica glass and higher nonlinearities of semiconductors. The waveguides are fabricated through conventional CMOS steps including chemical vapor film deposition, lithography and reactive ion etching without the need for high temperature annealing afterwards, making the entire process fully CMOS compatible. The main advantage of this platform stems from its ultra-low propagation losses allowing for the fabrication of very long waveguides suitable for nonlinear devices at lower pump powers [42]. However, a relatively small linear refractive index and weak nonlinearities leading to devices with large footprint and the need for thick cladding materials make it challenging to fully-integrate Hydex devices into silicon photonic circuits.

Silicon-Germanium (SiGe): Exploiting the strong nonlinearity and the wide transparency of germanium, which like silicon is a group-IV semiconductor, SiGe has been a material of interest for near to mid infrared photonics. Germanium has strong absorption below 2 μm wavelength, a behavior that has been widely exploited to fabricate germanium photodetectors [50], whereas it's transparency is the broadest of all CMOS photonics materials spanning to 15 μm wavelength. Therefore, there has been strong interest in exploiting germanium-based photonic devices to extended integrated photonics to wavelengths beyond 8 μm, the limit of silicon transparency [24]. In particular, various compositions of $Si_{1-x}Ge_x$ have been studied, offering flexibility in lattice and bandgap engineering. However, it has been found that increasing germanium composition comes at the expense of increasing both linear and nonlinear losses especially moving toward shorter wavelength in the NIR [23]. Nevertheless, SiGe devices have shown among the best

nonlinear photonic devices in the MIR, notably multiple octave(s) spanning supercontinuum generation [51].

Chalcogenides. Chalcogenides are alloys of sulfur, selenium and tellurium that are covalently bonded to network formers such as germanium, bismuth, gallium, silicon or phosphorus. The combination result into verities of glasses that are rich in optical properties such as broad transparency, high nonlinearity and photosensitivity, and can be fabricated at low temperature compatible with CMOS process [25]. A number of chalcogenide glasses of various composition have been extensively studied for on-chip nonlinear photonics. Their nonlinear indices can be as high as thousand times that of silica [26], with high Raman and Brillouin gain coefficients. Despite fostering rich nonlinear optical feature, thermal and optical instability of chalcogenide glasses remain a major challenge for their integration in CMOS PICs. For a detailed review of integrated photonics in chalcogenide glasses readers are directed to a review articles by B.J. Eggleton et al. [25], and B. Gholipour et al. [26].

Tantala: Tantalum pentoxide (Ta_2O_5), also referred to as tantala, is one of the novel silicon photonic platforms that has recently been explored for on-chip nonlinear photonics. Tantala has been reported to have an n_2 of approximately 3× that of Si_3N_4 [52]. It also has high index contrast that allows the fabrication of compact waveguides and wide transparency from 0.32 to 8 μm [28]. Ultra-low loss waveguides with losses down to 3 dB/m have been demonstrated in [53]. The waveguide dispersion can also be effectively engineered as shown in [27]. In addition, it has a relatively lower thermo-optic coefficient which makes it a highly desirable material for stable-operating optical microresonators [26]. Nonlinear devices such as supercontinuum sources and frequency combs have been demonstrated in this platform [52,54]. As a nonlinear photonics platform, tantala is relatively young, but with early works showing promising results, it has promising prospects.

Novel and hybrid CMOS materials: Due to the variety of nonlinear optical phenomena and promising applications of integrated nonlinear photonic devices, there are a large

number of optical materials that have been studied and not all are included in Table 1.1. Research on some of these materials is driven by the search for a better nonlinear platform, for niche applications where conventional CMOS materials are unsuitable, or for improving the nonlinearity of the well-developed platforms such as silicon and Si_3N_4. For example, studies of nonlinear devices in titanium oxide is presented in [55,56]. Also, there is a concept of a hybrid waveguide approach in which a typical SOI or Si_3N_4 waveguide is coated with highly nonlinear polymer or oxide [57]. Good examples of such waveguides include well performing nonlinear devices based on graphene oxide demonstrated in [57,58] . For further reading, a detailed review of silicon-based hybrid structures is given in [59].

Other nonlinear photonics materials: The discussion above is limited to amorphous materials in order to be consistent with the motivation of fabrication compatibility with CMOS processing. However, it is worth mentioning that the research on nonlinear integrated photonics is not limited to these materials. Several crystalline and compound semiconductor materials with far superior nonlinearities have also been extensively studied over the years. For example, nonlinear devices have been demonstrated in compound semiconductor materials such as aluminium gallium arsenide (AlGaAs) and indium gallium arsenide (InGaAs). A review of nonlinear photonics in compound semiconductor (III-V) materials is given in [60] while a review specific to AlGaAs is given in [61]. Also nonlinear devices have been demonstrated in crystalline materials such as lithium niobate (LN) [62], aluminium nitride [63], and diamond [64]. It should be noted that most of the crystalline materials require high processing temperatures that are above the level of the standard CMOS line and thus pose a technical obstacle of integrating them in a conventional CMOS process.

Tellurium oxide: TeO_2 is the least investigated for integrated photonics among the materials listed in Table 1.1. However, it has extensively been studied in fibers especially

for Raman amplification [65]. Owing to its attractive optical properties it has a huge potential as a material platform for integrated silicon photonics. TeO_2 has slightly higher linear refractive index than that of stoichiometric Si_3N_4 enabling fabrication of highly compact waveguides. Its higher nonlinearity and rare-earth dopants solubility are among the features that attract attention for monolithic nonlinear and active photonic applications. Stoichiometric TeO_2 waveguides can be fabricated through standard microfabrication steps [66] or can be integrated into other platforms such as SOI [67] and Si_3N_4 [68] forming a hybrid TeO_2-SOI or TeO_2-Si_3N_4 respectively, via straightforward post-processing. Importantly, the TeO_2-coating can be deposited at low temperature making it fully compatible with back end of line CMOS processes. An extensive review of the properties, fabrication and performance of waveguides based on this platform is given by Steve J. Madden and Khu T. Vu in [69]. TeO_2 has number of features that makes it a suitable candidate for not only independent linear, nonlinear and active photonic applications but also monolithic integration of all of these functionalities in one chip, and these features are well examined throughout this thesis. In particular, this thesis focuses on the hybrid TeO_2-Si_3N_4 waveguides rather than fabricating stoichiometric TeO_2 waveguides. This is due to number of reasons that are detailed in Chapter 2 including the challenges of efficiently etching TeO_2 into compact, small-footprint and low loss waveguides

Table 1.2 gives a qualitative comparison summary of materials that have been discussed above giving an overview of where each stands within the realm of nonlinear silicon photonics. While there will always be interests in developing a superior nonlinear silicon photonics platform, at the moment Si_3N_4 has been established as the most common platform especially for applications within telecommunication wavelengths. It has become the state of the art go-to platform for devices such as optical frequency combs and broadband supercontinuum sources.

Table 1.2. Qualitative comparison summary of various silicon photonic platforms

No	Platform	Advantages	Challenges
1	Silicon (SOI)	▪ Higher nonlinearity ▪ High index contrast ▪ Easy GVD engineering	▪ Higher nonlinear loss ▪ Non-transparent in visible wavelength region
2	Silica	▪ Ultra-low loss waveguides ▪ Transparency in visible and telecom band ▪ Negligible nonlinear losses	▪ Lower nonlinearity ▪ Small index contrast
3	Silicon nitride	▪ Ultra-low loss waveguides ▪ Moderate nonlinearity ▪ High index contrast ▪ Negligible nonlinear losses ▪ Wider transparency	▪ Complex fabrication processes ▪ Difficulties in GVD engineering
4	Silicon-rich nitride	▪ Higher nonlinearity ▪ Easy GVD engineering ▪ High index contrast ▪ Minimal nonlinear losses	▪ High propagation losses ▪ Some nonlinear losses
5	Hydex	▪ Ultra-low loss waveguides ▪ Transparency in visible and telecom band ▪ Negligible nonlinear losses	▪ Lower nonlinearity ▪ Small index contrast
6	Chalcogenide	▪ High nonlinearity ▪ Broadest transparency ▪ Flexible material engineering ▪ High index contrast	▪ Poor thermal stability ▪ Poor optical stability
7	Tantala	▪ Moderate nonlinearity ▪ Minimal nonlinear losses ▪ Low thermo-optic coefficient ▪ High index contrast	▪ Varying fabrication processes ▪ Relatively immature
6	Tellurite	▪ Higher nonlinearity ▪ High index contrast ▪ Negligible nonlinear losses ▪ Wider transparency	▪ Challenges in compact waveguides fabrication ▪ Relatively immature

1.4 Thesis Objectives

The main goal of this thesis work is to explore and introduce tellurite glass as a potential candidate for integrated CMOS-compatible nonlinear silicon photonic devices. In particular, the focus is on the development of hybrid TeO_2-coated Si_3N_4 waveguides as a nonlinear integrated photonics platform. Achieving this objective required modeling, design and optimization of the hybrid TeO_2-Si_3N_4 waveguides suitable for integrated nonlinear photonics. Also, numerical/theoretical and experimental demonstrations of functioning nonlinear devices on the platform. Furthermore, owing to other interesting optical properties, this work also explores and demonstrates the possibility of monolithic integration of linear, nonlinear and active functionalities in a single photonic chip. This thesis aims at providing the very first framework of integrated nonlinear photonics devices in the hybrid TeO_2-Si_3N_4 platform.

1.5 Statement of Thesis Work

This thesis consists of seven chapters covering modelling, simulation, design, measurements and characterization of the integrated TeO_2-Si_3N_4 nonlinear photonic devices. The thesis includes one published manuscript, one manuscript under review and two manuscripts in preparation for submission. Where a published manuscript is included in the thesis, a statement is given at the beginning of the chapter indicating the changes that were made due to the thesis preparation.

Chapter 2 gives a brief theoretical background of nonlinear optical phenomena in waveguides, their applications, and introduces the TeO_2-Si_3N_4 platform. The relevant equations are presented without detailed derivation, from the wave equation for nonlinear photonics, the nonlinear Schrödinger equation to the waveguide dispersion formulas. Also, the main properties of and nonlinear processes relevant to the waveguide platform under

study are discussed followed by their current and prospective future applications. Then, the hybrid TeO_2-Si_3N_4 platform is introduced covering its basics properties, the designed waveguide structure and general simulation parameters.

Chapter 3 covers the optical properties of TeO_2-Si_3N_4 waveguides focusing on dispersion engineering and nonlinear parameter optimization. It presents a summary of the nonlinear refractive indices of the tellurite that have been reported over the years in bulk glass, thin films, and waveguides. This is followed by a comprehensive analytical and numerical study, and simulation results showing tailoring of the waveguide dispersion and optimization of the waveguide nonlinearity on the hybrid TeO_2-Si_3N_4 platform.

Chapter 4 present an overview consisting of design, simulation and experimental results justifying the potential of the TeO_2-Si_3N_4 platform for linear, nonlinear, and active photonics. First, it covers a complete simulation summary on the waveguide design and optimization, list of designed devices and layout for fabrication. Experimental results on characterized devices such as microring resonators are presented along with measured anomalous dispersion confirming the proposition and simulations in Chapter 3. Furthermore, experimental results on demonstrated nonlinear performance are presented showing Kerr comb, supercontinuum, and third-harmonic generation. Lastly, experimental results on active functionalities are presented showing waveguide amplification and lasing in microdisk resonators.

Chapter 5 covers detailed experiments on SCG in waveguides. The efficient generation of an octave-spanning supercontinuum in the TeO_2-Si_3N_4 platform is presented followed by a discussion of potential areas to explore following this demonstration.

Chapter 6 presents a comprehensive numerical study of stimulated Raman amplification in integrated TeO_2-Si_3N_4 waveguides. A study on waveguide parameter optimization for Raman amplification is given followed by detailed Raman amplifier modeling.

Chapter 7 is reserved for discussion, an outlook and concluding remarks. It includes a brief discussion on the current status of the TeO_2-Si_3N_4 platform with respect to the results of this thesis and other related works. A roadmap and an outlook on the prospect of hybrid TeO_2-Si_3N_4 waveguides as a nonlinear silicon photonics platform is given followed by an overall conclusion of the thesis.

1.6 Publications

Below are published and submitted journal articles and manuscripts by the author that have contributed to the results presented in this thesis:

- **H. M. Mbonde**, H. C. Frankis, and J. D. B. Bradley, "Enhanced nonlinearity and engineered anomalous dispersion in TeO_2-coated Si_3N_4 Waveguides," *IEEE Photonics J.* **12**(2), 2200210 (2020).
- **H. M. Mbonde** and J. D. B. Bradley, "Numerical study of stimulated Raman amplification in CMOS-compatible integrated tellurite glass waveguides," *submitted for publication, August 2022*.
- **H. M. Mbonde**, N. Singh, B. L. Segat Frare, M. Sinobad, P. Torab Ahmadi, B. Hashemi, D. B. Bonneville, F. X. Kärtner, and J. D. B. Bradley, "Octave-spanning supercontinuum generation in a thin Si_3N_4 waveguide coated with highly nonlinear TeO_2," *manuscript in preparation*.
- **H. M. Mbonde**, P. Torab Ahmadi, T. Wildi, B. Hashemi, B. L. Segat Frare, M. A. Méndez-Rosales, H. C. Frankis, T. Herr, F. X. Kärtner, and J. D. B. Bradley, "Linear, nonlinear, and active photonics on a TeO_2-coated Si_3N_4 platform," *manuscript in preparation*.

Conference papers:

- **H. M. Mbonde**, N. Singh, B. L. Segat Frare, M. Sinobad, P. Torab Ahmadi, B. Hashemi, D. B. Bonneville, F. X. Kärtner, and J. D. B. Bradley, "Octave-spanning supercontinuum generation in a thin Si_3N_4 waveguide coated with highly nonlinear TeO_2," *in Frontiers in Optics (FiO)*, 9–12, October 2022.

- **H. M. Mbonde**, K. Miarabbas Kiani, H. C. Frankis, and J. D. B. Bradley, "TeO_2-coated Si_3N_4 waveguides with engineered dispersion and enhanced nonlinearity," in *Conference on Lasers and Electro-Optics (CLEO)*, Virtual Conference, 2020, OSA Technical Digest (online) (Optical Society of America, 2020), paper JTu2A.151.
- **H. M. Mbonde** and J. D. B. Bradley, "Numerical modelling of CW Raman amplification in integrated TeO_2 waveguides," presented at *Photonics North*, Virtual Conference, 26–28 May 2020, paper TD-4-27-5.
- **H. M. Mbonde**, H. C. Frankis, and J. D. B. Bradley, "Optimization of nonlinear optical properties of tellurium-oxide-coated silicon nitride waveguides," presented at **Photonics North**, Quebec City, Canada, 21–23 May 2019.

Coauthored journal articles that are not directly incorporated into this thesis:

- R. Wang, H. C. Frankis, **H. M. Mbonde**, D. B. Bonneville, and J. D. B. Bradley, "Erbium-ytterbium co-doped aluminum oxide thin films: Co-sputtering deposition, photoluminescence, luminescent lifetime, energy transfer and quenching fraction," *Opt. Mater.* **111**, 110692 (2021).
- N. Singh, **H. M. Mbonde**, H. C. Frankis, E. Ippen, J. D. B. Bradley, and F. X. Kärtner, "Nonlinear silicon photonics on CMOS-compatible tellurium oxide," *Photonics Res.* **8**(12), 1904–1909 (2020).
- K. Miarabbas Kiani, **H. M. Mbonde**, H. C. Frankis, R. Mateman, A. Leinse, A. P. Knights, and J. D. B. Bradley, "Four-wave mixing in high-Q tellurium-oxide-coated silicon nitride microring resonators," *OSA Continuum* **3**(12), 3497–3507 (2020).

- H. C. Frankis, **H. M. Mbonde**, D. B. Bonneville, C. Zhang, R. Mateman, A. Leinse, and J. D. B. Bradley, "Erbium-doped TeO_2-coated Si_3N_4 waveguide amplifiers with 5 dB net gain," *Photonics Res*. **8**(2), 127–134 (2020).
- K. Miarabbas Kiani, H. C. Frankis, **H. M. Mbonde**, R. Mateman, A. Leinse, A. P. Knights, and J. D. B. Bradley, "Thulium-doped tellurium oxide waveguide amplifier with 7.6 dB net gain on a silicon nitride chip," *Opt. Lett*. **44**(23), 5788–5791 (2019).

1.6.1 Internship Statement

During the course of the PhD, the author spent 4 months in an internship position at the Center for Free-Electron Laser Science (CFEL), Deutsches Elektronen-Synchrotron (DESY) in Hamburg, Germany. The internship was funded by a Mitacs Globalink research award. The associated research work during the internship involved experiments on waveguide dispersion measurements and supercontinuum generation. The dispersion measurements were conducted in Dr. Tobias Herr's lab in collaboration with his Ph.D. student, Thibault Wildi, whereas the supercontinuum generation experiment was carried out in Dr. Franz Kärtner's lab in collaboration with his research scientists, Dr. Neetesh Singh and Dr. Milan Sinobad.

Chapter 2

Background and Theory

In this chapter, a brief theoretical background of nonlinear optical phenomena is given followed by an introduction to the hybrid TeO_2-Si_3N_4 nonlinear integrated photonics platform studied in this thesis. It also includes a discussion of different nonlinear integrated photonic devices of interest and their applications, and the different design and characterization techniques that are to be used throughout this thesis.

In section 2.1, a general introduction to nonlinear optical phenomena in bulk media is given along with the derivation of the nonlinear wave equation from Maxwell's equations. Then, section 2.2 gives a brief explanation of the linear and nonlinear behavior of light in an optical waveguide, a basic structure/building block in integrated photonics. This section also introduces the various waveguide shapes that are typically used in the study of integrated nonlinear photonics in different platforms introduced in Chapter 1. Microring resonators form an integral part of the study of integrated nonlinear photonics. They are used to build some of the relevant nonlinear devices and as a means of characterizing waveguide properties. Thus, in section 2.3 a brief description of microring resonators is given, and their basic properties and relevant features are discussed.

Different nonlinear phenomena can be exploited to design various devices in integrated photonic platforms. Section 2.4 discusses different nonlinear photonic devices that are studied in this thesis and their respective current or prospective applications.

Section 2.5 introduces the hybrid TeO_2-Si_3N_4 nonlinear photonic platform under study. This section gives the separate properties of the constituent materials of the platform (i.e., Si_3N and TeO_2) followed by the waveguide properties of the combined TeO_2-Si_3N_4 platform such as the structure and simulated optical properties.

Lastly, section 2.6 gives a summary of this chapter.

2.1 Nonlinear Optical Response in Bulk Media

Since the very first observation of the nonlinear optical effect in the form of second harmonic generation (SHG) by Franken et al. in 1961 [70], the theory of nonlinear optics has been well established. Examples of well-detailed accounts of the theory of nonlinear optical phenomena can be found in the works of Boyd [71], Agrawal [72], and Lin et al. [15]. In this section, a brief discussion is given while introducing all necessary equations followed by the derivation of the nonlinear wave equation.

2.1.1 The Nonlinear Polarization

Nonlinear optical processes originate from the interactions of an intense optical field with electrons and phonons. To establish an understanding of this we can look at how a material-induced dipole moment per unit volume (polarization), depends upon an incident optical field [71]. For simplicity, if we assume an instantaneous response in a lossless and non-dispersive medium, the induced polarization can be expressed as a power series expansion:

$$P(t) = \epsilon_0(\chi^1 \cdot E(t) + \chi^2 \cdot E^2(t) + \chi^3 \cdot E^3(t) + \cdots), \qquad (1)$$

where E(t) is the electric field, ϵ_0 is the permittivity of free space and χ^n is n^{th} order susceptibility. Also, the fields $E(t)$ and $P(t)$ are assumed to be scalar, otherwise treating them as vectors will make the susceptibility terms tensors of rank $(n + 1)$. The susceptibility parameters (χ^n), determine how the medium responds to the incident optical field. The response can involve inducing a phase shift, absorption or amplification of the incident

field, and generation of new frequencies. All such possibilities can be understood by examining each susceptibility term independently.

χ^1 response: In most cases the response of the material to incident light is linear, and χ^1 is the dominant response. It is a complex parameter where its real part is related to the linear refractive index (n) and the imaginary part relates to the linear absorption (α).

χ^2 response: The second term (χ^2) gives rise to what are referred to as second order nonlinearities and it is only nonzero for materials without molecular symmetry. Since most amorphous and crystalline optical materials such as bulk Si_3N_4 and silicon are centrosymmetric, displaying inversion symmetry, the χ^2 term vanishes. However, experiments have shown that an effective χ^2 can be induced by symmetry breaking [73]. An example of the most common second-order nonlinearity is second harmonic generation. SHG is a very useful frequency doubling nonlinear process in which two incident photons at frequency ω_1 generate a photon at higher frequency $2\omega_1$. In particular, frequency doubling is commonly applied in the *f-2f* interferometer technique to measure the carrier envelop offset (CEO) frequency, an important parameter in application areas such as frequency metrology [74].

χ^3 response: The third term (χ^3) leads to the third-order nonlinearities that commonly occur in both centrosymmetric and noncentrosymmetric media. Since the higher-order susceptibility terms are several orders of magnitude smaller and have no noticeable presence in most applications, χ^3 is the lowest-order nonlinearity for most optical materials. The nonlinear processes resulting from χ^3 can be demonstrated by considering an electric field **E** comprising three frequency components (ω_k):

$$\mathbf{E}(r,t) = \sum_{k=1}^{3} \mathbf{E}_k = \frac{1}{2}\sum_{k=1}^{3} \mathbf{E}_{\omega_k k}(r,\omega_k)\, e^{i\omega_k t} + c.c, \qquad (2)$$

where *c.c.* is the complex conjugate of **E**, and *r* and *t* are displacement and time, respectively. Substituting the electric field equation (2) into equation (1) and expanding the frequency components of the third-order nonlinear polarization term, i.e. $P^3 = \chi^3 \cdot E^3(t)$, leads to several new terms comprising several possible nonlinear processes:

$$
\begin{aligned}
P^3 = {} & \frac{3}{4}\varepsilon_0\chi^3\left[\left|E_{\omega_1}\right|^2 E_1 + \therefore\right] && \text{SPM} \\
& + \frac{6}{4}\varepsilon_0\chi^3\left[\left(\left|E_{\omega_1}\right|^2 + \left|E_{\omega_2}\right|^2\right)E_1 + \therefore\right] && \text{XPM} \\
& + \frac{1}{4}\varepsilon_0\chi^3\left[\left(E_{\omega_1}^3 e^{i3\omega_1 t} + c.c\right) + \therefore\right] && \text{THG} \\
& + \frac{3}{4}\varepsilon_0\chi^3\left[\left(E_{\omega_1}^2 E_{\omega_2} e^{i(2\omega_1+\omega_2)t} + c.c\right) + \therefore\right] && \text{FWM} \qquad (3) \\
& + \frac{3}{4}\varepsilon_0\chi^3\left[\left(E_{\omega_1}^2 E_{\omega_2}^* e^{i(2\omega_1-\omega_2)t} + c.c\right) + \therefore\right] && \text{FWM} \\
& + \frac{6}{4}\varepsilon_0\chi^3\left[\left(E_{\omega_1} E_{\omega_2} E_{\omega_3}^* e^{i(\omega_1+\omega_2-\omega_3)t} + c.c\right) + \therefore\right] && \text{FWM} \\
& + \frac{6}{4}\varepsilon_0\chi^3\left[\left(E_{\omega_1} E_{\omega_2} E_{\omega_3} e^{i(\omega_1+\omega_2+\omega_3)t} + c.c\right) + \therefore\right] && \text{FWM}
\end{aligned}
$$

where ∴ stands for all possible frequency permutations that are not shown, for simplicity. Each of the acronyms on the right-hand side of equation (3) stands for a specific nonlinear phenomenon where SPM is self-phase modulation, XPM is cross-phase modulation, THG is a third-harmonic generation, and FWM is four-wave mixing. Energy level diagrams with visualization of the transitions involved for each process are shown in Fig. 2.1. The dipole transitions induced correspond to virtual but not actual bound eigenstates of the atom, hence they are followed by instantaneous relaxation releasing the fourth photon. In this case, initial quantum states are maintained, and the processes are referred to as **parametric processes**. Therefore, both energy and momentum conservation are required for an efficient excitation. This requirement is known as **phase-matching** and is examined further in later sections.

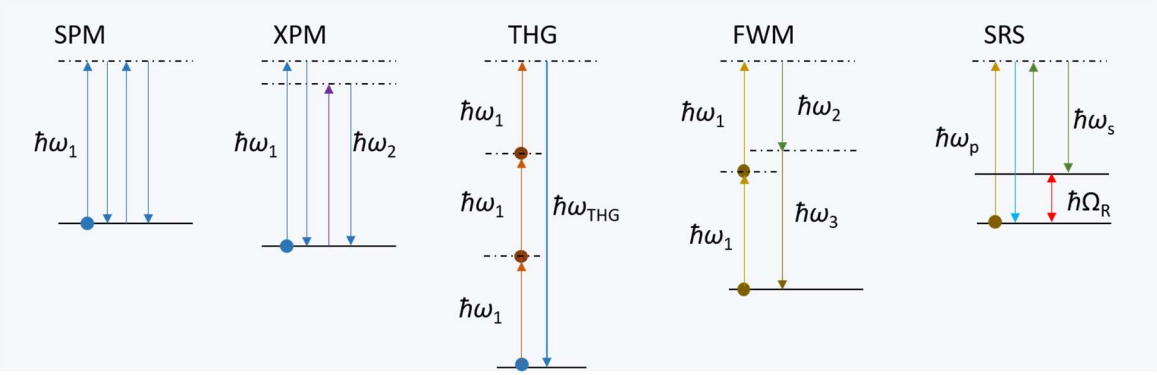

Figure 2.1. Illustration of possible energy levels resulting from third-order nonlinear dipole excitations [2].

SPM: The first term in equation (3) represents a phenomenon called self-phase modulation which means an optical field modifies its own phase. SPM leads to an intensity-depend refractive index (n_2), which consequently modifies the spectral components of the incident field that caused it leading to spectral broadening. Under high intensity, for example a case of short and narrow-band optical pulses, SPM can lead to an extreme spectral broadening covering more than an octave, a process referred to as supercontinuum generation. SCG is an important subject in this thesis and it is explained further later in this chapter. Adding the intensity dependence term to a regular refractive index leads to an overall intensity-depend refractive index represented by equation (4):

$$n = n_0 + n_2 I \tag{4}$$

where n_0 is the regular linear refractive index and n_2 is the nonlinear refractive index resulting from SPM. The n_2 parameter is also referred to as the Kerr index. The excitation leading to SPM can also excite an electron to higher bound states, for example, can excite electrons from valance to the conduction band leading to the creation of free carriers. An example of such a process is two-photon absorption (TPA) where two photons are subsequently absorbed. TPA is an absorptive non-parametric process that leads to an

intensity-dependent contribution to the linear absorption term (α_0). Accounting for this, equation (4) can be modified into (5):

$$n = n_0 + n_2 I - i\frac{\lambda}{4\pi}(\alpha_0 + \alpha_2 I), \tag{5}$$

where I is the intensity, n_0 and α_0 are the linear refractive index and absorption related to the real and imaginary parts of χ^1, and n_2 and α_2 are the nonlinear refractive index and absorption related to the real and imaginary parts of χ^3. The relations of n_2 and α_2 to χ^3 are given by equations (6) and (7) and can be derived from the nonlinear wave equation [72] that is presented in the next section. In the case of only TPA, the nonlinear absorption α_2 is also represented by the TPA coefficient, β_{TPA} [15].

$$n_2 = \frac{1}{cn_0^2\epsilon_0}\frac{3}{4}\mathrm{Re}(\chi^3) \tag{6}$$

$$\alpha_2 = \frac{-\omega}{c^2 n_0^2 \epsilon_0}\frac{3}{2}\mathrm{Im}(\chi^3) \tag{7}$$

For the materials listed in Table 1.1, in the previous chapter, TPA is strongly present in Si, SiGe, and various compositions of SRN. TPA is a detrimental effect for nonlinear silicon photonics as it creates free carriers that significantly reduce the efficiency of other useful nonlinear processes. However, for amorphous materials with higher band gaps, TPA is absent within telecommunication wavelengths. As previously shown in Chapter 1, Table 1.1, to date, there are no reports of TPA observation in stoichiometric Si_3N_4, Ta_2O_5, silica, TeO_2, and this thesis's hybrid TeO_2-Si_3N_4 platform.

XPM: The second term in equation (3) corresponds to a phenomenon called cross-phase modulation, which is similar to SPM, but signals at two different frequencies are involved. The signal at ω_1 modifies the phase of another signal at ω_2 leading to an intensity-dependent refractive index similar to SPM, but twice in magnitude.

THG: The third term in equation (3) leads to what is called third-harmonic generation, in which three photons of identical frequency ω_1, generate a photon at a triplet frequency, $3\omega_1$. THG is an important process that can be applied in the generation of light in wavelengths where sources are not readily available. For example, one can use an abundantly available ~1500 nm laser source to generate visible light around 500 nm. Results of THG in the hybrid TeO_2-Si_3N_4 waveguides is presented in chapter 5 of this thesis.

FWM: The fourth to the seventh terms of equation (3) represent a process called four-wave mixing, in which three incident photons generate a fourth photon at the idler frequency (ω_i). However, the incident photons are allowed to be degenerate with multiple possible combinations, some of which are shown in equation 3. The most common case of degenerate FWM is the one in which a strong pump photon at frequency ω_p, generates two other photons at an idler frequency (ω_i) and signal frequency (ω_s), with energy, conserved such that $2\omega_p = \omega_i + \omega_s$. The interplay of dispersion and waveguide nonlinearities has a significant influence on the efficiency of the process since each introduces a frequency-dependent phase shift in the process. Therefore, for an efficient FWM process, very precise control of waveguide parameters is required to insure *phase matching*. In the case of strong pump intensity and efficient phase matching, the FWM process can be cascaded where each of the new frequencies generates another pair of signal-idler frequencies and so on. Such a process is employed in the development of optical frequency combs in micro-ring resonators. The concept of OFC generation and experimental results in the TeO_2-Si_3N_4 platform is presented in Chapter 4.

Interactions involving phonons: The third-order nonlinearities deduced from equation (3) so far involve only electronic excitation. Another class of third-order nonlinearities involves the excitation of both photons and phonons and is related to the imaginary part of χ^3. Such processes include the inelastic effects of Raman and Brillouin scattering. Raman

scattering occurs as a result of the interaction of photons with vibrational modes of a material in which a strong pump wave (ω_p) transfers its energy to either lower energy photons called Stokes (ω_s) or a higher energy photon called anti-Stokes (ω_a). However, the latter process is relatively weaker while the former is more common and can be represented as $\omega_s = \omega_p - \Omega_R$, where Ω_R is called the Raman shift and $\hbar\Omega_R$ is the energy of a phonon excitation in the medium ($\hbar$ is the reduced Planck's constant). The Raman process can occur spontaneously or by being stimulated. The latter is referred to as stimulated Raman scattering (SRS) and is widely applied to make optical amplifiers. Raman amplification through SRS is further examined later in this chapter. Brillouin scattering is a process in which an incident photon is converted into a lower-energy photon and an acoustic phonon. Similar to Raman scattering it can occur spontaneously or be stimulated which is referred to as stimulated Brillouin scattering (SBS). SBS can be applied in photonics for making ultra-narrow linewidth lasers, amplifiers, and filters, and it is an enabling technology in the rising field of integrated microwave photonics. Review articles by B.J. Eggleton *et al.* [75], and D. Marpaung *et al.* [76] are highly recommended for the account of recent advancements in Brillouin integrated photonics and integrated microwave photonics respectively. For the TeO_2-Si_3N_4 platform, Brillouin SBS is currently being explored but its discussion is reserved for the future.

2.1.2 The Nonlinear Wave Equation

The wave equation that describes the propagation of an electromagnetic field in a dielectric medium can be derived by considering Maxwell's equations that have been developed for macroscopic cases, unifying electricity and magnetism:

- Faraday's law $$\nabla \times \mathbf{E} = -\frac{\partial \mathbf{B}}{\partial t} \quad (8)$$
- Ampere's law (with Maxwell's correction) $$\nabla \times \mathbf{H} = \mathbf{J} + \frac{\partial \mathbf{D}}{\partial t} \quad (9)$$

- Gauss' law (for electric field) $$\nabla \cdot \mathbf{D} = \rho \quad (10)$$
- Gauss' law (for magnetic field) $$\nabla \cdot \mathbf{B} = 0 \quad (11)$$

where **E** is the electric field, **H** is the magnetic field, **D** is the electric flux density, **B** is the magnetic flux density, **J** is the current density, and ρ is the charge density. We also consider the constitutive (materials) equations given as:

$$\mathbf{D} = \epsilon\mathbf{E} = \epsilon_0\mathbf{E} + \mathbf{P} \quad (12)$$

$$\mathbf{B} = \mu\mathbf{H} = \mu_0\mathbf{H} + \mu_0\mathbf{M} \quad (13)$$

where ϵ is the permittivity of a medium and ϵ_0 is the permittivity of free space, μ is the permeability of a medium and μ_0 is the permeability of free space, **P** is the electric polarizability and **M** is the magnetic polarizability. The values of ϵ_0 and μ_0 are 8.854×10^{-23} F/s and $4\pi\times10^{-7}$ H/m, respectively. **P** and **M** represent the material responses to an incident optical field. For the nonmagnetic dielectric materials considered in this thesis, **M** is zero, and hence $\mathbf{B} = \mu_0\mathbf{H}$. Also, we consider source-free dielectric media and therefore there are no free charges or current, so **J** and ρ each become zero, and Maxwell's and the constitutive relations are reduced to the form below:

$$\boldsymbol{\nabla} \times \mathbf{E} = -\frac{\boldsymbol{\partial}\mathbf{B}}{\boldsymbol{\partial t}} \quad (14)$$

$$\boldsymbol{\nabla} \times \mathbf{H} = \frac{\boldsymbol{\partial}\mathbf{D}}{\boldsymbol{\partial t}} \quad (15)$$

$$\boldsymbol{\nabla} \cdot \mathbf{D} = \mathbf{0} \quad (16)$$

$$\boldsymbol{\nabla} \cdot \mathbf{B} = \mathbf{0} \quad (17)$$

$$\mathbf{D} = \epsilon_0\mathbf{E} + \mathbf{P} \quad (18)$$

$$\mathbf{B} = \mu_0\mathbf{H} \quad (19)$$

The equations above can be solved for the two cases of a linear and nonlinear optical medium. First, we consider a general, nonlinear case that includes the polarization term for both linear and nonlinear responses. However, we assume the medium to be homogeneous

and isotropic such that the permittivity ϵ is constant. The wave equation can be derived by the following steps:

I. Apply the curl operator to equation (14)
II. Replace **D** and **H** in equation (15) with equations (18) and (19)
III. Eliminate ($\boldsymbol{\nabla} \times \mathbf{B}$) using modified equation (15)
IV. Lastly, apply the vector identity $\boldsymbol{\nabla} \times (\boldsymbol{\nabla} \times \mathbf{E}) = \boldsymbol{\nabla}(\boldsymbol{\nabla} \cdot \mathbf{E}) - \boldsymbol{\nabla}^{\mathbf{2}}\mathbf{E}$ and use the approximation $\boldsymbol{\nabla} \cdot \mathbf{E} = \mathbf{0}$ using equation (16)

The result is the wave equation shown below.

$$\nabla^2 \mathbf{E} - \mu_0 \epsilon_0 \frac{\partial^2 \mathbf{E}}{\partial t^2} = \mu_0 \frac{\partial^2 \mathbf{P}}{\partial t^2} \tag{20}$$

It is often advantageous to separate the polarization term into linear and nonlinear parts such that $\mathbf{P} = \mathbf{P_L} + \mathbf{P_{NL}}$. In this case, equation (20) is modified to:

$$\nabla^2 \mathbf{E} - \mu_0 \epsilon_0 \frac{\partial^2 \mathbf{E}}{\partial t^2} = \mu_0 \frac{\partial^2 \mathbf{P_L}}{\partial t^2} + \mu_0 \frac{\partial^2 \mathbf{P_{NL}}}{\partial t^2} \tag{21}$$

Now, we can write the linear polarization part in terms of the linear susceptibility term given in equation (1) as $\mathbf{P_L} = \epsilon_0 \chi^1 \mathbf{E}$ and substitute it into equation (21).

$$\nabla^2 \mathbf{E} - \mu_0 \epsilon_0 \frac{\partial^2 \mathbf{E}}{\partial t^2} = \mu_0 \epsilon_0 \chi^1 \frac{\partial^2 \mathbf{E}}{\partial t^2} + \mu_0 \frac{\partial^2 \mathbf{P_{NL}}}{\partial t^2} \tag{22}$$

We can group the electric filed terms into:

$$\nabla^2 \mathbf{E} - \mu_0 \epsilon_0 (1 + \chi^1) \frac{\partial^2 \mathbf{E}}{\partial t^2} = \mu_0 \frac{\partial^2 \mathbf{P_{NL}}}{\partial t^2} \tag{23}$$

we recall and rewrite the constitutive equation (12) for only linear polarization as:

$$\mathbf{D} = \epsilon \mathbf{E} = \epsilon_0 \mathbf{E} + \mathbf{P_L} = \epsilon_0 \mathbf{E} + \epsilon_0 \chi^1 \mathbf{E} = \epsilon_0 \mathbf{E}(1 + \chi^1) = \epsilon_0 \epsilon^1 \mathbf{E} \tag{24}$$

and define a new parameter $\epsilon^1 = 1 + \chi^1$, as the relative permittivity which is related to the permittivity of a medium by $\epsilon = \epsilon^1 \epsilon_0$. Equation (23) now becomes:

$$\nabla^2\mathbf{E} - \mu_0\epsilon_0\epsilon^1\frac{\partial^2\mathbf{E}}{\partial t^2} = \mu_0\frac{\partial^2\mathbf{P_{NL}}}{\partial t^2} \tag{25}$$

Looking at equation (22), we can realize that in absence of a medium the right-hand side is zero, hence we can define the speed of light in a vacuum, $c = 1/\sqrt{\mu_0\epsilon_0} = 2.998\times10^8$ m/s. We then deduce that in a medium, light will propagate slower with a speed $v = \frac{c}{\sqrt{\epsilon^1}} = \frac{c}{n}$, where we call the new parameter *n* the refractive index of a medium. It relates directly to the linear susceptibility as pointed out in the previous section by $n^2 = \epsilon^1 = 1 + \chi^1$. We can now write equation (25) as:

$$\nabla^2\mathbf{E} - \frac{n^2}{c^2}\frac{\partial^2\mathbf{E}}{\partial t^2} = \frac{1}{\epsilon_0 c^2}\frac{\partial^2\mathbf{P_{NL}}}{\partial t^2} \tag{26}$$

Equation (26) is one form of the nonlinear wave equation that can be solved to describe different nonlinear phenomena in optical waveguides. For example, with the slowly-varying envelope approximation, one can derive the equation that describes the propagation of short optical pulses commonly known as the nonlinear Schrödinger equation (NLSE). The time-varying polarization term in equation (26) acts as a source term leading to the generation of new frequencies. If we ignore the nonlinear polarization term, the equation satisfies a monochromatic plane wave solution propagating with a speed of *c*/*n*. In this case, one can derive a familiar frequency dependent wave equation of the form:

$$\nabla^2\mathbf{E}(\mathbf{r}) - n^2(\omega)\frac{\omega^2}{\mathrm{c}^2}\frac{\partial^2\mathbf{E}}{\partial t^2} = 0 \tag{27}$$

where the electric field is given by $\mathbf{E}(r) = \mathrm{E}_0 e^{j\mathbf{k}\cdot r}$, E_0 is a scalar electric field amplitude and **k** is the wave vector. The wave vector **k** is related to the refractive index and wavelength of the propagating field by:

$$|\mathbf{k}| = n(\omega)\frac{\omega}{c} = \frac{2\pi}{\lambda} \tag{28}$$

2.2 The Nonlinear Optical Response in Waveguides

The equations given in the previous section only describe light behavior in vacuum or bulk media, however for useful applications it is desired to confine light in a manner that it can be well controlled and manipulated. Therefore, optical waveguides have been designed to direct and confine light similar to metallic strips in electronics. In this section, a qualitative introduction to light propagation in waveguides is given. More importantly, the focus is on defining basic terms related to optical waveguide theory that are used throughout this thesis.

2.2.1 Optical Waveguides and Waveguide Modes

A waveguide is the most basic component in photonic integrated circuits. In a very basic form light can be guided by a high-index dielectric medium surrounded by a low-index medium such as a glass rod suspended in the air. A simple example of a dielectric waveguide is shown in Fig 2.2(a), a slab consisting of two distinct materials of refractive index n_a and n_b such that $n_a > n_b$. In this case, light can be confined in a higher index material called a core by total internal reflection at the interface with the low index material called a cladding. Typically, the dimensions of the core on the x and y axis (shown in the figure) are within the length scale of the order of the wavelength of light, and then light is confined in the two dimensions and propagates in the z-direction. In waveguides, the confinement of light can be conserved over a considerably long distance contrary to free space propagation where diffraction occurs. Figure 2.2(b) is a simplified representation of the waveguide in (a) that demonstrates how light is confined under total internal reflection. The ray optic approximation is governed by Snell's law of refraction and the law of reflection:

$$n_a sin\theta_a = n_b sin\theta_b \tag{29}$$

$$\theta_a = \theta_r \tag{30}$$

where θ_a, θ_r, and θ_b are the angles of incidence, reflection, and refraction. From Fig. 2 (b) there exists an angle of incidence for which the angle of refraction is 90^0 and no light will be refracted into the lower index material. This phenomenon is called total internal reflection and the corresponding incident angle is called the critical angle. We can derive the formula for the critical angle from Snell's law to be: $\theta_c = \sin^{-1}({}^{n_a}/_{n_b})$. For any other angle of incidence equal to or above the critical angle, the light will be confined to the higher index medium (core). This ray optic description is given to establish a very basic understanding of light confinement in waveguides. The ray optic description implies that any light at incident angle greater than the critical angle will be guided. However, due to a phase shifts for example at the interfaces of core with both upper and lower-clad, the phase matching condition has to be satisfied for constructive interference to occur, and therefore only specific *modes* of the incident optical field can be allowed to propagate in a particular waveguide.

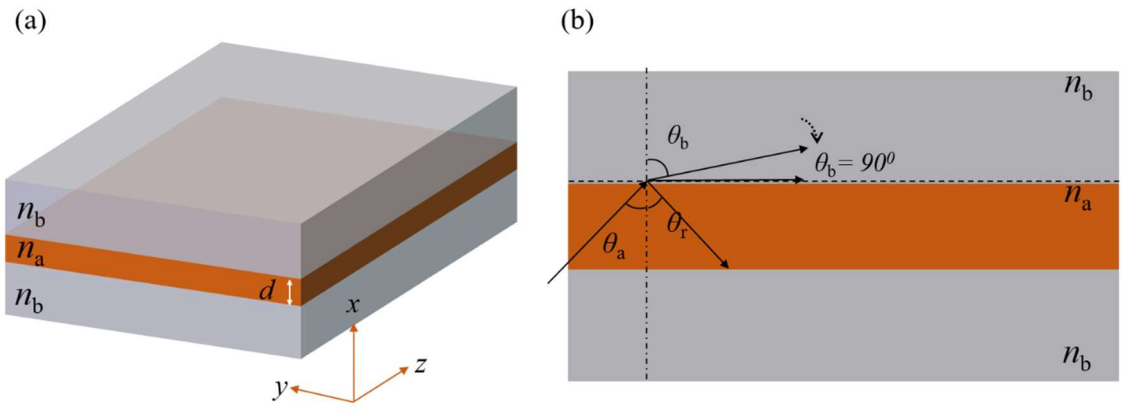

Figure 2.2. (a) Illustration of a slab waveguide, (b) a two-dimensional simplification of the slab waveguide treated with geometric optics.

As defined in [77], a mode is a spatial distribution of optical energy in one or more dimensions that remains constant in time. The waveguide modes are found by solving for

eigen-solutions of the wave equation under the boundary conditions given by the waveguide properties. For example, in Fig 2.2(a) if we assume light propagates in the *z*-direction and the slab has an infinite length along the *y*-direction, the light will be confined in the slab only when $n_a > n_b$. If we assume the electric field is polarized in the *y*-direction, the modes calculated are called transverse electric field (TE) modes. The *y*-component of the electric field is given by:

$$\boldsymbol{E_y}(x,z) = E_0 \boldsymbol{E_y}(x) e^{-j\beta z} \tag{31}$$

where β is the *z* component of the wave vector known as the propagation constant. The wave equation (27) is modified into a form shown below.

$$\frac{d^2 E_y}{dx^2} + [{k_0}^2 n_i^2(x) - \beta^2] E_y = 0 \tag{32}$$

where $k_0 = \omega/c$ is the free space-wave vector and n_i is the refractive index where $i = a,b$. Equation (32) needs to be solved for the three regions; the core with refractive indices n_a, upper and lower- clad each with refractive index n_b. We can simplify equation (32) by letting $k_a^2 = {k_0}^2 n_a^2 - \beta^2$ and $k_b^2 = {k_0}^2 n_b^2 - \beta^2$ and write two equations one for the core region and one for the upper and lower-clad as:

$$\frac{d^2 E_y}{dx^2} + {k_a}^2 E_y = 0 \tag{33}$$

$$\frac{d^2 E_y}{dx^2} + {k_b}^2 E_y = 0 \tag{34}$$

which are solved for the three regions; core, upper-clad, and lower-clad. The solution is shown in equation 35 below:

$$E(x) = \begin{cases} C exp(-k_b x) & for\ x > \frac{d}{2} \\ A\sin(k_a x) + B\cos(k_a x) & for -\frac{d}{2} < x < \frac{d}{2} \\ B exp(-k_b x) & for\ x < -\frac{d}{2} \end{cases} \quad (35)$$

where A, B, and C are constants. The boundary conditions require that the tangential component of the electric field, E_y, and its derivatives be continuous at $x = d/2$ and $x = -d/2$ that leads to the eigenvalue equation below, which is to be satisfied.

$$\frac{k_a d}{2}\tan\left(\frac{k_a d}{2}\right) = \frac{k_b d}{2} \quad (36)$$

Since $\tan\left(\frac{k_a d}{2}\right) = \tan\left(\frac{k_a d}{2} + m\pi\right)$, allowable values of β must satisfy the eigenvalue equation for m=0,1,2…, and each solution of β corresponds to the allowed modes. We have established a basic understanding of optical waveguides and demonstrated the formation of waveguide modes, shortly we will define terms that are related to confined modes in waveguides. However, first, we have to point out that to show the actual distribution of the electric field (**E**) and magnetic field (**H**) of the confined modes, known as the *mode profile*, one has to solve the full version of equation (32) for all directions and both the **E** and **H** fields. While there are analytical methods to approximate the optical modes such as the Marcatili method [78], more often numerical methods such as the finite element method (FEM) are used. In this thesis, a commercially developed FEM mode solver (Synopsis RSoft FemSIM) is used to calculate optical modes and the related parameters, which are briefly described below.

The effective index (n_{eff}): The effective index is the modified refractive index term that accounts for the distribution of the electric or magnetic field confined in a waveguide. It can be shown from the solution of the full version of the wave equation (32) that n_{eff} is a weighted average of the core and cladding refractive indices with the mode field distribution as a weighting factor. Therefore, n_{eff} is higher for modes that are more confined

to the waveguide than the modes that have a larger fraction of the $\boldsymbol{E}$ or $\boldsymbol{H}$ fields in the cladding. The n_{eff} relates to the propagation constant, β by $n_{\text{eff}} = \beta\lambda/2\pi$.

The effective mode area (A_{eff}): The effective mode area is the measure of the area that the waveguide mode covers in transverse dimensions. While by definition it appears to be straightforward, the mathematical definition of A_{eff} is subtle. The definition varies depending on the waveguide type. In this work, we use $\boldsymbol{A_{\text{eff}}}$ equation defined in [72].

Mode confinement factor (Γ): The confinement factor is a value that represents the fraction of power that is confined within the waveguide core. In a general case, this will be a fraction of the total power of the transverse $\boldsymbol{E}$ or $\boldsymbol{H}$ fields confined in the waveguide. However, for a waveguide with multiple cores and claddings the mode confinement factor for each section/material can be given separately as the fraction of partial power confined in a particular section.

The effective mode area and confinement factor are particularly important parameters when designing a waveguide for nonlinear applications. It is an essential requirement to reduce the mode area and increase the confinement factor for higher light intensities to be achieved. Therefore, depending on the material platform, nonlinear waveguides take varying geometries that are optimized for high confinements and small mode areas. Figure 2.3 shows 3D drawings of typical waveguide structures used in nonlinear silicon photonics. Two of the most common structures shown in Fig. 2.3(a) and (b) which are the strip/ridge and the rib waveguides. We make note that the strip/ridge waveguide is referred to as the strip waveguide throughout this thesis. In most cases, for example in standard CMOS SOI strip (also referred to as wire) waveguide the top clad is a thermal oxide similar to the underclad. However, in some cases, the top cladding can be a PECVD (plasma-enhance chemical vapor deposition) oxide with a slightly higher index than the underclad thermal oxide or can be even other low-index material than oxide. Hybrid waveguide designs are also very common in nonlinear silicon photonics for several reasons. Most of these reasons

stem from the desire to complement the main core material with certain features that it lacks such as anomalous dispersion, higher nonlinearities, or compatibility with certain materials for applications such as biosensing. Figures 2.3(c) and (d) show examples of such hybrid designs. The hybrid design 2 in (d) is what is being studied in this thesis and is explained further in later sections.

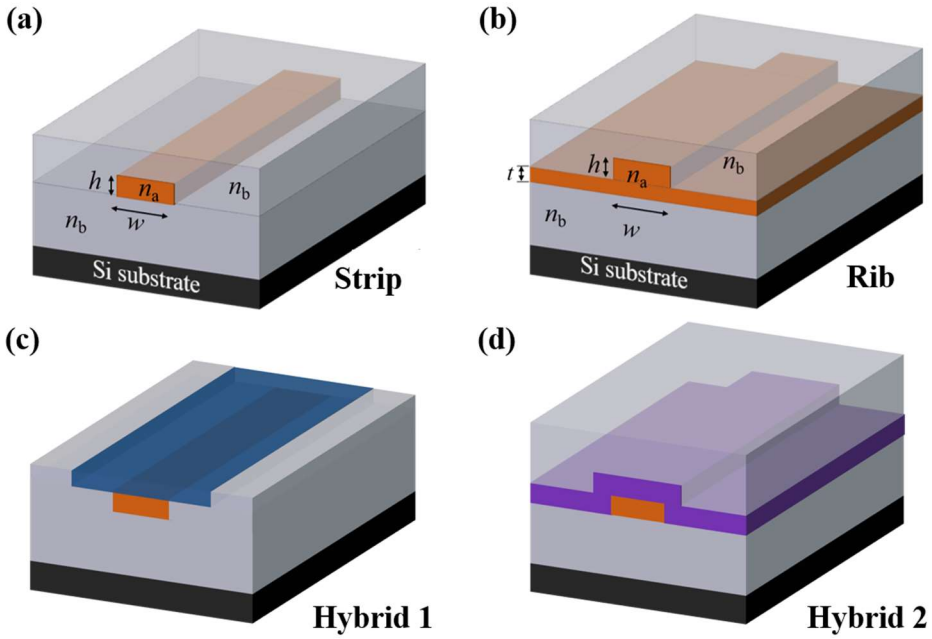

Figure 2.3. D drawings of typical waveguide structures used in nonlinear silicon photonics: (a) and (b) show the two standard waveguide structures commonly referred to as strip/ridge and rib waveguides respectively, (c) is one example of a hybrid design in which a window is opened and a highly-nonlinear material is filled in to enhance waveguide nonlinearities or other optical properties, and (d) shows another example of the hybrid design in which a high-index material is coated on top of a regular strip waveguide forming a multi-core/clad waveguide structure.

2.2.2 The Nonlinear Parameter of a Waveguide

The nonlinear refractive index defined in equation (6) is a purely material property. However, to express the strength of n_2 in an optical waveguide it is useful to define a new parameter, called the nonlinear parameter (γ):

$$\gamma = \frac{n_2.\omega}{A_{\text{eff}} \cdot c} \tag{37}$$

The nonlinear parameter depends on the material property (n_2), light property (ω), and the waveguide property (A_{eff}). For the derivation and complete account of γ readers are referred to reference [72]. To maximize the impact of nonlinearities in the waveguide it is desirable to have the highest value of γ. The easiest way to achieve that is to use a material with the highest n_2. At a particular operating frequency, the n_2 of a material will be fixed and then γ is optimized through A_{eff}. In this case, A_{eff} is tuned by adjusting the waveguide geometry. However, this is not straightforward since as the waveguide core size is decreased beyond a certain point, the mode begins to expand and the confinement decreases. The study of finding optimal waveguide dimensions for maximum nonlinear interactions through γ is well presented in [79] and is presented in Chapter 3 of this work for the case of the TeO_2-Si_3N_4 platform.

2.2.3 Group Velocity Dispersion (GVD)

In its very basic definition, dispersion is the property of refractive index dependence on wavelength. As an outcome, in a waveguide, the effective index will also have this wavelength dependence, and so do the propagation constant, group index, and ultimately the group velocity. We can develop an understanding and derive the formula for group velocity dispersion by defining some of the preceding terms.

As previously noted, each component of a wave propagates in a bulk medium with velocity given by the speed of light in free space divided by the refractive index. This value is called the phase velocity and is defined as:

$$v_p = \frac{c}{n} = \frac{\omega}{k} \tag{38}$$

However, for light propagating in a waveguide, the phase velocity is modified to account for the waveguide property into:

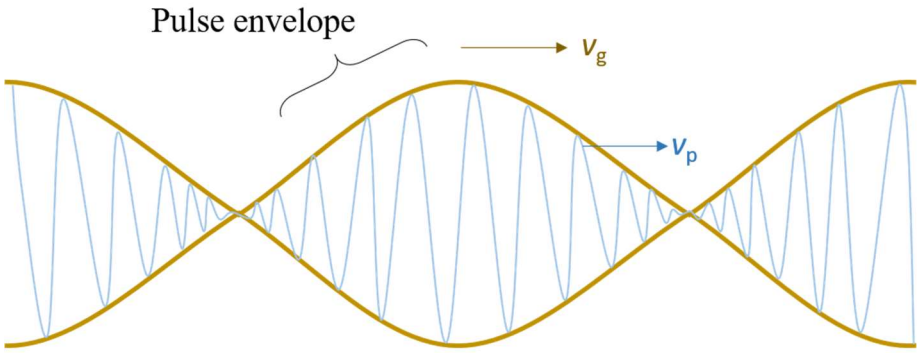

Figure 2.4. Pulse envelope showing the distinction between phase and group velocity.

$$v_p = \frac{c}{n_{\text{eff}}} = \frac{\omega}{\beta}, \tag{39}$$

in which the wavenumber is substituted by the propagation constant. Owing to the frequency dependence of the propagation constant, the phase velocity changes as well for different wavelengths. Therefore, for example in the case of an optical pulse consisting of multiple frequencies, it is useful to define a new term called group velocity, which is the speed at which the pulse envelope (energy) travels. The image in Fig. 2.4 shows how the phase velocity is distinguished from the group velocity.

$$v_g = \frac{\partial \omega}{\partial \beta} \tag{40}$$

A more comprehensive account of the waveguide dispersion effect can be expressed by expanding the mode-propagation constant β in a Taylor series expansion about the center frequency of the pulse ω_0.

$$\beta(\omega) = n(\omega)\frac{\omega}{c} = \beta_0 + \beta_1(\omega - \omega_0) + \frac{1}{2}\beta_2(\omega - \omega_0)^2 + \cdots, \quad (41)$$

where β_m is the mth order of dispersion given by $\beta_m = \left(\frac{d^m\beta}{d\omega^m}\right)_{\omega=\omega_0}$ $(m = 0, 1, 2\ldots)$. The various dispersion orders have different impacts on light propagating in waveguides. However, in general situations, only the first two orders are of significant impact, whereas the higher order terms play a more important part when it comes to short pulse propagation. The first two terms relate to the effective index and the previously defined group velocity by the following relations:

$$\beta_1 = \frac{1}{v_g} = \frac{1}{c}\left(n_{\text{eff}}(\omega) + \omega\frac{\partial n_{\text{eff}}}{\partial\omega}\right) = \frac{n_g}{c} \quad (42)$$

$$\beta_2 = \frac{d^2\beta}{d\omega^2} = \frac{\partial\beta_1}{\partial\omega} = \frac{1}{c}\left(2\frac{\partial n_{\text{eff}}}{\partial\omega} + \omega\frac{\partial^2 n_{\text{eff}}}{\partial\omega^2}\right) \quad (43)$$

where n_g is a new parameter called the group index which is equivalent to the effective index with a small addition that accounts for the effective index change with frequency. Therefore, the group velocity can now be computed directly from the group index as $v_g = c/n_g$. The parameter β_2 represents the change of group velocity with frequency/wavelength, which is dispersion, and therefore it is commonly referred to as the *group velocity dispersion* (GVD). Sometimes the GVD is represented by the dispersion parameter (D) which is calculated by the equation below:

$$D = \frac{\partial\beta_1}{\partial\lambda} = -\frac{2\pi c}{\lambda^2}\beta_2 = -\frac{\lambda}{c}\frac{d^2 n_{\text{eff}}}{d\lambda^2} \quad (44)$$

The value of β_2 can take a negative or positive sign and vice versa for the D parameter. For most optical materials such as silicon and Si_3N_4, it is positive ($\beta_2>0$, $D<0$) at common operating wavelengths, and therefore it is usually referred to as *normal*. On the other hand, the case of a negative dispersion ($\beta_2<0$, $D>0$) is referred to as *anomalous dispersion*. The sign of dispersion has significant importance, for example, it can determine whether a pulse

experiences an *up-chirp* or a *down-chirp*. The former happens in normal dispersion situations where the longer wavelength components of the pulse possess higher v_g than the shorter wavelength and vice versa for the latter.

2.2.4 Phase Matching and GVD Engineering

The various third-order nonlinear processes presented in section 2.11 involve the generation of new frequencies, and therefore phase matching is a requirement to ensure constructive interference. To get a clear insight into this concept we take a look at one of the χ^3 processes, FWM. To be precise, a degenerate case of FWM is considered in which a strong pump of frequency ($2\omega_p$) acts as two waves and generates a pair of waves of higher frequency called the signal (ω_s) and lower frequency called the idler (ω_i). First, the process involves energy conservation for the four waves involved:

$$2\hbar\omega_p - \hbar\omega_s - \hbar\omega_i = 0, \tag{45}$$

where $\hbar$ is the reduced Plank's constant. As a result of energy conservation, the spacing between the three waves is always the same, $\omega_p - \omega_i = \omega_s - \omega_p$. In addition, for an efficient conversion process phase matching must be satisfied such that the effective wavenumber mismatch (κ) is equal to zero:

$$\kappa = 2\beta_p - \beta_s - \beta_i + \gamma P = 0, \tag{46}$$

In the equation above, β_p, β_s, and β_i are the propagation constants for the pump, signal, and idler waves, and γP is the phase shift due to the Kerr effect where γ is the nonlinear parameter and P is the pump power. For example, if we consider a situation where the pump, signal, and idler wave are all traveling in the same mode, let's say the fundamental TE mode, the nonlinear phase shift is positive for most silicon photonics platforms. Therefore, in such a situation phase matching can be attained if the waveguide exhibits anomalous dispersion. Also, alternative phase matching techniques can be employed such as exploiting higher-order modes [80] or using the birefringent property [81]. Nevertheless,

for silicon photonics waveguides, phase matching through anomalous dispersion is the most applied approach.

Dispersion engineering is a subject that involves employing different techniques and waveguide designs to ensure that the desired dispersion profile, more often anomalous dispersion, is obtained to enhance the efficiency of various nonlinear optical processes. GVD engineering techniques include modification of the waveguide geometry (height-to-width ratio), implementation of multicore/cladding waveguide designs, and spatial mode coupling. A detailed account of GVD engineering in silicon photonic platforms and the hybrid TeO_2-Si_3N_4 waveguides used in this work is presented in the next chapter.

2.2.5 The Nonlinear Schrödinger Equation

To appropriately model the propagation of a high-intensity optical field in a waveguide such as that involving short pulses, one must account for all linear and nonlinear effects. This means solving the nonlinear wave equation (26) including linear losses, all dispersion terms, and all nonlinear terms including the relevant inelastic scattering effects. The equation that accounts for all these effects and is widely used in the nonlinear photonics community is referred to as the generalized nonlinear Schrödinger equation (GNLSE). The most common form of the GNLSE and the one that is relevant in this work is given by equation 47 below. For a derivation and a more detailed account of each term in the equation, it is recommended to refer to the work by Agrawal et al. [72] [15].

$$\frac{\partial \mathbf{A}}{\partial z} = -\frac{\alpha}{2}\mathbf{A} + \sum_{m\geq 2} \frac{i^{m+1}}{m!}\beta_m \frac{\partial^m \mathbf{A}}{\partial t^m} + i\gamma\left(1 + i\tau_s \frac{\partial}{\partial t}\right)\left(\mathbf{A}(z,t)\int_{-\infty}^{+\infty} R(t')\,|\mathbf{A}(z,t-t')|^2 dt'\right) \tag{47}$$

In the equation above **A** is the electric field with the slowly varying envelope approximation applied. Also, it is assumed that the electric field is unidirectional and maintains its polarization along the propagation distance, hence a scalar approximation is valid. The first

two terms on the right-hand side of the equation represent linear propagation, where α is the attenuation coefficient and β_m is the m^{th} order dispersion coming from the Taylor series expansion of the propagation constant $\beta(\omega)$ about ω_0 given in equation (41). The third term on the right-hand side models third-order nonlinear effects such as SPM, XPM, FWM, and Raman scattering. The derivative term accounts for the wavelength dependence of (γ) known as the shock term. It is usually associated with effects such as self-steepening and is characterized by a timescale $\tau_s=\tau_0=1/\omega_0$. $R(t)$ is the Raman response function representing Raman effects and modeled as $R(t) = (1 - f_R)\delta(t) + f_R h_R(t)$, where h_R is the Raman response function and f_R is the fractional contribution of the delayed Raman response to the instantaneous electronic response of the material.

Due to the nonlinear term, it is not possible to solve the GNLSE analytically. However, it can be solved with different numerical approaches and give a fairly accurate approximate solution. Examples of widely used methods are the Runge-Kutta scheme or the split-step Fourier method (SSFM) [72].

2.3 Microring Resonators

This section briefly introduces microring resonators and their features and related parameters that are used throughout this thesis

2.3.1 Basic Theory

A ring resonator is one of the basic waveguide shapes that is commonly used in integrated photonics. In a simple definition, it is a bent waveguide that goes around and connects back to itself to form a closed loop. Most often the closed loop is in a form of a circle, however, in a general sense, any waveguide loop that forms a closed path is a ring resonator. Figure 2.5(a) shows example drawing of a simple microring resonator and its related parameters. Light can be evanescently coupled in and out of the ring by a straight waveguide (also referred to as a bus waveguide) in close proximity. Depending on the design features, such

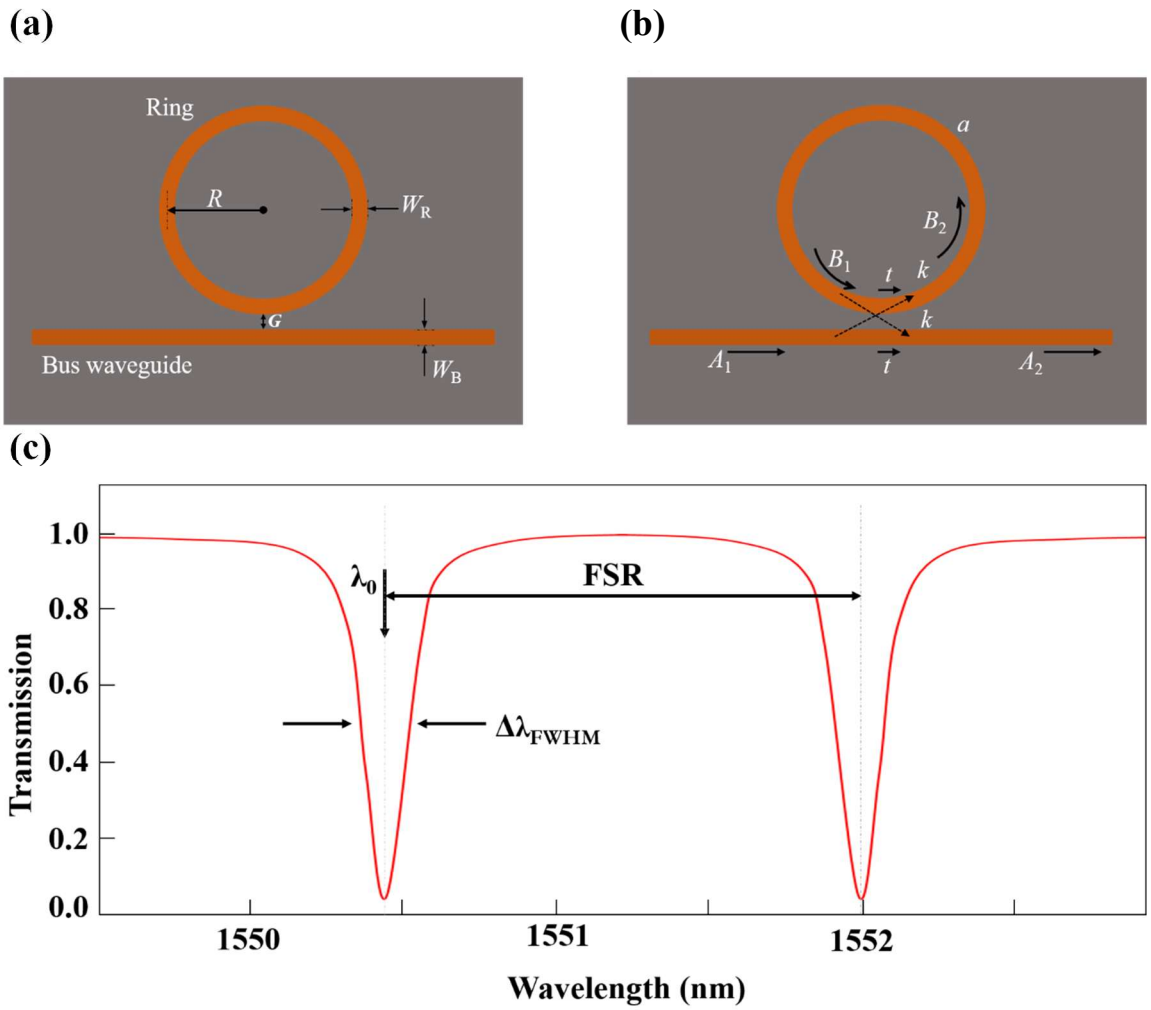

Figure 2.5. (a) and (b) Illustrations of a ring resonator and coupling bus waveguide indicating key design parameters and energy flow when light is coupled in, respectively, and (c) Typical ring resonator's transmission spectrum with main parameters.

as the ring dimensions and its proximity to the bus waveguide, light of specific wavelengths that satisfies the resonance condition (i.e. constructive interference) can be trapped into the ring, circulate and build up its intensity. Such high-intensity build-up can be exploited for various applications, particularly using intensity-dependent nonlinear processes. Besides

that, microring resonators have many other applications as laser cavities, optical modulators and filters, and biosensors.

Recalling equation (31), the phase of light is given by multiplying its propagation constant as a function of wavelength with the distance traveled as $\beta(\lambda)z$. For the circular-shaped ring resonator of radius R shown in Fig. 2.5(a), the total phase accumulated after a round-trip is given by $\phi(\lambda) = \beta(\lambda) \cdot 2\pi R$. For constructive interference to occur the round-trip phase shift must be zero. Therefore, from Fig. 2.5(b) we can define the resonance condition as when the phase of B_1 is equal to the phase of B_2. Hence, for a particular mode family (m), the resonance condition is satisfied when ϕ is an integer multiple of 2π such that:

$$m(\lambda_0) = \beta(\lambda_0)R = n_{eff}(\lambda_0)\frac{2\pi}{\lambda_0}R \tag{48}$$

where m=1,2,3…, is the resonant mode number, and λ_0 is the resonance wavelength. Figure 2.5(b) shows what happens when the light of power A_1 is coupled into a bus waveguide. A fraction of A_1 will be transmitted to the output end of the bus (A_2) and some will be evanescently coupled into the ring (B_2). The light with power B_2 will circulate through the ring into B_1, which similarly to A_2 will be partly transmitted (continue its path) through the ring and partly coupled into the bus waveguide (A_2). If we assume that there is no loss in the coupling region, the electric fields can be described by the transfer matrix [82]:

$$\begin{bmatrix} A_2 \\ B_2 \end{bmatrix} = \begin{bmatrix} A_1 \\ B_1 \end{bmatrix} \begin{bmatrix} t & ik \\ ik & t \end{bmatrix} \tag{49}$$

where t and k are the transmission and coupling coefficients. Since optical power relates to the square of the electric field, the coefficients t and k are related by $|t|^2 + |k|^2 = 1$. The electric field circulating in the ring cavity will experience losses from coupling out to the bus waveguide and from internal propagation loss. Therefore, we can define the cavity decay rate by $\kappa = a + k$, which includes the internal loss (a) and the external coupling loss (k). The internal loss includes the contribution of various loss mechanisms such as bulk

material absorption, surface roughness, scattering, and bending losses. Here the loss term a is in units of m^{-1} which relates to the commonly used loss in dB/cm as $a = e^{-\alpha\pi R}$. If we consider the case of normalized input power such that $|A_1|^2 = 1$, and define the circulating power B_1 in terms of coupled power B_2 as $B_1 = ae^{j\phi(\lambda)}B_2$ we can express the transmitted power (P_t) and circulating power (P_{in}) in the ring using equations (50) and (51) as :

$$P_t(\lambda) = \left|\frac{A_2}{A_1}\right|^2 = \frac{a^2 + t^2 - 2at\cos(\phi(\lambda))}{1 + a^2t^2 - 2at\cos(\phi(\lambda))} \tag{50}$$

$$P_{\text{in}}(\lambda) = \left|\frac{B_1}{A_1}\right|^2 = \frac{a^2\kappa^2}{1 + a^2t^2 - 2at\cos(\phi(\lambda))} \tag{51}$$

The maximum circulating power (P_{in}) is attained at a particular resonant wavelength when the resonance condition in equation (48) is satisfied. In this case, the transmitted power equation is reduced to:

$$P_t(\lambda) = \left|\frac{A_2}{A_1}\right|^2 = \frac{(a-t)^2}{(1-at)^2} \tag{52}$$

From equation (52) a complete extinction of the input field will be attained when the transmission coefficient is equal to the round-trip loss (i.e. $a = t$). This condition is referred to as ***critical coupling*** and it is important in the design of ring resonators for Kerr nonlinearities. Under critical coupling, the power circulating in the ring is maximized as:

$$\max|P_{\text{in}}(\lambda_0)| = \frac{a^2}{(1-a^2)} \tag{53}$$

Equation (53) tells us that in a lossless ring resonator where $a = 0$, the circulating power goes to infinity, and therefore the lower the round-trip losses the higher the trapped optical power, an important criterion in microring resonator design for nonlinear applications.

Quality factor: It is often the case that the power of an optical field circulating in a ring resonator is expressed in terms of the quality (Q) factor. As defined in [83], the Q-factor

represents the number of oscillations of the field before the circulating energy is depleted to 1/*e* of the initial energy. It is given by the equation:

$$Q = \frac{\lambda_0}{\text{FWHM}} \tag{54}$$

where λ_0 and FWHM are the resonance wavelength and the resonance full width at half maximum as shown in Fig. 2.5(c). In terms of matrix formalism, the Q-factor formula can be derived as:

$$Q = \frac{\sqrt{ka}L\pi n_g}{(1-ka)\lambda_0} \tag{55}$$

where $L=2\pi R$ is the cavity length. The Q defined by equations (54) and (55) is also referred to as the loaded Q-factor (Q_L). This is because it takes account of both intrinsic resonator losses and extrinsic losses due to output coupling. If we assume there is no output coupling, we can define an intrinsic quality factor that depends only on round-trip cavity losses (a).

$$Q_{\text{i}} = \frac{\sqrt{a}L\pi n_g}{(1-a)\lambda_0} \approx \frac{2\pi n_g}{\lambda_0 \alpha} \tag{56}$$

From equation (56), it can be seen that under ***critical coupling*** Q_{i} is twice Q_{L}. In practice, it is useful to couple some of the energy out of the resonator and hence we define a coupling Q-factor (Q_{c}) such that:

$$\frac{1}{Q_L} = \frac{1}{Q_i} + \frac{1}{Q_c} \tag{57}$$

From the relationships between coupling strength and quality factor, we can define three resonator coupling regimes as ***critically coupled***, ***undercoupled***, and ***overcoupled***.

I. ***Critically coupled***. As defined earlier, critical coupling occurs when the cavity round-trip loss is equal to the output coupling and therefore $Q_{\text{i}} = Q_{\text{c}}$. The resonance dip will show the highest extinction and the cavity will have the highest power

enhancement. This, in most cases, is the desired operating condition for intensity-dependent nonlinear processes.

II. ***Overcoupled.*** This happens when the intrinsic cavity losses are lower than the output coupling and hence $Q_i > Q_c$. The output coupling dominates and therefore shallow resonance dips or smaller extinction ratios are observed.

III. ***Undercoupled.*** This is the case when the intrinsic losses in the ring cavity are higher than the output coupling hence $Q_i < Q_c$.

In microring designs and experimental characterizations, the ring coupling behavior can be determined by looking at the transmission spectrum versus the coupling gaps for different wavelengths. Generally, the coupling strength decreases with gap size and increases with wavelength. For example, Fig. 2.6 shows the transmission spectrum of a typical Si_3N_4 microresonator for gaps of (a) 0.75 μm, (b) 0.85 μm, and (c) 0.95 μm. Zoomed-in relative transmissions at approximately 1550 nm for the three gaps are shown in Fig. 2.6 (d) along with the Lorentzian fit, and the corresponding calculated intrinsic and coupling Qs all at a wavelength near 1550 nm. It can be seen that the extinction ratio increases while increasing the gap from 0.75 μm to 0.85 μm and also decreases with a further increase of the coupling gap from 0.85 μm to 0.95 μm. From this trend, we can deduce that the critical coupling is near the 0.85 μm gap, and decreasing the gap moves the coupling to the overcoupled regime while increasing the gap moves it to the undercoupled regime. Also, it is evident from the calculated Qs that $Q_i > Q_c$ for the 0.75 μm gap (overcoupled) and $Q_i < Q_c$ for the 0.95 μm gap (undercoupled). However, $Q_i \neq Q_c$ as discussed above indicating that the ring is not exactly at critical coupling for the 0.85 μm gap as well.

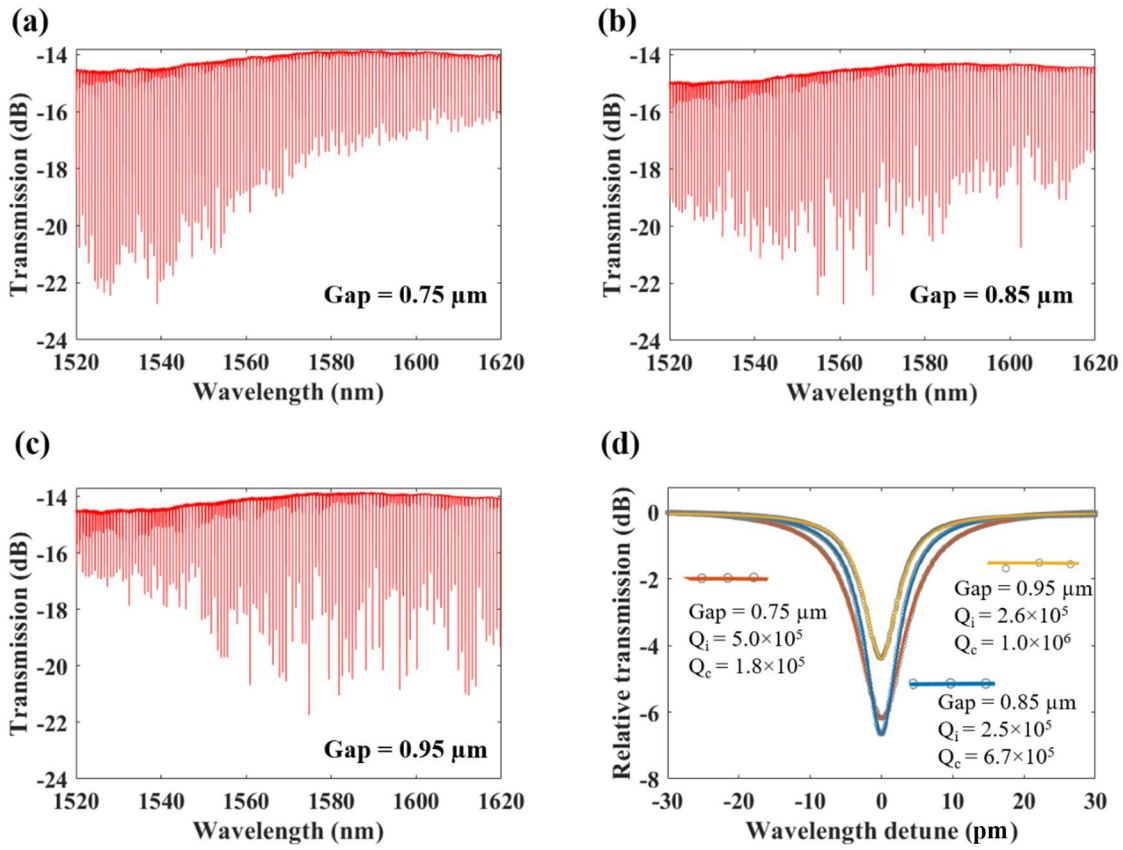

Figure 2.6. (a), (b) & (c) Microring characterization measurements results showing transmissions for three different gaps. (d) Lorentzian fit of the resonances with calculated Q factors for each gap at wavelengths near 1550 nm

Free spectral range: The resonance condition derived in equation (48) is a wavelength-dependent term and therefore the same mode family will be resonant at intervals for different wavelengths as shown in Fig. 2.5(c). The spacing between adjacent resonances of the same mode family is called the free spectra range (FSR). It is given by equation (58) below.

$$\mathrm{FSR} = \frac{\lambda_0^2}{2\pi R \cdot n_g}, \tag{58}$$

where n_g is the group index defined in equation (42) in terms of the effective index taking account the waveguide dispersion:

$$n_g = n_{\mathrm{eff}} - \lambda_0 \frac{dn_{\mathrm{eff}}}{d\lambda} \tag{59}$$

We note that from equation (58) knowing the FSR from ring measurements one can calculate the group index accordingly. The variations of ring FSR with wavelength can be used to estimate waveguide dispersion, a concept that is explained shortly.

Cavity finesse ($\mathcal{F}$): Finesse is another quantity that is commonly used to describe the power circulating in a ring cavity. It is given as the ratio of the cavity FSR and linewidth (or FWHM).

$$\mathcal{F} = \frac{\mathrm{FSR}}{\mathrm{FWHM}} \tag{60}$$

The finesse relates the pump power in the bus waveguide (P_{bus}) to the power circulating in the resonator. Under critical coupling condition, it can be shown that the circulating power in the cavity relates to the finesse by: $P_{\mathrm{in}} = \frac{\mathcal{F}}{\pi} P_{\mathrm{bus}}$. Therefore, the higher the finesse the more power circulates in the resonator.

2.3.2 Microring Dispersion

The dynamics of various nonlinear phenomena in integrated waveguides highly dependent on the dispersion parameter. Therefore, dispersion measurement is one of the important characterization processes in integrated nonlinear photonics. As pointed out earlier, one can extract dispersion by measuring the variations of ring resonator FSR with wavelength. A particular mode family can have quite a high resonance mode number of up to the order of m~10^2 to 10^4 excited by any external CW laser. Thus, we first represent the absolute mode number (m) in terms of a relative mode number μ such that $\mu = 0$ for the externally pumped

mode. The microresonator dispersion includes the combined effects of material and geometrical dispersion. The former comes from the usual frequency dependence of the refractive index (n_0) while the latter comes from the contribution of the optical mode profile after a roundtrip and the reduced refractive index of the evanescent component of the mode outside the resonator material. The total dispersion is the deviation of the resonances from equidistance $\Delta_\omega(\mu)$. If we approximate the pump frequency as $\omega_p = \omega_0$ we can write each of the resonance frequencies in terms of ω_0 and dispersion as:

$$\omega_\mu = \omega_0 + D_1\mu + \frac{1}{2}D_2\mu^2 + \frac{1}{6}D_3\mu^3 + \frac{1}{24}D_4\mu^4 + \cdots, \tag{61}$$

$$\omega_\mu = \omega_0 + D_1\mu + D_{\text{int}}, \tag{62}$$

where $D_1/2\pi$ is the equidistant microresonator FSR at the expansion frequency, $D_2/2\pi$ is the second-order dispersion related to the β_2 parameter defined in equation (43), and $D_3/2\pi$, $D_4/2\pi$..., are higher order dispersion terms in units of Hz. From equation (62) D_{int} is given as the deviation of the resonance frequency from $D_1/2\pi$ including all dispersion effects as illustrated in Fig 2.7. From ring transmission measurements one can extract the values of D_{in} for different resonant modes. Then, appropriate fitting is applied to extract individual values of the dispersion parameters. Of particular interest, the second-order dispersion (β_2) can be calculated from measured D_2 by the equation (63) below.

$$D_2 = -D_1^3\frac{\beta_2 L}{2\pi} = -\frac{c}{n}D_1^2\beta_2 \tag{63}$$

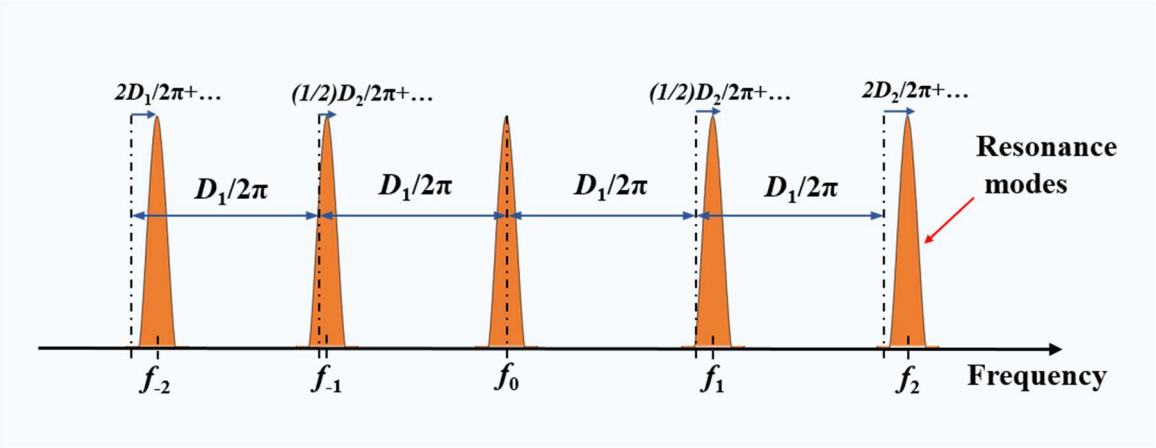

Figure 2.7. Resonance frequencies accounting for dispersion and showing the mismatch between equidistant reference comb lines (black) and the resonance modes (orange) corresponding to microresonator dispersion.

While it appears as a straightforward measurement process, it is challenging to characterize dispersion from microring resonator spectral properties. This is due to thermal instabilities that lead to drifting of the mode spectra. Also, for measurements to be accurate a wide scan range is important. Therefore, different techniques have been developed for microresonator dispersion characterization that involve wide-range scanning, referencing, and stabilization of the microring resonances using an external stable self-referenced comb. Such techniques include frequency comb-assisted diode laser spectroscopy [84,85], (fiber-loop) cavity calibrated diode laser spectroscopy [86], and RF-sideband laser spectroscopy [87]. Figure 2.7 gives a conceptual illustration of dispersion measurements from the frequency-dependent variations of a microresonators' resonant mode spacing. Dispersion measurement results for the TeO_2-Si_3N_4 waveguide platform is presented in Chapter 4 of this thesis.

2.3.3 Microresonators and Waveguide Loss Characterization

Equation (56) shows that the intrinsic quality factor of a microring resonator depends on its group index and intrinsic losses. Using equation (60), by measuring the ring FSR near the pump wavelength it is possible to estimate the propagation loss α. However, in this case, the loss comprises absorption from a resonator bulk material, scattering due to material surface roughness and material imperfections, coupling to higher order modes, and bending losses. Therefore, the loss value extracted from ring measurements might be different from the propagation loss experienced in a straight non-resonant waveguide. Nevertheless, for a ring resonator with sufficiently large bend radius and single mode excitation, the loss will be approximately equal to that in a straight waveguide.

In microresonator design, we usually consider a bending radius at which the radiation losses due to bending are negligible. In this case, the intrinsic resonator losses will be close to the waveguide propagation loss. We can find the minimum bend radius by considering only the radiation-limited quality factor (Q_R) given by the equation:

$$Q_R = \frac{n_{\mathrm{eff},r}}{4\pi n_{\mathrm{eff},i}}, \tag{64}$$

where $n_{\mathrm{eff},r}$ and $n_{\mathrm{eff},i}$ are the real and imaginary effective indices, respectively. A rule of thumb is that a minimum bend radius must have a Q_R>10^6 corresponding to radiation loss α_R<0.001dB/cm. From equation (64), $n_{\mathrm{eff},r}$ and $n_{\mathrm{eff},i}$ can be calculated directly from a mode solver software. Figure 2.8(a) shows a simulation result of Q_R versus bend radius for a TeO_2-Si_3N_4 waveguide with 400 nm thick TeO_2 coating and Si_3N_4 strip width of 1.6 µm. Following insight from Fig. 2.8(a) and other design criteria, ring resonators of radii 500 µm were fabricated and coated with 424 nm of TeO_2. The transmission spectrum of the ring for a 0.6 µm gap is shown in Fig. 2.8(b). To calculate Q-factors the resonance centered around 1550 nm was fitted to a Lorentzian model [88] as shown in Fig. 2.8(c) with the calculated intrinsic quality factor, FSR, and group index. The resulting loss of 0.62 dB/cm is also

shown in the figure. We compared this value to the loss measured using the ***cut-back*** method (explained below) with results shown in Fig. 2.8(d). The loss from the two methods differs by 0.07 dB/cm which can be attributed to the uncertainty of the two methods and the slight variations of properties of the different waveguides used in each case.

Cut back method. Another way of characterizing waveguide loss is the cut-back method. In this method, the total optical loss of a waveguide is measured by comparing the optical power (or intensity) of multiple waveguides of different lengths. Mathematically, if the optical power in a waveguide after propagating through a distance z is given by $P(z) = P(0)\exp(-\alpha z)$ where $P(0)$ is the input power and α is the attenuation coefficient, by taking the ratios of powers from two waveguides of different lengths it can be shown that the attenuation coefficient is given by the equation below:

$$\alpha = \frac{log_e\left[\frac{P(z_1)}{P(z_2)}\right]}{z_2 - z_1} \tag{65}$$

where z_1, z_2 are the propagation/waveguide lengths such that $z_2 > z_1$.The cutback method uses this simple linear equation to determine propagation loss in optical waveguides. It requires that the input conditions remain constant while optical power is measured from one waveguide of a certain length then the same waveguide is cut into a shorter length and power is measured again keeping everything else constant, eventually, the loss is calculated by the equation above taking the average for several lengths. While bending losses are typically the main source of errors in Q-based loss measurement, for the cut-back method the main source of errors comes from difficulties in maintaining the same coupling efficiency for each waveguide being measured

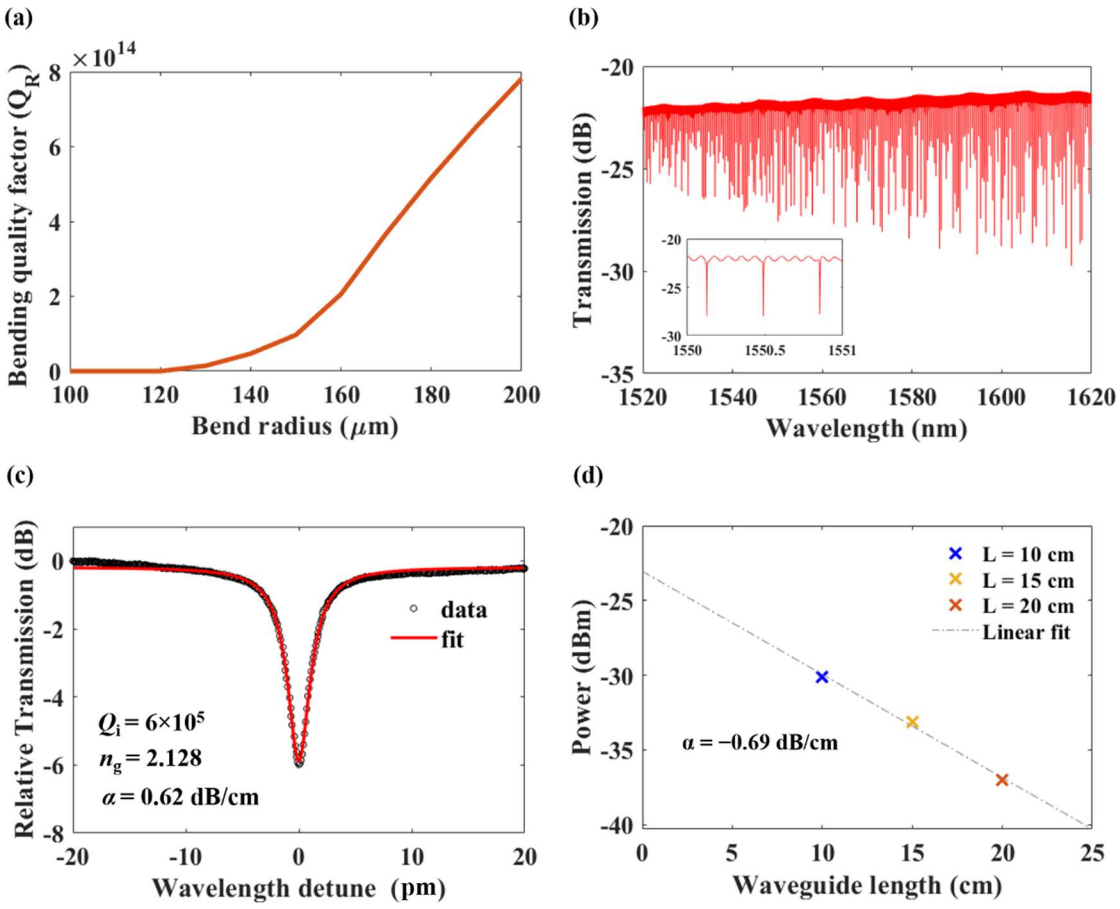

Figure 2.8. (a) Plot of the simulated bending quality factor for the TeO_2-coated 1.6 µm wide and 0.4 µm high Si_3N_4 waveguide. (b) Measured transmission in a 500 µm radius ring with inset showing fine transmission from 1550 nm to 1551 nm. (c) Lorentzian fit of the ring transmission at 0.6 um gap and 1550 nm wavelength. (d) Plot of measured optical power and a linear fit for 3 waveguide of different lengths used to calculate propagation loss by the cut-back technique.

2.4 Nonlinear Integrated Photonic Devices and Applications

2.4.1 Optical Frequency Combs

Optical frequency comb (OFC) generation is one of the widely studied nonlinear effects in integrated silicon photonics. An optical frequency comb is a spectrum of equidistant spaced and mutually coherent optical frequencies. It can be visualized as an ordinary ruler where equidistance spaced lines are used to measure distance. Similar to a ruler OFC can be used as a reference to precisely measure optical frequencies, the difference between optical frequencies, and many more applications. Fig 2.9(a) demonstrates this analogy where f_{rep} is the frequency spacing and f_{CEO} is the carrier envelope offset frequency. Unlike a rule which has length units starting from zero, OFC usually starts at a non-zero offset frequency which is referred to as the f_{CEO}. The discovery of OFCs has revolutionized the field of frequency metrology and optical spectroscopy, and in 2005 the Nobel Prize in physics was half-awarded to J. L. Hall and T. W. Hänsch for their work on precision spectroscopy including the invention of the frequency comb technique. OFCs can be generated through the two commonly known processes of supercontinuum generation or Kerr comb generation (KCG), as illustrated in Fig. 2.9(b) and described below. A thorough analysis, distinction, and review of the two processes is presented by Gaeta *et al.* in [89].

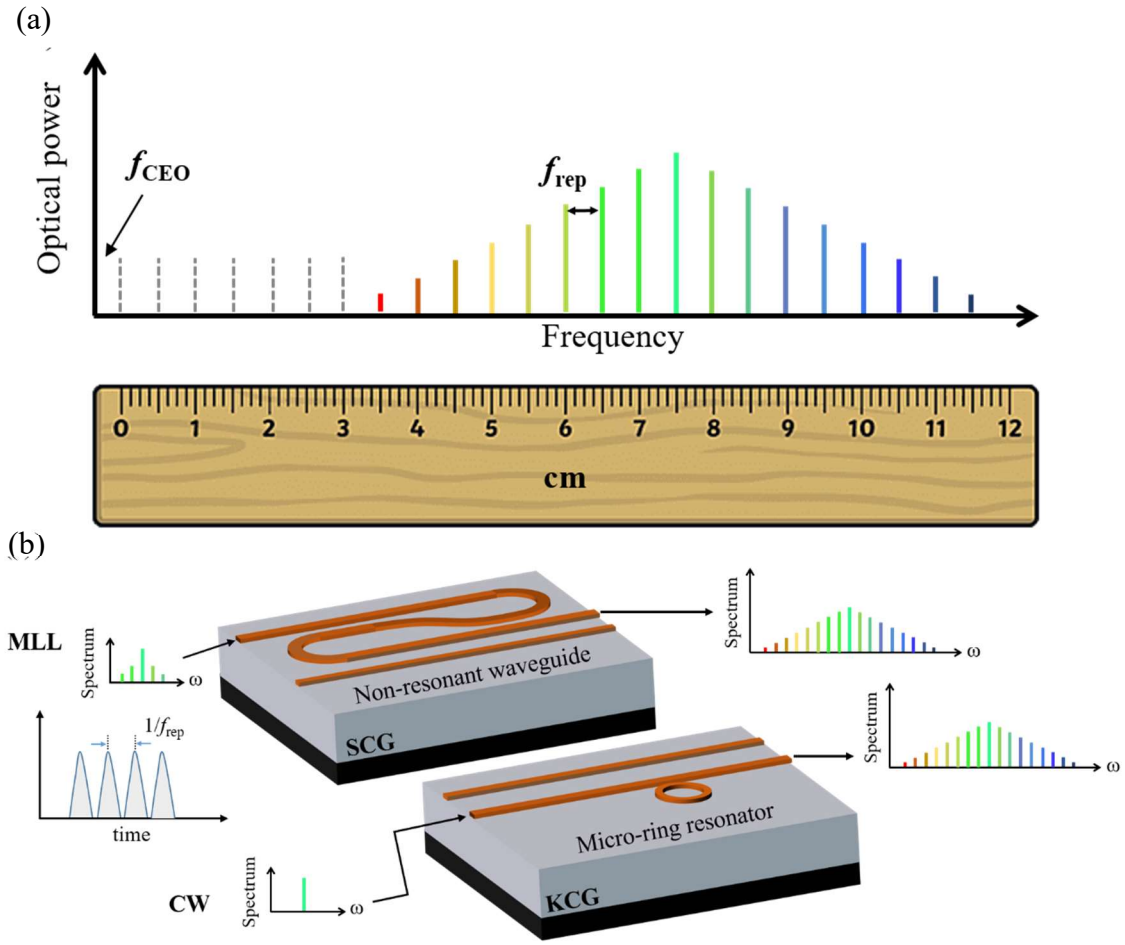

Figure 2.9. (a) A demonstration of the analogy of an optical frequency comb to an ordinary measuring ruler, (b) an illustration of the distinction between OFC generation from SCG and KCG processes.

SCG: Comb generation through SCG is achieved by pumping a nonlinear waveguide with a mode-locked laser (MLL) source which leads to the generation of new frequencies by a combinations of processes such as cascaded FWM, SPM, dispersive wave (DW) generation, and soliton fission. Figure 2.9(b) shows a mode-locked laser (MLL) source that can be used to generate SC by pumping a dispersion-engineered non-resonant waveguide.

Before its demonstration in integrated platforms, SCG has extensively been studied and revolutionized OFC generation in photonic crystal fibers. OFCs spanning beyond an octave have been demonstrated with a high degree of coherence, self-reference, and stabilization. The advancement of OFC generation in photonic crystal fiber has enabled the advancement of comb-based frequency metrology and opened several new applications, and also importantly it has allowed for theoretical studies and an accurate understanding of the dynamics of laser pulses in the SCG process. The dynamics of a laser pulse in the SCG process can be well understood by using the GNLSE equation (47). The review article by Dudley *et al.* [90] is a recommended reference for SCG in photonic crystal fibers while for waveguide platforms recommended references are [89,91,92]. The first SCG in Si_3N_4 was demonstrated in [93] with the SC spanning over an octave. This showed the attractive features of Si_3N_4 and thereafter it has grown to become a leading platform for on-chip SCG. The SCG subject is revisited further in detail in Chapter 5.

KCG: OFCs can also be generated by continuous wave (CW) light in an optical microresonator. An optical resonator can confine and trap light to very high intensities and if the resonator is made up of a third-order (Kerr) nonlinear medium, parametric processes such as FWM can be enhanced leading to OFC generation. This OFC generation technique is also referred to as Kerr comb generation. There are two classes of micro-resonators that are commonly used which are whispering gallery mode (WGM) resonators, such as micro-disks, microspheres, and micro-toroids, and micro-ring resonators (MRRs). Although WGM resonators were the first to be studied for KCG and eventually applied in the first reported on-chip demonstration in 2007 [94], due to a number of features that distinguish the two, MRRs have become more dominant in recent years. Issues such as the device footprint and efficient coupling of light into the resonator motivated the drive for a more robust solution and hence the monolithic chip-based MRRs. Consequently, 3 years later KCGs were reported in Si_3N_4 [95] and Hydex glass [96]. The basic driving process in KCG

is FWM such that if the signal and idler pair satisfy the resonator's resonance conditions the parametric process is enhanced and sidebands start to form around the pump frequency. The energy is conserved as usual for a FWM process, whereas the phase-matching condition is automatically satisfied for equally spaced modes. Under the right conditions, the process can be further enhanced such that each of the generated sidebands grows in intensity and generates its own sidebands, and so on. The process continues until dispersion perturbs the cavity resonance spacing, at which point the spectrum stops growing or can only be further expanded by another process such as the formation of dispersive waves under the right dispersion conditions. Through proper tuning of a pump frequency and/or amplitude dissipative Kerr solitons can be excited to facilitate the generation of ultra-broadband and highly coherent OFCs. A characteristic of KCG combs is that their frequency spacing is equivalent to the spacing of the resonator's resonances, unlike SCG-based combs which inherit their spacing from the source MLL. The dynamics of KCG in a microresonator can be described by the Lugiato-Lefever equation [97]. For a theoretical view of the process, readers are referred to references [98–101]. The discussion on the design and generation of Kerr combs in the hybrid TeO_2-Si_3N_4 platform is presented in Chapter 4.

2.4.2 Raman Amplification

In optical waveguides, the Raman process can occur easily under stimulated conditions rather than spontaneously. In such a situation, a small seed signal and pump are coupled into a waveguide and the process results in the amplification of the signal wave. This process is known as stimulated Raman scattering and has been studied extensively to make broadband optical amplifiers. Compared to other optical amplification techniques, such as those based on rare-earth atomic transitions, Raman amplification has advantages in terms of versatility and performance. First, SRS can be used to amplify a signal of any wavelength as long as the difference between the signal and pump corresponds to the Raman shift of

the material used. Second, if a waveguide is made up of a Raman material eliminate the need for any sort of doping and an entire length act as an amplifier providing what is known as distributed amplification. Furthermore, some Raman materials have very broad Raman emission bandwidth allowing for broadband amplification. While the detailed account of Raman amplification in silicon photonics platforms and a numerical study for the TeO_2-Si_3N_4 platform is presented in Chapter 6, here we present the basic equations for Raman amplification.

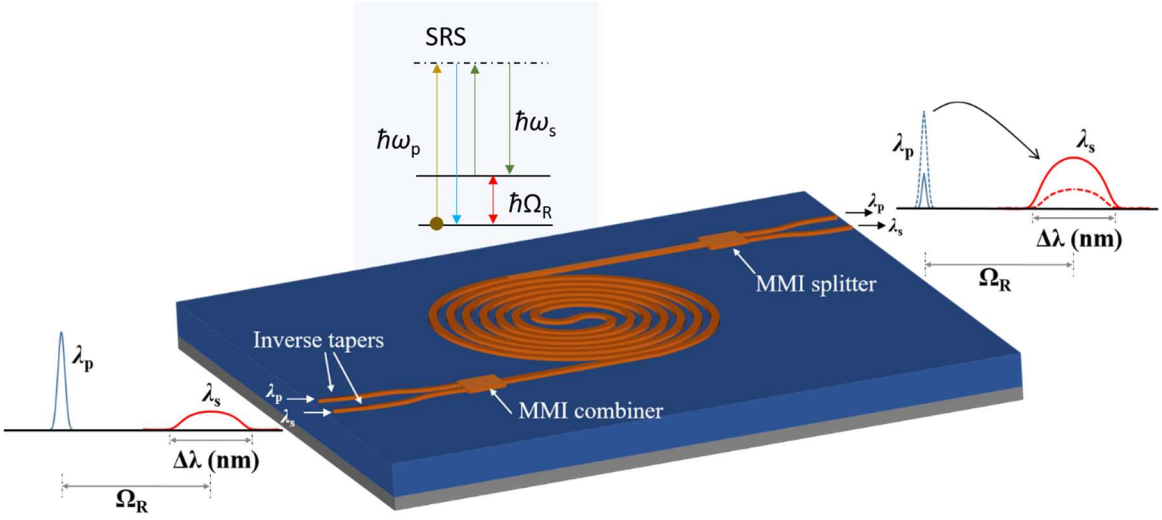

Figure 2.10. A conceptual drawing of an integrated Raman waveguide amplifier showing a narrow band pump used to amplify a broadband signal at longer wavelengths separated by the Raman shift (Ω_R).

In optical waveguides, the Raman effect is usually represented by a parameter called the Raman gain coefficient, γ_R which depends on the imaginary part of χ^3 [72]. The Raman gain coefficient describes the relationship between the intensities of the pump and Stokes signal light, namely how much the pump transfers power to the Stokes wave through the SRS process. If we consider the simple case of CW pumping, this relation can be represented by the equation below:

$$\frac{\partial I_s}{\partial z} = \gamma_R(\Delta\omega) I_s I_p, \tag{66}$$

where z is the propagation distance, I_s and I_p are the Stokes and pump intensities, and $\Delta\omega$ is the Raman shift given as $\omega_p - \omega_s$. The Raman gain coefficient is a polarization dependent parameter – it highly depends on the polarization relation between the pump and Stokes signal. The gain is maximum when the two waves are co-polarized and minimum when they are orthogonally polarized. The Raman gain coefficient parameter is sometimes expressed by dividing it by the effective mode area (A_{eff}) of a waveguide giving a new term referred to as Raman gain efficiency, $g_R = \gamma_R / A_{eff}$. In this case, the previous equation is modified to:

$$\frac{\partial P_s}{\partial z} = g_R(\Delta\omega) P_s P_p, \tag{67}$$

where P_s and P_p are the Stokes and pump powers in the waveguide. To model the evolution of pump and Stokes power along the waveguide under CW/quasi-CW pumping, equation (49) is modified to include the attenuation of both pump and Stokes waves and pump depletion due to its energy transfer to the Stokes wave. After these modifications the evolution of pump and Stokes power can be represented by a set of two coupled equations:

$$\frac{\partial P_s}{\partial z} = -\alpha_s P_s + g_R P_s P_p, \tag{68}$$

$$\zeta \frac{\partial P_p}{\partial z} = -\alpha_p P_p - \frac{\lambda_s}{\lambda_p} g_R P_s P_p, \tag{69}$$

where λ_s and λ_p are the signal and pump wavelengths, and α_s and α_p are the attenuations at the signal and pump wavelengths respectively. The symbol ζ in equation (69) can take values of +1 or –1 representing different pumping schemes, where +1 means a pump signal is launched in a forward direction whereas –1 means a pump is applied in the backward direction. The solution of the coupled amplifier equations can be estimated using numerical methods such as the finite element method (FEM) with good accuracy. Alternatively, one

can assume that with very high pump power of a few orders of magnitude greater than the signal, the pump depletion term (second term on the right-hand side of equation (69) is negligible and we arrive at an analytical solution with very good accuracy.

The CW model presented above has been developed under the assumption of no other nonlinear effects present in the waveguide. This assumption may hold, practically for low-power CW pumping and non-resonant structures such as fibers or straight waveguides However, the same case cannot be applied for pulsed laser pumping or in resonant structures such as high-Q MRRs where high intensity can build up. In such situations, combinations of various nonlinear effects are bound to happen, and therefore efficiently modeling the propagation of pump and Stokes pulses requires full consideration of the GNLSE presented earlier. In this case, the electric filed envelope is modified to include both pump and signal waves and becomes: $A = A_s e^{-\omega_s t} + A_p e^{-\omega_p t}$, where ω_s, ω_p are the signal and pump frequencies respectively. However, to make things easier, it is reasonable to separate the GNLSE into separate equations for the signal and pump. With a few assumptions and simplifications [72], the resulting equations are as follows:

$$\frac{\partial A_s}{\partial z} + \frac{\alpha_s}{2} A_s + i\frac{\beta_{2s}}{2}\frac{\partial^2 A_s}{\partial T^2} = i\gamma_s \left[|A_s|^2 + (2 - f_R)\left|A_p\right|^2\right] A_s + \frac{g_R}{2}\left|A_p\right|^2 A_s \tag{70}$$

$$\frac{\partial A_p}{\partial z} + \frac{\alpha_p}{2} A_p + d\frac{\partial A_p}{\partial T} + i\frac{\beta_{2p}}{2}\frac{\partial^2 A_p}{\partial T^2} = i\gamma_p \left[\left|A_p\right|^2 + (2 - f_R)|A_s|^2\right] A_p - \frac{g_R \omega_p}{2\omega_s}|A_s|^2 A_p \tag{71}$$

The first term on the right side of equation (70) accounts for the nonlinear effects of FWM and SPM, where f_R is a Raman contribution factor. The second term on the right side of the equation accounts for the contribution of Raman gain from the pump to signal. Similarly, the first term on the right side of equation (71) accounts for FWM and SPM while the

second term accounts for the pump depletion due to its energy transfer to the signal wave. The newly added third term on the left side of equation (71) accounts for the group velocity mismatch between pump and signal, $d = \beta_{1p} - \beta_{1s}$. Also, only the second-order dispersion term is included in the equations. For more details on the derivation and theoretical origin of Raman amplification in waveguides, readers are encouraged to refer to reference [15]. Similar to the GNLSE, the coupled amplifier equations above can only be solved by numerical techniques such as the commonly used SSFM. The study of Raman amplification in waveguides is presented in Chapter 6 of this thesis.

2.4.3 Applications of Nonlinear Optical Processes

Since the emergence of silicon-based nonlinear optics, it has been an enabling technology for broad applications underpinning the technological potential of silicon photonics. Particularly, nonlinear devices have excelled in areas where traditional (i.e., linear) silicon photonic components have failed to perform adequately, such as applications requiring broadband light, or frequency multiplying, and photon sources for quantum applications. In a very broad view applications of silicon photonics can be categorized into several areas, and in one way or another nonlinear silicon photonic devices have found applications in each of these areas. The leading application area and a major driving force for silicon photonics is communications, closely followed by computing and signal processing. There is a significant interest in medical applications driven by photonic biosensors and diagnostic equipment such as optical coherence tomography (OCT). Metrology is another important area where in particular Kerr combs are employed for distance-ranging and ultra-precise timekeeping. Furthermore, silicon photonics has found applications in various forms of defense and security systems and the recently emerging solid-state LIDAR technology which falls into the general area of sensing. Figure 2.11 shows a pictorial summary of all the application areas.

This thesis work, aims at improving the conversion efficiency of nonlinear processes applied in KCG and SCG leading to utilization of these devices in the applications highlighted above an unlock even further applications in the future. Also, there is a study of Raman amplification which could help pave the way for on-chip broadband and high-power amplifiers and lasers in a monolithic platform, opening a whole new window of applications. Table 2.1 gives a summary of the different applications of the nonlinear silicon photonics devices that have been demonstrated in the literature.

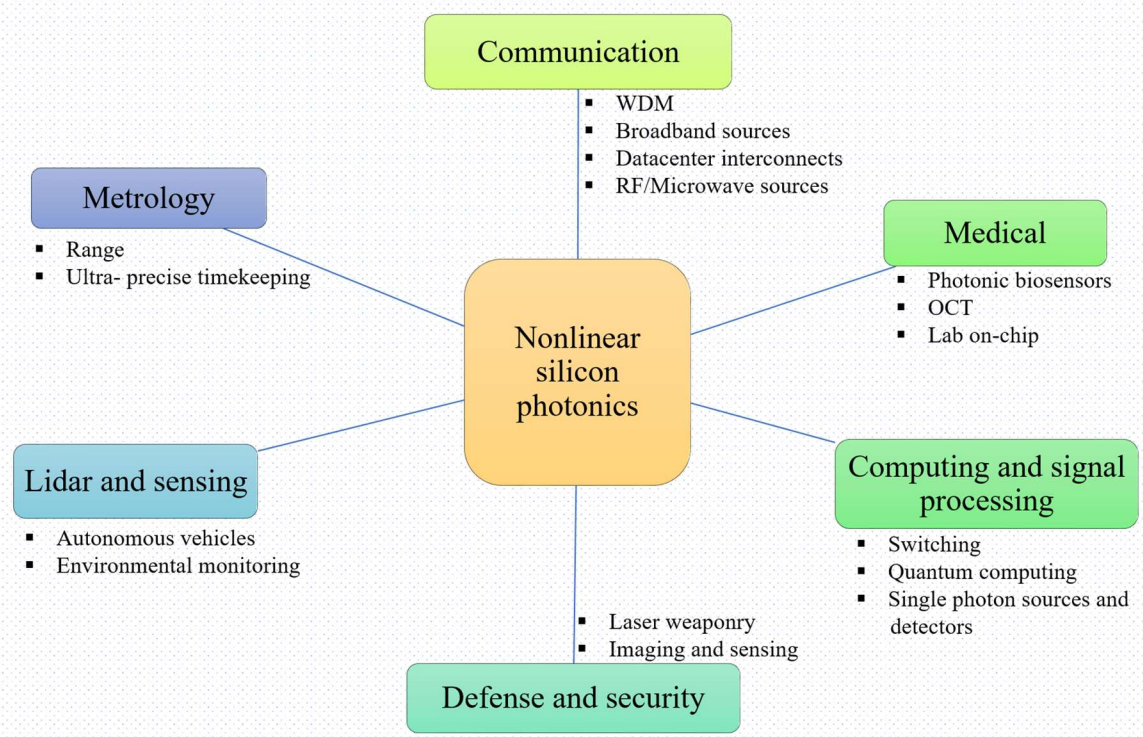

Figure 2.11. Broad view of potential applications of integrated nonlinear silicon photonics.

Table 2.1 Applications of the nonlinear optical phenomena

Nonlinear device	**Applications/References**
*SCG	Spectroscopy and imaging [92,102–104], optical coherence tomography (OCT) [105,106], Lidar [107–109], telecom, WDM [110–112]
*KCG	Spectral measurements [113,114], telecommunications [115–117], distance measurement [118,119], ultra-precise timekeeping and clocks [120], frequency sources [121], RF/microwave sources and devices [122]
*Raman amplifiers/lasers	Broadband sources [123,124], telecom, WDM [125,126], environmental monitoring and sensing [127–129]
*THG	THG microscopy [130,131], label-free biosensors [132], visible light sources [133,134], *f-3f* interferometry [135,136]
*FWM	Single photon sources [137,138], coherent anti-Stokes Raman spectroscopy [139,140], nonlinear phase conjugation [141]
*SPM & GVD engineering	Pulse compression [142–144], nonlinear phase conjugation [141]
Optical parametric oscillators (OPO)	Broadband light sources [145–147] and amplifiers [96,148–151]
SHG & parametric down-conversion	*f-2f* interferometry, single photon sources [137,138], visible light sources [133]
Brillouin scattering, amplifiers/lasers	Ultra-narrow-linewidth light sources [152,153], Microwave photonic filters [154–156] , RF & Microwave sources and devices [75]

*Indicates the specific phenomena that are directly or indirectly under study in this thesis

2.5 The Hybrid TeO_2-Si_3N_4 Platform

This section introduces the proposed hybrid TeO_2-Si_3N_4 nonlinear integrated photonics platform. First, a brief overview of the stoichiometric Si_3N_4 platform which forms an integral part of the hybrid platform is given. In particular, the discussion focuses on the development of the thick Si_3N_4 (>400 nm) that is typically needed for nonlinear devices. Next, a general overview of the motivation and development of the integrated TeO_2

platform is given. This is then followed by an overview and a generic discussion of the hybrid waveguide structure designed and used in this thesis.

2.5.1 The Stoichiometric Si_3N_4 Platform

Si_3N_4 is considered the third integrated photonics platform that is compatible with foundry-scale processes and it is complementary in characteristics and performance to the SOI and group III-V photonics platforms [157]. The first study on Si_3N_4 for photonics applications was reported in 1977 [158] where Si_3N_4 films were fabricated on a SiO_2 buffer on silicon wafers for 632-nm red light propagation. Although the research on the new platform continued, it highly intensified after ~2005 when significant process development and demonstration of applications in the NIR were reported [159,160]. The Si_3N_4 platform then received full attention and developed as a complementary material in application areas where SOI and III-V semiconductors such as InP are not suitable. It has now evolved into a mature technology surpassing SOI and InP in some application areas such as integrated nonlinear photonics. For a historical summary of the development of this platform, an invited article by Munoz *et al* is recommended [161]. Also, for recent reviews on the state-of-the-art of Si_3N_4 photonics readers are directed to the references [157,162–165].

The Si_3N_4 platform has numerous unique features that distinguish it from the other two leading integrated photonics platforms. It has wider transparency spanning from visible to MIR with low attenuation across its transparency. The losses in Si_3N_4 waveguides are as low as <1 dB/m, which is more than two orders of magnitude below those of the state-of-the-art SOI and InP platforms [157]. Also, it has a moderately high nonlinear refractive index but with negligible TPA, a feature that has made it an attractive platform for integrated nonlinear photonics. While the early phase of research on the Si_3N_4 platform focused heavily in reducing losses in which ultra-low loss waveguides were eventually achieved, more recently the focus shifted to increasing integration density and exploiting various nonlinear optical phenomena. In the fabrication studies, it was well established that

the main causes of loss are impurities, surface roughness, and mode confinement at the operation wavelength. The first two issues were mitigated by for example high temperature annealing and chemical-mechanical polishing (CMP) techniques. The third factor was addressed for linear applications by using low confinement waveguides that allowed the mode to propagate mainly in the SiO_2 cladding layer. Depending on the mode confinement, Si_3N_4 waveguides can be categorized into three groups which are *low confinement*, *moderate confinement*, and *high confinement* waveguides. Low confinement waveguides have a typical height of ~100 nm and a reported loss of down to 0.045 dB/m at 1580 nm [166]. Moderate confinement waveguides have heights between 150 − 400 nm and have reported propagation losses of 0.11 to 1.45 dB/cm at 1550 nm [161]. More important and relevant to the subject of integrated nonlinear photonics is the high confinement regime where waveguide heights range from 700 nm to 2500 nm. As pointed out in the previous paragraph, there has been more interest in developing Si_3N_4 waveguides that can provide small footprints with tighter bends and be exploited for nonlinear integrated photonic applications. While the waveguides in the moderate confinement region can ideally provide low-loss guiding and tighter bends, they are still inapplicable for nonlinear photonics devices, an area where Si_3N_4 stands out in performance. This limitation is imposed by the dispersion requirement where due to the high normal material dispersion only Si_3N_4 waveguide with heights >700 nm can have the anomalous GVD that is critical for phase matching of the nonlinear processes. This explains the jump from 400 nm to 700 nm thickness in the high confinement regime. Figure 2.12 summarizes this discussion, where Fig. 2.12(a) shows a plot of mode confinement versus Si_3N_4 core height and Fig. 2.12(b) shows how the dispersion profile changes for 400 and 700 nm core heights at a fixed width of 1600 nm. As shown by the dispersion plot in Fig 2.12(b) a waveguide of at least 700 nm thickness is needed for anomalous dispersion. However, the challenge is in the fabrication process, where it quickly became evident that it is difficult to fabricate such thick films with a low loss under the conventional CMOS deposition and etching techniques. This is

due to cracks caused by stress in the film introduced during the low-pressure chemical vapor deposition (LPCVD) process. Typically, tensile stress of > 800 MPa which are highly prone to cracks have been observed [167]. The challenge was addressed by exceptional efforts from photonic researchers worldwide and various techniques have been developed to overcome it, such as the photonic damascene reflow [167], stress release patterning [168], crack barrier [169], thermal cycling [95], *twist-and grow* [170], and dicing trench techniques [171]. Table 2.2 gives a summary of thick Si_3N_4 demonstrations by different groups and the nonlinear processes thereof.

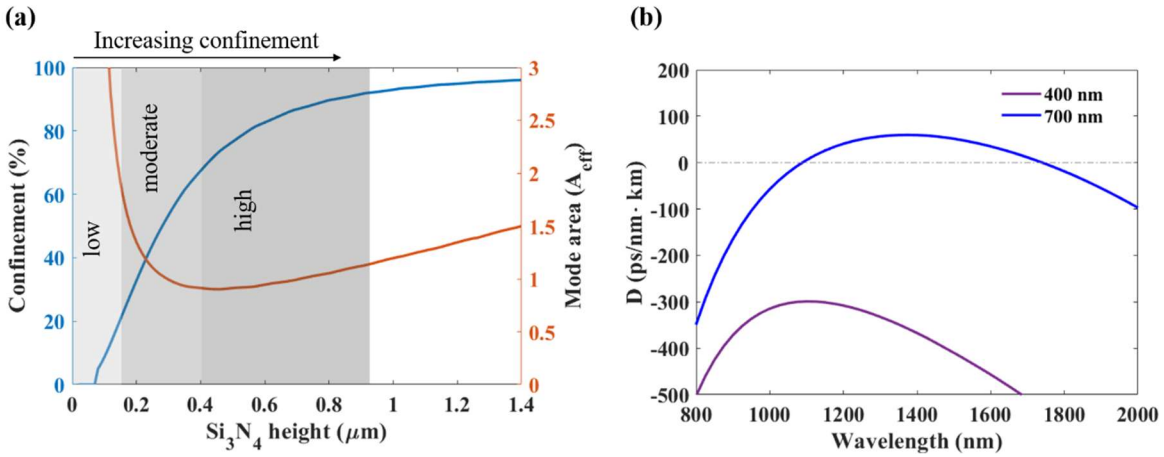

Figure 2.12. (a) Simulation of the waveguide confinement and mode area for the fundamental TE mode at 1550 nm in SiO_2-cladded Si_3N_4 strip waveguides, showing the three operating regimes. (b) Dispersion profile of the fundamental TE mode for the two thicknesses of 400 and 700 nm, corresponding to the moderate and high confinement regimes, respectively (the low confinement regime is omitted from the figure for clear visualization because it has strong normal dispersion significantly below the 400 nm profile). In both figures a constant width of 1600 nm is used but it is important to note that for different widths the effective mode area and dispersion parameters change accordingly.

Table 2.2 Thick Si_3N_4 waveguides for nonlinear photonics demonstrated by various research groups

Group/ Technique	Width (nm)	Thickness (nm)	Propagation loss (dB/cm)	Nonlinear demonstrations
Cornell & Columbia -Mechanical trenches isolating devices from propagating cracks	1800 2700	910 950	0.04 @ 1550 nm [169] 0.6 @ 2600 nm [172]	SCG [18], KCG [172], OPO [95]
LioniX/Twente -Etching and filling trenches	700–900	800/1000/1200	0.37 @ 1550 nm 0.45 @ 1550 nm 1.37 @ 1550 nm [173]	SCG [174,175], SHG [176,177] comb-laser [178]
Ligentec/EPFL -Etching and filling trenches (Damascene)	2000	800	Not reported [167]	SCG [116,121], KCG [179,180], frequency synthesizer [181]
CEA-LETI -Stepwise deposition while rotating the wafer (*twist-and grow*)	1400	730	0.3 @ 1550 nm [170]	FWM [182], SCG [170], KCG [183,184]
Twente -Crack barriers	1500	800	~ 0.35 @ 1550 [171]	SCG [185], OPO [186]

Despite the successful development of thick Si_3N_4 fabrication processes and subsequent achievements of well-performing nonlinear devices, it is still of great interest to develop nonlinear photonics devices in the moderate confinement regime. In particular, the 400 nm height which is now becoming a standard offered by various CMOS foundries across the globe. The 400-nm thickness offers advantages is several aspects, one is avoiding the extra-customized fabrication steps allowing fabrication with conventional deposition and etching techniques which ultimately lead to high yield volume manufacturing. Another advantage is that the thickness is ideal for single mode TE and TM waveguides with reasonable bend radii suitable for linear photonic functionalities in the same chip; also as will see potential for active functionality in hybrid waveguides for linear-nonlinear-active circuits. For such reasons, the 400-nm nitride platform is currently attracting growing interest and is offered in MPW or custom runs by several major photonic CMOS foundries such as LioniX

International [187], Interuniversity Microelectronics Centre (IMEC) [188], Advanced Micro Foundries (AMF) [189], and Applied Nanotools (ANT) [190].

2.5.2 TeO_2 Integrated Photonics

Tellurite glasses containing TeO_2 as the main component have very attractive linear and nonlinear optical properties among other oxide glasses. The properties have long been identified and extensively explored in fibers for applications including rare-earth doped amplifiers, broadband Raman amplification, and SCG. The Springer Series in Material Science 254, "Technological Advances in Tellurite Glasses" has a well-detailed account of the exploits of tellurite glass, especially in fibers [191]. With the growing interest in moving from bulky, bench-top systems into compact and scalable integrated platforms, TeO_2 has recently been considered as a potential material for integrated photonics. TeO_2 glass has a wide transparency spanning from the visible to 6 μm in the MIR with a high refractive index of about 2.08 at 1550 nm. The high refractive index allows for the fabrication of tight and compact photonic devices in a small footprint while the wider transparency permits broad coverage of many wavelengths of interest for diverse applications. It also has remarkable nonlinear optical properties, with a reported n_2 of 1.3 $\times 10^{18}$ m^2/W at 1900 nm [192] which is also experimentally verified by SCG measurements in Chapter 5, Brillouin gain coefficient of 3×10^{12} m/W [152], and Raman gain coefficient of more than 30 times that of silica[193]. The reported Raman gain coefficient varies with glass composition for which a summary and discussion are given in Chapter 6. Importantly, until the time of writing this thesis, there is no evidence reported of TPA in TeO_2 glass at NIR wavelengths, indicating that it can be an ideal candidate for efficient integrated nonlinear photonic applications.

Despite all the interesting optical properties and some recent significant demonstrations, the implementation of a standalone TeO_2 platform in integrated photonics is relatively much less mature than Si_3N_4. One of the main challenges lies in its chemical properties that

do not permit easy and efficient etching of its films into high-index contrast, low-loss, and compact waveguides [194]. Over the past two decades, several waveguide fabrication techniques have been employed. The proposed approaches include using UV direct writing [195], femtosecond laser direct-writing [196–198], ion exchange [199–201], ion implantation [202], sputter etching [203], and reactive ion etching [204]. State-of-the-art results were achieved in the work of S. J. Madden and K. T. Vu, showing low loss of down to ~0.05 dB/cm in most of the NIR spectrum and ~0.10 dB/cm at 1550 nm [204]. Through these exceptional efforts, high-performing devices have been demonstrated in the TeO_2 platform that motivated the research in this work. Such demonstrations include erbium-doped waveguide amplifiers and lasers [198,205,206] and nonlinear spectra broadening [204]. This work for the first time showed the potential for integrated nonlinear TeO_2 devices and motivated new directions of exploration for this promising material. First, for nonlinear optics, the waveguide cross-section in [204] was relatively large (1.6 x 4 μm^2) compared to Si_3N_4 and SOI. Maintaining high confinement and low-losses while reducing the effective area in more compact waveguides might enhance nonlinear phenomena. Second, further development of TeO_2 as its own platform would require enormous investments in research and development and infrastructure. As another approach, implementation of TeO_2 on traditional PIC platforms might exploit their mature, low-cost and high volume manufacturing while adding the material benefits of TeO_2 in densely-integrated PICs for a variety of applications.

Recently, our group developed methods to exploit the rich optical properties of TeO_2 by designing a hybrid platform that consists of a foundry stoichiometric Si_3N_4 coated with a TeO_2 film [207]. The TeO_2 film is coated at low temperature by a single post-processing reactive sputtering step, making it fully compatible with CMOS fabrication methods [207]. This approach offers two main advantages which are eliminating the need for etching the film and allowing for direct integration of the devices with the mature low-loss Si_3N_4

platform. This thesis work was preceded by the demonstration of high-Q microring resonators [208], erbium and thulium-doped waveguide amplifiers and lasers [209–211], and eventually the very first demonstration of nonlinear processes in form of SCG [212] and FWM [213] in the TeO_2-Si_3N_4 platform. All of those works focused on 200-nm-thick Si_3N_4, which was selected as an effective thickness for linear and active devices [207]. Following a similar approach, this thesis presents the hybrid TeO_2-Si_3N_4 platform as a candidate for efficient nonlinear photonics in a thin, crack-free, and moderate confinement 400-nm foundry Si_3N_4.

2.5.3 Hybrid TeO_2-Si_3N_4 Waveguides

In this thesis, we investigate hybrid TeO_2-Si_3N_4 waveguides which make use of a moderate confinement 400 nm-thick foundry Si_3N_4 platform. Besides the two key advantages of being etch-less and taking advantage of the mature low-loss Si_3N_4 platform, there are a number of other factors that motivate the work in this thesis. First, the 400 nm Si_3N_4 platform offers moderate confinement that allows for tight bends and small footprint devices. Also, in combination with the added TeO_2 film, the waveguide dispersion can be precisely engineered between the normal and anomalous regimes. Furthermore, the added highly-nonlinear TeO_2 enhances the waveguide nonlinearity and allows for potentially lower threshold nonlinear devices. In addition, it gives access to other nonlinear phenomena that are usually lacking or less efficient in stoichiometric Si_3N_4 such as SRS and SBS.

Material properties: Table 3 summarizes the important optical properties of the materials used in the design of the hybrid TeO_2-Si_3N_4 waveguides in this thesis. It includes the linear and nonlinear refractive indices and the Raman gain coefficient. The respective dispersion relations in form of Sellmeier equations are also given. The Sellmeier equations of SiO_2 and Si_3N_4 are taken from literature with references given in the table. While these equations are widely used by the research community, the author acknowledges that there might be slight variations in experimentally measured parameters caused by possible variations in

parameters used from the literature. Also, for the case of TeO_2, both the nonlinear refractive index and the Raman gain coefficient have shown significant variations depending on glass compositions. These variations and compositions are given and discussed in Chapter 3 and Chapter 6 for the nonlinear index and the Raman gain coefficient, respectively. The dispersion relation for TeO_2 given is an example and was obtained by experimentally fitting ellipsometric measurement based on a Sellmeier mode. Depending on the TeO_2 thickness and deposition conditions, the Sellmeier coefficients vary slightly and in each case throughout this thesis, the respective measured dispersion is given.

Table 2.3. Optical properties of the materials used in the design and simulation of the hybrid waveguide platform.

Material	**Refractive index at 1550 nm**	**Nonlinear refractive index (m^2/W)**	**Raman gain coefficient ($W^{-1}m^{-1}$)**	**Dispersion relation**
SiO_2	1.444 [214]	2.2×10^{-20} [215]	1×10^{-13} [216]	$n^2-1=\frac{0.6961662^2}{\lambda^2-0.0684043^2}+\frac{0.4079426^2}{\lambda^2-0.1162414^2}+\frac{0.8974794^2}{\lambda^2-9.8961661^2}$
Si_3N_4	1.996 [172]	2.4×10^{-19} [217]	Negligible	$n^2-1=\frac{3.0249\lambda^2}{\lambda^2-0.1353406^2}+\frac{40314\lambda^2}{\lambda^2-1239.842^2}$
TeO_2	2.080 [this work]	1.3×10^{-18} [192]	40×10^{-13} [193]	$n^2-1=\frac{2.8939\lambda^2}{\lambda^2-0.13967^2}$

The waveguide structure: The structure of the hybrid waveguide is simple consisting of a foundry Si_3N_4 strip waveguide on insulator (SiO_2) and a silicon substrate, that is coated with the TeO_2 film to form a high index cladding or a multi-core structure as shown in Fig. 1.13. It shows 3D images of the separate material layers and the combined structure and a 2D cross-section view with labels indicating the dimensions of each layer. Also, sometimes

the waveguide is covered by a low-index (n = 1.336 at 1550 nm) protective fluoropolymer (CYTOP) top-cladding layer, not shown in the drawing for clarity.

Simulated waveguide properties: Specific simulated waveguide properties relevant for each of the nonlinear phenomena are presented in the respective chapters throughout this thesis. However, to establish an overview and understanding of some basic properties of hybrid TeO_2-Si_3N_4 waveguides, some general simulation results are shown here. Figure 1.13(b) shows the mode profiles of a 1.6 μm wide waveguide without the TeO_2 coating, and 400 nm TeO_2 coating for the fundamental TE and TM modes, respectively. In addition, Fig. 1.13(c) shows a comparison of the resulting effective index and single mode cut-off widths for the uncoated and TeO_2 coated waveguides, respectively. It can be seen that the addition of the TeO_2 layer lowers the single mode cut-off width from 1.5 μm to 1 μm which is a direct consequence of increased overall waveguide height. We also simulate the waveguide confinement and effective mode areas comparing the two cases of the coated and uncoated waveguide and the results are plotted in Fig 1.13(d). From this figure, it can be seen that the TeO_2 overlap increases as the Si_3N_4 width decreases. The total mode overlap increases for the coated waveguide as shown in Fig. 1.13(d) due to the increased core size and higher index of the TeO_2 layer. However, the increase in the mode overlap comes at the expense of an increase in the effective mode area. Therefore, depending on the intended nonlinear application in each specific design, various factors are important to consider to reach optimal parameters, particularly the Si_3N_4 strip width and the TeO_2 coating thickness.

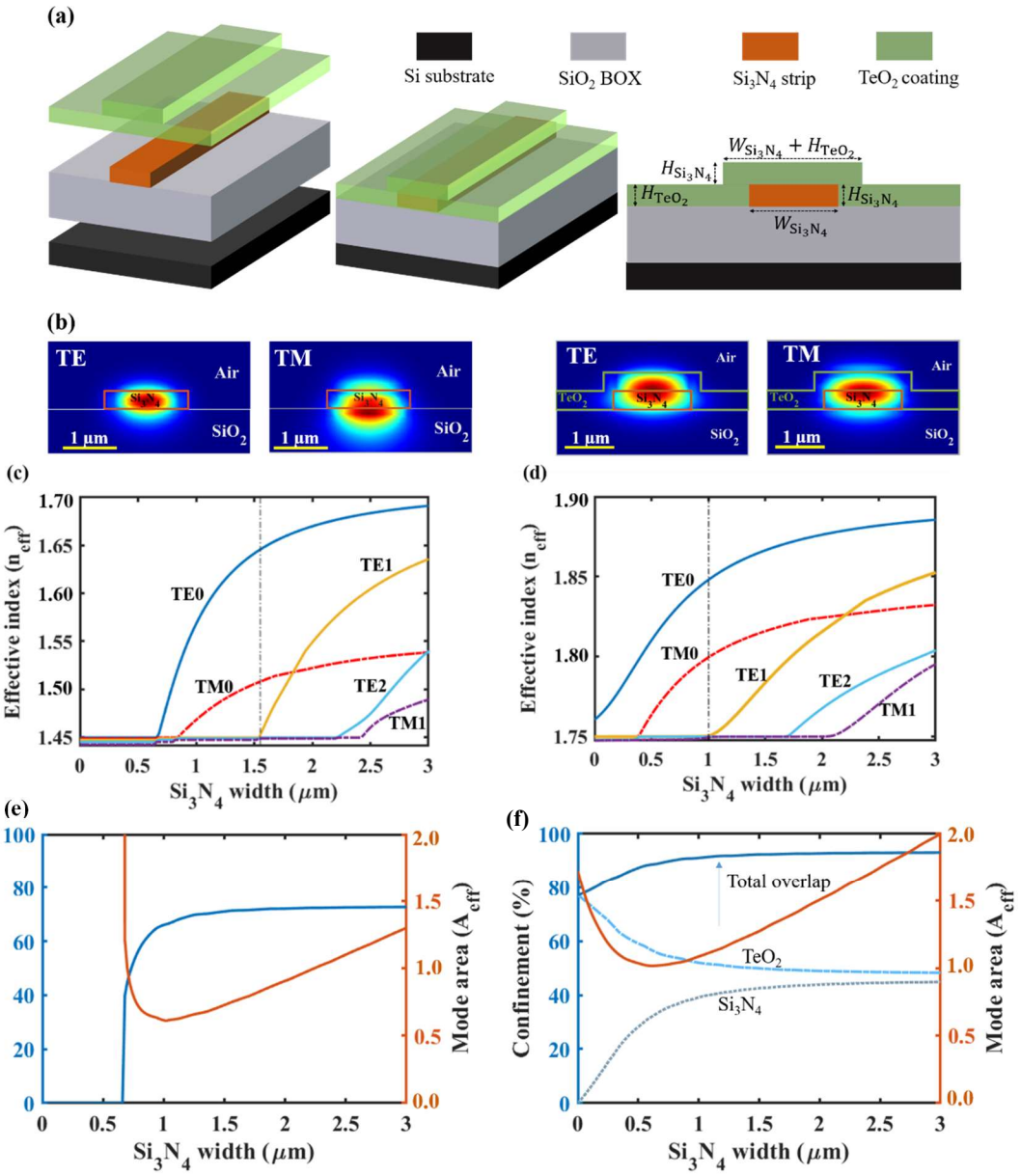

Figure 2.13. (a) Hybrid TeO_2-Si_3N_4 waveguide structure showing a 3D visualization of individual layers and a cross-section view with parameters. (b) Simulated mode profiles for uncoated and 0.4-µm TeO_2-coated, 0.4-µm-high by 1.6-µm-wide Si_3N_4 waveguides. (c) and (d) Simulation results of supported modes for the two waveguides cases indicating single mode cut-off widths (dotted gray lines). (e) and (f) Confinement and effective mode area versus Si_3N_4 width for the two waveguide cases.

2.6. Summary

In summary, this chapter has presented an overall theory and background of all subjects that are studied in this thesis. First, the origin of nonlinear response in bulk media was given followed by a summary of various nonlinear processes resulting from the such response. The nonlinear wave equation was then derived from Maxwell's equation. The nonlinear response in waveguide was examined alongside the definition of important terms such as the nonlinear and dispersion parameter that is to be used throughout this thesis. Microring resonators form an essential part of the study in this thesis and therefore their theoretical background was given here, and also their important applications in dispersion and loss measurements were discussed. Furthermore, different nonlinear devices that are being studied in this thesis were discussed in terms of their basic operating principles and potential applications. Lastly, the hybrid TeO_2-Si_3N_4 platform under study was also introduced in this chapter. The introduction includes motivation for choosing this platform, literature on previous studies, and simulation results showing an overview of some of its basic properties such as effective refractive indices, mode areas, and mode overlap.

Chapter 3

Enhanced Nonlinearity and Engineered Anomalous Dispersion in TeO_2-coated Si_3N_4 Waveguides

Reprinted in part with open access permission from H. M. Mbonde, H. C. Frankis, and J. D. B. Bradley, "Enhanced nonlinearity and engineered anomalous dispersion in TeO_2-coated Si_3N_4 Waveguides," *IEEE Photonics J.* **12**(2), 2200210 (2020).

DOI: 10.1109/JPHOT.2020.2973297

This chapter includes results published in a manuscript on the analytical and numerical study of how the TeO_2 coating can be used to enhance the S_3N_4 waveguide's effective nonlinearity and engineer the dispersion to anomalous. The study was the first step in the examination of the hybrid platform as a candidate for integrated nonlinear photonics. Therefore, it aimed to explore and optimize the waveguide geometry to enable the engineering of dispersion to the anomalous regime and enhance the effective nonlinearity by reducing mode areas and increasing overlap with the TeO_2 film. The results showed that the waveguide nonlinearity is enhanced up to three times that of a standalone stoichiometric S_3N_4 and anomalous dispersion can be obtained using a 400-nm thick Si_3N_4 and TeO_2 coating of about 500 nm. It is also shown that the nonlinearity can be improved even further by doping the TeO_2 itself with other metal oxides. All sections in this chapter were directly

copied from the published manuscript and the only changes made are the adjustment of formatting and reference numbering to match the rest of the thesis.

ABSTRACT: We propose designs of silicon nitride (Si_3N_4) waveguides with enhanced nonlinear parameter and engineered anomalous group velocity dispersion (GVD) by the addition of tellurium oxide (TeO_2) top-coating layers of various thicknesses. The proposed waveguides have calculated nonlinear parameters of up to three times that of stoichiometric Si_3N_4 and exhibit anomalous GVD at near-infrared wavelengths. The GVD of such waveguides can be tuned between the normal and anomalous regimes with different zero dispersion wavelengths by adjusting the thickness of the TeO_2 coating. These designs offer the promise of higher-performance nonlinear devices on a standard low-loss Si_3N_4 platform with the possibility of integration of active functionalities owing to the higher solubility of rare earth dopants in tellurium oxide.

3.1 Introduction

Over the last several years nonlinear optical devices have shown great progress and promise for a wide range of applications in integrated photonics, including in areas such as all-optical signal processing, ultra-low power all-optical switching, and quantum photonics [218]. Silicon nitride (Si_3N_4) in particular has become a leading platform for the development of various on-chip integrated nonlinear devices. The Si_3N_4 platform offers the advantage of compatibility with mature CMOS processing through which highly compact and low-loss waveguides can be fabricated [219], [220]. In addition, Si_3N_4 has negligible two-photon absorption (TPA) hence lower nonlinear losses making it an ideal candidate for on-chip nonlinear photonics [221], [222]. Different nonlinear devices have been demonstrated on an integrated Si_3N_4 platform mainly for supercontinuum generation [223]-[224] and ultra-broadband frequency comb generation [225]-[38], all based on the third-order Kerr optical nonlinearity.

Although stoichiometric Si_3N_4 has proven to be an excellent candidate for on-chip nonlinear photonics, its nonlinear refractive index is lower compared to other materials of interest such as silicon-on-insulator (SOI) or silicon-rich silicon nitrides [222]. Having a lower nonlinear index raises the need for tight confinement of light within the waveguide to enhance the optical intensity and ultimately increase the nonlinear coefficient which determines the extent of nonlinear interactions. Additionally, the efficiency of frequency conversion resulting from those interactions is also highly dependent on the phase-matching condition. It has been shown that the simplest way to achieve phase matching is through the engineering of the group velocity dispersion (GVD) of the waveguide, such that the phase shift resulting from dispersion balances with that arising from nonlinear interactions [226]. The requirement is to have anomalous and low GVD parameters over a wide range of wavelengths. However, the overall GVD is dependent not only on waveguide geometry but also on material dispersion. Therefore, the choice of material limits the overall GVD parameter. For stoichiometric Si_3N_4 the typical waveguide GVD is normal over most parts of telecommunication bands unless thicker waveguides of at least 720 nm are employed [15]. Fabricating such thicker low-loss waveguides through low-pressure- (LP-) or plasma-enhanced (PE-) chemical vapor deposition (CVD) is challenging due to cracks in the Si_3N_4 film induced by stress. Different fabrication techniques have been proposed to overcome this problem such as the damascene reflow process [227], [45] and the *twist-and-grow* scheme where Si_3N_4 deposition is carried out in steps while rotating the wafer (45°) midway [228]. Although these processes have proven to be effective in meeting the end goal, they also introduce undesired complexities into the fabrication process. Furthermore, the resulting Si_3N_4 waveguides have large core cross-sections, thus are highly multi-mode, which may be detrimental to implementing various linear or active optical functionalities on the same platform.

Tellurium oxide (TeO_2) has recently received quite some attention as the material of interest for active functionalities monolithically integrated into silicon photonics devices[229]-[230]. TeO_2 has a slightly higher linear refractive index (n) than that of Si_3N_4 enabling the fabrication of highly compact waveguides. It has a significantly higher nonlinear refractive index (n_2) and higher Raman gain coefficient than that of stoichiometric Si_3N_4 [229]. TeO_2 has a wide transparent window spanning from visible through the near-infrared (NIR) and into the mid-infrared. Similar to Si_3N_4, TeO_2 also has negligible two-photon absorption. Furthermore, TeO_2 has proven to be an excellent host of rare earth ions, exhibiting higher solubility with minimal quenching [231]. We have recently demonstrated a TeO_2 on Si_3N_4 waveguide platform with low losses and which exploits the advantages of both materials, and shown amplification in both erbium- and thulium-doped TeO_2-coated Si_3N_4 waveguides [231]-[68].

In this work we propose designs of Si_3N_4 waveguides coated with TeO_2 layers of varying thicknesses that enhance the nonlinear coefficient and offer a straightforward approach to engineering GVD in thinner Si_3N_4 waveguides, hence potentially avoiding the complex fabrication processes aforementioned. Our numerical results show that by varying the thickness of the TeO_2 coating we can tune the GVD parameter of Si_3N_4 strip waveguides (with as low as 300 nm thickness) between the normal and anomalous regime and achieve anomalous dispersion that may cover up to a 0.8 μm wavelengths span. We calculate a nonlinear parameter in TeO_2-coated Si_3N_4 waveguides that is up to three times higher than that of typical stoichiometric Si_3N_4 waveguides.

3.2 Material Properties and Waveguide Design

Our basic waveguide structure is shown in Fig. 3.1(a), where $h_{Si_3N_4}$, and $w_{Si_3N_4}$ are height and width of the Si_3N_4 strip and h_{TeO_2} is the TeO_2 coating thickness. By varying h_{TeO_2} from zero, the proposed waveguide can be tuned from single to multi-mode. Such a waveguide

can be fabricated by obtaining low-thickness Si_3N_4 waveguides from a standard CMOS foundry and then depositing a TeO_2 coating through a single step back end process [23]. The deposition is carried out using a radio frequency (RF) sputtering process, as described in [68]. The process is straightforward and low-cost and yields near stoichiometry TeO_2 layers which insures low propagation losses. Relevant to nonlinear optical devices, the TeO_2 coating can provide the additional height necessary to achieve anomalous GVD hence overcoming the need for thicker Si_3N_4 waveguides. Further insight regarding measurements and calculations of both insertion and propagation losses can be gained by referring to our previous works on waveguide structures of similar design [22], [23]. However, in the referred papers we reported waveguides of lower height than what we are proposing here. The differences in heights might lead to different levels of sidewall roughness and hence variations in losses. Minimizing the fiber-chip coupling and linear propagation loss while obtaining anomalous GVD will ultimately be critical in optimizing the nonlinear optical device performance for this design.

Figure 3.1(b) shows the material dispersion plot measured for bulk SiO_2 glass and Si_3N_4 and TeO_2 thin films. The material dispersion values were calculated using both Sellmeier's and Cauchy's equations. Sellmeier coefficients for SiO_2 in (1) were obtained from reference [26], and Si_3N_4 in (2) from reference [232] whereas Cauchy coefficients of TeO_2 in (3) were experimentally determined using ellipsometry.

$$n^2\text{-}1=\frac{0.6961663^2}{\lambda^2\text{-}0.0684043^2}+\frac{0.4079426^2}{\lambda^2\text{-}0.1162414^2}+\frac{0.8974794^2}{\lambda^2\text{-}9.896161^2}\ , \tag{1}$$

$$n^2\text{-}1=\frac{3.0249\lambda^2}{\lambda^2\text{-}0.1353406^2}+\frac{40314\lambda^2}{\lambda^2\text{-}1239.842^2}, \tag{2}$$

$$n^2=2.057+\frac{0.02323}{\lambda^2}+\frac{0.002}{\lambda^4}, \tag{3}$$

Figures 3.1(c) and (d) show simulated mode profiles for a waveguide with Si_3N_4 strip dimensions of 1 μm x 0.4 μm and a 0.5-μm-thick TeO_2 coating, for transverse-electric (TE) and transverse-magnetic (TM) polarized modes respectively.

Table 3.1 shows a summary of measured nonlinear refractive indices for tellurite glasses with different compositions obtained from the literature. It should be noted that for some values in Table 3.1 only the third-order nonlinear susceptibility had been measured by the respective reference source and we calculated its corresponding nonlinear refractive index according to the formula given in [71]. The values of n_2 reported in Table 3.1 vary depending on the glass composition. The highest reported value is 3.21 x 10^{-18} m^2/W for 90% TeO_2 and 10% $VO_{2.5}$ compositions while the lowest value reported is 3.53 x 10^{-19} m^2/W for 70% TeO_2, 20% ZnO, 5% Na_2O and 5% Nb_2O_5 compositions**.** These are all larger than the nonlinear refractive index of stoichiometric Si_3N_4 of 2.4 x 10^{-19} m^2/W as reported in [233]. It can be deduced from these values that we can expect n_2 for tellurite glass thin films of various compositions at a minimum of one and half times that of stoichiometric Si_3N_4. With the right selection and concentration of metal oxide dopants the n_2 value of TeO_2 might be increased up to 13 times that of Si_3N_4 or more. In our work we chose to use a (χ^3) value that has been experimentally determined for pure TeO_2 using the third harmonic generation (THG) method [234], then we calculated n_2 using the formula given in [71], to be 1.3 x 10^{-18} m^2/W.

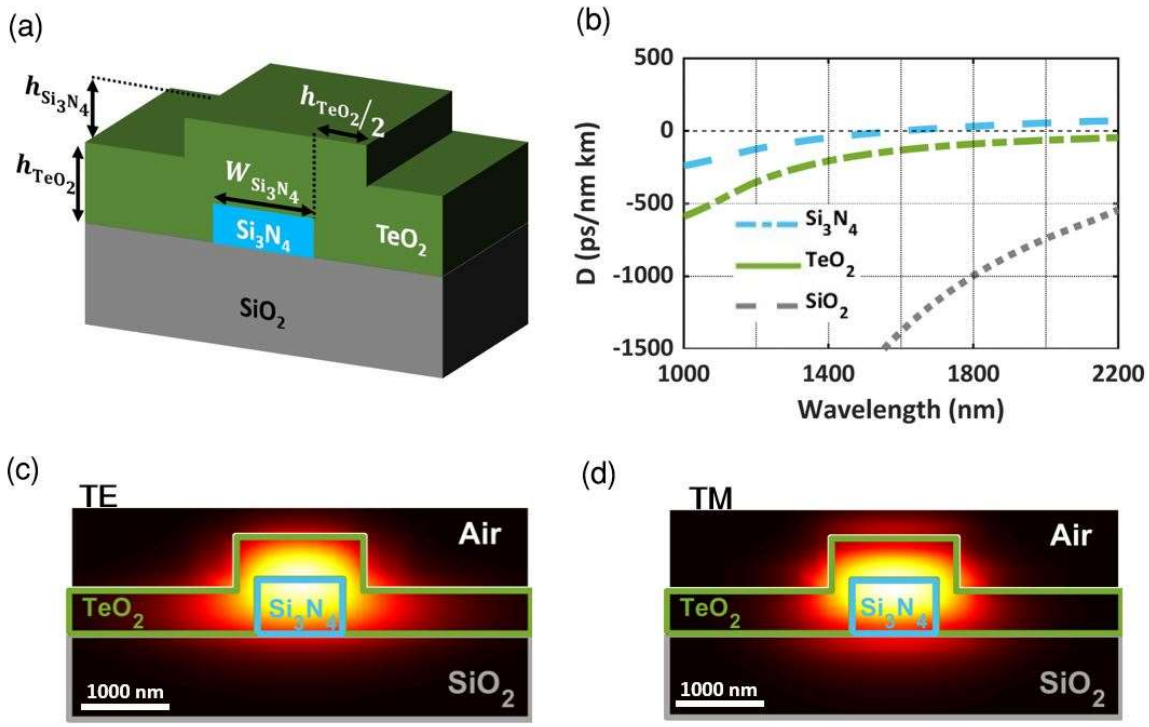

Figure 3.1. (a) 3D illustration of the proposed TeO_2-coated Si_3N_4 waveguide structure; (b) material dispersion for Si_3N_4 and TeO_2 thin films and bulk SiO_2 glass; (c) TE and (d) TM mode (electric field) profiles for waveguides with Si_3N_4 strip dimensions of 1 µm x 0.4 µm and a 0.5-µ-thickTeO_2 coating.

Table 3.1. Nonlinear refractive indices of different tellurite glasses

Medium	Glass Composition	n (λ)	n_2 (m^2/W)	Measurement Method	Reference
Bulk glass	Pure TeO_2	2.121 (1900nm)	1.30e–18	Third Harmonic Generation (THG)	[234]
Bulk glass	95TeO_2 - 5Nb_20_5	2.23 (840nm)	2.10e–18	Interferometry	[235]
Bulk glass	30 $NbO_{1.5}$.70 TeO_2	2.192 (1900nm)	1.39e–18	THG	[236]
Bulk glass	10$VO_{2.5}$.90 TeO_2	2.106 (1900nm)	3.21e–18	THG	[236]
Bulk glass	70TeO_2 –10ZnO–10Nb_2O_5 –10MoO_3	2.0885(1900nm)	2.04e–18	THG	[237]
Bulk glass	70TeO_2-20ZnO-5Na_2O- 5Nb_2O_5	unavailable	3.53e–19 ($\lambda = 800nm$)	Z-Scan	[238]
Bulk glass	80TeO_2 – 10GeO_2−10Li_2O	unavailable	1.89e–19 $\lambda = 1064nm$	Z-San	[239]
Bulk glass	85TeO_2-10Na_2O-5MgO	2.0212(1064nm)	5.89e–19	Z-Scan	[240]
Bulk glass	10PbO- 10TiO_2 - 70TeO_2	2.20 (633nm)	2.29e–18	THG	[241]
Bulk glass	85TeO_2-15WO_3	2.17 (800nm)	7.6e–19	unavailable	[242]
Fiber[1]	75TeO_2 -20ZnO-5Na_2O		5.0e–19	-	[243]
Waveguide[2]	Pure TeO_2		6.5e–19	-	[229]

[1]The n_2 value was calculated from the measured linear refractive index using the BGO formula.
[2]The n_2 value was extracted mathematically from the nonlinear experiment.

3.3. GVD Engineering

Nonlinear processes such as four-wave mixing (FWM) involve the generation of new frequencies with phase shifts introduced by both the third-order nonlinear susceptibility and group velocity dispersion. For an effective generation of new frequencies phase matching through anomalous GVD is required. Unfortunately for most optical materials, the GVD parameter is normal at telecommunication wavelengths. For this reason, different techniques have been proposed to engineer GVD between the anomalous and normal regime for silicon-based photonic waveguide platforms including Si_3N_4, SIO, and silicon-

rich nitrides. Such techniques involve modification of the waveguide geometry (height to width ratio) [244], implementing multicore/cladding waveguide designs [224], or through spatial mode coupling [245]. Here we study numerically how we can engineer the GVD of our waveguides between normal and anomalous for TE and TM modes accounting for both the material and waveguide dispersion. We employ both techniques of geometric manipulations as well as a multicore waveguide structure. Adjusting the TeO_2 coating thickness modifies both the waveguide geometry and the effective refractive index. Therefore, the GVD parameter can be controlled by tuning the TeO_2 coating thickness.

The dispersion parameter (D) of a waveguide is calculated by (4);

$$D = -\frac{\lambda}{c}\frac{d^2 n_{eff}}{d\lambda^2}, \tag{4}$$

where λ is the wavelength, c is the speed of light in vacuum and n_{eff} is the effective refractive index. The effective refractive index is obtained by calculating the mode solution of a given waveguide. In this work, we used a finite element method (FEM) eigen mode solver to find the mode profiles and effective refractive indices of different waveguide designs at a wavelength from 1 μm to 2.2 μm. While solving the modes and effective indices we incorporated the contribution of the material dispersion in the refractive indices of each material.

Numerical simulations were carried out to determine the GVD parameter for different waveguide geometries and the corresponding results are shown in Fig. 3.2 and 3.3. In Fig. 3.2, Si_3N_4 strip waveguides with a fixed width of 1 μm and heights of 0.3 μm,0.4 μm, and 0.5 μm were simulated for waveguide dispersion. In all cases, the thickness of TeO_2 coating was varied from 0 to 0.5 μm in 0.1 μm steps. In Figs. 3.2(a) and (b) the trend shows that increasing TeO_2 coating thickness shifts the GVD towards positive (anomalous) values. A similar trend can be observed in Figs. 3.2(c) and (d). Anomalous dispersion is shown for the TE mode for TeO_2 coating thickness of 0.1 μm and a Si_3N_4 layer thickness of only 0.4

μm with the latter considered to be the maximum thickness for crack-free LPCVD Si_3N_4 layers [246], [43]. However, after reaching a certain height further increase of the TeO_2 coating thickness does not make GVD more positive but rather shifts the zero-dispersion point toward higher NIR wavelengths. This trend is significant since many nonlinear applications involve pump and signals at these wavelengths. Figures 3.2(e) and (f) show that for a 0.5-μm-thick uncoated Si_3N_4 strip waveguide it is possible to obtain anomalous GVD, however, the values are centered at wavelengths of 1.2 μm and 0.9 μm for the TE and TM modes, respectively, which are typically wavelengths of less interest. The significance of the TeO_2 coating as shown here is that it shifts the GVD toward telecommunication wavelengths as the coating thickness increases. Working with the crack-free Si_3N_4 thickness of 0.4 μm, in Fig. 3.3 we show dispersion profiles for various Si_3N_4 strip widths and fixed 0.5 μm TeO_2 coating thickness, for TE (a) and TM mode (b). In both cases, it can be observed that increasing widths make the GVD parameter more positive as well as covering a much broader wavelength span. However, wider waveguides result in a lower calculated nonlinear parameter, as shown in the next section.

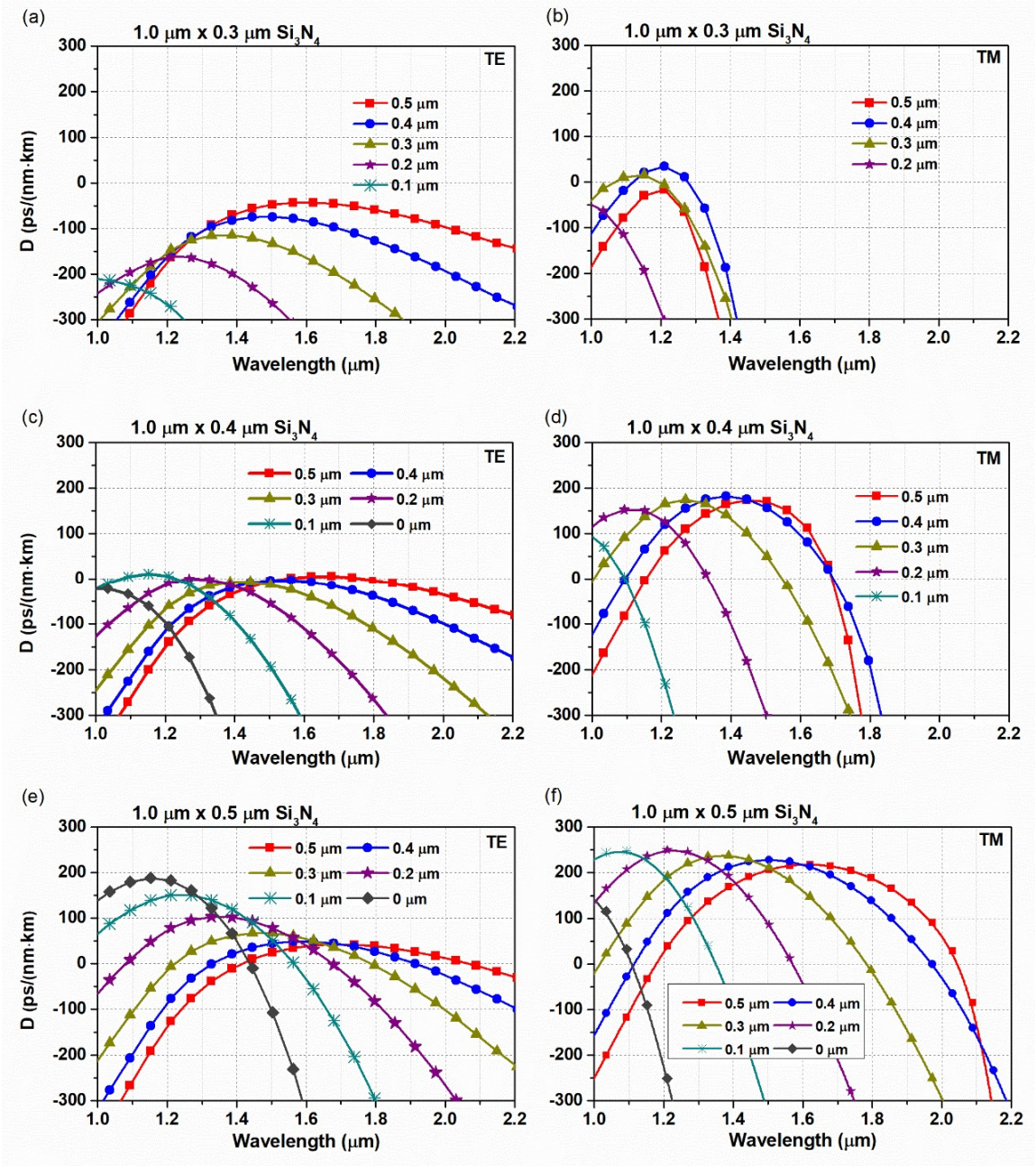

Figure 3.2. Calculated GVD parameter for a TeO_2-coated 1- μm -wide Si_3N_4 strip waveguide with varying Si_3N_4 heights of (a and b) 0.3 μm, (c and d) 0.4 μm and (e and f) 0.5 μm (for TE and TM modes, respectively). The TeO_2 coating thickness is varied from 0 to 0.5 μm in steps of 0.1 μm, shown in the legends.

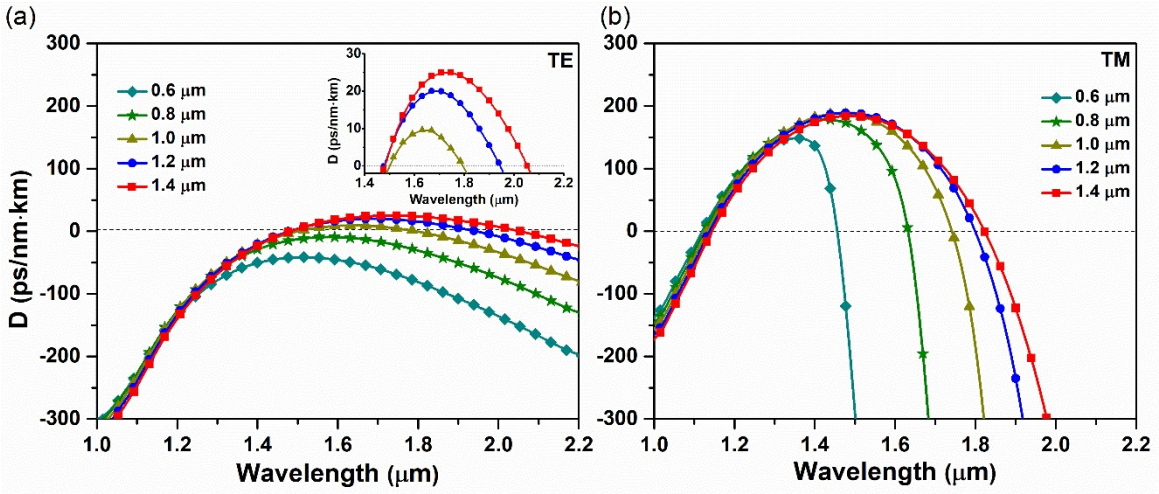

Figure 3.3. Calculated GVD parameter for a 0.4-µm-high Si_3N_4 strip waveguide and 0.5 µm TeO_2 coating thickness with varying Si_3N_4 widths of 0.6 µm, 0.8 µm, 1.0 µm, 1.2 µm and 1.4 µm for (a) TE and (b) TM modes.). The inset in (a) shows a zoomed anomalous dispersion region.

3.4. Optimization of Nonlinear Parameter

The origin of the nonlinear refractive index of optical materials is the third-order susceptibility (χ^3) term of induced polarization as described in [72], [45]. Its effects in optical waveguides are usually represented by the nonlinear parameter (γ), defined as [44], [45];

$$\gamma = \frac{n_2 \cdot \omega}{A_{eff} \cdot c} \quad , \tag{5}$$

where ω is frequency, c is the speed of light in free space, A_{eff} is effective mode area and n_2 is the nonlinear refractive index of a material. The nonlinear parameter depends on the wavelength of the incident light, the effective mode area (A_{eff}) of a waveguide, and the nonlinear refractive index. In this work, we demonstrate numerical optimization of the nonlinear parameter by increasing the effective nonlinear index of a waveguide and manipulating waveguide geometry for optimal core size. The former was achieved by

ensuring a large portion of the propagating light is confined within the TeO_2 coating since it has higher n_2 and the latter was achieved by tuning the ratio of waveguide width and height to optimal values. Intuitively, decreasing waveguide dimensions should increase the nonlinear parameter, however that trend only continues up to a certain optimal point and not continuously as pointed out in [247]. As the core size becomes smaller, eventually a larger percentage of the power propagates in the evanescent field increasing A_{eff} and ultimately reducing γ. There should be a balance between core size and light confinement, and for a given material there are optimal core dimensions that give a maximum value of γ. In our numerical study, we investigated various waveguide geometries for maximizing nonlinear interactions and the results are shown in Fig. 3.4, and 3.5. Through numerical simulations, we obtained the effective mode areas and overlap fractions of light with each material within the optical mode. Then we carried out numerical calculations to determine the nonlinear parameter by solving the overlap integral given in [46]. The calculated nonlinear parameter for a waveguide with 1 μm Si_3N_4 strip width with varying heights of Si_3N_4 as well as coating thickness of TeO_2 is shown in Figs. 3.4(a) and (b). The plots show that for each combination of waveguide dimensions there is an optimal point at which γ is maximum. In both plots, the bottommost (solid dark-gray) curve shows a γ value for stoichiometric Si_3N_4 which agrees with previous values reported in the literature [5]. The significance of the TeO_2 coating is shown in the plots where for each case of additional TeO_2 coating greater γ is obtained. Overall, the nonlinear parameter is increased up to three times that of stoichiometric Si_3N_4. For example, a Si_3N_4 strip waveguide with dimensions 1 μm by 0.4 μm gives γ of 1 W^{-1} m^{-1} and normal GVD of –820 ps/nm/km without a TeO_2 coating whereas adding a 0.5-μm-thick TeO_2 coating gives a γ of 2.8 W^{-1} m^{-1} and anomalous GVD of 4.5 ps/nm/km both at 1.55 μm and for the fundamental TE mode. Similarly, for the TM mode, a Si_3N_4 strip waveguide with the same dimensions gives a γ of 0.25 W^{-1} m^{-1} and normal GVD of –5120 ps/nm/km without a TeO_2 coating whereas adding a 0.5-μm-thick TeO_2 coating gives a γ of 2.6 W^{-1} m^{-1} and anomalous GVD of 155

ps/nm/km both at 1.55 µm. We also carried out similar calculations for a fixed 0.4 µm height of the Si_3N_4 strip while varying widths and the TeO_2 coating thickness, results are shown in Fig 3.4(c) for TE mode and 3.4(d) for TM mode. The slope, in this case, is less steep showing that changing width for a fixed Si_3N_4 strip height and TeO_2 coating decreases the nonlinear parameter at a lower rate which gives us flexibility in choosing waveguide width for dispersion engineering.

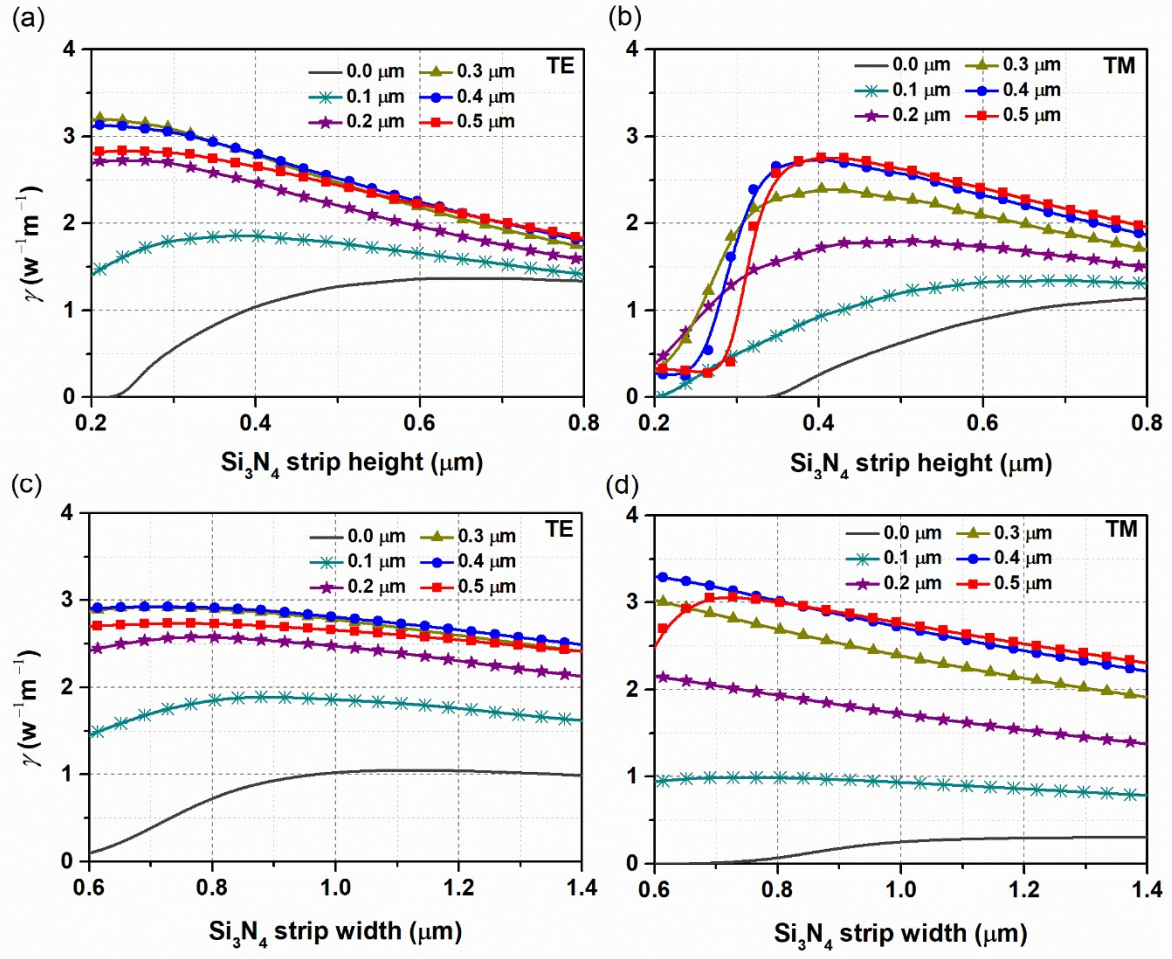

Figure 3.4. Nonlinear parameter (γ) for (a and b) 1-µm-wide Si_3N_4 strip waveguides with varying height and (c and d) 0.4-µm-high Si_3N_4 strip waveguides with varying width, in both cases the TeO_2 coating thickness varied from 0 to 0.5 µm in steps of 0.1 µm for (a and c) TE and (b and d) TM polarization

Our numerical investigation reveals that there is a trade-off between the wavelength span of anomalous dispersion and the nonlinear parameter calculated in relation to waveguide dimensions. Whereas wider waveguides result in a much broader anomalous dispersion region, the nonlinear parameter tends to decrease with an increase in widths. Also according to Kerr index values of tellurite glasses listed in Table 3.1, the nonlinear parameter may vary significantly depending on what value (glass composition) is chosen. These two points are both summarized in Figs. 3.5(a) for TE mode and (b) for TM mode. In both figures, we plotted values of γ versus n_2 picked from Table 3.1 (respective references are indicated in each plot) for three different waveguides of varying width with fixed Si_3N_4 strip height of 0.4 µm and TeO_2 coating thickness of 0.5 µm. Although we have stated the enhancement of γ up to three times that of stoichiometric Si_3N_4, Fig. 3.5 shows that it might be increased further with tellurite glasses of different compositions.

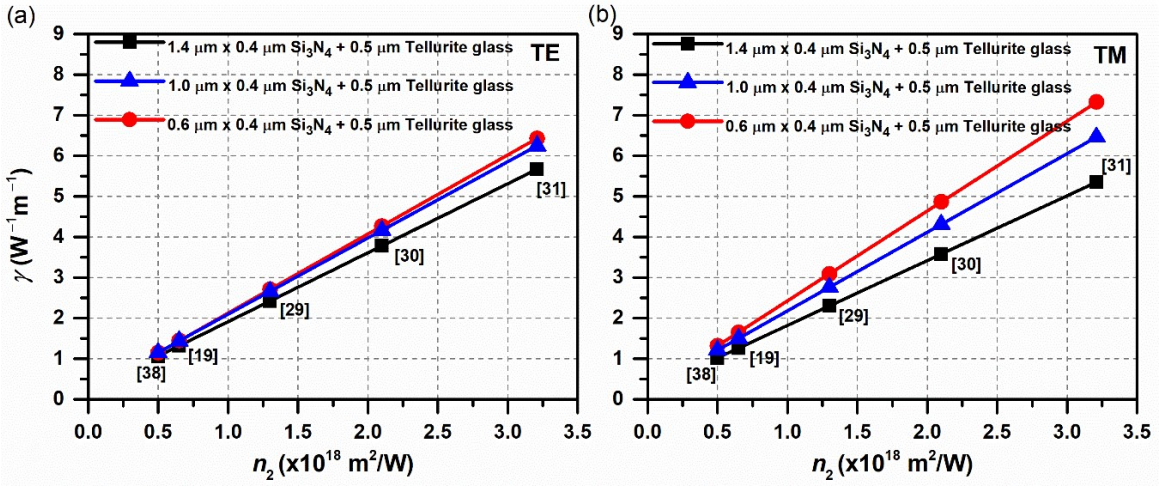

Figure 3.5. Nonlinear parameter (γ) for different n_2 values from Table 3.1 (respective references are indicated in square brackets) for waveguide dimensions indicated in legends, for (a) TE mode and (b) TM mode.

3.5 Conclusions

Silicon nitride is a very attractive and well-developed material for nonlinear applications in silicon photonics. Yet challenges related to the complexity of the fabrication of Si_3N_4 waveguides based on the requirement for thicker Si_3N_4 layers for nonlinear optical devices persist. In this work, we have presented numerical results that complement stoichiometric Si_3N_4 by offering improvement in nonlinear parameters and a simple way of tailoring GVD in thinner Si_3N_4 strip waveguides by the addition of the TeO_2 top coating layer. The results show a higher nonlinear parameter compared to that obtained in stoichiometric Si_3N_4 waveguides. Although the values obtained are lower compared to those obtained in silicon-rich nitrides or SOI [222] our designs offer the distinct advantages of lower linear losses [231], [68] and negligible nonlinear TPA losses in both Si_3N_4 and TeO_2. Our expectations are that the presented designs will offer improved performance in nonlinear devices by having higher nonlinear coefficients, lower nonlinear losses, and anomalous GVD which altogether reduce the threshold power and improve the efficiency of nonlinear interactions for applications such as supercontinuum generation and broadband frequency comb generation. Furthermore, due to the high solubility of rare earth dopants in TeO_2, we expect that proposed waveguides will offer the possibility of integrating active rare-earth doped devices such as amplifiers and lasers with nonlinear optical devices in a single low-loss CMOS compatible Si_3N_4 platform.

Chapter 4

Linear, Nonlinear, and Active Photonics on a TeO_2-Coated Si_3N_4 Platform

This chapter presents an experimental study of the TeO_2-coated 400-nm-thick Si_3N_4 platform as a viable candidate for linear, nonlinear, and active integrated photonics. The chapter covers the design, characterization, and experimental results of linear passive devices such as microring resonators, nonlinear devices showing Kerr combs, supercontinuum and third-harmonic generation, and active devices such as waveguide amplifiers and lasers.

The first section briefly introduces the platform, emphasizing the motivation for a thin wafer scale Si_3N_4 layer suitable for linear, nonlinear, and active photonics. Also, it highlights particular features that provide advantages and thus motive for using TeO_2 in the hybrid platform.

The second section discusses details about the device design, layout for fabrication, and characterization. Several devices were designed to test the platform such as waveguides of different dimensions, long spirals, micro disks, and microring resonators. Important linear measurement results for some of these devices is given in this section, especially loss characterization using microring resonances and the cut-back method on the spiral waveguides.

Dispersion is an important parameter in integrated nonlinear photonics and has always been one of the main deciding factors on the waveguide structure and overall choice of a suitable nonlinear platform. The third section of this chapter gives experimental results on dispersion measurements, verifying the designs presented in chapter 3.

The fourth and fifth sections present some experimental nonlinear and active device results. First, results of the main thesis subject of nonlinear photonics are presented starting with microresonator Kerr frequency combs generation, followed by SCG and THG results. Then, demonstrations of active performance are given including a microdisk laser and a waveguide amplifier. The last section is for the summary and conclusion.

4.1 Introduction

The silicon photonics field has reached a maturity stage where early prototypes have hit the commercial market and research is moving from component to circuit and systems levels. One of the desired criteria is to make integrated silicon photonics chips on a monolithic platform fabricated on a wafer scale and in a commercial CMOS foundry. However, despite the growth and maturity, monolithic integration of some functionalities is still proving to be a challenge to date. In particular, the integration of nonlinear functionalities with sources and other linear optical devices is a work in progress. This challenge is mainly due to the significant variations in properties and fabrication methods of the materials and waveguides that are typically employed for integrated nonlinear photonics [157,161,162]. For example, the need for anomalous dispersion place stringent requirements on waveguides geometries leading to dimensions that are less standardized. In particular, for Si_3N_4, which is a leading nonlinear silicon photonic platform, the need for thick Si_3N_4 waveguides to engineer waveguide dispersion has led to varieties of fabrication techniques to avoid high stress in thick films leading to cracks and low device yield [167,169,170]. On the other hand, thinner Si_3N_4 layers (< 400 nm) which fall in the normal dispersion regime

are highly standardized for linear photonic devices and provided in several commercial foundry services such as IMEC [189] and AMF [188]. Also, monolithic integration of 400-nm thick Si_3N_4 waveguides with other functionalities on the SOI platform has been demonstrated [248,249].

Light generation and amplification particularly are key functionalities that are highly desired to be monolithically integrated with nonlinear devices in PICs. However, there are only a few platforms that have demonstrated the capabilities of both functionalities. Notable examples are lithium niobate on insulator (LNOI) [250–252] and Si_3N_4 [253]. Despite exciting nonlinear and electro-optic properties, the application of LNOI in high-yield and scalable PICs is limited by its incompatibility with the CMOS process. Recently, high gain in the nonlinear thick Si_3N_4 has been demonstrated in [253]. However, the fabrication process involved custom non-standard fabrication methods as well as thermal annealing of up to 1000^0C which is beyond the thermal budget in the CMOS process. TeO_2 is another promising material that has been proposed for linear, nonlinear and active functionality [204]. The potential for these functions on one chip was shown in [204,206] and for integration on a silicon-compatible platform in [209,212,213]. In this work, the rare-earth solubility of the TeO_2 is exploited to show amplification and lasing in a dispersion-engineered platform that also shows promising nonlinear performances.

This chapter presents the hybrid TeO_2-Si_3N_4 platform based on a foundry 400 nm thick silicon nitride as a candidate for monolithic linear, nonlinear, and active silicon photonic circuits. The platform is characterized by the coating of the highly nonlinear TeO_2 that enhances the waveguide nonlinearities and provides a way to engineer waveguide dispersion to anomalous as presented in the previous chapter.

Experimental results are presented showing that the normal dispersion of 400 nm-thick Si_3N_4 waveguides can be precisely tuned to anomalous by adding the TeO_2 film. For a 1.6 μm wide, 500 μm bend radius ring resonator with a 424 nm thick TeO_2 coating, dispersion

values of ~25 and ~78 ps/nm·km was measured at 1552 nm for the TE and TM-modes, respectively. Also, microring resonators with Q factors of up to 6×10^5 at 1550 nm were characterized and showed the promising onset of a Kerr comb. An octave-spanning supercontinuum covering an entire telecommunication band for a low pump power centered at 1550 nm is also be presented. Furthermore, by exploiting the rare-earth solubility of the TeO_2 film and depositing an Er-doped TeO_2 coating, a microdisk laser was observed as well as 2.8 dB small signal amplification in a 6.7 cm long waveguide.

4.2 Device Design & Linear Characterization

This section discusses the designs and characterization of devices that were fabricated to study the platform.

4.2.1 Simulated Waveguide Properties

A comprehensive analytical and numerical study was carried out by simulation of basic waveguide properties get the guidelines of minimum design limits before generating layout for fabrication. Among the main factors to consider are the waveguide single-mode cut-off widths, minimum bed radii, effective mode areas, confinement factors, dispersion, and waveguide effective nonlinearity. The optimization of dispersion and waveguide nonlinearity was presented in the previous chapter and therefore is not covered in this section. Also, it should be noted that all simulation results that are presented in this and other coming sections, use the material properties listed in Chapter 2, Table 2.3.

A 3D drawing and a 2D cross-section view of the designed waveguide are shown in Fig. 4.1(a). It consists of a 400-nm thick Si_3N_4 strip on an insulator (SiO_2) to be fabricated on a silicon wafer. The strip is conformally coated with the TeO_2 film of varying thicknesses followed by spin-coating of a protective fluoropolymer (Cytop) top-cladding layer. Sample mode profiles are shown in Fig. 4.1(b) for uncoated, 200, 400, and 600-nm TeO_2-coated waveguides for the TE and TM polarization. The effective mode area and confinement

factor are particularly important parameters for designs tailored for nonlinear applications. Because of the intensity-dependent nature of χ^3 nonlinearities studied in this thesis, maximizing the intensity by reducing the effective mode area is required while keeping the mode overlap reasonably high. It also desired to maximize the mode overlap with the TeO_2 to achieve enhanced waveguide nonlinearities as explained in Chapter 3. Figures 4.1(c) and (d) are plotted to show the simulation results for the effective area (A_{eff}) and the mode overlap (Γ) with the TeO_2, respectively, for the fundamental TE modes. In Fig. 4.1 (c) it is shown that the overlap with the TeO_2 increases as the coating thickness increases while in Fig. 4.3 (d) A_{eff} increases with the increase in waveguide dimensions. A plot for TM polarization is not shown here due to the complexity of carrying out a parameter sweep in the simulation tool used. Except for the fundamental TE mode, the fundamental TM mode and different higher-order TE and TM start to mix up as the TeO_2 coating is increased for different Si_3N_4 strip widths which presents a challenge in isolating individual modes. However, TM simulation results for selected individual TeO_2 thicknesses showed similar trends to Figs. 4.1 (c) and (d).

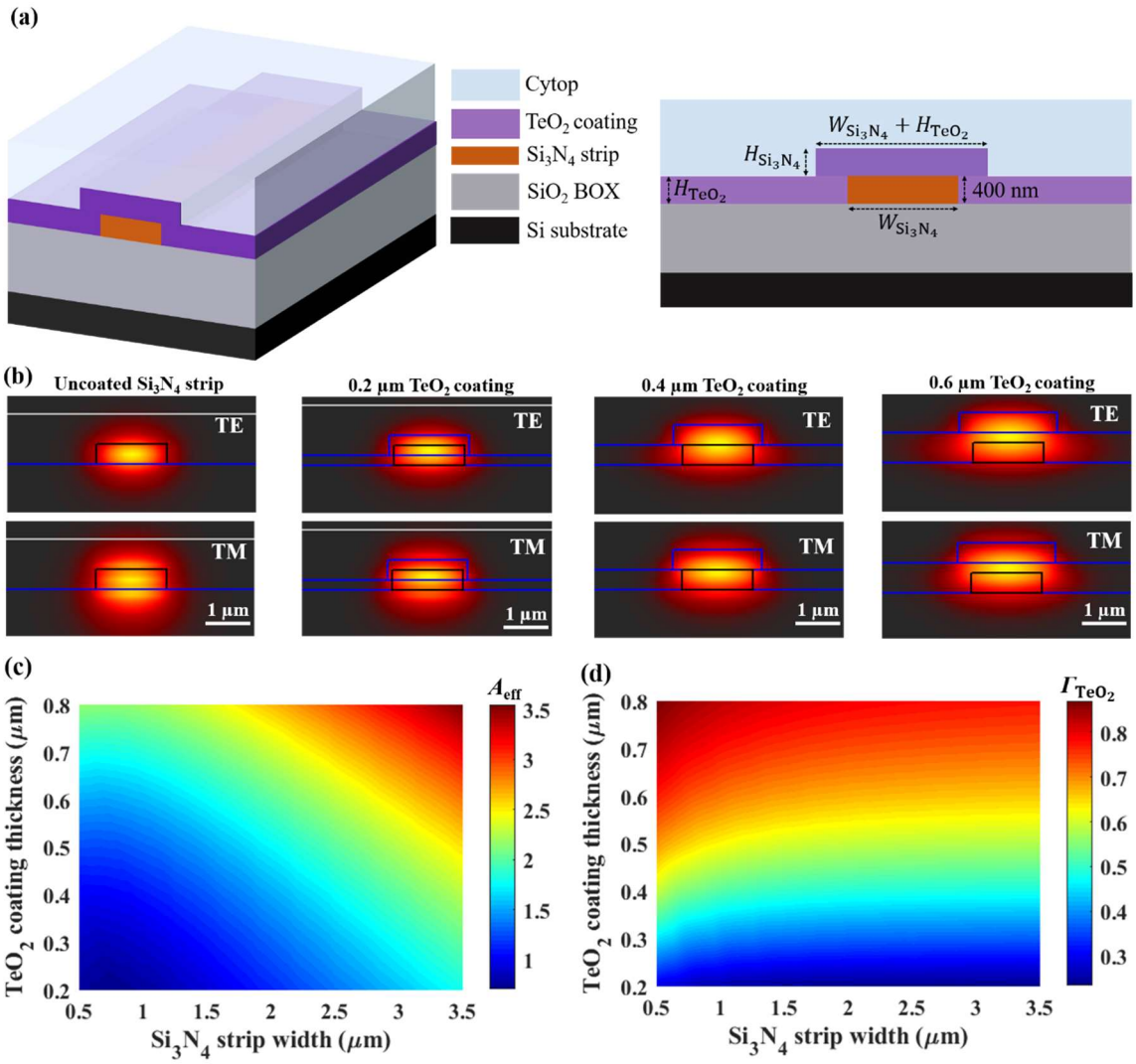

Figure 4.1. (a) A 3D drawing and 2D cross-section view of the designed hybrid waveguide. (b) Simulated mode profiles for the uncoated, and 400-nm TeO_2 coated waveguides at 1550 nm and for TE and TM polarization. Simulation results showing (c) the variation of the effective mode area, and (d) the optical intensity overlap with the TeO_2 layer for various Si_3N_4 strip widths and TeO_2 film thicknesses for TE polarization. It should be noted that specifically for this chapter, the Si_3N_4 strip thickness is kept constant at 400 nm unless otherwise stated.

In most applications, it is advantageous to have a single-mode operation as it reduces loss of power through coupling to higher order modes and ensures single mode emission in applications for example laser cavity designs. The TeO_2-coated 400-nm Si_3N_4 platform offer the flexibility of both single-mode and multi-mode operation at reasonable widths that permit tight and low-loss bend radii for small-footprint devices. However, the choice between large bends and single-mode operation, or small bends and multi-mode operation depends on specific applications and there is always a trade-off. Table 4.1 gives a summary of the minimum bend requirements and properties of single-mode width devices for TE and TM polarization. Table 4.2, and 4.3 give similar summary of the minimum bend requirements and properties of waveguide of varying widths that fall into both single-mode and multi-mode regimes for TE and TM modes respectively.

Table 4.1. Simulated parameters for single-mode TeO_2-Si_3N_4 waveguides at 1550 nm

TE polarization					
H_{TeO_2} **(µm)**	**Single mode cutoff width (µm)**	**Minimum bend radius (µm)**	$\Gamma_{Si_3N_4}$ **(%)**	Γ_{TeO_2} **(%)**	A_{eff} **(µm²)**
0	1.30	80	68	0	0.751
0.3	0.90	135	42	44	0.961
0.4	0.95	240	34	56	1.162
0.5	1.10	300	27	66	1.426
0.6	1.15	420	20	73	1.715
TM polarization					
0	1.60	115	70	0	0.847
0.3	1.45	90	56	33	1.215
0.4	1.70	125	47	46	1.477
0.5	2.00	170	38	57	1.877
0.6	2.30	215	30	66	2.813

Table 4.2. Simulated parameters for the fundamental mode for TeO_2-Si_3N_4 waveguides at 1550 nm and TE polarization

H_{TeO_2} (µm)	$W_{Si_3N_4}$ (µm)	Minimum bend radius (µm)	$\Gamma_{Si_3N_4}$ (%)	Γ_{TeO_2} (%)	A_{eff} (µm^2)
0	1.2	85	67	0	0.727
	1.6	75	70	0	0.847
	2.0	65	70	0	0.996
0.3	1.2	160	45	43	1.051
	1.6	120	47	42	1.221
	2.0	110	48	41	1.406
0.4	1.2	185	36	55	1.229
	1.6	165	38	54	1.395
	2.0	155	39	53	1.598
0.5	1.2	290	27	65	1.881
	1.6	260	30	64	1.884
	2.0	230	31	63	1.888
0.6	1.2	395	25	70	1.627
	1.6	350	27	68	1.800
	2.0	315	28	67	1.999

Table 4.3. Simulated parameters for the fundamental mode for TeO_2-Si_3N_4 waveguides at 1550 nm and TM polarization

H_{TeO_2} (μm)	$W_{Si_3N_4}$ (μm)	Minimum bend radius (μm)	$\Gamma_{Si_3N_4}$ (%)	Γ_{TeO_2} (%)	A_{eff} (μm^2)
0	1.2	145	52	0	1.364
	1.6	120	55	0	1.585
	2.0	110	57	0	1.851
0.3	1.2	100	54	34	1.084
	1.6	90	57	32	1.308
	2.0	85	55	33	1.771
0.4	1.2	145	44	48	1.184
	1.6	130	46	46	1.408
	2.0	120	47	46	1.779
0.5	1.2	210	35	60	1.328
	1.6	185	37	58	1.560
	2.0	170	38	57	1.877
0.6	1.2	285	27	69	1.516
	1.6	255	29	67	1.749
	2.0	230	30	66	2.040

The simulation results on mode overlap and effective area in Fig. 4.1, specific simulations in Tables 4.1,4.2, and 4.3, and dispersion and nonlinearity enhancement results in the previous chapter were all considered to select the designs to be fabricated. In terms of waveguide width, wider waveguides with relaxed minimum bend requirements are preferred especially for microring resonator designs. It has been shown in the previous nitride studies that rings with wider widths have higher Q-factors and perform better in nonlinear experiments than single-mode rings [86]. Therefore, for this study multimode (TE) waveguides of width 1.2, 1.6, and 2.0 μm were used for designed devices. In terms of the TeO_2 coating, it was shown in the previous chapter that at least 400 nm of TeO_2 coating is needed to achieve the anomalous dispersion required for nonlinear devices

4.2.2 Chip Layout and Fabrication

Following simulation and theoretical considerations, device layouts were drawn using a commercial CAD tool (Luceda IPKISS) and submitted to the silicon nitride foundry (LioniX International) for stepper lithography mask and chip fabrication. Figure 4.2 shows a top-view image of the layout with chip dimensions and blocks relevant to this work indicated by numbers 1 to 4. The first block consists of straight waveguides of 2.2 cm in length and varying widths, and paperclip-shaped waveguides of 6.7 cm length and varying widths with a minimum bending radius of 500 μm. These devices were intended to study supercontinuum generation and optical amplification on the platform. The second block consists of microring resonators aimed at exploring Kerr comb generation. The rings were designed for two bend radii of 500 μm and 250 μm, each with widths of 0.8 μm and 1.6 μm and varying coupling gaps of 0.6, 0.8, 1.0, 1.2, 1.4, 1.8, and 2.2 μm. Block 3 consists of spirals of 10, 15, and 20 cm lengths repeated in two widths of 1.6 μm and 2 μm. These spirals were designed for high-gain on-chip amplifiers and are also useful for loss characterization using the cut-back method. Lastly, block 4 includes pulley and point-coupled microdisks resonators intended for Kerr comb experiments and as rare-earth doped laser cavities.

The Si_3N_4 strip waveguides were fabricated at LioniX International using standard low-pressure chemical vapor deposition (LPCVD) and reactive ion etching (RIE) processes [207]. A 400-nm thick Si_3N_4 film was deposited via LPCVD onto 4 100-mm diameter silicon wafers with an 8-μm-thick wet thermal SiO_2 layer. The film was patterned by stepper lithography followed by RIE. The wafers were then annealed at high temperature in N_2 to drive out hydrogen from the Si_3N_4 waveguides and reduce absorption at wavelengths around 1.5 μm. The wafers were then laser diced [254] into 22×22 mm^2 chips and each chip into three chiplets as shown in Fig. 4.2. Laser dicing enabled smooth waveguide facets for efficient and repeatable fiber-chip light coupling. Afterwards, the

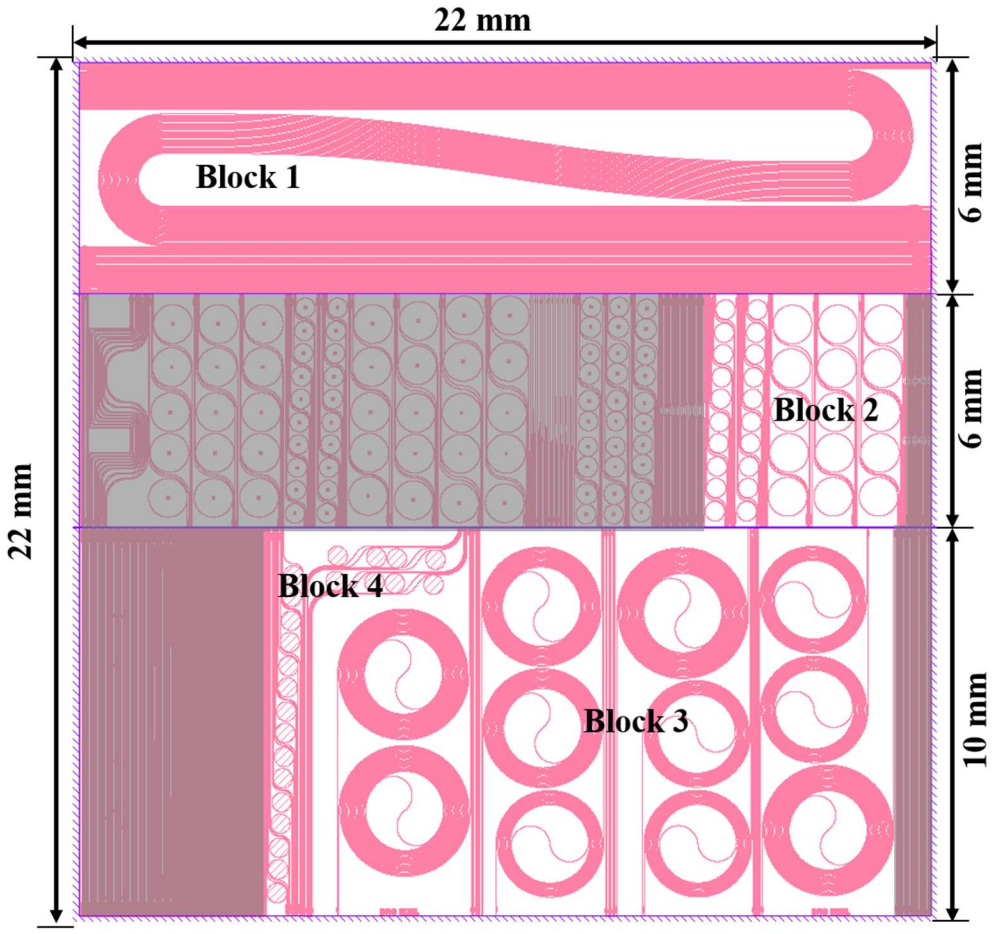

Figure 4.2. Silicon nitride chip GDS layout.

chips were shipped back to McMaster University where they were solvent cleaned and deposited with TeO_2 films of varying thicknesses. The TeO_2 deposition is carried out using reactive radio frequency (RF) magnetron sputtering process in McMaster's Centre for Emerging Device Technologies (CEDT) cleanroom. The deposition parameters varied slightly from run to run to optimize the Te-O ratio and included a tellurium target sputtering power of 145 W, chamber pressure of 2.7 mTorr, argon flow of 12 sccm, oxygen flow of 10 sccm, and substrate temperature of 150 °C. More comprehensive accounts of both the Si_3N_4 fabrication and the TeO_2 coating process are given in [207,208]. Figure 4.3 shows

SEM images of the devices after TeO_2 deposition. Figure 4.3(a) shows the end facets of 1.2, 1.6, and 2 µm wide waveguides with a zoomed-in image of the 1.6 µm wide waveguide facet. Figure 4.3(b) shows fabricated ring resonators with two radii of 500 µm (left) and 250 µm (right) with a zoomed-in image of the coupling gap in between the bus waveguide and ring.

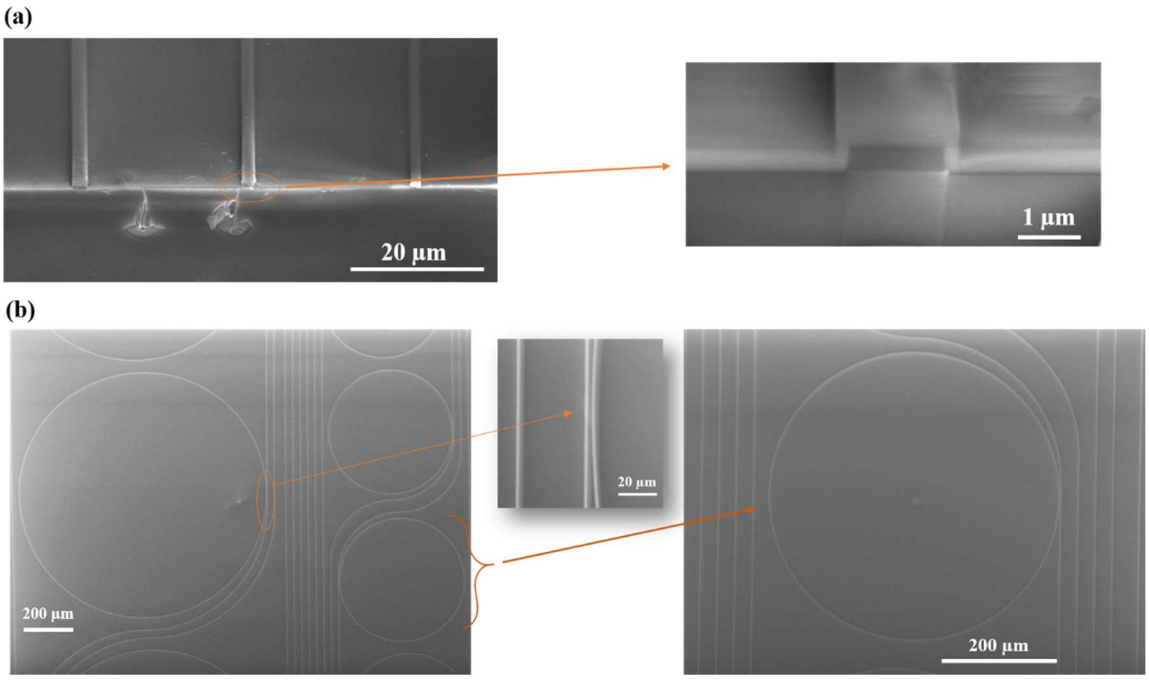

Figure 4.3. SEM images of the fabricated waveguide, including (a) end facets for 1.2, 1.6, and 2 µm wide waveguides (left), and zoomed-in facet for the 1.6 µm wide waveguide (right), and (b) ring top views for each of the 500 and 250 µm bend radii and a zoomed-in ring to bus waveguide coupling gap.

4.2.3 Ring Resonator Characterization and Loss Measurements

Microring resonators are important devices in nonlinear photonics research, especially for Kerr comb generation, as described in Chapter 2, section 2.3.1. They are also important for waveguide loss measurements as discussed in Chapter 2, section 2.5.3. To investigate the

linear properties of the platform, three different fabricated Si_3N_4 microring chips were coated with TeO_2 layers of 424, 500, and 592 nm thickness. The three sets of rings were characterized for both TE and TM polarizations. From the ring theory presented in Chapter 2, all important characteristics of a microring resonator such as the FSR, Q-factors, and group index can be found by measuring the ring transmission spectrum. The transmission spectra of the three rings at the smallest gap of 0.6 μm were measured by sweeping the tunable laser source from 1520 to 1620 nm. The results are shown in Figs. 4.4(a) and (b) for TE and TM polarizations, respectively, with an inset in each figure showing a zoomed-in fine spectrum at around 1550 nm. Weak resonances were observed in all rings for the 0.8 μm gap and none for gaps bigger than that.

The resonances near 1550 nm from the fine spectra were used to fit the transmissions to a Lorentzian model and the results are shown in Figs 4.4(c) and (d) for the fundamental TE and TM modes respectively. The measured ring parameters were then used to calculate the waveguide propagation losses for each case. Also, cut-back measurements were carried out on the 424 nm coated rings for the TE mode to compare the losses obtained in the two methods. Figure 4.4(e) plots the results of cutback measurements and Table 4.4 summarizes the results of all measurements.

From these results it can be seen that first the loss obtained from cutback is comparable to that from ring fitting, 0.62 dB/cm and 0.69 dB/cm for the 424 nm thick TeO_2 coated waveguide, which verifies the techniques and indicates that there is minimal loss contribution from waveguide bends. Therefore, the chosen bend radius of 500 μm is confirmed to be quite safe. The coupling loss for all devices were measured to an averaged value of 3 ±0.5 dB/facet for both TE and TM polarizations showing minimal polarization sensitivity similar to propagation loss as shown in Table 4.4. Also, from Table 4.4, it is shown that the coupling quality factor is relatively higher for most of the rings indicating they are operating in an undercoupled regime. The 0.6 μm gap used in these measurements

is the smallest gap designed for all these rings and therefore for future designs it is important to note that smaller gap sizes should be considered for achieving the critical coupling condition.

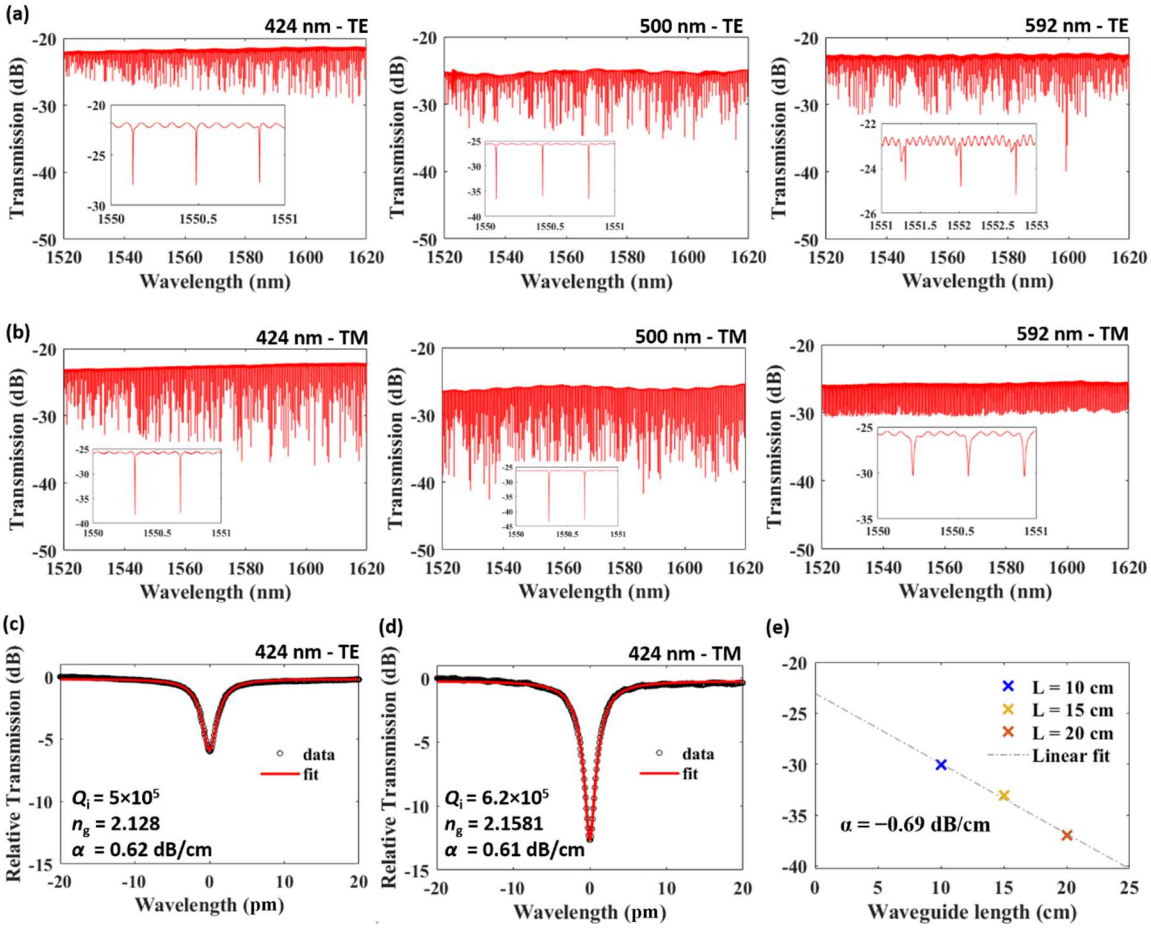

Figure 4.4. Ring measurements results showing (a & b) transmission spectra and (c & d) sample fitted resonances to obtain the quality factor at 1550 nm for TE and TM polarization, respectively, and (e) cutback measurements results for the spirals of 10, 15, and 20 cm lengths (TE-polarization only).

Table 4.4. Summary of rings and loss characterization results

TE polarization (λ_0 = 1550 nm, gap = 0.6 µm)							
TeO_2 thickness (nm)	Q_i ($\times 10^5$)	Q_c ($\times 10^5$)	Q_L ($\times 10^5$)	FSR (nm)	Extinction ratio (dB)	n_g	Loss (dB/cm)
424	6.0	19	4.6	0.3641	6.0	2.101	0.62
500	7.5	13	4.8	0.3571	10.9	2.142	0.50
592	5.2	15	3.9	0.3540	6.5	2.161	0.73
TM polarization (λ_0 = 1550 nm, gap = 0.6 µm)							
424	6.2	10	3.8	0.3555	12.5	2.152	0.61
500	5.2	6.9	3	0.3496	12.5	2.188	0.56
592	3.7	1	0.8	0.3500	4.1	2.185	1.05

4.3 Dispersion Measurements

A precise understanding of dispersion is required to design and describe the behavior of nonlinear photonic devices. One can determine the waveguide dispersion profile using known material dispersion relations (i.e., Sellmeier or Cauchy equations) and a mode solver to account for the geometrical effects. Then, the dispersion parameter is calculated using equation (44) given in Chapter 2. However, due to imperfections and slight material and dimensional variations in fabrication, the actual dispersion values vary slightly from that calculated using the mode solver. In this case, the actual dispersion needs to be measured for individual devices using an appropriately sensitive method. One way of measuring dispersion at a specific wavelength is to exploit the variations of a microring resonator's FSR with wavelength as described in Chapter 2, section 2.3.2. In particular, this approach can tell with high confidence if the sign of the dispersion parameter (D) is negative (normal) or positive (anomalous).

In this work, the dispersion profiles of the fabricated waveguides are calculated numerically using the material equations and a mode solver following the approach used in Chapter 3, then verified experimentally using microring resonators. For the former, the Sellmeier

equations given in Chapter 2, Table 2.1 were used to calculate the dispersion profile over a broad wavelength span. The dispersion of the microrings were then measured using the frequency comb-assisted diode laser spectroscopy technique described in [84,255]. A simplified schematic showing the dispersion measurement setup is shown in Fig 4.5. The setup consists of a tunable laser for resonance scanning, a polarization controller (PC), a coupling stage, band-pass filters (BPF1 and BPF2), photodetectors (PD1 and PD2), a beam splitter (BS) and a referencing ultra-stable mode-locked fiber laser. Microring resonances from the tunable laser were recorded by the oscilloscope with each resonant frequency precisely calibrated and marked using a fiber mode-locked laser comb.

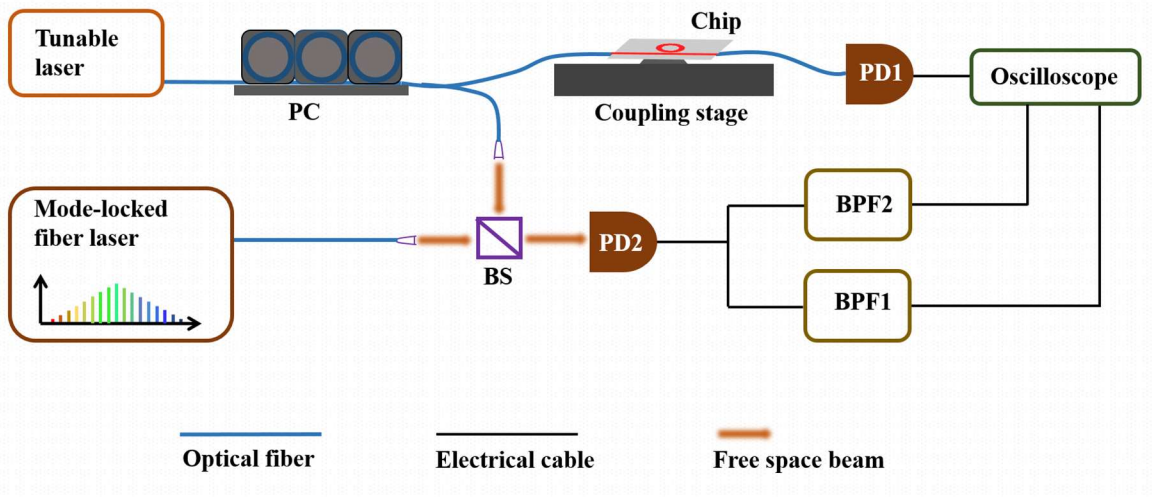

Figure 4.5. Dispersion measurements setup consisting of a tunable laser, a polarization controller (PC), a coupling stage, band-pass filters (BPF1 and BPF2), photodetectors (PD1 and PD2), a beam splitter (BS) and a mode-locked fiber laser.

The results of both measurements and simulation are shown in Fig. 4.6. Figures 4.6 (a), (b), and (c) show the integrated dispersion data at a wavelength near 1552 nm for different mode families and the resulting polynomial fit as given by equation (61) in Chapter 2. In

these figures the upward bending indicates anomalous dispersion while the downward bending indicates a normal dispersion. The resulting dispersion parameters $D_1/2\pi$, $D_2/2\pi$, and $D_3/2\pi$ are shown inside each plot. The respective second-order dispersion or the group velocity dispersion (GVD) parameter (D) is calculated according to equation (63) given in Chapter 2. Figures 4.6(d) and (e) show the calculated dispersion profiles with the dots indicating the measured dispersion parameters at 1552 nm for the fundamental TE and TM modes, respectively. A quantitative summary of the measure and calculated D values is given in Table 4.5. The discrepancy between measured and simulated dispersion values is mainly attributed to the errors in either approaches. From Fig 4.3(a), the SEM image shows that there's a small angle in a vertical elevation of the Si_3N_4 strip that is not accounted for in simulations as shown by the mode profiles in Fig. 4.1(b), thus may account for some errors in calculations. Overall, these measurement results confirm the theoretical prediction of the dispersion engineering study presented in Chapter 3. In addition, the changes in dispersion profiles for different TeO_2 coating show high flexibility and controllability in dispersion engineering for both TE and TM modes.

Table 4.5. Summary of measured and calculated dispersion (D) values

	***D* (ps/nm·km) - TE**		***D* (ps/nm·km) - TM**	
TeO_2 coating	Measured	Calculated	Measured	Calculated
325	-27.7908	83.5505	-15.0188	142.8171
424	24.7835	119.7565	77.7914	281.5930
500	-16.5195	142.4772	97.2873	371.7212

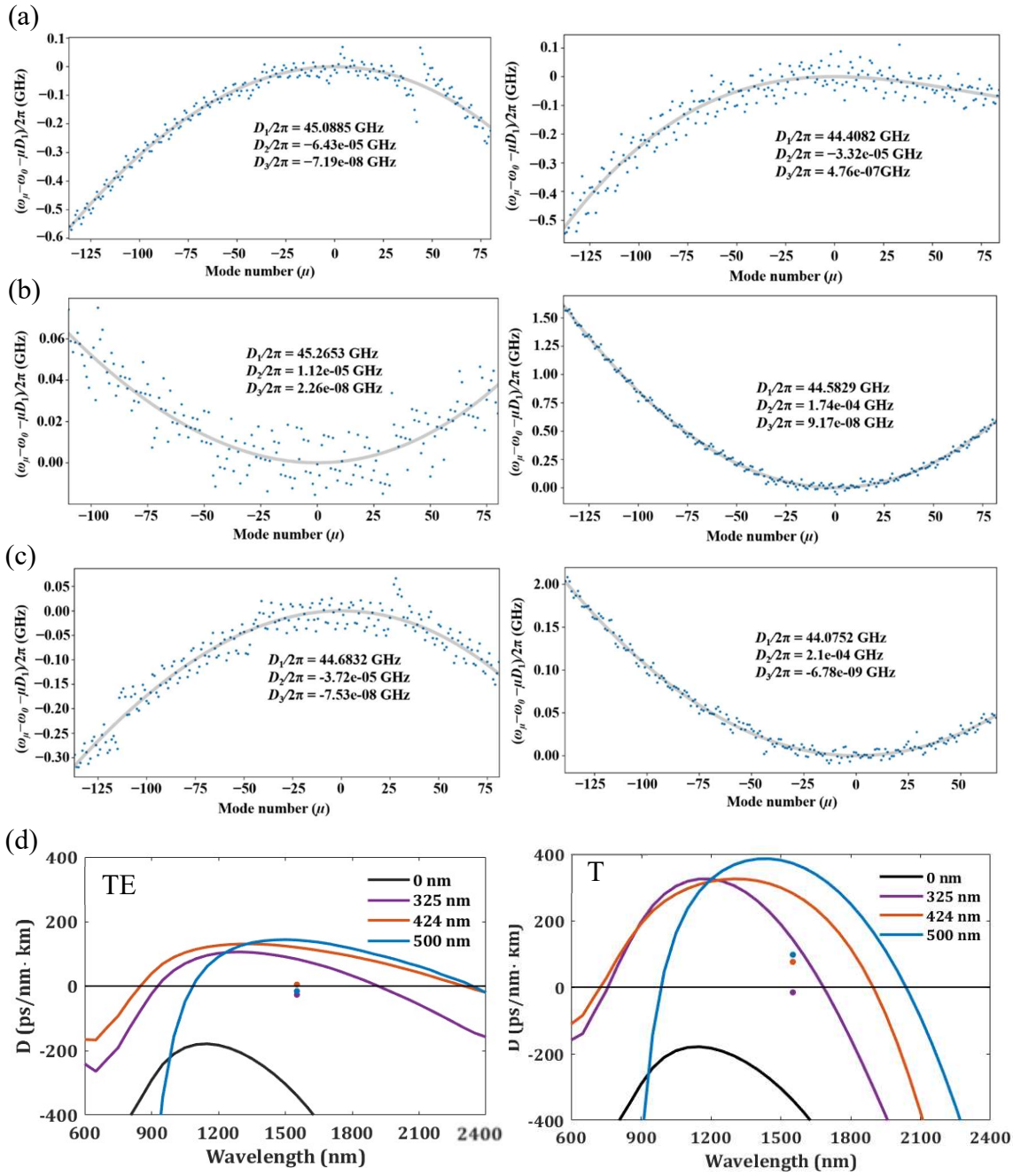

Figure 4.6. (a, b & c) Dispersion measurements results and (d) simulation results for the 325, 424, and 500 nm thick TeO_2-coated rings and TE and TM polarization (left and right), respectively.

4.4 Nonlinear Demonstrations

This section presents experimental results showing promising and well-performing nonlinear devices. The main nonlinear applications investigated include FWM, KCG, SCG, and THG. It is demonstrated that the platform shows promising signs of comb generation, well-performing octave-spanning supercontinuum, and strong third harmonic generation.

4.4.1 Nonlinear Optical Demonstrations on Normal Dispersion Waveguides

The work presented in this chapter is an outcome of an optimization study in the previous chapter, and earlier experimental results on similar hybrid waveguides but with normal dispersion. Before fabrication of the dispersion-engineered 400-nm thick Si_3N_4-based waveguides, nonlinear experiments were carried out on normal dispersion, 200-nm thick Si_3N_4-based hybrid waveguides. The 200-nm thickness was selected for suitable geometry for exploring linear and active devices [207]. As a result, high-Q microring resonators [208], erbium-doped [209], and thulium-doped [210] waveguide amplifiers were demonstrated. Regardless of having normal dispersion, experiments were carried out to explore the possibilities of nonlinear phenomena. The results are shown in Fig 4.7 where FWM in microring resonators [213], SCG, and THG in a 7 mm waveguide [212] were demonstrated.

The FWM experiment was carried out by pumping uncoated, 260-nm, and 380-nm TeO_2-coated microring resonators. The rings had bend radii of 600 μm and waveguide widths identical to that of the coupling bus waveguide width of 1.2 μm. Figure 4.7 (a) shows the details of the designed waveguides where (I) shows a 2D cross-sectional view, (II) shows an SEM image of the coated waveguide, and (III) and IV show the electric field profiles of the fundamental TE mode for the uncoated and the 380-nm TeO_2-coated waveguides, respectively. The rings were characterized to have internal Q-factors of 1×10^6, 8.9×10^5 and 6×10^5 for the uncoated, 260-nm, and 380-nm coated rings respectively at 1590 nm and a

coupling gap of 1.8 μm. They were pumped with a CW laser and coupled power of ~65 mW at 1590 nm. The results are plotted in Fig 4.7(b) where FWM is observed only for the TeO_2-coated rings due to the enhanced nonlinearity from the highly nonlinear TeO_2, as predicted in the optimization study in the previous chapter.

Supercontinuum and third harmonic generation were also observed by pumping a 7 mm long waveguide with a pulsed laser source. The waveguide had a width of 1.2 μm and a TeO_2-coating of 370 nm thickness. It was pumped by an optical parametric oscillator (OPO) laser with 200 fs pulses centered at 1550 nm, and a repetition rate of 80 MHz. The coupled peak power was estimated to be 600 W. The resulting SC is shown in Fig. 4.7(c) taking a characteristic form of SPM-based SC generation spectrum covering over 500 nm at a −30 dB level. THG was also observed at a wavelength around 517 nm for different coupled peak powers as shown in Fig. 4.7(d). Also, the right-hand side of Fig. 4.7(d) shows glowing images of the chip for THG at different wavelengths as the pump wavelength is varied between 1600 nm, 1550 nm, and 1460 nm. In summary, promising nonlinear performances were first observed in a normal dispersion hybrid platform based on the 200-nm thick Si_3N_4. These results paved the way for the further investigation leading to the numerical optimization work in the previous chapter and eventually the experimentally demonstrated anomalous dispersion platform based on 400-nm thick Si_3N_4 presented in this chapter.

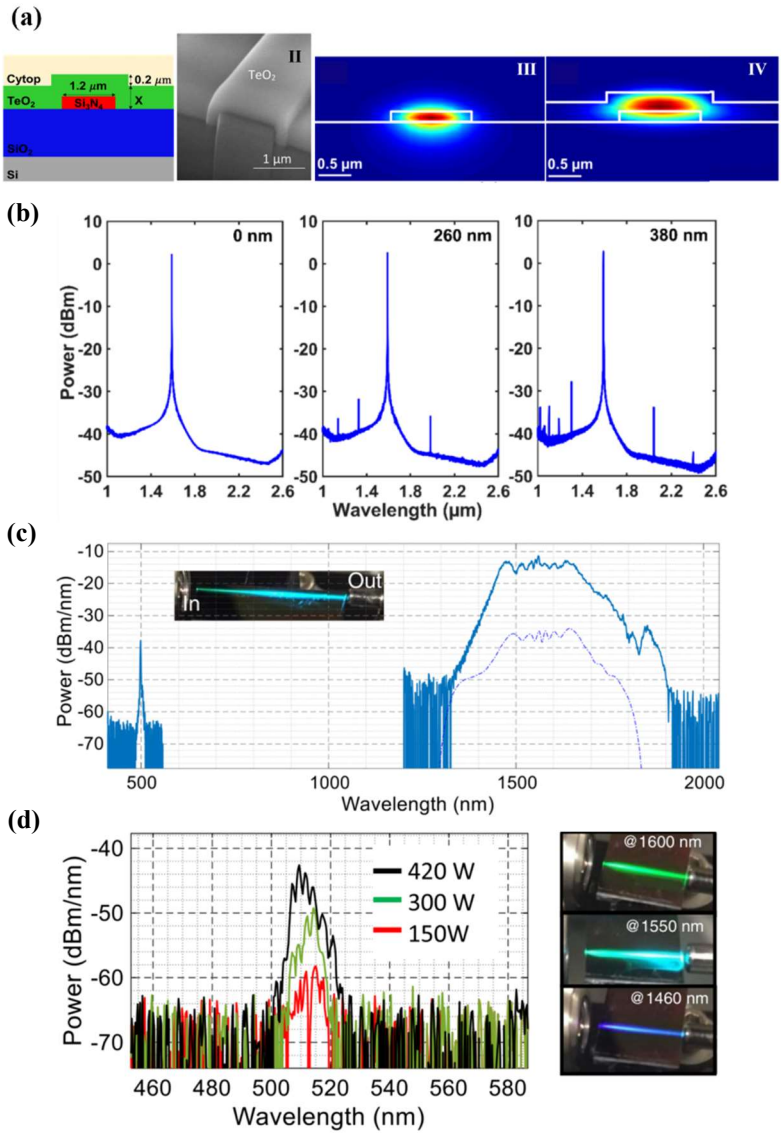

Figure 4.7. Nonlinear demonstrations on normal dispersion waveguides with 200-nm-thick Si_3N_4 strips showing: (a) the waveguide cross-section (I), an SEM image (II) and TE mode profiles for the uncoated and 380-nm TeO_2 coated waveguides (III and IV); (b) FWM results for rings pumped with –65 mW power for the uncoated and 260-nm and 380-nm TeO_2 coated waveguides; (c) SCG and THG spectra with an image of the THG along the length of the waveguide (inset) and a simulated spectrum (dashed curve) shifted down for clarity; (d) zoomed-in THG spectra at different pump powers (left) and images of the chip showing changing THG color for pump wavelengths of 1600, 1550, and 1460 nm (right).

4.4.2 Kerr Comb Generation

Building on the FWM results in a normal dispersion, 200-nm thick S_3N_4 coated with 260 nm and 380 nm TeO_2 [213], FWM and eventually, KCG was investigated on the proposed dispersion-engineered 400-nm thick Si_3N_4-based hybrid platform. KCG is a process that in the early stage is mainly dominated by FWM where sidebands form on each side of the pump, as the pump power increases the sidebands grow into a full comb. However, to reach a full soliton and dissipative comb with anomalous dispersion, high intra-cavity power, enabled by high Q and near critical coupling, and careful cavity resonance detuning are required. In this work an early FWM-sideband comb is achieved, several performance features and technical limitations are investigated and appropriate recommendations for future work are given.

To investigate KCG, the microresonators were pumped with a CW laser. The experimental setup is shown in Fig. 4.8(a). A tunable CW laser source with wavelengths ranging from 1520 to 1620 was used. The laser has a wavelength tuning resolution of 0.1 pm allowing for accurately aligning the pump wavelength to the microresonator resonances. The tunable laser was amplified by a high-power L-band erbium-ytterbium co-doped fiber amplifier (EYDFA). The pump light was then coupled into a mechanical polarization controller and to the chip by a lensed fiber on a mechanical tri-axis coupling stage. The polarization of the pump was adjusted between TE and TM using a reference sample that has waveguides designed to support only the fundamental TE mode. Hence by looking at insertion losses one can adjust the polarization paddles to the desired polarization accordingly. The output from the chip was first observed in a power meter to tune the pump onto resonance and then connected to the optical spectrum analyzer. To ensure the stability of the ring resonances a thermoelectric cooler (TEC) was mounted on the chip holder on the tri-axis stage and maintained at a constant temperature of 23 °C. While on resonance, the pump power was increased slowly until sidebands and eventually, a comb was observed. Also to

ensure the stability of ring resonances a thermal locking technique was used. In thermal locking, a pump laser is first tuned at a frequency slightly higher than the microresonator resonant frequency. When the pump power is increased the resonance shifts to a higher frequency hence sliding and locking itself onto the pump frequency.

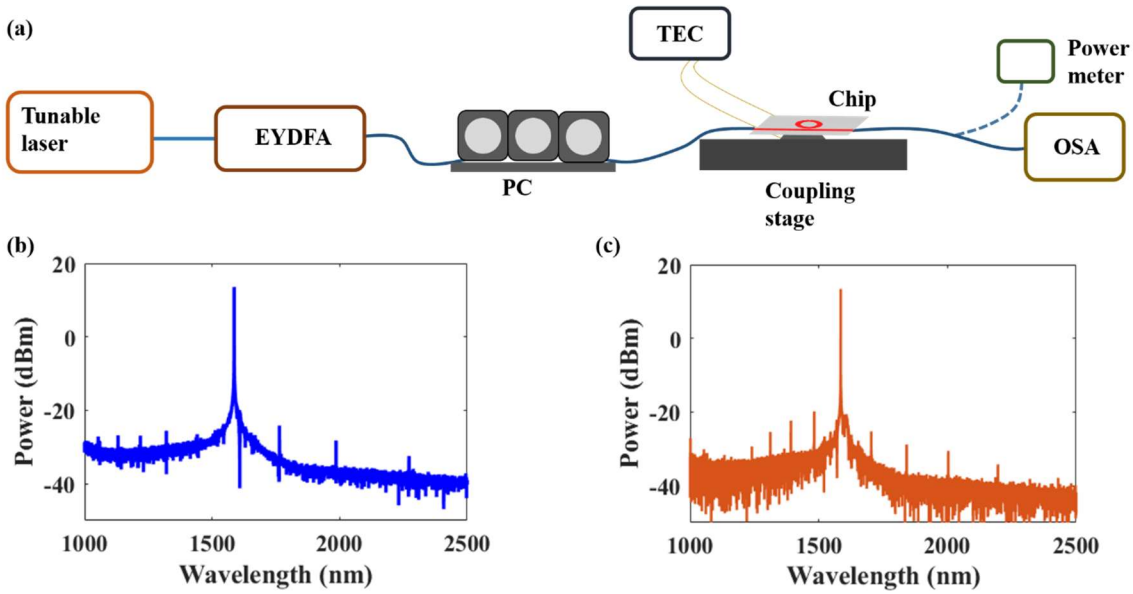

Figure 4.8. (a) Experimental setup for comb experiment consisting of a tunable laser, EYDFA, polarization controller (PC), a tri-axis coupling stage, power meter, optical spectrum analyzer (OSA), and a temperature controller (TEC). Results of observed Kerr combs for (b) 424 nm (TE) and (c) 413 nm (TM) thick TeO_2 coated ring resonators, pumped at 1586.4564 nm and 1585.2247 nm, respectively, and with approximately equal power in the bus waveguide of 251 mW.

Microring resonators with properties listed in Table 4.4 were pumped and investigated for KGC. Each of the rings was pumped at varying wavelengths from 1575 nm to 1610 nm and a 0.6 µm coupling gap for TE and TM polarization. The pumping wavelength was dictated by the amplification window of the high-power EYDFA used in the experiment. The results showed at least a few FWM sidebands similar to and/or slightly better than what was initially reported in [213] and discussed in the previous section. Among the rings from

Table 4.4, the 424-nm coated ring and another ring of 413-nm coating (not shown in Table 4.4) had the most promising results, and are shown in Figs. 4.8(b) and (c) respectively. In Fig. 4.8(b) the ring was pumped with TE polarized light and had an internal quality factor of 6×10^5 resulting in a propagation loss of 0.62 dB/cm. Using this loss value and measured transmission through a bus waveguide with no coupling to the ring (wider gap) the coupling loss was estimated to be ~3 dB/facet. The pump power was measured to be 27 dBm before the chip, subtracting the coupling loss resulted in a power of ~24 dBm (251 mW) in the bus waveguide. For Fig. 4.8(c) the ring was pumped with TM polarized light. Similarly, the internal quality factor, propagation loss, and coupling loss were measured to be 5.7×10^5, 0.66 dB/cm, and ~3 dB/facet, respectively. Also, the pump power was measured to be 27 dBm before the chip which resulted in a power of ~24 dBm (251 mW) in the bus waveguide. Because of the insufficient proximity of the bus waveguide to the cavity, even at the smallest gap, the coupling strength was found to be highest and most suitable for pumping at longer wavelengths. However, due to a decrease in the dispersion value, it was found that at the longer wavelengths the sidebands generated were farther apart than at the shorter wavelength reducing the possibility of them growing into a full comb. Therefore, careful and fine scanning showed that stronger and more closely spaced sidebands were obtained at wavelengths between 1580 to 1590 nm. The comb results in Figs. 4.8(b) and (c) were obtained at resonant wavelengths of 1586.4564 nm and 1585.2247 nm, respectively. To analyze these results, the ring properties at these wavelengths were considered. In particular, an analytical calculation was carried out to estimate the threshold power required to start the parametric process. The equation for threshold power in the bus waveguide (P_{th}) is given in [256] as:

$$P_{th} = \frac{(1 + (Q_i/Q_c))^3}{(Q_i/Q_c)} \frac{\pi^2}{2} \frac{n_g^2 R A_{eff}}{n_2 \lambda_0 Q_i^2}, \quad (1)$$

where $Q_i/Q_c = \kappa$ is the coupling coefficient. The parameters and calculated results are given in Table 4.6. From Table 4.6, the resulting threshold is similar for the two resonators at 30 mW and 32 mW for the 424-nm and 413-nm coated waveguides respectively. In the experimental results given in Fig. 4.8, up to eight times the threshold power is coupled while the emerging sidebands started to appear at a power of ~21 dBm (126 mW). During the experiment, it was observed that the OSA saturated at a power of 13 dBm (20 mW), and while in saturation the noise level increases by almost 20 dB, perhaps preventing some early sidebands from being observed. Another possible reason explaining the mismatch between theoretical and experimental threshold values is that the threshold calculations are done with cold resonance properties. However, in practice, there is a shift of resonance frequency at higher power due to heating and nonlinear phase shift. Nevertheless, the threshold equation provides useful guidance in resonator designs for future improvements. Example of possible improvements includes a reduction of the resonator sizes, a reduction of background losses to increase Q_i, and an improvement in coupling to optimize the ratio Q_i/Q_c.

Table 4.6. Summary of microring resonator parameters and results of parametric oscillation threshold calculations

Parameter	λ_0 **(nm)**	Q_i **(×10^5)**	Q_c **(×10^5)**	$\Gamma_{Si_3N_4}$ **(%)**	Γ_{TeO_2} **(%)**	n_2 **(×10^{-19})**	n_g	A_{eff} **(μm^2)**	P_{th} **(mW)**
424 nm (TE)	1585.4564	5.6	17	40	52	7.72	2.1724	1.39	30
413 nm (TM)	1585.2247	5.7	7.4	45	48	7.32	2.1648	1.47	32

4.4.3 Supercontinuum and Third Harmonic Generation

In previous work SCG was observed in a normal dispersion, 200 nm thick S_3N_4 coated with 370 nm TeO_2 [212], presented in section 4.4.1. In this thesis work, SCG was extensively studied in the dispersion-engineered 400-nm thick Si_3N_4-based hybrid platform. The paperclip waveguides of 6.7 cm length shown in Fig 4.2, block 1 were pumped by a

femtosecond mode-locked fiber laser. The experimental details and an overall discussion of SCG in silicon-based photonic platforms are given in Chapter 5. However, to be consistent with the motivation of this chapter in giving an overview presentation of linear and nonlinear performances of the platform, some of the SCG results are given here in the context of the waveguide dispersion engineering.

The 424-nm TeO_2 coated paperclips with measured anomalous dispersion near 1550 nm shown in Fig 4.5(b) for the TE mode, were pumped to investigate SCG. The pump laser had 100 fs pulses, a 200 MHz repetition rate, centered at 1565 nm, and the coupled peak power was 485 W. The results are shown in Fig. 4.9(a) for waveguides with 4 different widths of 0.8, 1.2, 1.6, and 2.0 μm. Strong THG is also observed for 1.2 μm wide waveguides covering a 50 nm wavelength range from 450 to 500 nm. As explained in Chapter 2, SCG under anomalous dispersion is characterized by soliton fission and dispersive wave formation. To illustrate and confirm this theoretical explanation, the dispersion profiles of the four waveguides are plotted in Fig. 4.9(b). Looking at the two figures it can be seen that the narrowest anomalous dispersion span corresponds to the narrow SC span characterized by less dispersive wave formation.

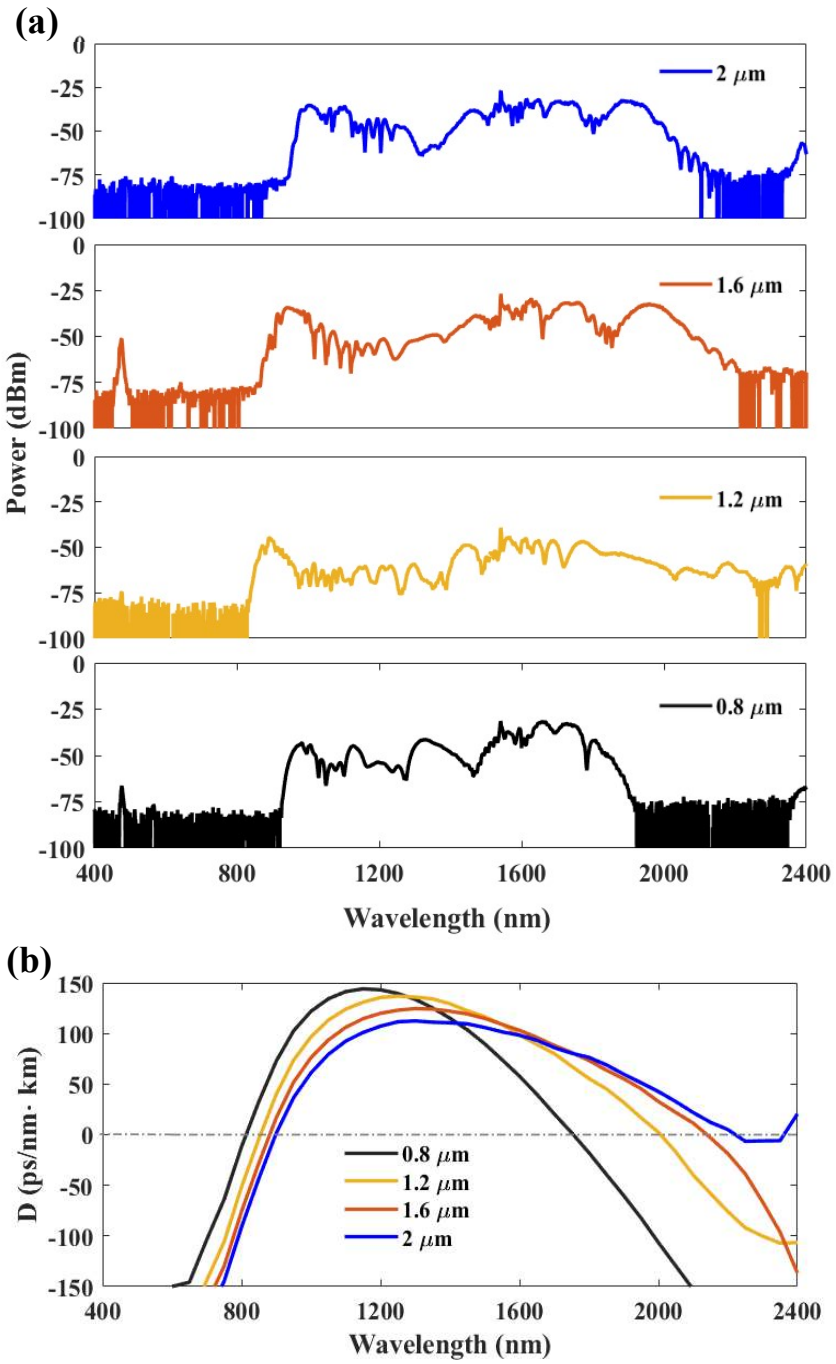

Figure 4.9. (a) SCG in 6.7-cm-long paperclip waveguides of various widths and (b) their corresponding calculated dispersion profiles.

4.5 Rare-Earth Lasers and Amplifiers

One of the most exciting properties of tellurite glass and a great motivation for this work is the solubility of the rare-earth dopants. The ability of the hybrid TeO_2-Si_3N_4 platform to host rare-earth dopants such as erbium, ytterbium, and thulium offers a prospect of delivering chip-level light emission and amplification. In combination with the excellent nonlinear and linear properties discussed in previous sections, the platform is in a unique position for attaining monolithic functionalities in a single chip. In this section, preliminary demonstrations of light emission and amplification is presented in waveguides with similar properties to those that showed nonlinear performance in previous sections.

4.5.1 Microdisk Laser

Microdisks are useful resonant structures similar to microrings, but instead of propagating in a waveguide structure the light in the cavity is guided at the edge of a fully-filled circular plate in a whispering gallery mode. Microdisks have several advantages for applications such as laser cavities over microrings, including relaxation in the minimum bend radius, higher Q factors, and stable resonant behavior. Microdisk lasing in Tm-doped TeO_2 was previously demonstrated in a TeO_2-SOI platform [257]. In this work, 250 μm bend radius TeO_2-Si_3N_4 microdisks were designed and investigated for Kerr comb and rare-earth doped laser applications, and the results for the latter are presented here.

The disk structure and simulated TE mode profiles are shown in Fig. 4.10. Figures 4.10(a) shows a 3D drawing of the disk and coupling bus waveguide while 4.10(b) shows a 2D cross-section view of the disk with the dimensions indicated. The simulated electric field profiles for the fundamental TE modes are shown in Figs. 4.10(c) and (d) for a pump wavelength of 1480 nm and a signal wavelength of 1550 nm respectively. The resulting material overlaps, effective indices, and effective areas are summarized in Table 4.7.

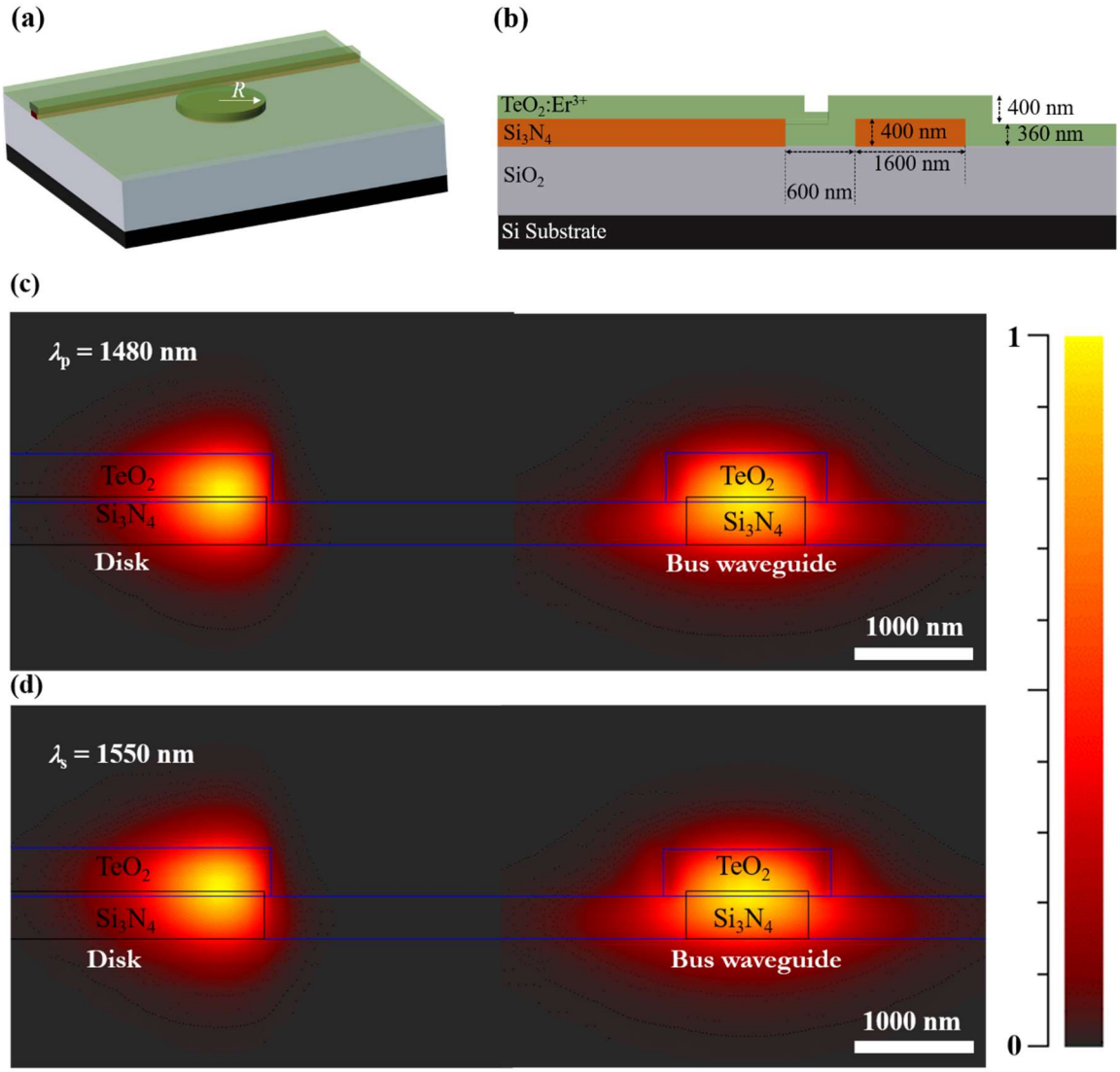

Figure 4.10. Microdisks properties, (a) 3D drawing, (b) 2D cross-sectional view with dimensions of each layer, (c) and (d) simulated TE mode profiles for the disk and bus waveguide at the pump (1480 nm) and signal (1550 nm) wavelengths respectively.

Table 4.7. Summary of calculated microdisk properties for the fundamental TE mode

	λ (nm)	$\Gamma_{Si_3N_4}$ (%)	Γ_{TeO_2} (%)	n_{eff}	A_{eff} (μm^2)
Microdisk	1480	30	37	1.8931	2.35
	1550	30	37	1.8846	2.49
Bus waveguide	1480	43	46	1.8457	0.97
	1550	43	47	1.8317	1.01

The fabricated microdisks are shown in block 4 of the GDS layout image in Fig. 4.2. After being received from the foundry a chiplet with microdisks was cleaned and coated with a 360 nm TeO_2:Er^{3+} film by RF reactive co-sputtering deposition process in the CEDT cleanroom. The deposition used the recipe presented in [88]. The film was characterized to have loss of 3.7 dB/cm at 638 nm and dopant concentration of approximate $1.5\times10^{20}/cm^3$.

Similar to microring resonators, passive characterization of microdisks involves measuring the transmission spectrum and fitting resonance dips to a Lorentzian model. The results of these characterizations are shown in Fig. 4.11. Fig. 4.11(a) shows a broadband transmission spectrum from 1450 to 1650 nm. The dip in the transmission indicates the erbium absorption region. Figure 4.11(b) shows a fine transmission spectrum for a 3 nm wavelength span with a zoomed-in Lorentzian fit of the fundamental TE resonance mode. The resonance of the fundamental TE mode was fitted at a wavelength of 1645 nm where erbium absorption is assumed to be negligible. An internal quality factor of 7×10^5 was obtained which corresponds to a propagation loss of 0.5 dB/cm in the microdisk cavity. Also, internal Q factors of 2.7×10^5 and 2.1×10^5 were obtained for the signal and pump wavelengths of 1550 nm and 1480 nm which correspond to cavity losses of 2.4 dB/cm and 2.9 dB/cm respectively. While the losses at 1645 nm are mainly dominated by material absorption and scattering, the losses at 1550 and 1480 nm also include the absorption by erbium ions. Using the measured loss value at the pump wavelength and measured transmission for a disk with a 1.8 μm gap to the waveguide (where no coupling to the cavity was observed), the coupling loss was estimated to be ~3.2 dB/facet.

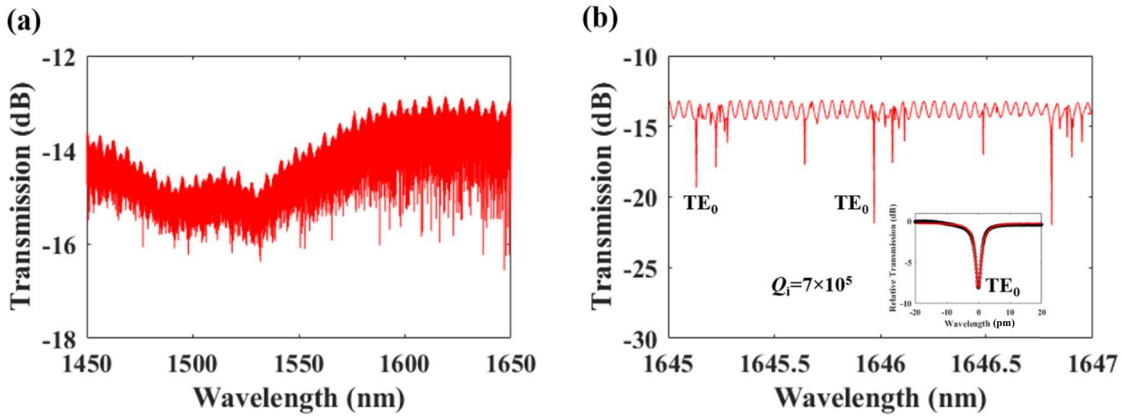

Figure 4.11. Microdisk resonance characterizations: (a) coarse transmission spectrum and (b) fine transmission spectrum with a zoomed-in resonance fit at 1645 nm.

The experimental setup for laser characterization is shown in Fig. 4.12(a) consisting of a tunable broadband laser source coupled to an S-band high-power amplifier, polarization controller (PC), a coupling stage, WDM, OSA, and a power meter. In the laser experiment, first, low power pump was tuned onto the disk resonance by observing the drop in output power level at the power meter. Also, a disk in resonance can be easily seen by the bright green glow due to erbium emission from upper states, as shown in Fig. 4.12(b). Once the pump was on resonance, the power was gradually increased until laser emission started to appear on the OSA. Figure 4.12(c) shows a microscope image of the microdisk taken during the laser experiment. Figures 4.12(d) and (e) show examples of laser emission spectra observed in the microdisk for pump powers of 26 mW and 63 mW before the chip, which correspond to ~12 mW and ~30 mW coupled into the bus waveguide respectively. It was observed that for lower pump powers, only one or a few lasing modes are observed as

shown in Fig. 4.12(d). Upon increasing the pump power more modes start to appear as shown in Fig. 4.12(e) resembling the resonance plot in Fig 4.11(b).

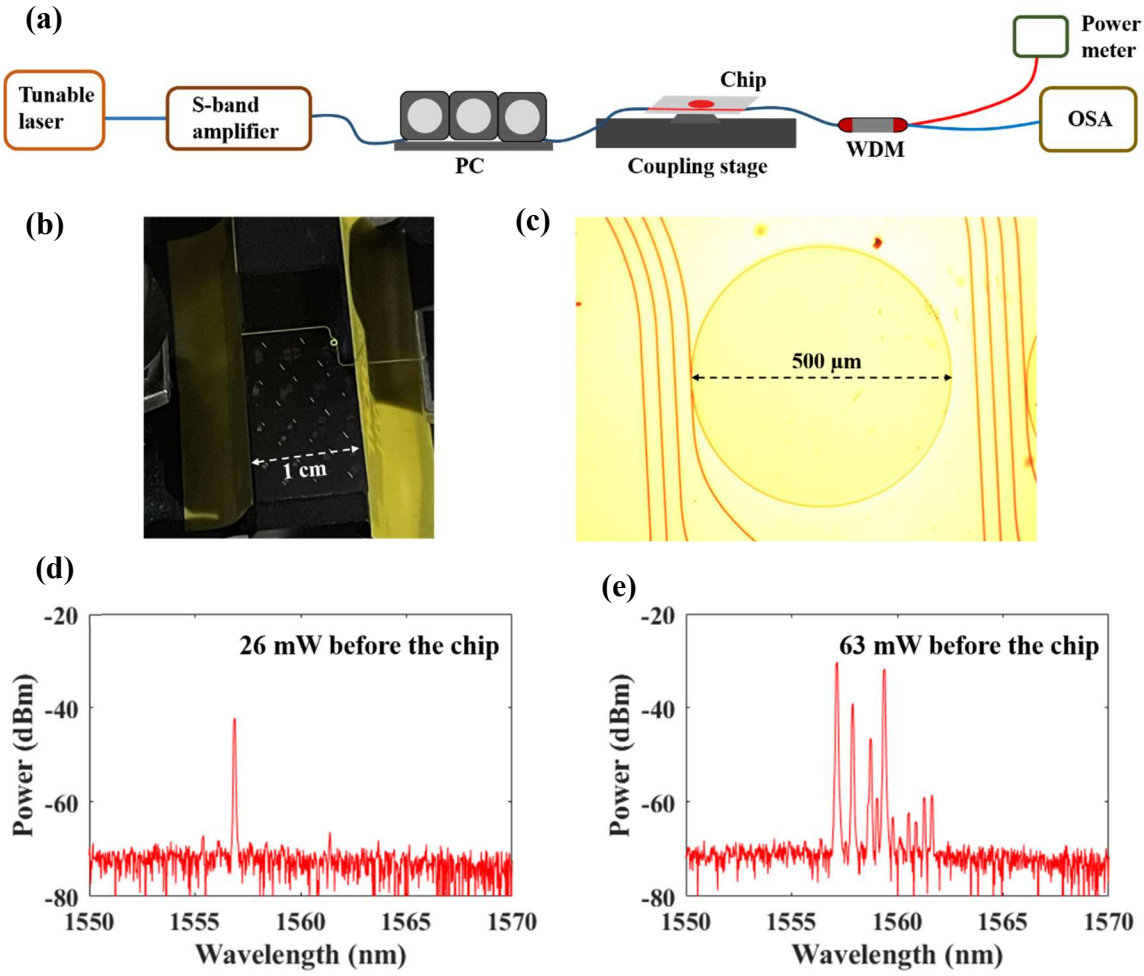

Figure 4.12. (a) Schematic view of the experimental setup used for the microdisk laser experiment. (b) Top view image of the chip showing light coupled into the disk and green emission from erbium upper state transitions. (c) Image of the fabricated microdisk taken by a camera through the light microscope using on the coupling setup. (d & e) Microdisk laser emission at 26 mW (~12 mW coupled) and 63 mW (~30 mW coupled) pump power measured out of the fiber and incident on the chip facet, respectively.

4.5.2 Optical Amplification

The absence of monolithic and efficient optical amplification is one of the biggest challenges in silicon photonics to date. The problem stems from the fundamental limitation of silicon as a light emitter due to its indirect band gap. Tellurite as a host material for rare-earth dopants such as erbium and thulium is in a good position to offer an alternate route to light emission in silicon-based platforms. It has been demonstrated in two approaches, one as a standalone waveguide fabricated on a silicon wafer [205,206], and another in similarTeO_2-Si_3N_4 hybrid waveguides [209,210]. However, previous hybrid TeO_2-based works particularly in integration with Si_3N_4 were on the thin 200-nm nitride platform which inhibits the exploitation of rich nonlinearities in the platform due to normal dispersion. Thus, in this work, using the 400 nm thick nitride with proven anomalous dispersion, optical amplification can be attained alongside nonlinear functionalities such as SCG and KCG.

In a preliminary study, a chiplet with paperclips waveguides, block 1 in Fig. 4.2, was deposited with a 352 nm thick TeO_2:Er^{3+} film. The deposition followed a similar procedure and recipe to that developed in [88]. The film was characterized to have loss of 3.6 dB/cm at 638 nm and dopant concentration of approximate $2.4\times10^{20}/cm^3$.The waveguides in the chip were then characterized for gain measurements. Figure 4.13(a) shows a schematic diagram of the setup used in gain characterization with a glowing image of the chip from erbium upper states excitation. In the experiment, a 6.7 cm long paperclip waveguide was pumped with a 1480 nm pump at varying powers. A small signal of ~1 μW at 1550 nm was also launched into the waveguide to observe the signal enhancement. First, the signal was coupled into the waveguide under test without the pump and the transmitted spectrum was recorded by the OSA. Then, the pump was turned on and again the transmitted and emitted signal spectrum was recorded by the OSA. Signal enhancement is defined as the difference in dB between the measured signal power when the pump is off and when it is on. From

the measured enhancement, the gain is calculated by subtracting the total waveguide background loss and erbium absorption loss. Figure 4.13(b) shows the measured signal enhancement at 1550 nm. A signal enhancement of 18 dB was measured. The combined background loss and erbium absorption loss were measured together using the cutback method on 3 spiral waveguides of length 10, 15, and 20 cm. The results of the cutback measurements are plotted in Fig. 4.13(c) from which a total loss of 2.27 dB/cm is obtained. Multiplying this loss by the waveguide length (6.7 cm), and assuming similar propagation loss in the paperclip waveguide, and subtracting it from the measured 18 dB signal enhancement leads to a net gain of 2.8 dB.

The net gain obtained here is almost half of what was previously measured in the same length waveguide on a 200-nm thick Si_3N_4 coated with a 340-nm TeO_2:Er^{3+} film [209]. Several reasons can explain the inferior performance one being the poor overlap of the signal mode with the gain layer of 48% compared to the previous 60%.

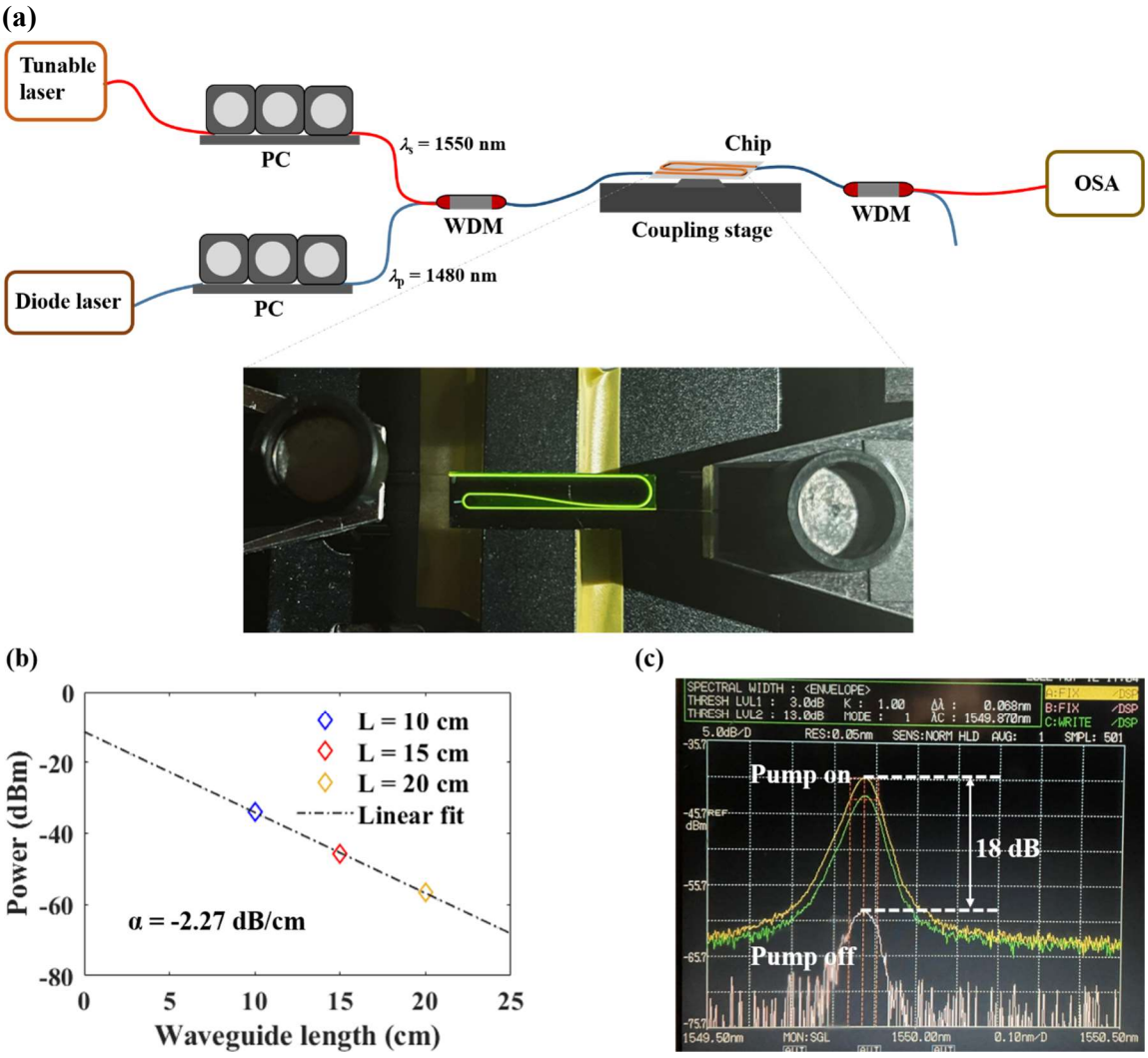

Figure 4.13. (a) Experimental setup for gain measurements with an image of the chip showing green emission from erbium upper levels transitions, (b) Cut-back measurements result on spirals of length 10, 15 and 20 cm respectively, and (c) Image of OSA screen showing the output spectra of the un-pumped and pumped signal and signal enhancement of 18 dB.

4.6 Summary

In summary, this chapter has provided a broad overview of the hybrid TeO_2 on 400-nm-thick Si_3N_4 platform as a candidate for monolithic photonic circuits. Various simulated waveguide properties were presented, for example investigation of minimum bend radii that show possible tight bends for compact and small-footprint devices. Measurements confirming anomalous dispersion were presented which also show high flexibility in dispersion on the platform. Experimental results on the key nonlinear processes of SCG and KCG generation were also presented. While the former showed performance on par with other well-developed platforms and provided motivation for the detailed study presented in the next chapter, the latter shows promising results that serve as a good starting point for future work. Furthermore, both lasing and optical amplification were also demonstrated in waveguides with similar properties to those showing nonlinear functionalities. With the combination of design flexibility, dispersion tunability, high nonlinearity, and rare-earth solubility, this platform offers a promising future for monolithic integrated silicon photonic circuits for linear, nonlinear and active functionalities.

Chapter 5

Octave-spanning Supercontinuum Generation in a Thin Si_3N_4 Waveguide Coated with Highly Nonlinear TeO_2

This chapter presents experimental results on supercontinuum generation in hybrid TeO_2-Si_3N_4 waveguides. It was highlighted in Chapter 3 that one of the aims of adding the TeO_2 coating is to enhance the overall waveguide nonlinearity owing to the higher nonlinear refractive index of the TeO_2. Consequently, one should expect the hybrid waveguides to perform better than the standalone stoichiometric Si_3N_4 waveguides, particularly in terms of threshold powers and efficiency of the nonlinear processes. The experimental results presented in this chapter align well with this proposition where highly efficient octave-spanning supercontinuum is generated at a relatively lower power than what is typically needed in stoichiometric Si_3N_4 waveguides. Also, the waveguide nonlinearity is extracted from the experimental data showing a similar value to what was initially estimated in the numerical study in Chapter 3. These results represent a manuscript that is to be submitted for publication and is included here to provide further experimental evidence of the high potential of the hybrid TeO_2-Si_3N_4 waveguides for photonic chip-based nonlinear applications.

ABSTRACT: We report on efficient octave-spanning supercontinuum generation in a 400-nm-thick silicon nitride waveguide coated with tellurite glass. The 400-nm Si_3N_4 has

reduced film stress and cracking offering a versatile integrated photonics platform compatible with both the front and the back end of a line CMOS process. The normal dispersion of a thin Si_3N_4 waveguide is engineered to be anomalous by depositing a TeO_2 coating of similar thickness, which also enhances the effective nonlinearity. The TeO_2-coating is deposited at low temperatures also compatible with the CMOS process. An octave-spanning supercontinuum is achieved at a low peak power of 258 W using a 100-fs laser centered at 1565 nm. We measure an average output power of 1 mW across the spectrum for an input power of 10.94 mW giving a conversion efficiency of 9.14 %. Our numerical simulations agree well with the experimental results giving a nonlinear parameter (γ) of 2.5 ± 0.5 $m^{-1}W^{-1}$ which is approximately three times that of standalone Si_3N_4. This platform paves the way for efficient nonlinear photonics in thin Si_3N_4 that can also be integrated monolithically with linear and active functionalities for photonic integrated circuits.

5.1 Introduction

Supercontinuum generation (SCG) involves the spectral broadening of short and narrow-band optical pulses that can expand to cover an octave or multiple octaves, leading to broadband light sources for a tremendous variety of applications in communications, frequency metrology, spectroscopy, and imaging [92]. In the early years, SCG was extensively studied in fibers [90], but recent research has intensively focused on generating supercontinuum (SC) in integrated photonic chips that can offer high performance at more compact form factors.

In particular, significant efforts have been directed towards complementary metal oxide semiconductor (CMOS) compatible platforms, which promise cost-effective and compact devices that can be mass-produced and co-integrated with electronic circuits. In addition, it is also desired to generate over an octave of SC and at near-infrared (NIR) wavelengths.

The formal is important for the self-stabilization of optical frequency combs using *f-2f* interferometry enabling precise measurement of absolute optical frequencies [258]. The latter allows the use of readily available laser sources (erbium-emission window) and applications in telecommunication wavelengths.

Over the last two decades, on-chip SCG with results covering at least an octave at NIR have been demonstrated in CMOS platforms such as silica, silicon-on-insulator (SOI), tantalum pentoxide (Ta_2O_5), silicon nitride (Si_3N_4), and silicon-rich nitride (SRN). For silica-based waveguides, an octave SCG was first demonstrated in [259], however, the platform suffers from small index contrast and weak nonlinearity leading to large-footprint devices. Silicon has higher nonlinearity with a nonlinear index (n_2) of 2 orders of magnitude higher than that of silica [260]. However, due to its small band gap, SOI devices experience strong nonlinear losses in form of two-photon absorption (TPA) when pumped at a wavelength below 2 μm [91], limiting its application in the NIR. Nevertheless, using a ridge waveguide geometry an octave-spanning SC was demonstrated at NIR in [261]. Tantalum pentoxide (Ta_2O_5), referred to as tantala is one of the novel silicon photonic platforms that has recently been explored for on-chip nonlinear photonics. SCG generation in this platform has been reported in [262–264] whereas an octave within the NIR is reported in [262]. Notably, SRN is a hybrid platform that has been developed to take advantage of silicon and Si_3N_4 bringing about higher nonlinearity, ultra-low loss, and minimal TPA. Despite showing promising performances with octave-spanning SC [265], the platform has not taken full advantage of the ultra-low loss feature of Si_3N_4 as expected and hence higher waveguide propagation loss remains a major concern.

With the consideration of CMOS compatibility, octave-spanning in the NIR, transparency, and negligible TPA, Si_3N_4 is the most attractive platform. In the last decade, over-octave and coherent SCs have been demonstrated by various research groups [93,135,174,179,266–271]. Despite extensive demonstrations of SCG in Si_3N_4, the

conversion efficiency in terms of the input power per nanometer of wavelength span has been relatively low [185], a constraint imposed by its relatively lower n_2. Another constraint arises from the difficulties of fabricating low-loss thick Si_3N_4 waveguides, which are required for anomalous dispersion to enable phase-matching and efficient SCG, using conventional thin film deposition and etching methods. This is due to cracks caused by tensile stress in the film introduced during low-pressure chemical vapor (LPCVD) deposition, which has necessitated the development of custom processes to achieve exceptional performance such as the photonic damascene [167], stress release patterns [168], or the dicing trenches techniques [171].

Tellurium dioxide (TeO_2) is one of the oxide glasses with very attractive linear and nonlinear optical properties. It has been widely studied in fibers for rare-earth doped amplifiers and lasers, broadband Raman amplification, and SCG [191]. Recently, TeO_2 has also been explored for integrated planar waveguide applications. The TeO_2 glass has wide transparency spanning from visible to MIR and a high refractive index allowing the fabrication of compact waveguides. It is a highly nonlinear medium with n_2 of up to 20× that of silica and reported the highest Raman gain coefficient among all oxide glasses [30]. Furthermore, TeO_2 has proven to be an excellent host of rare earth ions where integrated rare earth doped amplifiers and lasers have been demonstrated in a standalone TeO_2 [205,206], and the TeO_2-coated Si_3N_4 and SOI waveguides [209,210,257]. SCG in TeO_2 waveguide was first studied by S. J. Madden and K. T. Vu [204] showing ~50 nm spectral broadening in a 4 μm wide waveguide. However, they reported no observation of TPA and extracted n_2 of $0.65 \times 10^{-20} m^2 W^{-1}$. Later on, we demonstrated an improved result with an SC spectrum expanding ten times more, covering an entire telecom band [212]. The SC was generated in a normal dispersion regime with a waveguide of 200-nm thick Si_3N_4 strip coated with a 370 nm TeO_2.

In this work, we present observation of an octave-spanning SCG in a CMOS-compatible, crack-free 400-nm-thick Si_3N_4 waveguide coated with highly nonlinear TeO_2. The observed SC reaches an octave for a pulse peak power of just 258 W which to the best of our knowledge is the lowest power for an octave SC in a commercial Si_3N_4 platform pumped at telecom wavelengths. The 400 nm Si_3N_4 is a standard thickness fabricated in wafer-scale silicon nitride and silicon photonics platforms and offered by commercial foundries such as AMF [189] and IMEC [188]. It is an attractive platform that has been proven can be monolithically integrated into 3D photonic circuits and devices for example in silicon at high-temperature front-end-of-line (FEOL) or low-temperature back-end-of-line (BEOL) [248]. The added TeO_2 serves the role of engineering the dispersion of the thin Si_3N_4 into the anomalous regime while also enhancing the nonlinearity owing to its higher n_2 [30]. Also, TeO_2 is an excellent host of rare-earth dopants for on-chip optical amplifiers and lasers [205,206,209,210,257]. Therefore, this platform has the potential of providing an easy route to compact photonic circuits consisting of nonlinear, passive, and active functionalities in one chip.

5.2 Waveguide Design

The designed hybrid TeO_2-Si_3N_4 waveguide has a simple geometry consisting of a Si_3N_4 strip coated with TeO_2 film as shown in Fig. 5.1 (a). The Si_3N_4 strip was fabricated in the LioniX foundry using standard LPCVD and etching followed by in-house reactive sputter deposition of the TeO_2 at ambient temperature, which is fully compatible with a back-end of the line CMOS process. More details on the fabrication process are given in our previous work [29]. It should be noted that the Si_3N_4 fabrication involves high-temperature LPCVD deposition and annealing making it incompatible with foundry BEOL. However, the use of thin crack-free thickness allows compatibility with FEOL and large-scale monolithic integration with other platforms such as SOI [248]. Also, the results demonstrated here can

be obtained on Si_3N_4 fabricated by the low-temperature plasma-enhanced chemical vapor deposition (PECVD) at a slightly higher loss but full compatibility with the CMOS BEOL [272]. Figure 5.1(a-c) shows a cross-section, SEM image, and a transverse electric (TE) field profile of the designed waveguide respectively consisting of a 1.6 µm × 0.4 µm Si_3N_4 strip coated with a 0.424 µm thick TeO_2 film. The waveguide propagation loss is 0.6 dB/cm, measured by Q fitting a 500 µm-diameter ring resonator in the same chip and with the same waveguide dimension at a resonance wavelength of around 1550 nm [209].

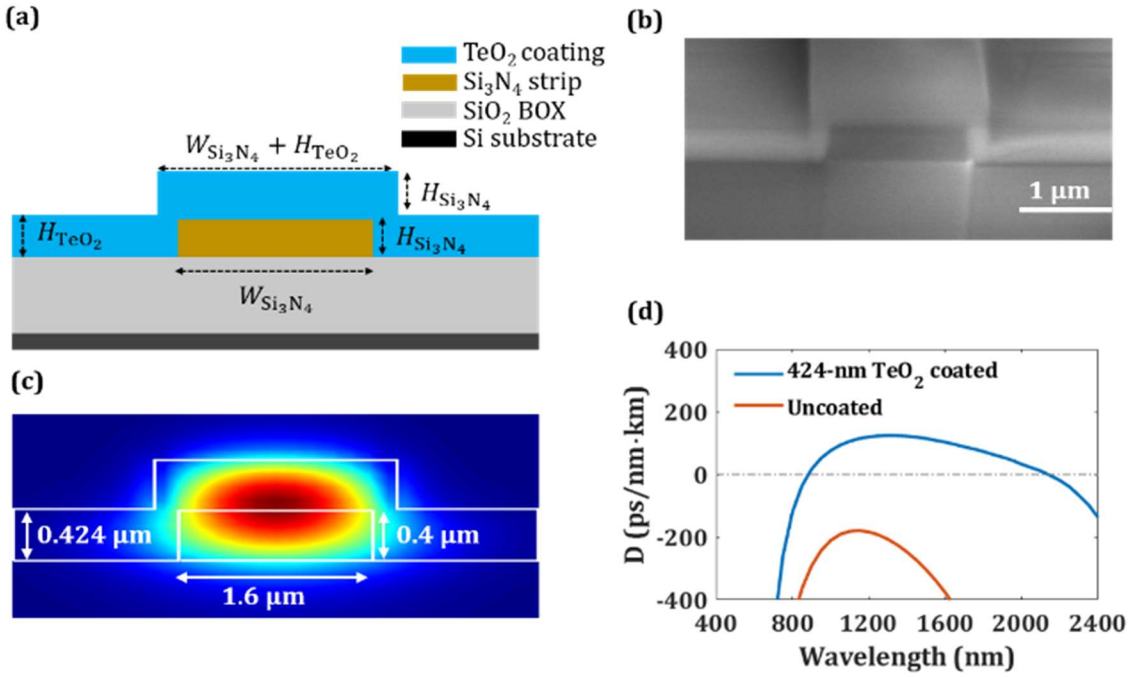

Figure 5.1. (a) Cross-section, (b) SEM image, (c) TE mode profile of the TeO_2-coated Si_3N_4 waveguide, and (d) calculated TE-mode dispersion profile for the uncoated and 400-nm TeO2-coated waveguides.

We calculated waveguide dispersion accounting for both material and geometrical contributions. There are three materials in our waveguides which are SiO_2 lower cladding, Si_3N_4 core, and the TeO_2 coating. For the TeO_2, we measured the refractive indices of the

film using the ellipsometry technique and then fitted it to a Sellmeier model for wavelengths from 400 nm to 1750 nm (data given in Table 2.1). For SiO_2 and Si_3N_4 we used Sellmeier equations previously used in [30]. Figure 1(d) shows the calculated dispersion profile of the fundamental TE mode for the 400-nm uncoated Si_3N_4 strip and 424-nm TeO_2 coated. It can be seen, as shown in [30], by adding a TeO_2 coating layer to a normal dispersion thin Si_3N_4, anomalous dispersion can be achieved for our waveguide structure

5.3 Supercontinuum Generation Experiment and Results

For SCG experiments, a 6.7-cm-long waveguide was pumped by a 1565 nm-centered laser source with 100 fs pulses, 200 MHz repetition rate, and 76 mW average power. Figure 5.2 (a) shows the experimental setup consisting of a femtosecond fiber laser free-space coupled to a waveguide through mirrors (M1, M2), a half-wave plate (HWP), a quarter-wave plate (QWP), and a focusing lens (L). The lens is characterized to have a coupling to chip loss of 8 dB. We measured the lens-to-chip coupling loss by first characterizing loss per facet using identical lens fibers and then replacing one of the lens fibers with a free-space focusing lens and recording the increase in coupling loss. The output is collected by a butt-coupled fluoride multimode fiber which is fed to two optical spectrum analyzers (OSA). The first OSA span from 350 nm to 1750 nm and the second is from 1200 nm to 2400 nm. Figure 5.2(b) shows the experimental results of the generated SC with the inset showing an image of the chip and strong third harmonic generation (THG) across the visible wavelengths. The maximum coupled average power was 10.94 mW, corresponding to a peak power of 482 W, for which the generated spectrum (solid red) spans from 0.89 μm to 2.11 μm at -20 dB level.

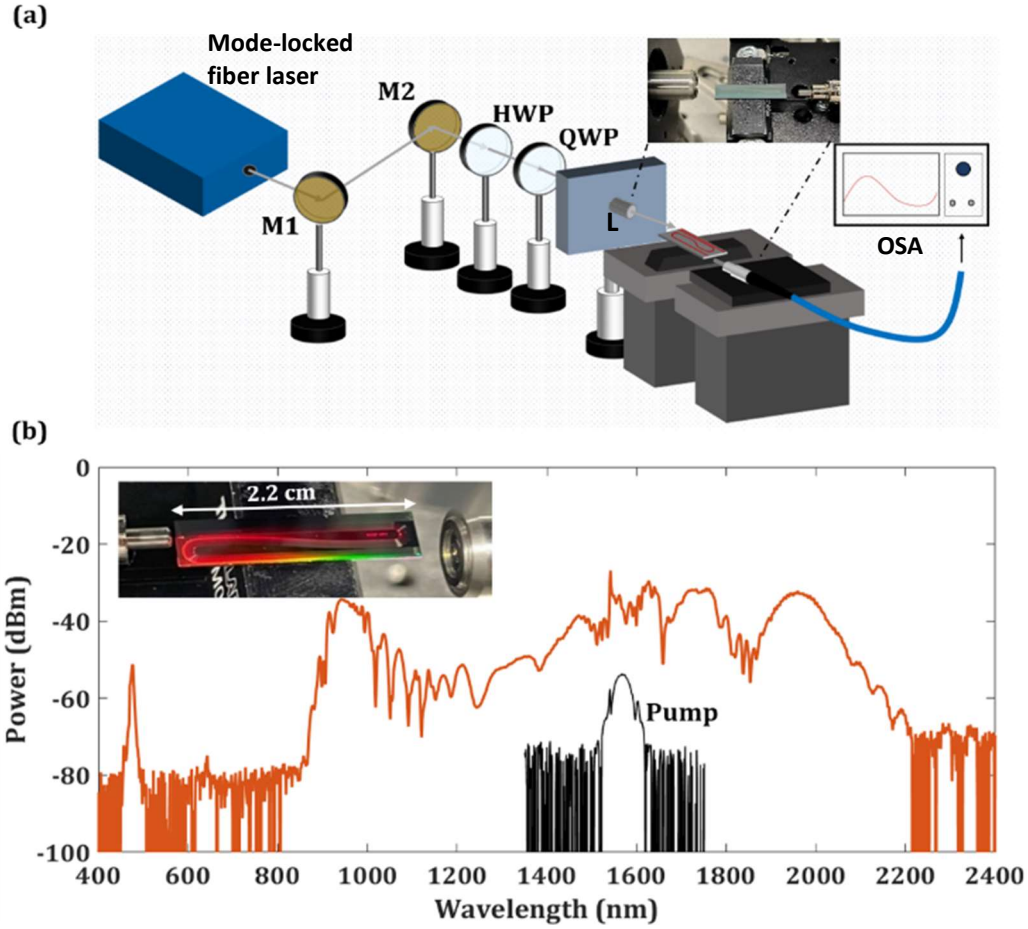

Figure 5.2. (a) Experimental setup, (b) generated SC (red), pump (black), and an image of the chip showing THG.

We varied the input power and plot the generated SC versus coupled peak power in Fig 5.3(a). The coupled power is varied using a broadband optical attenuator from 48.5, 153, 258 to 482 W. For an input power of 258 W, an octave-spanning SC is observed. This power corresponds to an average power of just about 5.86 mW and 29.3 pJ pulse energy which to the best of our knowledge is the lowest power for an octave-spanning SC in Si_3N_4-based platform pumped at telecom wavelengths.

Furthermore, we carried out a numerical simulation of the supercontinuum based on a well-known generalized nonlinear Schrödinger equation [90]. Simulation results are shown in Fig. 5.3(b and c). In Fig. 5.3(b) we plot the output SC spectra for varying power similar to experimental results in Fig. 5.3(a). To obtain this figure we initially used a calculated nonlinear parameter (γ) of 2.28 $W^{-1}m^{-1}$ using equations in [30]. We then varied this value from 1 to 3 $W^{-1}m^{-1}$and found the simulated SCG matches the experiment for a γ value of about 2.5 $W^{-1}m^{-1}$, and further scanning showed this value can have an error of up to ±0.5 $W^{-1}m^{-1}$ possibly contributed by the errors in power measurement and input pulse properties. We used γ to estimate the n_2 of the TeO_2 and obtained a value of 1.443×10^{-18} m^2/W. This value is approximately 6 times higher than that of a stoichiometric Si_3N_4[217]

The spectral evolution of the supercontinuum along the waveguide length for the highest input power of 482 W is plotted in Fig. 5.3(c). It can be seen from Fig. 5.3(c) that soliton fission starts to take place at a relatively shorter length of only 0.6 cm. Hence, a much shorter waveguide could have been used to achieve similar results with much higher output power. For the current results, we measured an output average power of about 1 mW across the spectrum for maximum input average power of 10.94 mW giving a 9.14% conversion efficiency. Since the input power was measured before the chip, the output power and hence this conversion efficiency is limited by the output coupling. From the waveguide length, we estimate a loss reduction of up to 3 dB with a shorter waveguide of < 2cm. Therefore, using a shorter waveguide and improving output coupling would see improved conversion efficiency with a much higher power across the spectrum to a level that the SCG can be potentially useful for example as a broadband white light source for chip-scale applications.

The observed THG is replotted in a zoomed-in spectra shown in Fig. 5.3(d). The spectra are similar to but much stronger than what we previously reported [212]. THG is a nonlinear process involving three photons and requires phase matching [273]. The faded

gray line in Fig. 5.3(d) indicates the FWHM level covering 12 nm bandwidth from 469 nm to 481 nm. Also, the peak of the spectrum is at -20 dB level of the entire SC. The average power is estimated to be 232 nW from the 10.94 mW input power. We notice that the spectrum is missing most of the observed visible colors. While we see colors from green, and yellow to red (400 nm to 700 nm) in the chip image in Fig. 5.2(b), the collected spectrum only covers the blue bandwidth (450 nm to 500 nm). This is likely due to higher propagation losses at shorter wavelengths and hence most of the generated third harmonic signal is lost along the way.

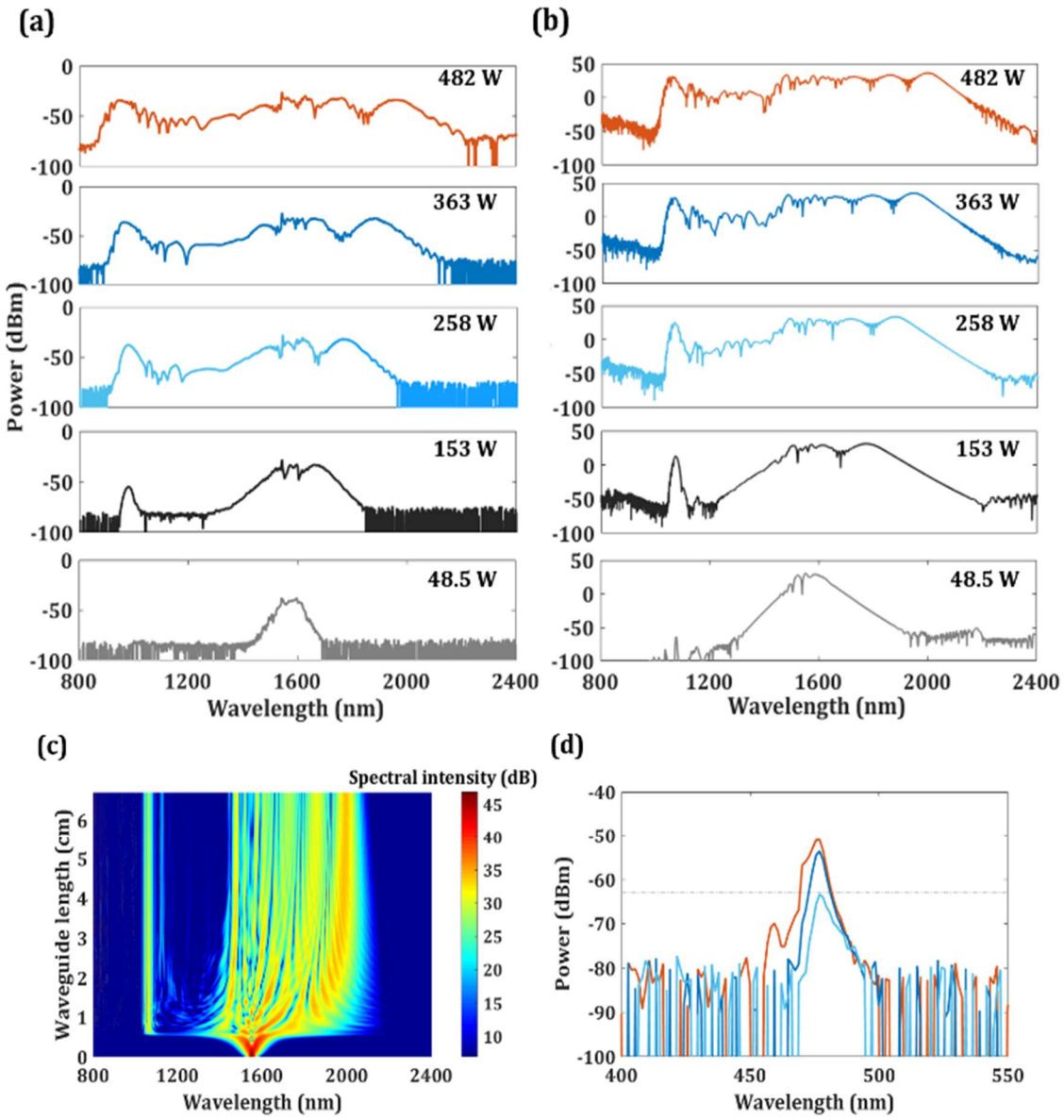

Figure 5.3. (a) The experimental and (b) simulated SC spectra at different pump powers, (c) spectrogram, and (d) zoomed-in third harmonic spectra for different powers.

5.4 Discussion and Conclusion

5.4.1 Discussion

Table 5.1 shows a summary of demonstrated SCs in various CMOS platforms with spectral coverage within the NIR wavelengths. In this comparison, our results fair well with most of the previous demonstrations. In particular, the TeO_2-Si_3N_4 platform performs well in terms of peak power requirement showing higher or comparable powers to only 4 out of 15 references shown in the table. Also, in our experiment we have shown that a useful octave-spanning SC can be generated at peak power as low as 258 W, the lowest compared to all other stoichiometric Si_3N_4. Furthermore, in our SCG, a used waveguide length appears to be relatively longer than most of the other results in Table 1, but we have shown in Fig. 5.3(c) that the same bandwidth and potentially higher output power can be achieved with a waveguide as short as 0.6 cm. Lastly, among a few others, we report strong THG. THG is of significant interest for example as a source in a visible wavelength where pulsed lasers are not readily available [274].

Table 5.1. Visible to NIR SCG in silicon photonics platforms

Ref/ Platform	Length (cm)	Loss (dB/cm)	Pulse duration (fs), λ_0 (nm)	Peak Power (kW)	Bandwidth (μm) @ dB level
* TeO_2-Si_3N_4	6.7	0.6	100, 1565	0.258 0.482	0.94 – 1.93@-30 0.89 – 2.11 @-20
[261]/SOI	0.5	1.5	>50, 1900	0.159	1.1-2.4 @ -20
*[268]/Si_3N_4	2	0.6	200, 1510	≈ 0.31	0.8 – 1.7
[265]/USRN	0.3	3	500, 1555	0.34	1.06 – 2.24 @ -40
[266]/Si_3N_4	0.8	0.7	92, 1000	≈ 0.346	0.67 – 1.944 @ -40
[93]/Si_3N_4	4.3	0.8	200, 1300	0.704	0.665 – 2.025 @ -30
[275]/Silica	45	0.06	100, 1550	1.7	1.4 – 1.7 @ -20
[270]/Si_3N_4	5.5	-	78, 2100	3.84	1.2 – 2.9
*[269]/Deuterated SiN	0.5	0.5	74, 1560	5.7	0.4 – 2.5 @ -45
[135]/Si_3N_4	20	0.0209	50, 1560	6.56	1.01 – 2.02 @ -20
[179]/Si_3N_4	0.5	< 6	< 90, 1550	≈ 6.7	0.4 – 4.5
[262]/Ta_2O_5	0.5	0.1	80, 1560	≈ 9.9	0.7-2.4 @-20
[259]/Silica	350	0.00037	180, 1330	≈ 10.6	0.936 – 1.888 @ -5
*[267]/Si_3N_4	1	-	80, 1550	11.7	0.5 – 3
[174]/Si_3N_4	0.6	0.5	120, 1560	11.67	0.5 – 2.6 @ -30
[271]/Si_3N_4	0.5	-	100, 3200	90	0.5 – 4.44

*Results where THG is also reported

5.4.2 Conclusion

In summary, we have demonstrated octave-spanning SCG in a Si_3N_4 waveguide coated with a highly nonlinear TeO_2 film using a CMOS-compatible process. We showed that an octave-spanning SC covering an entire telecom band can be obtained at low peak power of 258 W. For the maximum input average power of 10.94 mW, we measured an output average power of 1mW. We have estimated a nonlinear refractive index of the TeO_2 to be at least 6 times that of stoichiometric LPCVD Si_3N_4. The TeO_2 can be used to enhance the nonlinearity, offers a route to easy dispersion engineering in thin Si_3N_4, and act as a host of rare-earth dopants for waveguide amplifiers and lasers. The 400-nm Si_3N_4 is commonly incorporated in volume wafer-scale integrated photonic chips and offers versatility in terms of fabrication and is flexible for various applications. Hence, the TeO_2-Si_3N_4 platform

offers not only an alternate route to nonlinear photonics in thinner Si_3N_4 but also a path to monolithic integration of waveguide amplifiers and lasers, and linear and nonlinear functionalities on a single silicon photonic chip.

Chapter 6

Numerical Study of Stimulated Raman Amplification in CMOS-Compatible Integrated Tellurite Glass Waveguides

This chapter presents an analytical and numerical investigation of Raman amplification in hybrid TeO_2-Si_3N_4 waveguides. From a literature study, it was found that the TeO_2-based glasses have the highest Raman gain coefficient among all other oxide glasses. Thus, it has been studied extensively for Raman amplification in fiber and showed high gain and broadband amplification capabilities. In this work, a literature summary of several materials that have been studied for Raman amplification is given. Then, a comprehensive study on the TeO_2 glass is presented through analytical calculations and numerical modeling. The design of optimum waveguide dimensions for Raman amplification in the TeO_2-Si_3N_4 platform is presented. Raman amplification equations are solved and the potential for on-chip net gain is demonstrated. These results represent a manuscript that has been submitted for publication and are included here for completeness highlighting the rich nonlinearities that the TeO_2 can offer in the hybrid platform under study.

ABSTRACT: We numerically investigate tellurite glass (TeO_2) coated silicon nitride (Si_3N_4) waveguides as a prospective platform for on-chip Raman amplifiers. Tellurite glass has one of the highest Raman gain coefficients among oxide glasses and negligible two-photon absorption at telecommunications wavelengths, while Si_3N_4 offers mature silicon-

compatible processing, high-resolution feature definition for compact waveguides, and the ultra-low waveguide losses required for Raman gain. Using a model based on coupled equations describing the pump and signal evolution, we show that losses of ≤ 0.1 dB/cm are required for net Raman gain in TeO_2-Si_3N_4 waveguides for practical launched pump powers of ≤ 1 W. Such waveguide losses are slightly smaller than the lowest loss yet demonstrated in TeO_2-Si_3N_4 waveguides of 0.25 dB/cm, but larger than the lowest loss reported in standalone TeO_2 and Si_3N_4 waveguides of 0.05 and < 0.001 dB/cm, respectively, thus indicating that a roadmap exists towards achieving Raman gain. Our results show the possibility of an integrated Raman amplifier with an expected gain of up to 10 dB for a propagation loss of 0.01 dB/cm and 1 W pump power in a 1.3-m-long TeO_2-coated Si_3N_4 spiral waveguide.

6.1. Introduction

Over the last three decades, silicon photonics has emerged as a leading technology for photonic integrated circuits (PICs) applicable in telecommunications and data interconnects [1],[276]. Silicon photonics offers advantages including low losses, high speed, and large bandwidth, and it leverages the low cost and volume production offered by the pre-existing complementary metal oxide semiconductor (CMOS) technology. In recent years applications of photonic devices and circuits have expanded beyond traditional areas, spanning into other fields like biomedical sensing [11], detection and ranging [12], space [277], and defense and security [278]. Despite such growth, the absence of monolithic optical amplifiers and lasers has been a major challenge toward full integration in silicon photonics. Particularly, on-chip optical amplifiers have grown to be increasingly important owing to the increased scale and complexity of PICs. Due to its indirect bandgap, silicon itself is an unsuitable gain material. Several alternatives have been adopted to achieve monolithic light amplification in silicon photonic chips including epitaxial growth

of III/IV materials onto silicon [37],[279] and rare-earth doping of dielectric thin films on silicon or silicon nitride waveguides [280][281]. However, the former method suffers from high materials and fabrication costs and the latter approach has the drawback of the gain being limited to specific bands within the emission range of rare-earth dopants. An alternative is to generate/manipulate light through nonlinear optical phenomena in waveguides. This includes third-order (Kerr) nonlinearities such as self-phase modulation (SPM), cross-phase modulation (XPM), four-wave mixing (FWM), and the inelastic scattering processes of stimulated Raman scattering (SRS), and stimulated Brillouin scattering (SBS). Through nonlinear processes, widely tunable light emission can be achieved as well as broadband wavelength sources through supercontinuum generation (SCG) and chip-based optical frequency combs (OFCs). In this approach, silicon has proven to be inefficient around telecommunications wavelengths due to high nonlinear losses in form of two-photon absorption (TPA) [15]. Nevertheless, using silicon-on-insulator (SOI) or other CMOS-compatible materials with minimal/negligible nonlinear losses such as the stoichiometric Si_3N_4 and silicon-rich Si_3N_4, various high-performance nonlinear devices have been demonstrated, from broadband frequency combs to supercontinuum sources and optical parametric amplifiers (OPOs) [38]–[282].

Raman amplification through SRS offers quite an interesting alternative approach to monolithic waveguide amplifiers. By stimulated Raman scattering, any wavelength can be amplified with the right pump wavelength, allowing for widely tunable gain. Furthermore, an entire section of a waveguide can act as an amplifier providing distributed amplification, and allowing for low noise performance [283]. In addition, multiple pump schemes can be adopted where respective pump intensities are adjusted to provide not only broadband gain but flat gain bandwidth in amorphous materials [284]. For silicon photonics applications, Raman amplification has been studied extensively in SOI waveguides. Waveguide amplifiers have been demonstrated under continuous wave (CW) pumping [285–287] and

pulsed laser pumping [288–290]. Recently, other waveguide platforms have been explored for on-chip Raman amplification and lasing such as doped silica microresonators [291,292], aluminum nitride [293], diamond [294, 295], and lithium niobate [296]. While higher TPA and narrow gain bandwidth are the main limitations of silicon-based Raman devices, silica devices would require a relatively long gain length and large footprint due to the weak Raman gain coefficient and large cross-sectional area, low index contrast waveguides. On the other hand, crystalline materials such as aluminum nitride, lithium niobate, or diamond are less attractive due to their relatively narrow Raman gain spectra [297-299].

Tellurite is an oxide glass with a relatively high Raman gain coefficient and wide gain bandwidth, making it a promising alternative material for on-chip Raman amplification. It can be integrated into CMOS-compatible circuits, including low-loss hybrid waveguides on SOI and Si_3N_4 platforms [29,67]. TeO_2 is a highly nonlinear material with a reported nonlinear refractive index (n_2) of more than 20 times that of silica and a Raman gain coefficient of up to 60 times that of silica [30,66]. It also has a wide transparency window and high linear refractive index (n) which allow for the fabrication of low-loss and highly compact waveguides. In addition, TeO_2 has proven to be an excellent host of rare earth ions with minimal quenching where integrated rare earth doped amplifiers and lasers have been demonstrated in TeO_2 [205,206], and TeO_2-coated Si_3N_4 waveguides [209–211]. Tellurite glass Raman fiber amplifiers have been extensively studied in the past showing relatively high gain at shorter lengths and broader bandwidth compared to silica-based Raman fiber amplifiers [300,301]. However, Raman amplification in integrated tellurite glass waveguides has yet to be explored.

Despite having low loss and high refractive index, the demonstrated waveguides based on only stoichiometric TeO_2 have relatively large cross-sections [69], where smaller cross-sections are desirable for high intensities and efficient Raman gain. Recently, our group has reported a hybrid platform based on low-loss, CMOS-compatible Si_3N_4 coated with

TeO_2 films that omit the need for etching TeO_2 films [29]. This platform is particularly promising because of the potential for Si_3N_4 ultra-low loss waveguide [302] and small mode areas [29], both requirements for efficient Raman gain, and fabrication of long waveguide structures in a compact form factor and with high yield [303].

In this work, we present a numerical study of stimulated Raman amplification in an integrated CMOS-compatible TeO_2 waveguide platform. The organization of this work is as follows. In section 2 we present a thorough literature review of several optical materials that have the potential for on-chip Raman amplification. We also present a brief introduction to the hybrid TeO_2-coated Si_3N_4 waveguide platform. Section 3 begins with numerical calculations of the prospective waveguide parameters to be used in the amplifier model. We then present the equations for the CW Raman amplifier model followed by the amplifier simulation results. The last section includes a brief discussion of the outcomes of this work, the next steps, and conclusions. Our results show that TeO_2-Si_3N_4 waveguides have the potential for compact on-chip Raman amplifiers.

6.2. Material Properties

6.2.1 Materials for On-Chip Raman Amplification

A variety of different oxide glasses have been explored for Raman fiber amplifiers. To show how tellurite, stands out compared to other oxide glasses, we compiled a collection of the most common oxides that have been explored for Raman fiber amplification. Figure 6.1 presents a summary of the Raman gain coefficients for common glasses used in fibers. It should be noted also we added silicon for reference, aluminum nitride, diamond, and lithium niobate owing to the recent demonstrations of integrated Raman lasers in these platforms [293–296]. Also, a color-coded bar chart showing full width half maximum (FWHM)bandwidth at the highest reported gain peak for the five oxides is included as an inset. The figure clearly shows how the tellurite glass stands out with the highest peak gain

and a broad FWHM bandwidth of ~225 cm^{-1} nearing that of silica glass (~240 cm^{-1}). Furthermore, tellurite offers a possibility of adjusting the gain coefficient by doping it with other metal oxides where it has been shown that the gain coefficient can be increased beyond 2 orders of magnitude of that of silica, 170×10^{-13} m/W for the composition 65% TeO_2–15%P_2O_5–15%Na_2O–5% ZnO [54]. There have been some variations on the measured Raman gain coefficient from different research groups and glass compositions where 90×10^{-13} m/W is reported in [304], 58×10^{-13} m/W in [305], 40×10^{-13} m/W in [306,307] for a similar glass composition of 85% TeO_2 + 15% WO_3. Nevertheless, the reasons for such variations have been thoroughly studied and explained in [307], which point to the value of 40×10^{-13} m/W as justifiably most accurate for the given composition. This value is for bulk glass with the composition of 85% TeO_2 + 15% WO_3 which has been extensively studied in the literature. Therefore, the rest of this work assumes a Raman gain coefficient for TeO_2 of 40×10^{-13} m/W unless otherwise stated.

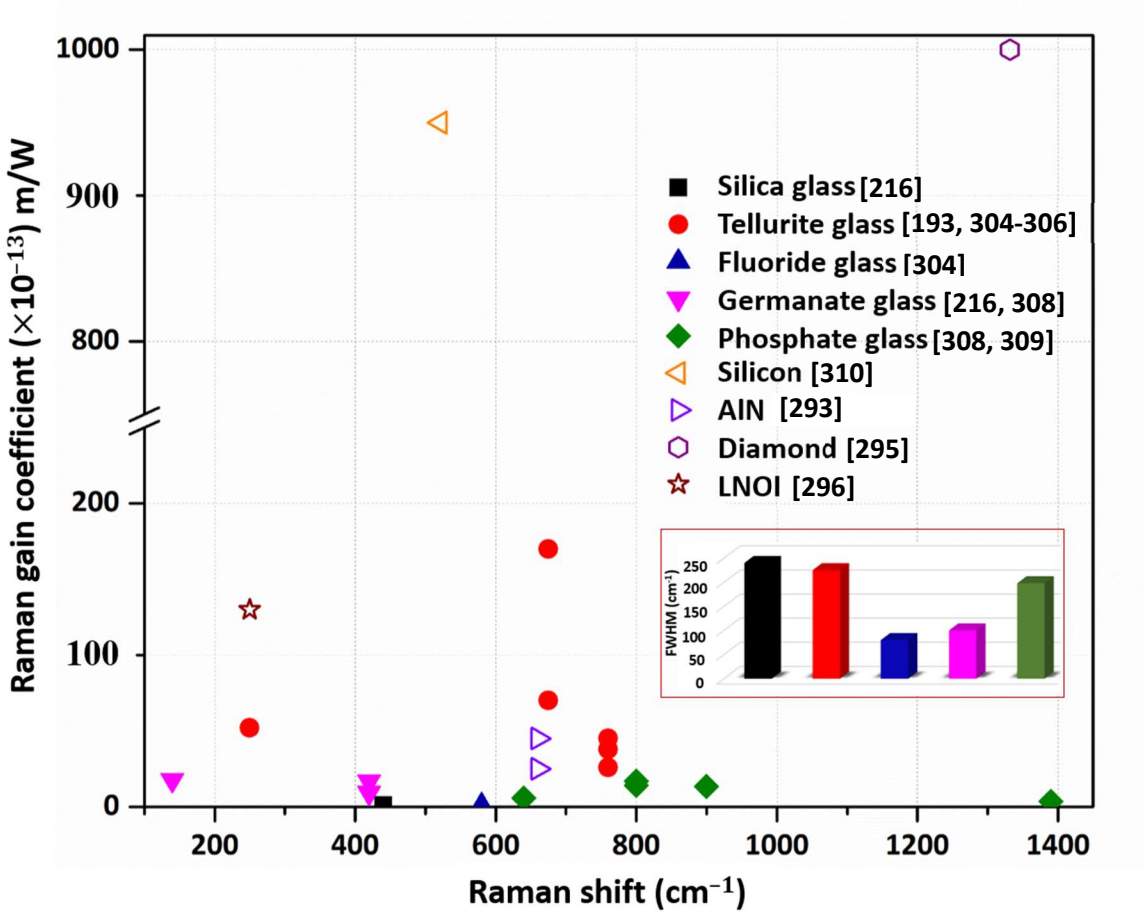

Figure 6.1. Peak Raman gain coefficients of different waveguide materials; the inset is a color-coded bar chart showing FWHM Raman gain bandwidth of the five oxides glasses

6.2.2 TeO_2-Coated Si_3N_4 Waveguide Platform

In this work, we explore TeO_2-Si_3N_4 waveguides for Raman gain, which exhibit low losses and have been applied in linear, rare-earth-doped light-emitting, and nonlinear optical devices [209−212]. Details on the waveguide design can be found in reference [29], while here we provide a brief overview of the properties relevant to this work. Figure 6.2(a) shows a cross-section of the TeO_2-coated Si_3N_4 waveguide structure. It consists of a standard foundry Si_3N_4 strip waveguide of ~ 200 nm height with a post-processing coating layer of

TeO_2 and a top-cladding spin-on fluoropolymer layer (Cytop). The TeO_2 film is deposited through a single-step low-temperature back-end-of-line process by reactive sputtering with further details of the experiment given in [29].

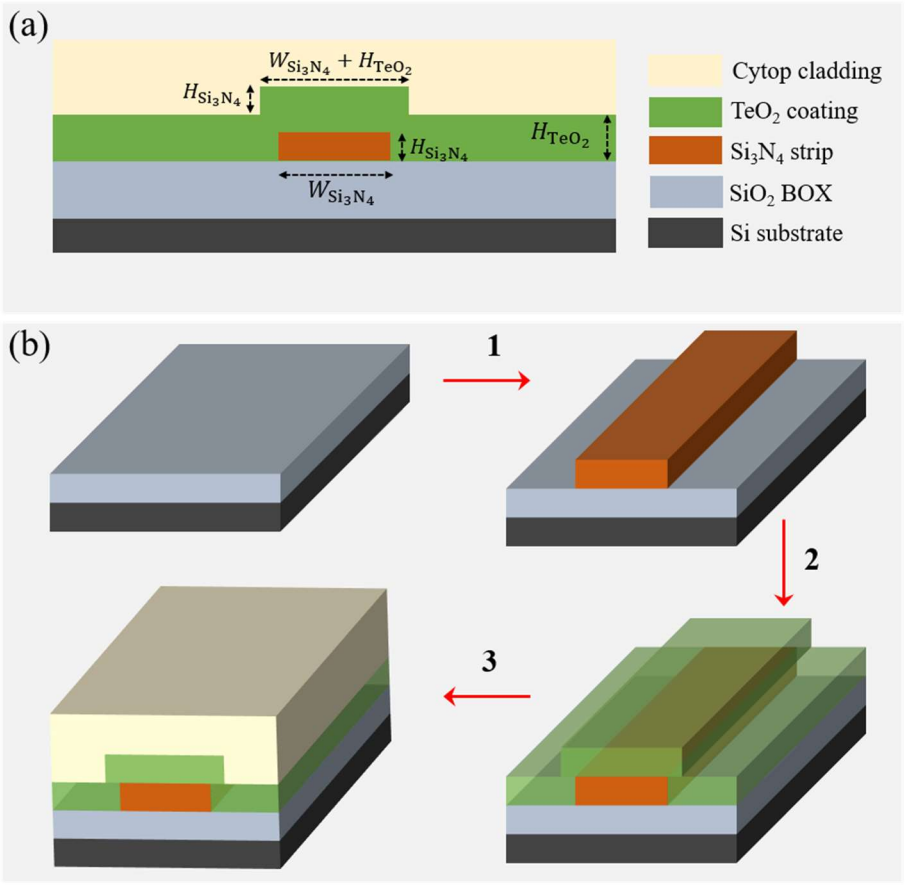

Figure 6.2. 3D structure of TeO_2-coated Si_3N_4 waveguide depicting materials layers and essential fabrication steps: (a) waveguide cross-section and parameters, (b) fabrication steps including 1. LPCVD deposition and RIE etching of Si_3N_4, 2. reactive sputter deposition of the terullite film, and 3. spin coating of protective polymer (Cytop) top-cladding.

6.3 Amplifier Modeling

6.3.1 Waveguide Parameters

In this section, we provide a brief justification and summary of the waveguide parameters that have been selected and are to be investigated in the amplifier model. Stimulated Raman scattering is an intensity-dependent nonlinear process [11], and thus it is desirable to maximize the light intensity in the waveguide by increasing the optical confinement (r) and reducing the effective mode area (A_{eff}). Where r is calculated as a fractional partial power in the respective waveguide segment. At the same time due to the negligible Raman gain coefficient of Si_3N_4 [60], we need to ensure the waveguide mode has maximum interaction with the tellurite. However, this is challenging because the two materials have close refractive indices. While reducing the waveguide dimensions would lower the A_{eff} to a certain limit, the effect is opposite for confinement of the mode with TeO_2 (r_{TeO_2}). Therefore, simulations were carried out to find optimal combinations of waveguide dimensions that improve r_{TeO_2} while ensuring optimal A_{eff} is attained as well. The Si_3N_4 strip height was varied from 50 nm, 100 nm to 200 nm, which are typical waveguide heights applied in low-loss Si_3N_4 waveguides fabricated by LPCVD deposition and reactive ion etching and offered in the multi-project wafer (MPW) runs [187]. While ultrathin Si_3N_4 strips are ideal for low-loss waveguides [287], a thicker strip provides stronger lateral confinement and is good for tighter waveguide bends. For the three Si_3N_4 strip heights we varied the width and the TeO_2 coating thickness to optimize the two aforementioned parameters. The simulation results are shown in Fig. 6.3. Figure 6.3(a) shows electric field profiles of optimal waveguide cross-sections and TeO_2 film thickness for the three Si_3N_4 strip heights, I (50 nm), II (100 nm), and III (200 nm) respectively. Figure 6.3(b) shows r_{TeO_2} while Fig. 6.3(c) shows the A_{eff} both as functions of changing waveguide width and TeO_2 coating thickness. It can be seen in Fig. 6.3(b), due to a slightly higher refractive index of TeO_2 relative to Si_3N_4, changing the Si_3N_4 strip height or width does not result in any

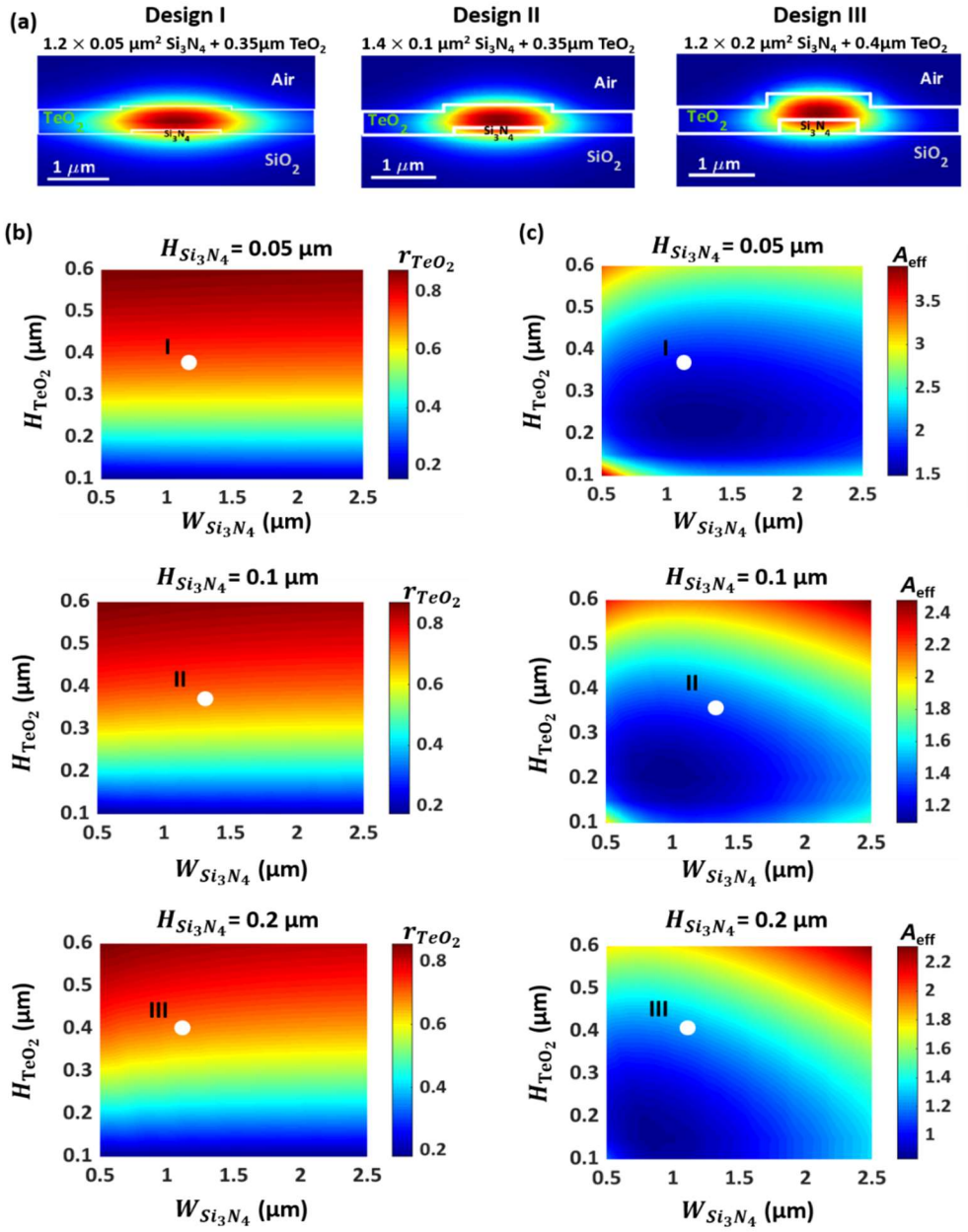

Figure 6.3. Waveguide optimization study for the Si_3N_4 heights 0.05, 0.1 and 0.2 μm. (a)Finite element mode solver calculations of the properties of the fundamental TE modes for the optimal waveguide dimensions (b) partial power confinement in the TeO_2 (r_{TeO_2}) and (c) effective mode area (A_{eff}) versus Si_3N_4 strip width and TeO_2 film thickness.

significant change in r_{TeO_2}. Figure 6.3(c) shows that a thicker nitride strip is generally desirable for a smaller effective mode area. Therefore, design III is for the rest of this work as it shows the best parameters out of the three considered.

6.3.2 Amplifier Model

A numerical model of Raman amplification in a waveguide under CW pumping was applied in this study. Stimulated Raman Scattering occurs when a strong pump transfers a fraction of its power to a lower-frequency wave called a Stokes-shifted wave or a higher-frequency wave called an anti-Stokes wave. For simplicity, only the stokes wave is considered in this study since the emission of the anti-stokes wave is relatively weaker [11]. Signal amplification by SRS under a CW pump can be modeled by a set of coupled equations, [15] 1 and 2.

$$\frac{dP_s}{dz} = -\alpha_s P_s + g_R P_s P_p, \tag{1}$$

$$\xi \frac{dP_p}{dz} = -\alpha_p P_p - \frac{\lambda_s}{\lambda_p} g_R P_s P_p, \tag{2}$$

where $P_s, P_p, \lambda_s, \lambda_p, \alpha_s, \alpha_p$ are power, wavelengths, and attenuations for signal and pump, respectively, z is propagation length, g_R is the Raman gain efficiency term given by $\gamma_R / A_{\text{eff}}$ where γ_R is the Raman gain coefficient and A_{eff} is the effective mode area. The symbol ξ in equation (2) takes a value of 1 or –1 depending on the pumping directionality, where +1 is for pumping in the forward direction and –1 for backward pumping. In this work, only forward pumping is considered and ξ is kept constant at +1 unless otherwise stated.

Equations 1 and 2 can be solved using numerical techniques such as the finite element method (FEM). However, in the case of significantly higher pump powers relative to the

signal, an assumption can be made where the pump depletion (third) term of equation 2 is ignored, in which case an analytical solution can easily be reached. In this work, we solved the equations both numerically and analytically, and in both cases, the solutions have shown very close agreement.

It should be noted that under the presence of TPA, the coupled equations 1 and 2 should include additional terms representing nonlinear losses through a TPA coefficient and free carrier absorption [15]. Here, these terms are neglected. In addition, these equations are only valid for the case of CW pumping without the presence of other nonlinear effects such as FWM. The case of high-intensity pulsed laser pumping would require full consideration of the Nonlinear Schrödinger equation and we reserve that for future studies.

All the parameters to be used in the simulation are listed in Table 6.1. The waveguide parameters were extracted from Fig. 6.3, in combination with consideration for minimum bend radii simulations. Table 6.1 also lists other simulation parameters including the Raman gain coefficient, pump and signal wavelengths, and variable pump and signal losses. The losses are chosen starting from the lowest value that has currently been measured in this platform, 0.25 dB/cm [209], and lowered to 0.1, 0.05, and 0.01 dB/cm within the range of what is the lowest loss reported in standalone TeO_2 (<0.05 dB/cm) [66] and in Si_3N_4 waveguides (<0.001 dB/cm) [302].

Table 6.1. TeO_2-Si_3N_4 waveguide parameters to be used in amplifier simulations

Parameter	**Value**
Si_3N_4 strip dimensions $\boldsymbol{W_{Si_3N_4}} \times \boldsymbol{H_{Si_3N_4}}$ (μm^2)	1.2 × 0.2 (Design III)
TeO_2 coating thickness, $\boldsymbol{H_{TeO_2}}$(μm)	0.4
Effective mode area, A_{eff} (μm^2)	1.2
TeO_2 intensity overlap, $\boldsymbol{r_{TeO_2}}$(%)	70
TeO_2 Raman gain coefficient, γ_R ($\boldsymbol{x10^{-13}}$ m/W)	40
Pump wavelength, λ_p (nm)	1400

Signal wavelength, λ_s (nm)	1550
Signal loss, α_s (dB/cm)	0.25/0.1/0.05/0.01
Pump loss, α_p (dB/cm)	0.25/0.1/0.05/0.01
Amplifier length (cm)	(up to) 150

6.3.3 Simulation Results

Using the model in the previous section, we investigated the small signal Raman gain for varying background loss, pump power, and waveguide length. In all cases, the launched signal power was kept constant at 1 μW. However, before applying the amplifier model to the waveguides we estimated an optimal waveguide length for simulation. Due to the intensity dependency of SRS, the pump intensity needs to remain relatively high along the full propagation length. Hence, a maximum length is defined that accounts for propagation loss and within which the pump intensity remains strong enough to incite the nonlinear response. This length is referred to as the effective length (L_{eff}), which is always less than the total waveguide length and is given by $L_{\text{eff}} = \frac{1-\exp(\alpha_p L)}{\alpha_p}$.

Figure 6.4(a) shows the plot of L_{eff} versus α_p for different waveguide lengths. It can be observed that for higher propagation losses the effective lengths are much closer for the four waveguide lengths, but the case is different when the losses are $\lesssim$ 0.2 dB/cm. Once a certain propagation loss threshold is achieved (e.g., $\lesssim$ 0.1 dB/cm for typically 10's of cm long integrated spiral waveguides), it is advantageous to use as long a waveguide as possible, and it is shown in that situation that the amplifier gains increases approximately linearly with increasing waveguide length and/or pump powers. Figure 6.4(b) shows a conceptual drawing of the high gain spiral with input and output multi-mode interferometers combiner and splitter. Also, a table above it shows the calculated spiral footprint for different lengths at fixed minimum bend radii (R_{min}). The parameter R_{min} is the minimum bend radius at the center of the spiral calculated based on the radiation-limited

quality factor defined in chapter 2, section 2.3.3 whereas R_{max} is the length from the center to the outermost waveguide for a given spiral length.

We then investigated the amplifier gain for varying propagation loss. In Fig. 6.4(c) we plot amplifier gain versus waveguide length and pump power for propagation losses of 0.25, 0.1, 0.05, and 0.01 dB/cm, respectively. In Fig. 6.4(c), (I) it can be seen that within the simulation range of up to 2 W pump power and 150 cm length there is no net gain. As the loss is reduced by a factor of 2 a small signal gain is observed as shown in (II). Decreasing the losses further down to 0.05 dB/cm and 0.01 dB/cm in Fig. 6.4(c) III and IV shows a significant increase of the net gain and it is almost linearly dependent on waveguide length at 0.01 dB/cm loss. Results in Fig. 6.4(c) to a great extent agree with the effective length concept depicted in Fig. 6.4(a) whereas at lower losses it is beneficial to use longer waveguide length and vice versa at higher losses. For the loss of 0.01 dB/cm, it is shown that a 10 dB level or higher amplifier gain can be achieved with 1 W of pump power and a waveguide length of at least 130 cm.

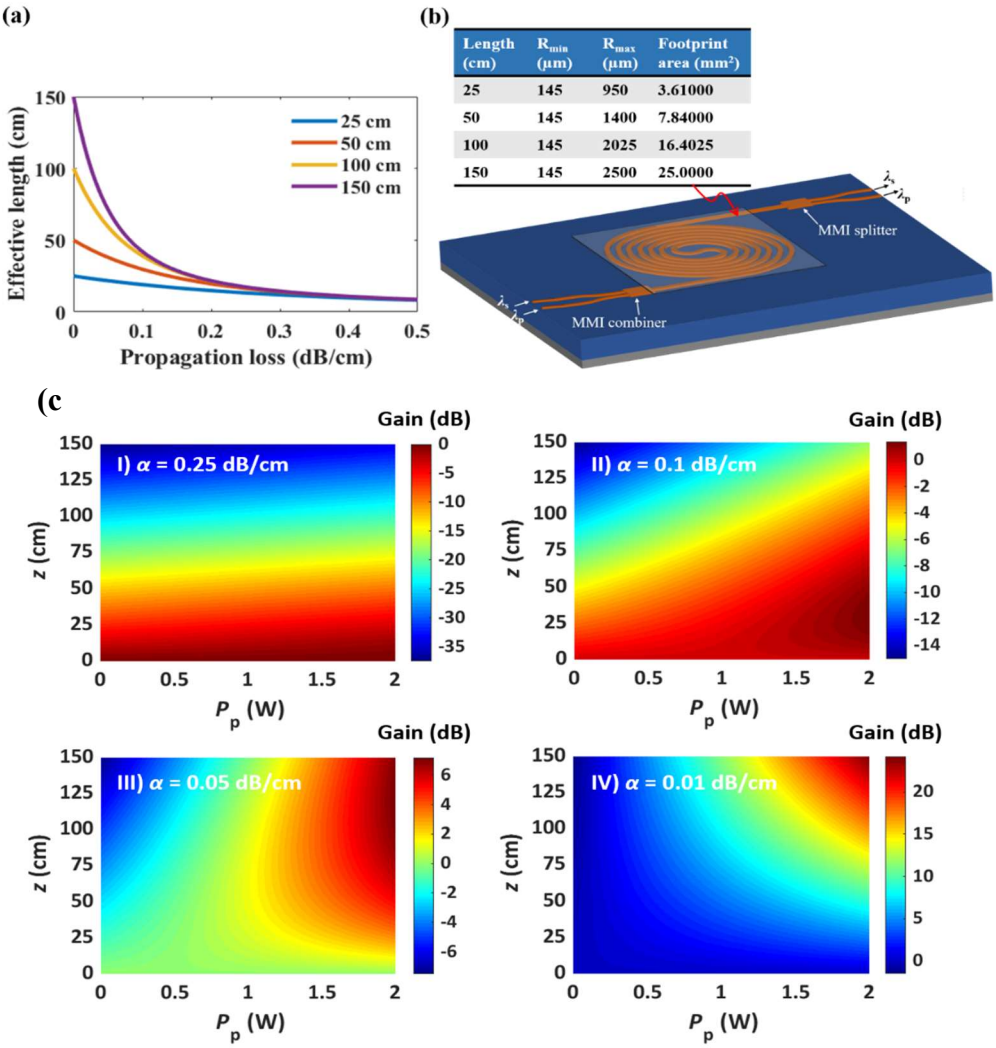

Figure 6.4. (a) Effective length for Raman amplification versus propagation loss for various waveguide lengths. (b) Conceptual drawing of the high gain spiral consisting of MMI combine and splitters at the input and output, and a table showing an estimated footprint for various gain lengths (c)Gain versus waveguide lengths and pump powers; (I) for the lowest propagation losses as measured in our current waveguides; and for the minimum projected losses of 0.1 (II), 0.05 (III), and 0.01 (IV) dB/cm respectively, using 0.2μm Si_3N_4 strip parameters in Table 6.1.

Furthermore, we show the amplifier gain and loss vs. length for a pump power of 1 W in Fig. 6.5(a) which it clearly shows how waveguide attenuation impacts the net gain along the waveguide length. In Fig 6.5 (b) we plot amplifier gain versus pump power for a theoretically lowest loss of about 0.01 dB/cm showing the highest potential gain for this waveguide platform. We also vary the Raman gain coefficient and show how the gain can be optimized by employing different TeO_2 compositions. The compositions of each of the Raman gain coefficients used in Fig. 6.5(b) are shown in Table 6.2. It is shown that the amplifier gain can be tuned from 11 dB to 53 dB at 1W pump power for a 150 cm long waveguide.

Table 6.2. TeO_2-Si_3N_4 waveguide parameters to be used in amplifier simulations

Composition	γ_R **(**$x10^{-13}$ **m/W)**	**Reference**
85% TeO_2 - 15% WO_3	40	[312]
60% TeO_2-20%P_2O_5 - 20%Na_2O 50% TeO_2 - 50% $TlO_{0.5}$	52	[311,312]
70% TeO_2-15%P_2O_5 - 15%Na_2O	70	[311]
65% TeO_2-15%P_2O_5 - 15%Na_2O- 5% ZnO	170	[311]

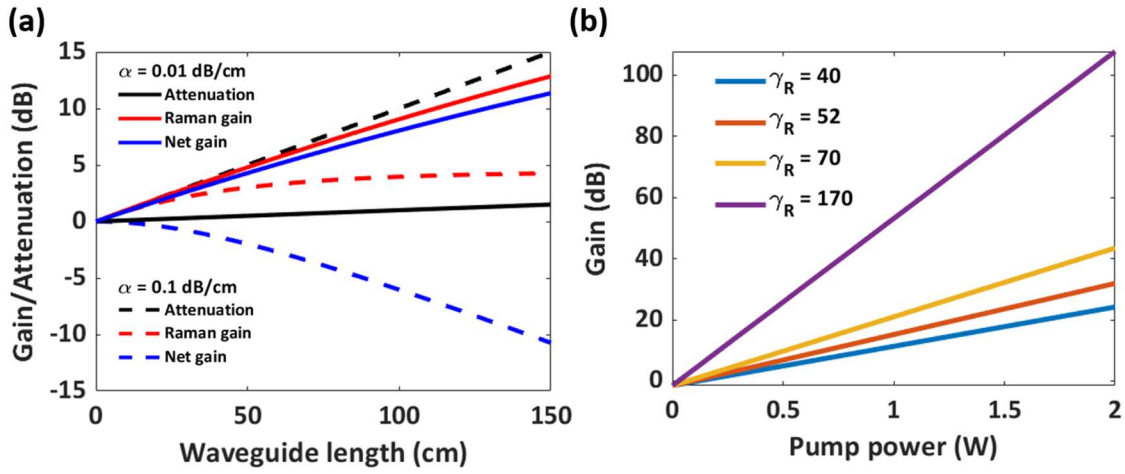

Figure 6.5. (a)The plot of gain versus TeO_2-coated Si_3N_4 waveguide length shows the progression of losses, Raman signal enhancement, and the net gain along the waveguide for a pump power of 1 W, and propagation losses of 0.1 dB/cm and 0.01 dB/cm. (b)Gain versus pump power for a 150 cm-long waveguide, 0.01 dB/cm propagation loss, and various values of the Raman gain coefficient ($\times 10^{-12}$ W/m).

6.4 Conclusion

In summary, we have presented a literature and numerical study showing the possibility of on-chip Raman amplification in TeO_2-based waveguides. The hybrid TeO_2-coated Si_3N_4 waveguide design has promising properties for Raman gain, including a high Raman gain coefficient, high material stability for high pump power handling, small effective mode area for high intensities, and small waveguide bend radius for compact spiral footprints. For a realistic pump power of 1 W, the total gain is highly dependent on propagation losses and waveguide length. By employing optimized fabrication steps that can scale down propagation losses and using the small bend radius of TeO_2-Si_3N_4 waveguides to design compact and sufficiently long spiral waveguides, the proposed amplifiers devices may offer

a promising source of very broadband on-chip optical amplification for silicon-based photonic integrated circuits.

Chapter 7

Discussion and Conclusion

7.1 Summary and Discussion

This thesis work aimed at exploring and developing the hybrid TeO_2-Si_3N_4 platform as a candidate for integrated nonlinear photonics based on highly nonlinear TeO_2 and utilizing a thin Si_3N_4 layer that is compatible with conventional fabrication processes and offered in commercial CMOS foundries.

In the first two chapters, the goals, motivation, and the underlying theoretical background of the main concepts were given. In chapter one, the motivation for this work was highlighted by looking at different materials platforms that have been explored for integrated nonlinear photonics focusing on silicon-based materials that are CMOS compatible. The features, strengths, and weaknesses of each material were summarized in which Si_3N_4 was shown to stand out as the most suitable material platform. It was also highlighted how this work aims to complement the state-of-the-art Si_3N_4 technology by mitigating some of its shortcomings including challenges in fabricating low-loss dispersion engineered waveguides by introducing the hybrid TeO_2-Si_3N_4 platform. In Chapter 2, a brief theoretical introduction was given emphasizing key design terms and parameters that were then used to describe the features of the hybrid platform.

In Chapter 3, the optimization of waveguide nonlinearity and dispersion engineering were explored in a comprehensive numerical study. It was shown that the effective nonlinearity of a 400 nm stoichiometric Si_3N_4 is enhanced up to 3 times with the added 500 nm TeO_2

film and also anomalous dispersion can be achieved for both TE and TM polarization. These results were both verified experimentally in Chapters 4 and 5. The nonlinearity enhancement was confirmed in an SCG experiment where a TeO_2 nonlinear refractive index of 1.443×10^{-18} m^2/W was extracted, which is similar to that obtained from literature and used in simulations (1.3×10^{-18} m^2/W). The dispersion was experimentally measured in microring resonators confirming anomalous dispersion with 424 nm thick TeO_2 coatings. The results showed anomalous dispersion for a 400 nm thick, 1.6 μm wide Si_3N_4 strip coated with a 424 nm TeO_2 film with values of ~25 and ~78 ps/nm·km at 1552 nm for the TE and TM-modes respectively. In addition, these results were verified by the generated SC spectra characterized by typical features observed in anomalous dispersion waveguides such as dispersive waves and soliton fission.

Optical frequency comb generation through the KCG process in microring resonators was also demonstrated. Ring resonators with up to half a million internal Q factors were measured and pumped with a CW laser at around 1585 nm. For a pump power of 251 mW coupled into the bus waveguides a comb with up to 8 comb lines was observed covering up to 1000 nm wavelength span. The comb lines were far apart separated by multiple FSR indicating that upon increasing pump powers there is a possibility of more lines forming in between. However, the pump power could not be increased further due to the saturation of the OSA used to observe the output. A narrowband notch filter is required to attenuate the pump at the output to resolve this issue. A family of tunable fiber Bragg gratings (FBG) can potentially be used to attenuate the pump accordingly. At the time of writing this thesis, efforts were made to acquire the FBG but significantly longer lead times prohibited the author from using them in the experimental results presented in this thesis.

Supercontinuum generation is another nonlinear phenomenon studied and successfully demonstrated in this work. An octave-spanning SC was demonstrated at a low peak power of just 258 W covering wavelengths from 940 to 1930 nm and pumped at a telecom

wavelength, of 1565 nm. The generated continuum showed a fair comparison with similar work in other silicon photonic platforms. Particularly, in comparison to results in stoichiometric Si_3N_4, it shows the lowest power required for an octave coverage to the best of the author's knowledge.

A higher Raman gain coefficient is another attractive feature of tellurite compared to other oxide glasses. A comprehensive analytical and numerical study of Raman amplification in the hybrid TeO_2-Si_3N_4 platform was presented in chapter 6. The results showed the possibility of an integrated Raman amplifier with an expected gain of up to 10 dB for a propagation loss of 0.01 dB/cm and 1 W pump power in a 1.3-m-long TeO_2-coated Si_3N_4 spiral waveguide. While the current loss figures prohibited practical demonstration of Raman amplification, the simulation work in chapter three provides a roadmap toward practical realization. In addition, these results open a window of opportunity for the investigation of other nonlinear phenomena such as the Brillouin scattering.

Lastly, light generation and optical amplification were investigated, and the results were presented. Multimode lasing and a net gain of 2.8 dB was observed in an Er-doped TeO_2-coated Si_3N_4 microdisk resonator and a 6.7 cm long paperclip waveguide, respectively. These are preliminary results that can be improved with further investigation. For example, the Er-doped TeO_2 coatings were about 360 nm thick, permitting only 48% overlap of the signal mode with gain media, whereas more overlap and higher gain can be achieved with a thicker film. Also, the author notes that a few months before the writing of this thesis, the deposition system in the CEDT required repairs and was indisposed until the end of finalizing this thesis, preventing detailed investigation and optimization of the Er-doped TeO_2 coating layer. Overall, these results help in establishing a foundation for further exploration of this platform for light generation, amplification, and eventually their monolithic integration with nonlinear and other linear functionalities.

7.2 Future Work

This thesis work serves as a framework and the very first study of TeO_2 as a complementary material for integrated nonlinear photonics on the mature Si_3N_4 platform. Therefore, there is a lot to improve upon from what has been presented in the immediate future and several new avenues to explore in the long term future. The next paragraphs give brief details of what can be improved and further explored in the near and far future for each of the results presented in this thesis.

First, in the dispersion measurements results, there was something very interesting that needs further exploration. The measured dispersion was normal for thinner TeO_2 coatings and increased to anomalous with an increase in film thickness continuously for TM polarization but only up to a certain point for the TE mode. This means there is a range of film thicknesses at which the dispersion is normal for TE and anomalous for TM. This is something that needs to be explored further, particularly for SCG. Having an on-chip SC source with tunability from normal to anomalous is useful since the generation mechanisms and eventual spectral profiles for the two differ. Anomalous dispersion SC spectra are usually very broad and useful in applications such as spectroscopy, whereas they are noisy and highly incoherent limiting their applications in telecom. On the other hand, normal dispersion SC spectra are less broad but can be free of noise and highly coherent. In addition, the dispersion profile appears shifting to the longer wavelengths with the increase of the Si_3N_4 strip width and the TeO_2 coating. This need further investigation for potentially extending the platform to Mid-IR applications as both materials used are transparent toward that wavelength range.

The demonstrated KCG in this work still lacks characteristics of the state-of-the-art frequency combs developed in stoichiometric Si_3N_4. The first step to get to the desired soliton combs is to improve the resonator's design. This includes enhancing the Q factor

by reducing waveguide losses, investigating a better range of coupling gaps that will allow sufficient coupling of the pump into the cavity, and reducing the resonator's size. Also in the future, it will be interesting to pump rare-earth doped resonators, for example, erbium-doped devices pumped at 1480 nm which can lead to comb generation and lasing around the 1550 nm telecommunication window for application as an on-chip multi-wavelength-source.

Another idea that is worth exploring in the future is amplified supercontinuum generation. One of the main limitations of utilizing chip-based SC as a broadband source is the low output power resulting from the low conversion efficiency of the nonlinear media used. Even though this work demonstrated improved efficiency and hence above average output power of the generated spectra still the power levels are too low for practical applications. Typically, an average output power of 1 mW is considered high for many on-chip generated SCs, however that power translates to only a few nanowatts for an individual comb line. Combining the efficient SCG demonstrated and potential high gain amplification it could be possible to have amplified SCG. It can be implemented separately such that a short undoped waveguide is used to generate the SC and it is coupled to a longer doped waveguide for amplification, or the same doped waveguide can be co-pumped for SCG and amplification. The latter approach is simpler but not very feasible as the erbium might absorb most of the pump (for SCG) before reaching enough length for the SC to be generated.

The promising results on active functionalities also open further avenues to explore. Starting with the microdisk laser, one proposition for future designs is to reduce the disk sizes such that the FSR and consequently modes separation is increased so that individual lasing modes can be excited to obtain a single-mode laser. If this is achieved micro heaters can then be incorporated to tune between resonances. The next step for amplifier design is to improve the gain by optimizing the erbium concentration and using thicker films for

more overlap of the mode with the gain medium. In addition, several other dopants such as thulium and praseodymium can be explored for emission in other wavelengths.

Last, an important and ultimate theme to explore is to combine all functionalities and capabilities demonstrated in this platform into a single monolithic photonic chip, followed by further integration with other well-developed platforms such as SOI. By then, the ultimate and long-term objective of this work will be achieved which is developing a linear, nonlinear and active photonic platform that is compatible with standard wafer scale processing and conventional fabrication processes and can be integrated into larger scale PICs based on mature and well-developed CMOS platforms.

References

1. D. Thomson, A. Zilkie, J. E. Bowers, T. Komljenovic, G. T. Reed, L. Vivien, D. Marris-Morini, E. Cassan, L. Virot, J.-M. Fédéli, J.-M. Hartmann, J. H. Schmid, D.-X. Xu, F. Boeuf, P. O'brien, G. Z. Mashanovich, and M. Nedeljkovic, "Roadmap on silicon photonics," Journal of Optics **18**(7), 073003 (2016).

2. J. Shalf, "The future of computing beyond Moores Law," Philosophical Transactions of the Royal Society A **378**(2166), (2020).

3. E. Masanet, A. Shehabi, N. Lei, S. Smith, and J. Koomey, "Recalibrating global data center energy-use estimates," Science **367**(6481), 984–986 (2020).

4. M. Koot and F. Wijnhoven, "Usage impact on data center electricity needs: A system dynamic forecasting model," Applied Energy **291**, 116798 (2021).

5. M. Borghi, C. Castellan, S. Signorini, A. Trenti, and L. Pavesi, "Nonlinear silicon photonics," Journal of Optics **19**(9), 093002 (2017).

6. S. Royo and M. Ballesta-Garcia, "An overview of lidar imaging systems for autonomous vehicles," Applied Sciences (Switzerland) **9**(19), (2019).

7. D. J. Blumenthal, R. Heideman, D. Geuzebroek, A. Leinse, and C. Roeloffzen, "Silicon Nitride in Silicon Photonics," Proceedings of the IEEE **106**(12), 2209–2231 (2018).

8. F. Kish, V. Lal, P. Evans, S. W. Corzine, M. Ziari, T. Butrie, M. Reffle, H. S. Tsai, A. Dentai, J. Pleumeekers, M. Missey, M. Fisher, S. Murthy, R. Salvatore, P. Samra, S. Demars, N. Kim, A. James, A. Hosseini, P. Studenkov, M. Lauermann, R. Going, M. Lu, J. Zhang, J. Tang, J. Bostak, T. Vallaitis, M. Kuntz, D. Pavinski, A. Karanicolas, B. Behnia, D. Engel, O. Khayam, N. Modi, M. R. Chitgarha, P. Mertz, W. Ko, R. Maher, J. Osenbach, J. T. Rahn, H. Sun, K. T. Wu, M. Mitchell, and D. Welch, "System-on-Chip Photonic Integrated Circuits," IEEE Journal of Selected Topics in Quantum Electronics **24**(1), (2018).

9. J. E. Bowers, T. Komljenovic, M. Davenport, J. Hulme, A. Y. Liu, C. T. Santis, A. Spott, S. Srinivasan, E. J. Stanton, and C. Zhang, "Recent advances in silicon photonic integrated circuits," SPIE OPTO, **9774**, 977402 (2016).

10. C. G. H. Roeloffzen, L. Zhuang, C. Taddei, A. Leinse, R. G. Heideman, P. W. L. van Dijk, R. M. Oldenbeuving, D. A. I. Marpaung, M. Burla, and K.-J. Boller, "Silicon nitride microwave photonic circuits," Optics Express **21**(19), 22937 (2013).

11. A. Fernández Gavela, D. Grajales García, J. C. Ramirez, and L. M. Lechuga, "Last Advances in Silicon-Based Optical Biosensors," Sensors **16**(3), 285 (2016)..

12. X. Sun, L. Zhang, Q. Zhang, and W. Zhang, "Si Photonics for Practical LiDAR Solutions," Applied Sciences 2019, Vol. 9, Page 4225 **9**(20), 4225 (2019).

13. S. N. Frequency Comb and T. W. Picqué, "Nathalie Picqué and Theodor W. Hänsch, Frequency comb spectroscopy," Nature Photonics **13**, 146–157 (2019).

14. G. Moody, V. J. Sorger, D. J. Blumenthal, P. W. Juodawlkis, W. Loh, C. Sorace-Agaskar, A. E. Jones, K. C. Balram, J. C. F. Matthews, A. Laing, M. Davanco, L. Chang, J. E. Bowers, N. Quack, C. Galland, I. Aharonovich, M. A. Wolff, C. Schuck, N. Sinclair, M. Lončar, T. Komljenovic, D. Weld, S. Mookherjea, S. Buckley, M. Radulaski, S. Reitzenstein, B. Pingault, B. Machielse, D. Mukhopadhyay, A. Akimov, A. Zheltikov, G. S. Agarwal, K. Srinivasan, J. Lu, H. X. Tang, W. Jiang, T. P. McKenna, A. H. Safavi-Naeini, S. Steinhauer, A. W. Elshaari, V. Zwiller, P. S. Davids, N. Martinez, M. Gehl, J. Chiaverini, K. K. Mehta, J. Romero, N. B. Lingaraju, A. M. Weiner, D. Peace, R. Cernansky, M. Lobino, E. Diamanti, L. T. Vidarte, and R. M. Camacho, "2022 Roadmap on integrated quantum photonics," Journal of Physics: Photonics **4**(1), 012501 (2022).

15. Q. Lin, O. J. Painter, and G. P. Agrawal, "Nonlinear optical phenomena in silicon waveguides: modeling and applications," Optics Express **15**(25), 16604 (2007).

16. R. K. W. Lau, Y. Okawachi, M. R. E. Lamont, and A. L. Gaeta, "Effects of multiphoton absorption on parametric comb generation in silicon microresonators," Optics Letters, **40**(12), 2778–2781 (2015).

17. B. Kuyken, F. Leo, S. Clemmen, U. Dave, R. Van Laer, T. Ideguchi, H. Zhao, X. Liu, J. Safioui, S. Coen, S. P. Gorza, S. K. Selvaraja, S. Massar, R. M. Osgood, P. Verheyen, J. Van Campenhout, R. Baets, W. M. J. Green, and G. Roelkens, "Nonlinear optical interactions in silicon waveguides," Nanophotonics **6**(2), 377–392 (2017).

18. R. Adar, V. Mizrahi, and M. R. Serbin, "Less than 1 dB per meter Propagation Loss of Silica Waveguides Measured Using a Ring Resonator," Journal of Lightwave Technology **12**(8), 1369–1372 (1994).

19. K. Li and A. C. Foster, "Parametric Nonlinear Silicon-Based Photonics," Proceedings of the IEEE **106**(12), 2196–2208 (2018).

20. D. T. H. Tan, K. J. A. Ooi, and D. K. T. Ng, "Nonlinear optics on silicon-rich nitride—a high nonlinear figure of merit CMOS platform [Invited]," Photonics Research **6**(5), B50 (2018).

21. D. J. Blumenthal, R. Heideman, D. Geuzebroek, A. Leinse, and C. Roeloffzen, "Silicon Nitride in Silicon Photonics," Proceedings of the IEEE **106**(12), (2018).

22. D. Moss, R. Morandotti, A. Gaeta et al. "New CMOS-compatible platforms based on silicon nitride and Hydex for nonlinear optics". Nature Photon **7**, 597–607 (2013).

23. K. Hammani, M. A. Ettabib, A. Bogris, A. Kapsalis, D. Syvridis, M. Brun, P. Labeye, S. Nicoletti, D. J. Richardson, and P. Petropoulos, "Optical properties of silicon germanium waveguides at telecommunication wavelengths," Optics Express **21**(14), 16690 (2013).

24. D. Marris-Morini, V. Vakarin, J. M. Ramirez, Q. Liu, A. Ballabio, J. Frigerio, M. Montesinos, C. Alonso-Ramos, X. Le Roux, S. Serna, D. Benedikovic, D. Chrastina, L. Vivien, and G. Isella, "Germanium-based integrated photonics from near- to mid-infrared applications," Nanophotonics **7**(11), 1781–1793 (2018).

25. B. J. Eggleton, B. Luther-Davies, and K. Richardson, "Chalcogenide photonics," Nature Photonics 2011 5:3 **5**(3), 141–148 (2011).

26. B. Gholipour, M. J. Müller, Y. Li, S. S. Jo, Y. Cui, A. Mandal, B. Eggleton, M. Rochette, M. Rezaei, I. Alamgir, M. H. M. Shamim, R. Kormokar, A. Anjum, G. Zeweldi, T. S. Karnik, J. Hu, S. Kasap, G. Belev, A. Reznik, stephen R. elliott, M. Wuttig, D. W. Hewak, B. Hayden, R. Jaramillo, R. E. Simpson, and J. Tominaga, "Roadmap on Chalcogenide Photonics," J. Phys. Photonics (2022).

27. J. A. Black, R. Streater, R. Streater, K. F. Lamee, K. F. Lamee, D. R. Carlson, S.-P. Yu, S.-P. Yu, S. B. Papp, and S. B. Papp, "Group-velocity-dispersion engineering of tantala integrated photonics," Optics Letters, Vol. 46, Issue 4, pp. 817-820 **46**(4), 817–820 (2021).

28. H. Jung, H. Jung, H. Jung, S.-P. Yu, S.-P. Yu, D. R. Carlson, T. E. Drake, T. C. Briles, T. C. Briles, S. B. Papp, and S. B. Papp, "Tantala Kerr nonlinear integrated photonics," Optica, Vol. 8, Issue 6, pp. 811-817 **8**(6), 811–817 (2021).

29. H. C. Frankis, K. M. Kiani, D. B. Bonneville, C. Zhang, S. Norris, R. Mateman, A. Leinse, N. D. Bassim, A. P. Knights, and J. D. B. Bradley, " Low-loss TeO_2 -coated Si_3N_4 waveguides for application in photonic integrated circuits," Optics Express **27**(9), 12529 (2019).

30. H. M. Mbonde, H. C. Frankis, and J. D. B. Bradley, "Enhanced nonlinearity and engineered anomalous dispersion in TeO_2-coated Si_3N_4 Waveguides," IEEE Photonics Journal **12**(2), (2020).

31. H. Lee, T. Chen, J. Li, O. Painter, and K. J. Vahala, "Ultra-low-loss optical delay line on a silicon chip," Nature Communications, **3**(1), 1–7 (2012).

32. D. K. Armani, T. J. Kippenberg, S. M. Spillane, and K. J. Vahala, "Ultra-high-Q toroid microcavity on a chip," Nature, **421**(6926), 925–928 (2003).

33. M. Ferrera, L. Razzari, D. Duchesne, R. Morandotti, Z. Yang, M. Liscidini, J. E. Sipe, S. Chu, B. E. Little, and D. J. Moss, "Low-power continuous-wave nonlinear optics in doped silica glass integrated waveguide structures," Nature Photonics **2**(12), 737–740 (2008).

34. D. Y. Oh, D. Sell, H. Lee, K. Y. Yang, S. A. Diddams, and K. J. Vahala, "Supercontinuum generation in an on-chip silica waveguide," Optics Letters **39**(4), 1046 (2014).

35. L. Razzari, D. Duchesne, M. Ferrera, R. Morandotti, S. Chu, B. E. Little, and D. J. Moss, "CMOS-compatible integrated optical hyper-parametric oscillator," Nature Photonics **4**(1), 41–45 (2010).

36. T. J. Kippenberg, R. Holzwarth, and S. A. Diddams, "Microresonator-based optical frequency combs," Science **332**(6029), 555–559 (2011).

37. Z. Fang, Q. Y. Chen, and C. Z. Zhao, "A review of recent progress in lasers on silicon," Optics and Laser Technology **46**(1), 103–110 (2013).

38. A. L. Gaeta, M. Lipson, and T. J. Kippenberg, "Photonic-chip-based frequency combs," Nature Photonics **13**(3), 158–169 (2019).

39. R. Soref, "Mid-infrared photonics in silicon and germanium," Nature Photonics **4**(8), 495–497 (2010).

40. H. Lin, Z. Luo, T. Gu, L. C. Kimerling, K. Wada, A. Agarwal, and J. Hu, "Mid-infrared integrated photonics on silicon: A perspective," Nanophotonics **7**(2), 393–420 (2017).

41. C. Li, D. Liu, and D. Dai, "Multimode silicon photonics," Nanophotonics **8**(2), 227–247 (2018).

42. D. J. Moss, R. Morandotti, A. L. Gaeta, and M. Lipson, "New CMOS-compatible platforms based on silicon nitride and Hydex for nonlinear optics," Nature Photonics **7**(8), 597–607 (2013).

43. J. Liu, G. Huang, R. N. Wang, J. He, A. S. Raja, T. Liu, N. J. Engelsen, and T. J. Kippenberg, "High-yield, wafer-scale fabrication of ultralow-loss, dispersion-engineered silicon nitride photonic circuits," Nature Communications **12**(1), 1–9 (2021).

44. H. El Dirani, L. Youssef, C. Petit-Etienne, S. Kerdiles, P. Grosse, C. Monat, E. Pargon, and C. Sciancalepore, "Ultralow-loss tightly confining Si_3N_4 waveguides and High-Q microresonators," Optics Express **27**(21), (2019).

45. M. H. P. Pfeiffer, J. Liu, A. S. Raja, T. Morais, B. Ghadiani, and T. J. Kippenberg, "Ultra-smooth silicon nitride waveguides based on the Damascene reflow process: fabrication and loss origins," Optica **5**(7), 884 (2018).

46. A. W. Poon and K. Wu, "Stress-released Si_3N_4 fabrication process for dispersion-engineered integrated silicon photonics," Optics Express **28**(12), 17708–17722 (2020).

47. C. Xiang, J. Guo, W. Jin, L. Wu, J. Peters, W. Xie, L. Chang, B. Shen, H. Wang, Q. F. Yang, D. Kinghorn, M. Paniccia, K. J. Vahala, P. A. Morton, and J. E. Bowers, "High-performance lasers for fully integrated silicon nitride photonics," Nature Communications, **12**(1), 1–8 (2021).

48. C. Lacava, S. Stankovic, A. Z. Khokhar, T. D. Bucio, F. Y. Gardes, G. T. Reed, D. J. Richardson, and P. Petropoulos, "Si-rich Silicon Nitride for Nonlinear Signal Processing Applications," Scientific Reports **7**(1), 22 (2017).

49. IEEE Communications Society., Lasers and Electro-optics Society (Institute of Electrical and Electronics Engineers), and Optical Society of America., "Optical Fiber Communications Conference (OFC) : postconference digest," (2003).

50. D. Benedikovic, L. Virot, G. Aubin, J. M. Hartmann, F. Amar, X. Le Roux, C. Alonso-Ramos, É. Cassan, D. Marris-Morini, J. M. Fédéli, F. Boeuf, B. Szelag, and L. Vivien, "Silicon-germanium receivers for short-wave-infrared optoelectronics and communications High-speed silicon-germanium receivers (invited review)," Nanophotonics **10**(3), 1059–1079 (2021).

51. Milan Sinobad, "Nonlinear photonics in silicon germanium waveguides for mid-infrared supercontinuum generation" Doctoral Dissertation, RMIT University, Research Repository (2019).

52. K. F. Lamee, K. F. Lamee, D. R. Carlson, D. R. Carlson, Z. L. Newman, Z. L. Newman, S.-P. Yu, S.-P. Yu, S. B. Papp, and S. B. Papp, "Nanophotonic tantala waveguides for supercontinuum generation pumped at 1560 nm," Optics Letters, **45**(15), 4192–4195 (2020).

53. M. Belt, M. L. Davenport, J. E. Bowers, and D. J. Blumenthal, "Ultra-low-loss Ta_2O_5-core/SiO_2-clad planar waveguides on Si substrates," Optica **4**(5), 532 (2017).

54. Jonathan R. C. Woods, Jake Daykin, Amy S. K. Tong, Cosimo Lacava, Periklis Petropoulos, Anne C. Tropper, Peter Horak, James S. Wilkinson, and Vasilis Apostolopoulos, "Supercontinuum generation in tantalum pentoxide waveguides for pump wavelengths in the 900 nm to 1500 nm spectral region," Optics Express 28(**21**), 32173-32184 (2020)

55. C. C. Evans, K. Shtyrkova, J. D. B Bradley, O. Reshef, E. Ippen, E. Mazur, V. R. Almeida, C. A. Barrios, R. R. Panepucci, M. Lipson, J. Baker, L. B. Fu, K. Finsterbusch, M. R. E Lamont, D. J. Moss, H. C. Nguyen, B. J. Eggleton, D. Y. Choi, S. Madden, and B. Luther-Davies, "Spectral broadening in anatase titanium dioxide waveguides at telecommunication and near-visible wavelengths," Optics Express, **21**(15), 18582–18591 (2013).

56. X. Guan, L. K. Oxenløwe, L. H. Frandsen, R. Nagarajan, C. H. Joyner, R. P. Schneider, J. S. Bostak, T. Butrie, A. G. Dentai, V. G. Dominic, P. W. Evans, M. Kato, M. Kauffman, D. J. H Lambert, S. K. Mathis, A. Mathur, R. H. Miles, M. L. Mitchell, M. J. Missey, S. Murthy, A. C. Nilsson, F. H. Peters, S. C. Pennypacker, J. L. Pleumeekers, R. A. Salvatore, R. K. Schlenker, R. B. Taylor, M. F. Huan-Shang Tsai, M. F. Van Leeuwen, J. Webjorn, M. Ziari, D. Perkins, J. Singh, S. G. Grubb, M. S. Reffle, D. G. Mehuys, F. A. Kish, and D. F. Welch, "Compact titanium dioxide waveguides with high nonlinearity at telecommunication wavelengths," Optics Express, **26**(2), 1055–1063 (2018).

57. K. Alexander, N. A. Savostianova, S. A. Mikhailov, B. Kuyken, and D. Van Thourhout, "Electrically Tunable Optical Nonlinearities in Graphene-Covered SiN Waveguides Characterized by Four-Wave Mixing," ACS Photonics **4**(12), 3039–3044 (2017).

58. Y. Qu, J. Wu, Y. Yang, Y. Zhang, Y. Liang, H. El Dirani, R. Crochemore, P. Demongodin, C. Sciancalepore, C. Grillet, C. Monat, B. Jia, and D. J. Moss, "Enhanced Four-Wave Mixing in Silicon Nitride Waveguides Integrated with 2D Layered Graphene Oxide Films," Advanced Optical Materials **8**(23), 2001048 (2020).

59. D.-X. Dai, L.-M. Tong, L. Zhang, and M. Li, "Hybrid silicon nonlinear photonics [Invited]," Photonics Research, Vol. 6, Issue 5, pp. B13-B22 **6**(5), B13–B22 (2018).

60. K. Vyas, D. H. G. Espinosa, D. Hutama, S. K. Jain, R. Mahjoub, E. Mobini, K. M. Awan, J. Lundeen, K. Dolgaleva, and S. Kumar Jain, "Group III-V semiconductors

as promising nonlinear integrated photonic platforms," Advances in Physics, **7**(1), 2097020 (2022).

61. Mobini E, Espinosa DHG, Vyas K, Dolgaleva K. "AlGaAs Nonlinear Integrated Photonics" Micromachines (Basel), **13**(7), 991(2022).

62. Y. Qi and Y. Li, "Integrated lithium niobate photonics," Nanophotonics **9**(6), 1287–1320 (2020).

63. N. Li, C. P. Ho, S. Zhu, Y. H. Fu, Y. Zhu, and L. Y. T. Lee, "Aluminium nitride integrated photonics: A review," Nanophotonics **10**(9), 2347–2387 (2021).

64. B. J. M. Hausmann, I. Bulu, V. Venkataraman, P. Deotare, and M. Loncar, "Diamond nonlinear photonics," Nature Photonics **8**(5), 369–374 (2014).

65. A. Mori and H. Masuda, "Tellurite fiber Raman amplifiers," NTT Technical Review **2**(12), 51–55 (2004).

66. S. J. Madden and K. T. Vu, "Very low loss reactively ion etched Tellurium Dioxide planar rib waveguides for linear and non-linear optics," Optics Express **17**(20), 17645 (2009).

67. K. Miarabbas Kiani, D. B. Bonneville, A. P. Knights, and J. D. B. Bradley, "High-Q TeO_2–Si Hybrid Microring Resonators," Applied Sciences **12**(3), 1363 (2022).

68. H. C. Frankis, K. M. Kiani, D. B. Bonneville, C. Zhang, S. Norris, R. Mateman, A. Leinse, N. D. Bassim, A. P. Knights, and J. D. B. Bradley, " Low-loss TeO 2 -coated Si 3 N 4 waveguides for application in photonic integrated circuits ," Optics Express **27**(9), 12529 (2019).

69. S. J. Madden and K. T. Vu, "High-Performance Integrated Optics with Tellurite Glasses: Status and Prospects," International Journal of Applied Glass Science **3**(4), 289–298 (2012).

70. P. A. Franken, A. E. Hill, C. W. Peters, and G. Weinreich, "Generation of Optical Harmonics," Physical Review Letters **7**(4), 118 (1961).

71. R. W. Boyd, *Nonlinear Optics*, Academic Press (2008).

72. G. P. Agrawal, *Nonlinear Fiber Optics*, Elsevier Science (2013).

73. M. Cazzanelli and J. Schilling, "Second order optical nonlinearity in silicon by symmetry breaking," Applied Physics Reviews **3**(1), 011104 (2016).

74. H. R. Telle, G. Steinmeyer, A. E. Dunlop, J. Stenger, D. H. Sutter, and U. Keller, "Carrier-envelope offset phase control: A novel concept for absolute optical

frequency measurement and ultrashort pulse generation," Applied Physics B **69**(4), 327–332 (1999).

75. B. J. Eggleton, C. G. Poulton, P. T. Rakich, M. J. Steel, and G. Bahl, "Brillouin integrated photonics," Nature Photonics **13**(10), 664–677 (2019).

76. D. Marpaung, J. Yao, and J. Capmany, "Integrated microwave photonics," Nature Photonics **13**(2), 80–90 (2019).

77. R. G. Hunsperger, "Optical Waveguide Modes," in *Integrated Optics: Theory and Technology*, R. G. Hunsperger, Springer, (2009).

78. Wouter J. Westerveld, Suzanne M. Leinders, Koen W. A. van Dongen, H. Paul Urbach, and Mirvais Yousefi, "Extension of Marcatili's Analytical Approach for Rectangular Silicon Optical Waveguides," J. Lightwave Technol. **30**, 2388-2401 (2012)

79. M. A. Foster, K. D. Moll, and A. L. Gaeta, "Optimal waveguide dimensions for nonlinear interactions," Opt. Express, OE **12**(13), 2880–2887 (2004).

80. R. Stolen, "Phase-matched-stimulated four-photon mixing in silica-fiber waveguides," IEEE Journal of Quantum Electronics **11**(3), 100–103 (1975).

81. R. H. Stolen, M. A. Bösch, and C. Lin, "Phase matching in birefringent fibers," Optics Letters., **6**(5), 213–215 (1981).

82. A. Yariv, "Universal relations for coupling of optical power between microresonators and dielectric waveguides," Electronics Letters **36**(4), 321–322 (2000).

83. W. Bogaerts, P. De Heyn, T. Van Vaerenbergh, K. De Vos, S. Kumar Selvaraja, T. Claes, P. Dumon, P. Bienstman, D. Van Thourhout, and R. Baets, "Silicon microring resonators," Laser & Photon. Rev. **6**(1), 47–73 (2012).

84. P. Del'Haye, O. Arcizet, M. L. Gorodetsky, R. Holzwarth, and T. J. Kippenberg, "Frequency comb assisted diode laser spectroscopy for measurement of microcavity dispersion," Nature Photonics **3**(9), 529–533 (2009).

85. J. Liu, V. Brasch, M. H. P. Pfeiffer, A. Kordts, A. N. Kamel, H. Guo, M. Geiselmann, and T. J. Kippenberg, "Frequency-comb-assisted broadband precision spectroscopy with cascaded diode lasers," Opt. Lett., OL **41**(13), 3134–3137 (2016).

86. S.W. Huang, H. Liu, J. Yang, M. Yu, D.-L. Kwong, and C. W. Wong, "Smooth and flat phase-locked Kerr frequency comb generation by higher order mode suppression," Scientific Reports **6**(1), 26255 (2016).

87. J. Li, H. Lee, K. Y. Yang, and K. J. Vahala, "Sideband spectroscopy and dispersion measurement in microcavities," Opt. Express, **20**(24), 26337–26344 (2012).

88. H. C. Frankis, "Low-loss tellurium oxide devices integrated on silicon and silicon nitride photonic circuit platforms," PhD Thesis, McMaster University, MacSphere (2021).

89. A. L. Gaeta, M. Lipson, and T. J. Kippenberg, "Photonic-chip-based frequency combs," Nature Photon **13**(3), 158–169 (2019).

90. J. M. Dudley, G. Genty, and S. Coen, "Supercontinuum generation in photonic crystal fiber," Rev. Mod. Phys. **78**(4), 1135–1184 (2006).

91. L. Yin, Q. Lin, and G. P. Agrawal, "Soliton fission and supercontinuum generation in silicon waveguides," Opt. Lett., **32**(4), 391–393 (2007).

92. C. Lafforgue, M. Montesinos-Ballester, T.-T.-D. Dinh, X. L. Roux, E. Cassan, D. Marris-Morini, C. Alonso-Ramos, L. Vivien, and L. Vivien, "Supercontinuum generation in silicon photonics platforms," Photon. Res., **10**(3), A43–A56 (2022).

93. R. Halir, Y. Okawachi, J. S. Levy, M. A. Foster, M. Lipson, and A. L. Gaeta, "Ultrabroadband supercontinuum generation in a CMOS-compatible platform," Opt. Lett., **37**(10), 1685–1687 (2012).

94. P. Del'Haye, A. Schliesser, O. Arcizet, T. Wilken, R. Holzwarth, and T. J. Kippenberg, "Optical frequency comb generation from a monolithic microresonator," Nature **450**(7173), 1214–1217 (2007).

95. J. S. Levy, A. Gondarenko, M. A. Foster, A. C. Turner-Foster, A. L. Gaeta, and M. Lipson, "CMOS-compatible multiple-wavelength oscillator for on-chip optical interconnects," Nature Photon **4**(1), 37–40 (2010).

96. L. Razzari, D. Duchesne, M. Ferrera, R. Morandotti, S. Chu, B. E. Little, and D. J. Moss, "CMOS-compatible integrated optical hyper-parametric oscillator," Nature Photon **4**(1), 41–45 (2010).

97. L. A. Lugiato and R. Lefever, "Spatial Dissipative Structures in Passive Optical Systems," Phys. Rev. Lett. **58**(21), 2209–2211 (1987).

98. S. Coen, H. G. Randle, T. Sylvestre, and M. Erkintalo, "Modeling of octave-spanning Kerr frequency combs using a generalized mean-field Lugiato–Lefever model," Opt. Lett., **38**(1), 37–39 (2013).

99. Y. K. Chembo and C. R. Menyuk, "Spatiotemporal Lugiato-Lefever formalism for Kerr-comb generation in whispering-gallery-mode resonators," Phys. Rev. A **87**(5), 053852 (2013).

100. T. Herr, K. Hartinger, J. Riemensberger, C. Y. Wang, E. Gavartin, R. Holzwarth, M. L. Gorodetsky, and T. J. Kippenberg, "Universal formation dynamics and noise of Kerr-frequency combs in microresonators," Nature Photonics **6**(7), 480–487 (2012).

101. T. Herr, V. Brasch, J. D. Jost, C. Y. Wang, N. M. Kondratiev, M. L. Gorodetsky, and T. J. Kippenberg, "Temporal solitons in optical microresonators," Nature Photonics **8**(2), 145–152 (2014).

102. S. Mukamel, *Principles of Nonlinear Optical Spectroscopy*, Oxford University Press (1995).

103. K. Shi, S. H. Nam, P. Li, S. Yin, and Z. Liu, "Wavelength division multiplexed confocal microscopy using supercontinuum," Optics Communications **263**(2), 156–162 (2006).

104. D. R. Carlson, D. D. Hickstein, A. Lind, J. B. Olson, R. W. Fox, R. C. Brown, A. D. Ludlow, Q. Li, D. Westly, H. Leopardi, T. M. Fortier, K. Srinivasan, S. A. Diddams, and S. B. Papp, "Photonic-Chip Supercontinuum with Tailored Spectra for Counting Optical Frequencies," Phys. Rev. Applied **8**(1), 014027 (2017).

105. G. Humbert, W. J. Wadsworth, S. G. Leon-Saval, J. C. Knight, T. A. Birks, P. S. J. Russell, M. J. Lederer, D. Kopf, K. Wiesauer, E. I. Breuer, and D. Stifter, "Supercontinuum generation system for optical coherence tomography based on tapered photonic crystal fibre," Opt. Express, **14**(4), 1596–1603 (2006).

106. N. M. Israelsen, C. R. Petersen, A. Barh, D. Jain, M. Jensen, G. Hannesschläger, P. Tidemand-Lichtenberg, C. Pedersen, A. Podoleanu, and O. Bang, "Real-time high-resolution mid-infrared optical coherence tomography," Light Sci Appl **8**(1), 11 (2019).

107. Z. Wang, C. Li, M. Zhou, H. Zhang, W. He, W. Li, and Y. Qiu, "Recent development of hyperspectral LiDAR using supercontinuum laser," in *Hyperspectral Remote Sensing Applications and Environmental Monitoring and Safety Testing Technology*, SPIE.,**10156**, 141–146 (2016).

108. G. Méjean, J. Kasparian, E. Salmon, J. Yu, J.-P. Wolf, R. Bourayou, R. Sauerbrey, M. Rodriguez, L. Wöste, H. Lehmann, B. Stecklum, U. Laux, J. Eislöffel, A. Scholz, and A. P. Hatzes, "Towards a supercontinuum-based infrared lidar," Appl Phys B **77**(2), 357–359 (2003).

109. A. Saleh, A. Aalto, P. Ryczkowski, G. Genty, and J. Toivonen, "Short-range supercontinuum-based lidar for temperature profiling," Opt. Lett., **44**(17), 4223–4226 (2019).

110. R. R. Alfano et al., "Supercontinuum in Wavelength Division Multiplex Telecommunication," in *The Supercontinuum Laser Source: Fundamentals with Updated References*, Springer, (2006).

111. C. Ware, S. Cordette, C. Lepers, I. Fsaifes, B. Kibler, C. Finot, and G. Millot, "Spectral Slicing of a Supercontinuum Source for WDM/DS-OCDMA Application," in *2008 10th Anniversary International Conference on Transparent Optical Networks*, **4**, pp. 158–161(2008).

112. T. Ohara, H. Takara, T. Yamamoto, H. Masuda, T. Morioka, M. Abe, and H. Takahashi, "Over-1000-channel ultradense WDM transmission with supercontinuum multicarrier source," Journal of Lightwave Technology **24**(6), 2311–2317 (2006).

113. I. Coddington, N. Newbury, and W. Swann, "Dual-comb spectroscopy," Optica, **3**(4), 414–426 (2016).

114. A. Dutt, C. Joshi, X. Ji, J. Cardenas, Y. Okawachi, K. Luke, A. L. Gaeta, and M. Lipson, "On-chip dual-comb source for spectroscopy," Science Advances **4**(3), e1701858 (2018).

115. A. N. Willner, P. Liao, K. Zou, Y. Cao, A. Kordts, M. Karpov, M. H. P. Pfeiffer, A. Almaiman, A. Fallahpour, F. Alishahi, K. Manukyan, M. Tur, T. J. Kippenberg, and A. E. Willner, "Scalable and reconfigurable optical tapped-delay-line for multichannel equalization and correlation using nonlinear wave mixing and a Kerr frequency comb," Opt. Lett.,**43**(22), 5563–5566 (2018).

116. P. Marin-Palomo, J. N. Kemal, M. Karpov, A. Kordts, J. Pfeifle, M. H. P. Pfeiffer, P. Trocha, S. Wolf, V. Brasch, M. H. Anderson, R. Rosenberger, K. Vijayan, W. Freude, T. J. Kippenberg, and C. Koos, "Microresonator-based solitons for massively parallel coherent optical communications," Nature **546**(7657), 274–279 (2017).

117. A. Fülöp, M. Mazur, A. Lorences-Riesgo, T. A. Eriksson, P.-H. Wang, Y. Xuan, D. E. Leaird, M. Qi, P. A. Andrekson, A. M. Weiner, and V. Torres-Company, "Long-haul coherent communications using microresonator-based frequency combs," Opt. Express, **25**(22), 26678–26688 (2017).

118. P. Trocha, M. Karpov, D. Ganin, M. H. P. Pfeiffer, A. Kordts, S. Wolf, J. Krockenberger, P. Marin-Palomo, C. Weimann, S. Randel, W. Freude, T. J.

Kippenberg, and C. Koos, "Ultrafast optical ranging using microresonator soliton frequency combs," Science **359**(6378), 887–891 (2018).

119. M.-G. Suh and K. J. Vahala, "Soliton microcomb range measurement," Science **359**(6378), 884–887 (2018).

120. S. B. Papp, K. Beha, P. Del'Haye, F. Quinlan, H. Lee, K. J. Vahala, and S. A. Diddams, "Microresonator frequency comb optical clock," Optica, OPTICA **1**(1), 10–14 (2014).

121. D. T. Spencer, T. Drake, T. C. Briles, J. Stone, L. C. Sinclair, C. Fredrick, Q. Li, D. Westly, B. R. Ilic, A. Bluestone, N. Volet, T. Komljenovic, L. Chang, S. H. Lee, D. Y. Oh, M.-G. Suh, K. Y. Yang, M. H. P. Pfeiffer, T. J. Kippenberg, E. Norberg, L. Theogarajan, K. Vahala, N. R. Newbury, K. Srinivasan, J. E. Bowers, S. A. Diddams, and S. B. Papp, "An optical-frequency synthesizer using integrated photonics," Nature **557**(7703), 81–85 (2018).

122. J. Wu, X. Xu, T. G. Nguyen, S. T. Chu, B. E. Little, R. Morandotti, A. Mitchell, and D. J. Moss, "RF Photonics: An Optical Microcombs' Perspective," IEEE Journal of Selected Topics in Quantum Electronics **24**(4), 1–20 (2018).

123. H. M. Pask, P. Dekker, R. P. Mildren, D. J. Spence, and J. A. Piper, "Wavelength-versatile visible and UV sources based on crystalline Raman lasers," Progress in Quantum Electronics **32**(3), 121–158 (2008).

124. R. H. Stolen, "Fundamentals of Raman Amplification in Fibers," in *Raman Amplifiers for Telecommunications 1: Physical Principles*, Springer Series in Optical Sciences, Springer, (2004).

125. T. N. Nielsen, "Raman amplifiers in WDM systems," *IEEE Lasers and Electro-Optics Society 1999 Annual Meeting (Cat. No.99CH37009)* **2**, 471–472 (1999).

126. M. N. Islam, "Raman amplifiers for telecommunications," IEEE Journal of Selected Topics in Quantum Electronics **8**(3), 548–559 (2002).

127. J. H. Lee, Y. M. Chang, Y.-G. Han, H. Chung, S. H. Kim, and S. B. Lee, "Raman amplifier-based long-distance remote, strain and temperature sensing system using an erbium-doped fiber and a fiber Bragg grating," Opt. Express, **12**(15), 3515–3520 (2004).

128. S. Bakhtiari Gorajoobi, A. Masoudi, and G. Brambilla, "Long Range Raman-Amplified Distributed Acoustic Sensor Based on Spontaneous Brillouin Scattering for Large Strain Sensing," Sensors **22**(5), 2047 (2022).

129. A. Malakzadeh, R. Pashaie, and M. Mansoursamaei, "150 km φ-OTDR sensor based on erbium and Raman amplifiers," Opt Quant Electron **52**(6), 326 (2020).

130. L. Moreaux, O. Sandre, S. Charpak, M. Blanchard-Desce, and J. Mertz, "Coherent scattering in multi-harmonic light microscopy.," Biophys J **80**(3), 1568–1574 (2001).

131. M. Rehberg, F. Krombach, U. Pohl, and S. Dietzel, "Signal improvement in multiphoton microscopy by reflection with simple mirrors near the sample," Journal of Biomedical Optics **15**(2), 026017 (2010).

132. S. Dietzel, J. Pircher, A. K. Nekolla, M. Gull, A. W. Brändli, U. Pohl, and M. Rehberg, "Label-Free Determination of Hemodynamic Parameters in the Microcirculaton with Third Harmonic Generation Microscopy," PLoS One **9**(6), e99615 (2014).

133. M. Asano, S. Komori, R. Ikuta, N. Imoto, Ş. K. Özdemir, and T. Yamamoto, "Visible light emission from a silica microbottle resonator by second- and third-harmonic generation," Opt. Lett., **41**(24), 5793–5796 (2016).

134. S. Sederberg and A. Y. Elezzabi, "Coherent Visible-Light-Generation Enhancement in Silicon-Based Nanoplasmonic Waveguides via Third-Harmonic Conversion," Phys. Rev. Lett. **114**(22), 227401 (2015).

135. A. Ishizawa, A. Ishizawa, K. Kawashima, K. Kawashima, K. Kawashima, R. Kou, R. Kou, X. Xu, T. Tsuchizawa, T. Aihara, K. Yoshida, K. Yoshida, T. Nishikawa, K. Hitachi, G. Cong, N. Yamamoto, K. Yamada, and K. Oguri, "Direct f-3f self-referencing using an integrated silicon-nitride waveguide," Opt. Express, **30**(4), 5265–5273 (2022).

136. K. Hitachi, A. Ishizawa, T. Nishikawa, M. Asobe, and T. Sogawa, "Carrier-envelope offset locking with a 2f-to-3f self-referencing interferometer using a dual-pitch PPLN ridge waveguide," Opt. Express, **22**(2), 1629–1635 (2014).

137. D. E. Chang, V. Vuletić, and M. D. Lukin, "Quantum nonlinear optics — photon by photon," Nature Photon **8**(9), 685–694 (2014).

138. G. Moody, V. J. Sorger, D. J. Blumenthal, P. W. Juodawlkis, W. Loh, C. Sorace-Agaskar, A. E. Jones, K. C. Balram, J. C. F. Matthews, A. Laing, M. Davanco, L. Chang, J. E. Bowers, N. Quack, C. Galland, I. Aharonovich, M. A. Wolff, C. Schuck, N. Sinclair, M. Lončar, T. Komljenovic, D. Weld, S. Mookherjea, S. Buckley, M. Radulaski, S. Reitzenstein, B. Pingault, B. Machielse, D. Mukhopadhyay, A. Akimov, A. Zheltikov, G. S. Agarwal, K. Srinivasan, J. Lu, H. X. Tang, W. Jiang, T. P. McKenna, A. H. Safavi-Naeini, S. Steinhauer, A. W. Elshaari, V. Zwiller, P.

S. Davids, N. Martinez, M. Gehl, J. Chiaverini, K. K. Mehta, J. Romero, N. B. Lingaraju, A. M. Weiner, D. Peace, R. Cernansky, M. Lobino, E. Diamanti, L. T. Vidarte, and R. M. Camacho, "2022 Roadmap on integrated quantum photonics," J. Phys. Photonics **4**(1), 012501 (2022).

139. A. Virga, C. Ferrante, G. Batignani, D. De Fazio, A. D. G. Nunn, A. C. Ferrari, G. Cerullo, and T. Scopigno, "Coherent anti-Stokes Raman spectroscopy of single and multi-layer graphene," Nat Commun **10**(1), 3658 (2019).

140. S. Li, Y. Li, R. Yi, L. Liu, and J. Qu, "Coherent Anti-Stokes Raman Scattering Microscopy and Its Applications," Frontiers in Physics **8**, (2020).

141. Guang S. He, "Optical Phase Conjugation", Nonlinear Optics and Photonics, Chapter 8, Oxford Academic (2014)

142. D. T. H. Tan, A. M. Agarwal, and L. C. Kimerling, "Nonlinear photonic waveguides for on-chip optical pulse compression," Laser & Photonics Reviews **9**(3), 294–308 (2015).

143. A. M. Weiner, J. P. Heritage, and R. H. Stolen, "Self-phase modulation and optical pulse compression influenced by stimulated Raman scattering in fibers," J. Opt. Soc. Am. B, **5**(2), 364–372 (1988).

144. J. W. Choi, E. Sahin, B.-U. Sohn, G. F. R. Chen, D. K. T. Ng, A. M. Agarwal, L. C. Kimerling, and D. T. H. Tan, "High spectro-temporal compression on a nonlinear CMOS-chip," Light Sci Appl **10**(1), 130 (2021).

145. X. Lu, X. Lu, X. Lu, G. Moille, G. Moille, A. Rao, A. Rao, D. A. Westly, K. Srinivasan, and K. Srinivasan, "On-chip optical parametric oscillation into the visible: generating red, orange, yellow, and green from a near-infrared pump," Optica, **7**(10), 1417–1425 (2020).

146. W. Liang, A. A. Savchenkov, Z. Xie, J. F. McMillan, J. Burkhart, V. S. Ilchenko, C. W. Wong, A. B. Matsko, and L. Maleki, "Miniature multioctave light source based on a monolithic microcavity," Optica, **2**(1), 40–47 (2015).

147. N. L. B. Sayson, K. E. Webb, S. Coen, M. Erkintalo, and S. G. Murdoch, "Widely tunable optical parametric oscillation in a Kerr microresonator," Opt. Lett., **42**(24), 5190–5193 (2017).

148. M. A. Foster, A. C. Turner, J. E. Sharping, B. S. Schmidt, M. Lipson, and A. L. Gaeta, "Broad-band optical parametric gain on a silicon photonic chip," Nature **441**(7096), 960–963 (2006).

149. S. Kumar and M. Sen, "Low-power, high-performance, and small-footprint, single-pump optical parametric amplifier for photonic integrated circuits," Journal of Applied Physics **132**(12), 123106 (2022).

150. L. Ledezma, L. Ledezma, R. Sekine, Q. Guo, R. Nehra, S. Jahani, and A. Marandi, "Intense optical parametric amplification in dispersion-engineered nanophotonic lithium niobate waveguides," Optica, **9**(3), 303–308 (2022).

151. X. Liu, R. M. Osgood, Y. A. Vlasov, and W. M. J. Green, "Mid-infrared optical parametric amplifier using silicon nanophotonic waveguides," Nature Photonics **4**(8), 557–560 (2010).

152. G. Qin, A. Mori, and Y. Ohishi, "Brillouin lasing in a single-mode tellurite fiber," Opt. Lett., OL **32**(15), 2179–2181 (2007).

153. P. T. Rakich, E. Kittlaus, N. Otterstrom, and R. O. Behunin, "Brillouin lasers and amplifiers in silicon photonics," in *Integrated Optics: Devices, Materials, and Technologies XXII* (SPIE, 2018), **10535**, pp. 68–70.

154. A. Casas-Bedoya, B. Morrison, M. Pagani, D. Marpaung, and B. J. Eggleton, "Tunable narrowband microwave photonic filter created by stimulated Brillouin scattering from a silicon nanowire," Opt. Lett., **40**(17), 4154–4157 (2015).

155. D. Marpaung, B. Morrison, M. Pagani, R. Pant, D.-Y. Choi, B. Luther-Davies, S. J. Madden, and B. J. Eggleton, "Low-power, chip-based stimulated Brillouin scattering microwave photonic filter with ultrahigh selectivity," Optica, **2**(2), 76–83 (2015).

156. Q. Zhang, X. Han, X. Shao, Y. Wang, H. Jiang, W. Dong, and X. Zhang, "Stimulated Brillouin Scattering-Based Microwave Photonic Filter With a Narrow and High Selective Passband," IEEE Photonics Journal **14**(4), 1–7 (2022).

157. D. J. Blumenthal, R. Heideman, D. Geuzebroek, A. Leinse, and C. Roeloffzen, "Silicon Nitride in Silicon Photonics," Proceedings of the IEEE **106**(12), 2209–2231 (2018).

158. W. Stutius and W. Streifer, "Silicon nitride films on silicon for optical waveguides," Appl. Opt., **16**(12), 3218–3222 (1977).

159. M. Melchiorri, N. Daldosso, F. Sbrana, L. Pavesi, G. Pucker, C. Kompocholis, P. Bellutti, and A. Lui, "Propagation losses of silicon nitride waveguides in the near-infrared range," Appl. Phys. Lett. **86**(12), 121111 (2005).

160. K. Worhoff, E. Klein, G. Hussein, and A. Driessen, "Silicon oxynitride based photonics,"*10th Anniversary International Conference on Transparent Optical Networks*, **3**,266–269(2008).

161. P. Muñoz, J. D. Doménech, C. Domínguez, A. Sánchez, G. Micó, L. A. Bru, D. Pérez, and D. Pastor, "State of the art of Silicon Nitride photonics integration platforms," in *2017 19th International Conference on Transparent Optical Networks (ICTON)*, 1–4(2017).

162. T. Sharma, J. Wang, B. K. Kaushik, Z. Cheng, R. Kumar, Z. Wei, and X. Li, "Review of Recent Progress on Silicon Nitride-Based Photonic Integrated Circuits," IEEE Access **8**, 195436–195446 (2020).

163. S. Y. Siew, B. Li, F. Gao, H. Y. Zheng, W. Zhang, P. Guo, S. W. Xie, A. Song, B. Dong, L. W. Luo, C. Li, X. Luo, and G.-Q. Lo, "Review of Silicon Photonics Technology and Platform Development," J. Lightwave Technol.,**39**(13), 4374–4389 (2021).

164. D. J. Moss, R. Morandotti, A. L. Gaeta, and M. Lipson, "New CMOS-compatible platforms based on silicon nitride and Hydex for nonlinear optics," Nature Photon **7**(8), 597–607 (2013).

165. "J. D. B. Bradley, R. Wang, H. C. Frankis, D. B. Bonneville, K. Miarabbas Kiani, and H. M. Mbonde, "Silicon Nitride Integrated Optics," to appear in Integrated Optics: Recent Advances and Prospects, edited by Giancarlo C. Righini and Maurizio Ferrari, The Institution of Engineering and Technology, London, 1–50(2020).

166. J. F. Bauters, M. J. R. Heck, D. D. John, J. S. Barton, C. M. Bruinink, A. Leinse, R. G. Heideman, D. J. Blumenthal, and J. E. Bowers, "Planar waveguides with less than 0.1 dB/m propagation loss fabricated with wafer bonding," Opt. Express, **19**(24), 24090–24101 (2011).

167. M. H. P. Pfeiffer, A. Kordts, V. Brasch, M. Zervas, M. Geiselmann, J. D. Jost, and T. J. Kippenberg, "Photonic Damascene process for integrated high-Q microresonator based nonlinear photonics," Optica, **3**(1), 20–25 (2016).

168. K. Wu and A. W. Poon, "Stress-released Si_3N_4 fabrication process for dispersion-engineered integrated silicon photonics," Opt. Express, **28**(12), 17708–17722 (2020).

169. K. Luke, A. Dutt, C. B. Poitras, and M. Lipson, "Overcoming Si_3N_4 film stress limitations for high quality factor ring resonators," Opt. Express, **21**(19), 22829–22833 (2013).

170. H. El Dirani, M. Casale, S. Kerdiles, C. Socquet-Clerc, X. Letartre, C. Monat, and C. Sciancalepore, "Crack-Free Silicon-Nitride-on-Insulator Nonlinear Circuits for

Continuum Generation in the C-Band," IEEE Photonics Technology Letters **30**(4), 355–358 (2018).

171. R. M. Grootes, M. Dijkstra, Y. Klaver, D. Marpaung, and H. L. Offerhaus, "Crack barriers for thick SiN using dicing," Opt. Express, **30**(10), 16725–16733 (2022).

172. K. Luke, Y. Okawachi, M. R. E. Lamont, A. L. Gaeta, and M. Lipson, "Broadband mid-infrared frequency comb generation in a Si_3N_4 microresonator," Opt. Lett., **40**(21), 4823–4826 (2015).

173. J. P. Epping, M. Hoekman, R. Mateman, A. Leinse, R. G. Heideman, A. van Rees, P. J. M. van der Slot, C. J. Lee, and K.-J. Boller, "High confinement, high yield Si_3N_4 waveguides for nonlinear optical applications," Opt. Express, **23**(2), 642–648 (2015).

174. M. A. G. Porcel, F. Schepers, J. P. Epping, T. Hellwig, M. Hoekman, R. G. Heideman, P. J. M. van der Slot, C. J. Lee, R. Schmidt, R. Bratschitsch, C. Fallnich, and K.-J. Boller, "Two-octave spanning supercontinuum generation in stoichiometric silicon nitride waveguides pumped at telecom wavelengths," Opt. Express, **25**(2), 1542–1554 (2017).

175. J. P. Epping, T. Hellwig, M. Hoekman, R. Mateman, A. Leinse, R. G. Heideman, A. van Rees, P. J. M. van der Slot, C. J. Lee, C. Fallnich, and K.-J. Boller, "On-chip visible-to-infrared supercontinuum generation with more than 495 THz spectral bandwidth," Opt. Express, **23**(15), 19596–19604 (2015).

176. M. A. G. Porcel, J. P. Epping, M. Hoekman, P. van der Slot, and K.-J. Boller, "Second-harmonic generation in stoichiometric silicon nitride glass waveguides," in *2017 Conference on Lasers and Electro-Optics Europe & European Quantum Electronics Conference (CLEO/Europe-EQEC)* (2017).

177. M. A. G. Porcel, J. Mak, C. Taballione, V. K. Schermerhorn, J. P. Epping, P. J. M. van der Slot, and K.-J. Boller, "Photo-induced second-order nonlinearity in stoichiometric silicon nitride waveguides," Opt. Express, **25**(26), 33143–33159 (2017).

178. J. Mak, A. van Rees, Y. Fan, E. J. Klein, D. Geskus, P. J. M. van der Slot, and K.-J. Boller, "Integrated frequency comb laser with narrow intrinsic optical linewidth based on a dielectric waveguide feedback circuit," Opt. Express **27**(9), 13307 (2019).

179. H. Guo, C. Herkommer, A. Billat, D. Grassani, C. Zhang, M. H. P. Pfeiffer, W. Weng, C.-S. Brès, and T. J. Kippenberg, "Mid-infrared frequency comb via coherent dispersive wave generation in silicon nitride nanophotonic waveguides," Nature Photon **12**(6), 330–335 (2018).

180. B. Shen, L. Chang, J. Liu, H. Wang, Q.-F. Yang, C. Xiang, R. N. Wang, J. He, T. Liu, W. Xie, J. Guo, D. Kinghorn, L. Wu, Q.-X. Ji, T. J. Kippenberg, K. Vahala, and J. E. Bowers, "Integrated turnkey soliton microcombs," Nature **582**(7812), 365–369 (2020).

181. W. Weng, A. Kaszubowska-Anandarajah, J. He, P. D. Lakshmijayasimha, E. Lucas, J. Liu, P. M. Anandarajah, and T. J. Kippenberg, "Gain-switched semiconductor laser driven soliton microcombs," Nat Commun **12**(1), 1425 (2021).

182. Y. Qu, J. Wu, Y. Yang, Y. Zhang, Y. Liang, H. El Dirani, R. Crochemore, P. Demongodin, C. Sciancalepore, C. Grillet, C. Monat, B. Jia, and D. J. Moss, "Enhanced Four-Wave Mixing in Silicon Nitride Waveguides Integrated with 2D Layered Graphene Oxide Films," Advanced Optical Materials **8**(23), 2001048 (2020).

183. H. El Dirani, A. Kamel, M. Casale, S. Kerdiles, C. Monat, X. Letartre, M. Pu, L. K. Oxenløwe, K. Yvind, and C. Sciancalepore, "Annealing-free Si3N4 frequency combs for monolithic integration with Si photonics," Appl. Phys. Lett. **113**(8), 081102 (2018).

184. S. Boust, H. E. Dirani, F. Duport, L. Youssef, Y. Robert, A. Larrue, C. Petit-Etienne, E. Vinet, S. Kerdiles, E. Parfon, M. Faugeron, M. Vallet, C. Sciancalepore, and F. van Dijk, "Compact optical frequency comb source based on a DFB butt-coupled to a silicon nitride microring," in *International Topical Meeting on Microwave Photonics (MWP)* (2019).

185. H. Zia, K. Ye, Y. Klaver, D. Marpaung, and K.-J. Boller, "Ultra-Efficient On-Chip Supercontinuum Generation from Sign-Alternating-Dispersion Waveguides," arXiv 2205.06227 (2022).

186. M. Gao, N. M. Lüpken, K.-J. Boller, K.-J. Boller, and C. Fallnich, "Optical Parametric Oscillator Based on Silicon Nitride Waveguides," in *Optica Advanced Photonics Congress, Paper JTh4A.3* (2022)

187. LioniX International, "Custom MEMS and Photonic Integrated Circuits," https://www.lionix-international.com/.

188. IMEC, "Silicon nitride-based photonics" https://www.imec-int.com/en/what-we-offer/development/system-development-technologies/Integrated-photonics/silicon-nitride-based-photonics.

189. Advanced Micro Foundry "Silicon Nitride on SOI platform," https://www.advmf.com/silicon-nitride-on-soi-platform/

190. "Applied Nanotools Inc.," https://www.appliednt.com/nanosoi-fabrication-service/ (

191. V. A. G. Rivera and D. Manzani, eds., *Technological Advances in Tellurite Glasses: Properties, Processing, and Applications*, Springer Series in Materials Science, Springer International Publishing (2017)

192. S.-H. Kim, T. Yoko, and S. Sakka, "Linear and Nonlinear Optical Properties of TeO2 Glass," Journal of the American Ceramic Society **76**(10), 2486–2490 (1993).

193. R. Stegeman, "Direct Nonlinear Optics Measurements Of Raman Gain In Bulk Glasses And Estimates Of Fiber Performance," Electronic Theses and Dissertations (2006).

194. S. J. Madden and K. T. Vu, "High-Performance Integrated Optics with Tellurite Glasses: Status and Prospects," International Journal of Applied Glass Science **3**(4), 289–298 (2012).

195. E. Chierici, M. C. Didavide, A. Moro, O. Rossotto, and L. Tallone, "Direct writing of channel waveguide on a tellurite glass using a focused ultraviolet laser beam," in *Proceedings of 2002 IEEE/LEOS Workshop on Fibre and Optical Passive Components (Cat.No.02EX595)* (2002), pp. 24–28.

196. Y. Tokuda, M. Saito, M. Takahashi, K. Yamada, W. Watanabe, K. Itoh, and T. Yoko, "Waveguide formation in niobium tellurite glasses by pico- and femtosecond laser pulses," Journal of Non-Crystalline Solids **326–327**, 472–475 (2003).

197. P. Nandi, G. Jose, C. Jayakrishnan, S. Debbarma, K. Chalapathi, K. Alti, A. K. Dharmadhikari, J. A. Dharmadhikari, and D. Mathur, "Femtosecond laser written channel waveguides in tellurite glass," Opt. Express, **14**(25), 12145–12150 (2006).

198. T. T. Fernandez, G. D. Valle, R. Osellame, G. Jose, N. Chiodo, A. Jha, and P. Laporta, "Active waveguides written by femtosecond laser irradiation in an erbium-doped phospho-tellurite glass," Opt. Express, **16**(19), 15198–15205 (2008).

199. G. N. Conti, V. K. Tikhomirov, M. Bettinelli, S. Berneschi, M. Brenci, B. Chen, S. Pelli, A. Speghini, A. B. Seddon, and G. C. Righini, "Characterization of ion-exchanged waveguides in tungsten tellurite and zinc tellurite Er^{3+}-doped glasses," **42**(10), 2805–2811 (2003).

200. G. N. Conti, S. Berneschi, M. Bettinelli, M. Brenci, B. Chen, S. Pelli, A. Speghini, and G. C. Righini, "Rare-earth doped tungsten tellurite glasses and waveguides: fabrication and characterization," Journal of Non-Crystalline Solids **345–346**, 343–348 (2004).

201. Y. Ding, S. Jiang, T. Luo, Y. Hu, and N. Peyghambarian, "Optical waveguides prepared in Er3+-doped tellurite glass by Ag+-Na+ ion exchange," in *Rare-Earth-Doped Materials and Devices V*, SPIE, **4282**, 23–30(2001).

202. S. Berneschi, M. Brenci, G. Nunzi Conti, S. Pelli, G. C. Righini, I. Bányász, A. Watterich, N. Q. Khanh, M. Fried, and F. Pászti, "Channel waveguides fabrication in Er $^{3+}$-doped tellurite glass by ion beam irradiation," in Y. Sidorin and C. A. Waechter, eds. (2007), p. 647509.

203. S. M. Pietralunga, M. Lanata, M. Ferè, D. Piccinin, G. Cusmai, M. Torregiani, and M. Martinelli, "High-contrast waveguides in sputtered pure TeO_2 glass thin films," Opt. Express, **16**(26), 21662–21670 (2008).

204. S. J. Madden and K. T. Vu, "Very low loss reactively ion etched Tellurium Dioxide planar rib waveguides for linear and non-linear optics," Opt. Express, **17**(20), 17645–17651 (2009).

205. K. Vu, S. Farahani, and S. Madden, "980nm pumped erbium doped tellurium oxide planar rib waveguide laser and amplifier with gain in S, C and L band," Opt. Express, **23**(2), 747–755 (2015).

206. K. Vu and S. Madden, "Tellurium dioxide Erbium doped planar rib waveguide amplifiers with net gain and 2.8dB/cm internal gain," Opt. Express, **18**(18), 19192–19200 (2010).

207. H. C. Frankis, K. M. Kiani, D. B. Bonneville, C. Zhang, S. Norris, R. Mateman, A. Leinse, N. D. Bassim, A. P. Knights, and J. D. B. Bradley, "Low-loss TeO_2-coated Si_3N_4 waveguides for application in photonic integrated circuits," Opt. Express, **27**(9), 12529–12540 (2019).

208. H. C. Frankis, K. M. Kiani, D. Su, R. Mateman, A. Leinse, and J. D. B. Bradley, "High-Q tellurium-oxide-coated silicon nitride microring resonators," Opt. Lett., **44**(1), 118–121 (2019).

209. H. C. Frankis, H. M. Mbonde, D. B. Bonneville, C. Zhang, R. Mateman, A. Leinse, and J. D. B. Bradley, "Erbium-doped TeO_2-coated Si_3N_4 waveguide amplifiers with 5 dB net gain," Photon. Res., **8**(2), 127–134 (2020).

210. K. M. Kiani, H. C. Frankis, H. M. Mbonde, R. Mateman, A. Leinse, A. P. Knights, and J. D. B. Bradley, "Thulium-doped tellurium oxide waveguide amplifier with 7.6 dB net gain on a silicon nitride chip," Opt. Lett., **44**(23), 5788–5791 (2019).

211. K. M. Kiani, H. C. Frankis, R. Mateman, A. Leinse, A. P. Knights, and J. D. B. Bradley, "Thulium-doped tellurium oxide microring lasers integrated on a low-loss silicon nitride platform," Opt. Mater. Express, **11**(11), 3656–3665 (2021).

212. N. Singh, H. M. Mbonde, H. C. Frankis, E. Ippen, J. D. B. Bradley, J. D. B. Bradley, and F. X. Kärtner, "Nonlinear silicon photonics on CMOS-compatible tellurium oxide," Photon. Res., **8**(12), 1904–1909 (2020).

213. K. M. Kiani, H. M. Mbonde, H. C. Frankis, R. Mateman, A. Leinse, A. P. Knights, and J. D. B. Bradley, "Four-wave mixing in high-Q tellurium-oxide-coated silicon nitride microring resonators," OSA Continuum, **3**(12), 3497–3507 (2020).

214. I. H. Malitson, "Interspecimen Comparison of the Refractive Index of Fused Silica" J. Opt. Soc. Am., **55**(10), 1205–1209 (1965).

215. A. Boskovic, S. V. Chernikov, J. R. Taylor, L. Gruner-Nielsen, and O. A. Levring, "Direct continuous-wave measurement of n_2 in various types of telecommunication fiber at 1.55 μm," Opt. Lett., **21**(24), 1966–1968 (1996).

216. F. L. Galeener, J. C. Mikkelsen, R. H. Geils, and W. J. Mosby, "The relative Raman cross sections of vitreous SiO_2, GeO_2, B_2O_3, and P_2O_5," Appl. Phys. Lett. **32**(1), 34–36 (1978).

217. K. Ikeda, R. E. Saperstein, N. Alic, and Y. Fainman, "Thermal and Kerr nonlinear properties of plasma-deposited silicon nitride/silicon dioxide waveguides," Opt. Express, **16**(17), 12987–12994 (2008).

218. S. M. Hendrickson, A. C. Foster, R. M. Camacho, and B. D. Clader, "Integrated nonlinear photonics: emerging applications and ongoing challenges [Invited]," Journal of the Optical Society of America B, **31**(12), 3193 (2014).

219. S. Romero-García, F. Merget, F. Zhong, H. Finkelstein, and J. Witzens, "Silicon nitride CMOS-compatible platform for integrated photonics applications at visible wavelengths," Optics Express **21**(12), 14036 (2013).

220. Y. Huang, J. Song, X. Luo, T.-Y. Liow, and G.-Q. Lo, "CMOS compatible monolithic multi-layer Si_3N_4-on-SOI platform for low-loss high performance silicon photonics dense integration," Optics Express **22**(18), 21859 (2014).

221. D. J. Moss, R. Morandotti, A. L. Gaeta, and M. Lipson, "New CMOS-compatible platforms based on silicon nitride and Hydex for nonlinear optics," Nature Photonics **7**(8), 597–607 (2013).

222. D. T. H. Tan, K. J. A. Ooi, and D. K. T. Ng, "Nonlinear optics on silicon-rich nitride—a high nonlinear figure of merit CMOS platform [Invited]," Photonics Research **6**(5), B50 (2018).

223. M. A. G. Porcel, F. Schepers, J. P. Epping, T. Hellwig, M. Hoekman, R. G. Heideman, P. J. M. van der Slot, C. J. Lee, R. Schmidt, R. Bratschitsch, C. Fallnich, and K.-J. Boller, "Two-octave spanning supercontinuum generation in stoichiometric silicon nitride waveguides pumped at telecom wavelengths," Optics Express **25**(2), 1542 (2017).

224. J. M. Chávez Boggio, A. Ortega Moñux, D. Modotto, T. Fremberg, D. Bodenmüller, D. Giannone, M. M. Roth, T. Hansson, S. Wabnitz, E. Silvestre, and L. Zimmermann, "Dispersion-optimized multicladding silicon nitride waveguides for nonlinear frequency generation from ultraviolet to mid-infrared," Journal of the Optical Society of America B **33**(11), 2402 (2016).

225. T. J. Kippenberg, A. L. Gaeta, M. Lipson, and M. L. Gorodetsky, "Dissipative Kerr solitons in optical microresonators," Science **361**(6402), eaan8083 (2018).

226. A. C. Turner, C. Manolatou, B. S. Schmidt, M. Lipson, M. A. Foster, J. E. Sharping, and A. L. Gaeta, "Tailored anomalous group-velocity dispersion in silicon channel waveguides," Optics Express **14**(10), 4357 (2006).

227. M. H. P. Pfeiffer, J. Liu, T. Morais, B. Ghadiani, and T. J. Kippenberg, "Photonic Damascene process with reflow step for ultra-smooth Si_3N_4 waveguides," in *Conference on Lasers and Electro-Optics* (OSA, 2018), p. STh1I.1.

228. H. El Dirani, M. Casale, S. Kerdiles, C. Socquet-Clerc, X. Letartre, C. Monat, and C. Sciancalepore, "Crack-free silicon-nitride-on-insulator nonlinear circuits for continuum generation in the c-band," IEEE Photonics Technology Letters **30**(4), 355–358 (2018).

229. S. J. Madden and K. T. Vu, "Very low loss reactively ion etched Tellurium Dioxide planar rib waveguides for linear and non-linear optics," Optics Express **17**(20), 17645 (2009).

230. S. M. Pietralunga, M. Lanata, M. Feré, D. Piccinin, G. Cusmai, M. Torregiani, and M. Martinelli, "High-contrast waveguides in sputtered pure TeO_2 glass thin films," Optics Express **16**(26), 21662 (2008).

231. H. C. Frankis, K. M. Kiani, D. Su, R. Mateman, A. Leinse, and J. D. B. Bradley, "High-Q tellurium-oxide-coated silicon nitride microring resonators," Optics Letters **44**(1), 118 (2019).

232. K. Luke, Y. Okawachi, M. R. E. Lamont, A. L. Gaeta, and M. Lipson, "Broadband mid-infrared frequency comb generation in a Si_3N_4 microresonator," Optics Letters **40**(21), 4823 (2015).

233. K. Ikeda, R. E. Saperstein, N. Alic, and Y. Fainman, "Thermal and Kerr nonlinear properties of plasma-deposited silicon nitride/ silicon dioxide waveguides," Optics Express **16**(17), 12987 (2008).

234. S.-H. Kim, T. Yoko, and S. Sakka, "Linear and Nonlinear Optical Properties of TeO2 Glass," Journal of the American Ceramic Society **76**(10), 2486–2490 (1993).

235. A. Berthereau, Y. Le Luyer, R. Olazcuaga, G. Le Flem, M. Couzi, L. Canioni, P. Segonds, L. Sarger, and A. Ducasse, "Nonlinear optical properties of some tellurium (IV) oxide glasses," Materials Research Bulletin **29**(9), 933–941 (1994).

236. S.-H. Kim and T. Yoko, "Nonlinear Optical Properties of TeO_2-Based Glasses: MOx-TeO_2 (M = Sc, Ti, V, Nb, Mo, Ta, and W) Binary Glasses," Journal of the American Ceramic Society **78**(4), 1061–1065 (1995).

237. R. Jose, "Higher Nonlinear Indices, Raman Gain Coefficients, and Bandwidths in the TeO_2-ZnO-Nb_2O_5-MoO_3 Quaternary Glass System Photovoltaics View project Battery super capacitor hybrid View project," (2007).

238. F. Eroni. P. dos Santos, F. C. Fávero, A. S. L. Gomes, J. Xing, Q. Chen, M. Fokine, and I. C. S. Carvalho, "Evaluation of the third-order nonlinear optical properties of tellurite glasses by thermally managed eclipse Z-scan," Journal of Applied Physics **105**(2), 024512 (2009).

239. G. Yankov, I. Stefanov, K. Dimitrov, I. Piroeva, L. T. Dimowa, M. P. Tarassov, B. L. Shivachev, H. Yoneda, and T. Petrov, "Measurement of nonlinear refractive index and multiphoton absorption by the subpicosecond *z* -scan method of tellurite multicomponent glassy matrixes having nonlinear susceptibility," Physica Scripta **T157**, 014026 (2013).

240. S. Manning, H. Ebendorff-Heidepriem, and T. M. Monro, "Ternary tellurite glasses for the fabrication of nonlinear optical fibres," Optical Materials Express **2**(2), 140 (2012).

241. H. Nasu, J. Matsuoka, and K. Kamiya, "Second- and third-order optical non-linearity of homogeneous glasses," Journal of Non-Crystalline Solids **178**, 23–30 (1994).

242. R. Stegeman, L. Jankovic, H. Kim, C. Rivero, G. I. Stegeman, K. Richardson, P. Delfyett, Y. Guo, A. Schulte, and T. Cardinal, "Tellurite glasses with peak absolute

Raman gain coefficients up to 30 times that of fused silica.," Optics letters **28**(13), 1126–1128 (2003).

243. X. Feng, J. Shi, M. Segura, N. M. White, P. Kannan, L. Calvez, X. Zhang, L. Brilland, and W. H. Loh, "Towards Water-Free Tellurite Glass Fiber for 2-5 μm Nonlinear Applications," **1**, 70–81 (2013).

244. J. M. Chavez Boggio, D. Bodenmüller, T. Fremberg, R. Haynes, M. M. Roth, R. Eisermann, M. Lisker, L. Zimmermann, and M. Böhm, "Dispersion engineered silicon nitride waveguides by geometrical and refractive-index optimization," Journal of the Optical Society of America B **31**(11), 2846 (2014).

245. Y. Li, J. Li, Y. Huo, M. Chen, S. Yang, and H. Chen, "Spatial-mode-coupling-based dispersion engineering for integrated optical waveguide," Optics Express **26**(3), 2807 (2018).

246. J. P. Epping, M. Hoekman, R. Mateman, A. Leinse, R. G. Heideman, A. van Rees, P. J. M. van der Slot, C. J. Lee, and K.-J. Boller, "High confinement, high yield Si_3N_4 waveguides for nonlinear optical application," Opt. Express **23**, 642-648 (2015).

247. M. A. Foster, K. D. Moll, and A. L. Gaeta, "Optimal waveguide dimensions for nonlinear interactions," Optics Express **12**(13), 2880 (2004).

248. W. D. Sacher, J. C. Mikkelsen, Y. Huang, J. C. C. Mak, Z. Yong, X. Luo, Y. Li, P. Dumais, J. Jiang, D. Goodwill, E. Bernier, P. G.-Q. Lo, and J. K. S. Poon, "Monolithically Integrated Multilayer Silicon Nitride-on-Silicon Waveguide Platforms for 3-D Photonic Circuits and Devices," Proceedings of the IEEE **106**(12), 2232–2245 (2018).

249. W. D. Sacher, Y. Huang, G.-Q. Lo, and J. K. S. Poon, "Multilayer Silicon Nitride-on-Silicon Integrated Photonic Platforms and Devices," J. Lightwave Technol., JLT **33**(4), 901–910 (2015).

250. Y. Liang, J. Zhou, Z. Liu, H. Zhang, Z. Fang, Y. Zhou, D. Yin, J. Lin, J. Yu, R. Wu, M. Wang, and Y. Cheng, "A high-gain cladded waveguide amplifier on erbium doped thin-film lithium niobate fabricated using photolithography assisted chemo-mechanical etching," Nanophotonics **11**(5), 1033–1040 (2022).

251. Q. Luo, C. Yang, R. Zhang, Z. Hao, D. Zheng, H. Liu, X. Yu, F. Gao, F. Bo, F. Bo, F. Bo, Y. Kong, Y. Kong, G. Zhang, G. Zhang, G. Zhang, J. Xu, J. Xu, and J. Xu, "On-chip erbium-doped lithium niobate microring lasers," Opt. Lett., **46**(13), 3275–3278 (2021).

252. J. Zhou, Y. Liang, Z. Liu, W. Chu, H. Zhang, D. Yin, Z. Fang, R. Wu, J. Zhang, W. Chen, Z. Wang, Y. Zhou, M. Wang, and Y. Cheng, "On-Chip Integrated Waveguide Amplifiers on Erbium-Doped Thin-Film Lithium Niobate on Insulator," Laser & Photonics Reviews **15**(8), 2100030 (2021).

253. Y. Liu, Z. Qiu, X. Ji, A. Lukashchuk, J. He, J. Riemensberger, M. Hafermann, R. N. Wang, J. Liu, C. Ronning, and T. J. Kippenberg, "A photonic integrated circuit–based erbium-doped amplifier," Science **376**(6599), 1309–1313 (2022).

254. M. Kumagai, N. Uchiyama, E. Ohmura, R. Sugiura, K. Atsumi, and K. Fukumitsu, "Advanced dicing technology for semiconductor wafer -Stealth Dicing," in *2006 IEEE International Symposium on Semiconductor Manufacturing* (2006)

255. S. Fujii and T. Tanabe, "Dispersion engineering and measurement of whispering gallery mode microresonator for Kerr frequency comb generation," Nanophotonics **9**(5), 1087–1104 (2020).

256. Y. Xuan, Y. Liu, L. T. Varghese, A. J. Metcalf, X. Xue, P.-H. Wang, K. Han, J. A. Jaramillo-Villegas, A. A. Noman, C. Wang, S. Kim, M. Teng, Y. J. Lee, B. Niu, L. Fan, J. Wang, D. E. Leaird, A. M. Weiner, and M. Qi, "High-Q silicon nitride microresonators exhibiting low-power frequency comb initiation," Optica, **3**(11), 1171–1180 (2016).

257. K. Miarabbas Kiani, H. C. Frankis, C. M. Naraine, D. B. Bonneville, A. P. Knights, and J. D. B. Bradley, "Lasing in a Hybrid Rare-Earth Silicon Microdisk," Laser & Photonics Reviews **16**(1), 2100348 (2022).

258. D. J. Jones, S. A. Diddams, J. K. Ranka, A. Stentz, R. S. Windeler, J. L. Hall, and S. T. Cundiff, "Carrier-Envelope Phase Control of Femtosecond Mode-Locked Lasers and Direct Optical Frequency Synthesis," Science **288**(5466), 635–639 (2000).

259. D. Y. Oh, D. Sell, H. Lee, K. Y. Yang, S. A. Diddams, and K. J. Vahala, "Supercontinuum generation in an on-chip silica waveguide," Opt. Lett., **39**(4), 1046–1048 (2014).

260. L. Zhang, A. M. Agarwal, L. C. Kimerling, and J. Michel, "Nonlinear Group IV photonics based on silicon and germanium: from near-infrared to mid-infrared," Nanophotonics **3**(4–5), 247–268 (2014).

261. N. Singh, M. Xin, D. Vermeulen, K. Shtyrkova, N. Li, P. T. Callahan, E. S. Magden, A. Ruocco, N. Fahrenkopf, C. Baiocco, B. P.-P. Kuo, S. Radic, E. Ippen, F. X. Kärtner, and M. R. Watts, "Octave-spanning coherent supercontinuum generation in silicon on insulator from 1.06 μm to beyond 2.4 μm," Light Sci Appl **7**(1), 17131–17131 (2018).

262. K. F. Lamee, K. F. Lamee, D. R. Carlson, D. R. Carlson, Z. L. Newman, Z. L. Newman, S.-P. Yu, S.-P. Yu, S. B. Papp, and S. B. Papp, "Nanophotonic tantala waveguides for supercontinuum generation pumped at 1560 nm," Opt. Lett., **45**(15), 4192–4195 (2020).

263. R. Fan, Y.-Y. Lin, L. Chang, A. Boes, J. Bowers, J.-W. Liu, C.-H. Lin, T.-K. Wang, J. Qiao, H.-C. Kuo, G.-R. Lin, M.-H. Shih, Y.-J. Hung, Y.-J. Chiu, and C.-K. Lee, "Higher order mode supercontinuum generation in tantalum pentoxide (Ta_2O_5) channel waveguide," Sci Rep **11**(1), 7978 (2021).

264. J. R. C. Woods, J. Daykin, A. S. K. Tong, C. Lacava, P. Petropoulos, A. C. Tropper, P. Horak, J. S. Wilkinson, and V. Apostolopoulos, "Supercontinuum generation in tantalum pentoxide waveguides for pump wavelengths in the 900 nm to 1500 nm spectral region," Opt. Express, **28**(21), 32173–32184 (2020).

265. Y. Cao, B.-U. Sohn, H. Gao, P. Xing, G. F. R. Chen, D. K. T. Ng, and D. T. H. Tan, "Supercontinuum generation in a nonlinear ultra-silicon-rich nitride waveguide," Sci Rep **12**(1), 9487 (2022).

266. A. R. Johnson, A. S. Mayer, A. Klenner, K. Luke, E. S. Lamb, M. R. E. Lamont, C. Joshi, Y. Okawachi, F. W. Wise, M. Lipson, U. Keller, and A. L. Gaeta, "Octave-spanning coherent supercontinuum generation in a silicon nitride waveguide," Opt. Lett., **40**(21), 5117–5120 (2015).

267. D. R. Carlson, D. D. Hickstein, A. Lind, S. Droste, D. Westly, N. Nader, I. Coddington, N. R. Newbury, K. Srinivasan, S. A. Diddams, and S. B. Papp, "Self-referenced frequency combs using high-efficiency silicon-nitride waveguides," Opt. Lett., **42**(12), 2314–2317 (2017).

268. Y. Okawachi, M. Yu, J. Cardenas, X. Ji, A. Klenner, M. Lipson, and A. L. Gaeta, "Carrier envelope offset detection via simultaneous supercontinuum and second-harmonic generation in a silicon nitride waveguide," Opt. Lett.,**43**(19), 4627–4630 (2018).

269. I. Rebolledo-Salgado, I. Rebolledo-Salgado, Z. Ye, S. Christensen, F. Lei, K. Twayana, J. Schröder, M. Zelan, and V. Torres-Company, "Coherent supercontinuum generation in all-normal dispersion Si_3N_4 waveguides," Opt. Express, **30**(6), 8641–8651 (2022).

270. E. Tagkoudi, C. G. Amiot, G. Genty, and C.-S. Brès, "Extreme polarization-dependent supercontinuum generation in an uncladded silicon nitride waveguide," Opt. Express, **29**(14), 21348–21357 (2021).

271. Y. Fang, C. Bao, Z. Wang, B. Liu, L. Zhang, X. Han, Y. He, H. Huang, Y. Ren, Z. Pan, and Y. Yue, "Three-Octave Supercontinuum Generation Using SiO_2 Cladded Si_3N_4 Slot Waveguide with All-Normal Dispersion," J. Lightwave Technol., **38**(13), 3431–3438 (2020).

272. A. Frigg, A. Frigg, A. Frigg, A. Boes, G. Ren, I. Abdo, D.-Y. Choi, S. Gees, A. Mitchell, and A. Mitchell, "Low loss CMOS-compatible silicon nitride photonics utilizing reactive sputtered thin films," Opt. Express, **27**(26), 37795–37805 (2019).

273. R.W. Boyd, *Nonlinear optics*. Academic Press, (2020)

274. J. Zou, C. Dong, H. Wang, T. Du, and Z. Luo, "Towards visible-wavelength passively mode-locked lasers in all-fibre format," Light Sci Appl **9**(1), 61 (2020).

275. D. Duchesne, M. Peccianti, M. R. E. Lamont, M. Ferrera, L. Razzari, F. Légaré, R. Morandotti, S. Chu, B. E. Little, and D. J. Moss, "Supercontinuum generation in a high index doped silica glass spiral waveguide," Opt Express **18**(2), 923–930 (2010).

276. D. Liang and J. E. Bowers, "Recent progress in lasers on silicon," Nature Photonics **4**(8), 511–517 (2010).

277. G. N. Tzintzarov, S. G. Rao, and J. D. Cressler, "Integrated Silicon Photonics for Enabling Next-Generation Space Systems," Photonics **8**(4), 131 (2021).

278. R. Chandrasekar, Z. J. Lapin, A. S. Nichols, R. M. Braun, and A. W. Fountain, "Photonic integrated circuits for Department of Defense-relevant chemical and biological sensing applications: state-of-the-art and future outlooks," Optical Engineering **58**(02), 1 (2019).

279. J. I. Mackenzie, "Dielectric solid-state planar waveguide lasers: A review," IEEE Journal on Selected Topics in Quantum Electronics **13**(3), 626–637 (2007).

280. J. D. B. Bradley and M. Pollnau, "Erbium-doped integrated waveguide amplifiers and lasers," Laser and Photonics Reviews **5**(3), 368–403 (2011).

281. Z. Chen, L. Wan, S. Gao, K. Zhu, M. Zhang, Y. Li, X. Huang, and Z. Li, "On-Chip Waveguide Amplifiers for Multi-Band Optical Communications: A Review and Challenge," J. Lightwave Technol. **40**(11), 3364–3373 (2022)

282. K. J. A. Ooi, D. K. T. Ng, T. Wang, A. K. L. Chee, S. K. Ng, Q. Wang, L. K. Ang, A. M. Agarwal, L. C. Kimerling, and D. T. H. Tan, "Pushing the limits of CMOS optical parametric amplifiers with USRN: Si_7N_3 above the two-photon absorption edge," Nature Communications **8**(1), 13878 (2017).

283. C. R. S. Fludger, V. Handerek, and R. J. Mears, "Fundamental Noise Limits in Broadband Raman Amplifiers," Optical Fiber Communication Conference and International Conference on Quantum Information (2001), paper MA5 **54**(1), MA5 (2001).

284. J. Hu, B. S. Marks, and C. R. Menyuk, "Flat-gain fiber Raman amplifiers using equally spaced pumps," Journal of Lightwave Technology **22**(6), 1519–1522 (2004).

285. R. Claps, D. Dimitropoulos, V. Raghunathan, Y. Han, and B. Jalali, "Observation of stimulated Raman amplification in silicon waveguides," Opt. Express 11(15), 1731 (2003).

286. R. L. Espinola, J. I. Dadap, R. M. Osgood, Jr., S. J. McNab, and Y. A. Vlasov, "Raman amplification in ultrasmall silicon-on-insulator wire waveguides," Opt. Express 12(16), 3713 (2004).

284. R. Jones, H. Rong, A. Liu, A. W. Fang, M. J. Paniccia, D. Hak, and O. Cohen, "Net continuous wave optical gain in a low loss silicon-on-insulator waveguide by stimulated Raman scattering," Opt. Express 13(2), 519 (2005).

288. Q. Xu, V. R. Almeida, and M. Lipson, "Demonstration of high Raman gain in a submicrometer-size silicon-on-insulator waveguide," Opt. Lett. 30(1), 35 (2005).

289. A. Liu, H. Rong, M. Paniccia, O. Cohen, and D. Hak, "Net optical gain in a low loss silicon-on-insulator waveguide by stimulated Raman scattering," Opt. Express 12(18), 4261 (2004).

290. T. K. Liang and H. K. Tsang, "Efficient Raman amplification in silicon-on-insulator waveguides," Appl. Phys. Lett. 85(16), 3343–3345 (2004).

291. T. J. Kippenberg, S. M. Spillane, D. K. Armani, and K. J. Vahala, "Ultralow-threshold microcavity Raman laser on a microelectronic chip," Opt. Lett. 29(11), 1224 (2004).

292. H. Choi, D. Chen, F. Du, R. Zeto, and A. Armani, "Low threshold anti-Stokes Raman laser on-chip," Photon. Res. 7(8), 926 (2019)

293. X. Liu, C. Sun, B. Xiong, L. Wang, J. Wang, Y. Han, Z. Hao, H. Li, Y. Luo, J. Yan, T. Wei, Y. Zhang, and J. Wang, "Integrated continuous-wave aluminum nitride Raman laser," Optica **4**(8), 893 (2017).

294 P. Latawiec, V. Venkataraman, M. J. Burek, B. J. M. Hausmann, I. Bulu, and M. Lončar, "On-chip diamond Raman laser," Optica 2(11), 924 (2015).

295. P. Latawiec, V. Venkataraman, A. Shams-Ansari, M. Markham, and M. Lončar, "Integrated diamond Raman laser pumped in the near-visible," Opt. Lett. 43(2), 318

(2018).

296. M. Yu, Y. Okawachi, R. Cheng, C. Wang, M. Zhang, A. L. Gaeta, and M. Lončar, "Raman lasing and soliton mode-locking in lithium niobate microresonators," Light: Science and Applications **9**(1), (2020).

297. L. E. McNeil, M. Grimsditch, and R. H. French, "Vibrational Spectroscopy of Aluminum Nitride," J American Ceramic Society 76(5), 1132–1136 (1993).

298. T. T. Basiev, A. A. Sobol, P. G. Zverev, L. I. Ivleva, V. V. Osiko, and R. C. Powell, "Raman spectroscopy of crystals for stimulated Raman scattering," Optical Materials 11(4), 307–314 (1999).

299. M. Chen, J. Shu, X. Xie, D. Tan, and H. Mao, "Natural diamond formation by self-redox of ferromagnesian carbonate," Proc. Natl. Acad. Sci. U.S.A. 115(11), 2676–2680 (2018).

300. A. Mori, H. Masuda, K. Shikano, and M. Shimizu, "Ultra-wide-band tellurite-based fiber raman amplifier," J. Lightwave Technol. 21(5), 1300–1306 (2003).

301. G. S. Murugan, T. Suzuki, and Y. Ohishi, "Tellurite glasses for ultrabroadband fiber Raman amplifiers," Appl. Phys. Lett. 86(16), 161109 (2005).

302. J. F. Bauters, M. J. R. Heck, D. John, D. Dai, M.-C. Tien, J. S. Barton, A. Leinse, R. G. Heideman, D. J. Blumenthal, and J. E. Bowers, "Ultra-low-loss high-aspect-ratio Si_3N_4 waveguides," Optics Express **19**(4), 3163 (2011).

303. J. F. Bauters, M. J. R. Heck, D. D. John, J. S. Barton, C. M. Bruinink, A. Leinse, R. G. Heideman, D. J. Blumenthal, and J. E. Bowers, "Planar waveguides with less than 0.1 dB/m propagation loss fabricated with wafer bonding," Optics Express **19**(24), 24090 (2011).

304. E. M. Dianov, I. A. Grishin, M. F. Churbanov, V. G. Plotnichenko, V. O. Sokolov, and V. V. Koltashev, "Raman band intensities of tellurite glasses," Optics Letters, **30**(10), 1156–1158 (2005).

305. G. S. Murugan, T. Suzuki, and Y. Ohishi, "Tellurite glasses for ultrabroadband fiber Raman amplifiers," Applied Physics Letters **86**(16), 1–3 (2005).

306. Robert. Stegeman, "Direct Nonlinear Optics Measurements of Raman Gain in Bulk Glasses and Estimates of Fiber Performance," Electronic Theses and Dissertations. 907, https://stars.library.ucf.edu/etd/907

307. C. Rivero, R. Stegeman, M. Couzi, D. Talaga, T. Cardinal, K. Richardson, G. Stegeman, H. Seo, K. Oh, F. Galeener, J. C. Mikkelsen Jr, R. H. Geils, W. J. Mosby, A. Mori, H. Masuda, K. Shikano, K. Oikawa, K. Kato, M. Shimizu, R. Stegeman, L. Jankovic, H. Kim, C. Rivero, G. Stegeman, K. Richardson, P. Delfyett, Y. Guo, A. Schulte, T. Cardinal, E. Fargin, M. Couzi, A. Pope, P. Thomas, J. Champarnaud-Mesjard, G. Dai, F. Tassone, A. Li Bassi, V. Russo, and C. Bottani, "Resolved discrepancies between visible spontaneous Raman cross-section and direct near-infrared Raman gain measurements in TeO_2-based glasses," Optics Express, **13**(12), 4759–4769 (2005).

308. M. E. Lines, "Raman-gain estimates for high-gain optical fibers,''*J. Appl. Phys.* 62, 4363 (1987).

309. Y. Guo, "Raman Spectroscopy of Glasses with High and Broad Raman Gain in The Boson Peak Region" *Electronic Theses and Dissertations*, 996 https://stars.library.ucf.edu/etd/996

310. H. Rong *et al.*, "Low-threshold continuous-wave Raman silicon laser," *Nat. Photonics* 1 (**4**), 232–237 (2007).

311. M. Irannejad, G. Jose, A. Jha, and P. Steenson, "Raman gain in modified tellurite glasses and thin films," *Opt. Commun.*, 285(**10–11**), 2646–2649 (2012).

312. M. G. Donato *et al.*, "Raman optical amplification properties of sodium-niobium-phosphate glasses," *Appl. Phys. Lett.*97 (**23**), 23111 (2010).